

### LIBRARY Michigan State University

### This is to certify that the dissertation entitled

### SINGLE TOP QUARK PRODUCTION AND DECAY IN HADRON COLLISION AT NEXT-TO-LEADING ORDER

presented by

#### **QINGHONG CAO**

has been accepted towards fulfillment of the requirements for the

Doctoral	degree in	Physics
4	Major Pro	pressor's Signature  Aug. 16, 2005  Date

MSU is an Affirmative Action/Equal Opportunity Institution

PLACE IN RETURN BOX to remove this checkout from your record.

TO AVOID FINES return on or before date due.

MAY BE RECALLED with earlier due date if requested.

DATE DUE	DATE DUE	DATE DUE

2/05 c:/CIRC/DateDue.indd-p.15

# SINGLE TOP QUARK PRODUCTION AND DECAY IN HADRON COLLISION AT NEXT-TO-LEADING ORDER

 $\mathbf{B}\mathbf{y}$ 

Qinghong Cao

#### A DISSERTATION

Submitted to
Michigan State University
in partial fulfillment of the requirements
for the degree of

DOCTOR OF PHILOSOPHY

Department of Physics and Astronomy

2005

#### ABSTRACT

## SINGLE TOP QUARK PRODUCTION AND DECAY IN HADRON COLLISION AT NEXT-TO-LEADING ORDER

by

#### Qinghong Cao

The top quark is by far the heaviest known fermion and the only known fermion with a mass at the electroweak symmetry breaking scale. Thus, it is hoped that a detailed study of top quark coupling to other particles will be of great utility in determining if the Standard Model mechanism for electroweak symmetry-breaking is the correct one, or if new physics is responsible. If the top quark does play a special role in nature, one must discover this fact through careful study of its properties which requires more accurate theoretical prediction. In this work we present a calculation of the next-to-leading order QCD corrections, with one-scale phase space slicing method, to the s-channel and the t-channel single top quark production and decay process at hadron colliders. Using the helicity amplitude method, the angular correlation of the final state particles and the spin correlation of the top quark are preserved. We discuss the effects of different contributions on the inclusive cross section of the single top production as well as various kinematic distributions after imposing the relevant cuts to select the single top signal events. The physics of single top production at the Tevatron is carefully studied, with a particular eye towards various kinematical distributions of the final state particles which can help to disentangle the single top event from the copious QCD backgrounds. After reconstructing the single top event, its polarization is examined in different spin bases.

To my parents, my wife and my daughter,

my true love and inspiration

#### ACKNOWLEDGMENTS

I am grateful to my thesis advisor, Prof. C.-P. Yuan, whose generous support and his helpful advice have kept me on track through the years. He has spent a significant effort and time to teach me new knowledge and skills. I have benefited continuously from his ability to spot what is important. I own my deep appreciation to Prof. Wu-Ki Tung who supported me financially even I did not work with him. I would like to express my gratitude to my mentor, Chong Sheng Li, for sparking my interest in this field.

I would like to thank my colleagues in the High Energy group: Raymond Brock, R. Sekhar Chivukula, Joey Huston, Jon Pumplin, Wayne Repko, Carl Schmidt, Elizabeth H. Simmons, Dan Stump and Wu-Ki Tung. They gave me very important information and advice. I also want to thank my committee members Prof. Vladimir Zelevinsky and Prof. Bhanu Mahanti for useful guidance.

I am further grateful to our former and current post-docs: Alexander S. Belyaev, Shrihari Gopalakrishna, Yu Jia, Shinya Kanemura, Stefan Kretzer, Daisuke Nomura, Reinhard Schwienhorst and Kazuhiro Tobe for many illuminating discussions; to my graduate student colleagues: Aws Abdo, Jorge Benitez, Chuan-Ren Chen, Roshan Foadi, Iris Gebauer, HyeongKwan Kim and Pavel Nadolsky for the happy time in our office.

I am sincerely grateful to Debbie Simmons and Brenda Wenzlick for their kindness and help during my years at Michigan State University.

## Contents

LI	ST (	OF FI	GURES	ix
LI	IST (	OF TA	BLES	xv
1	Inti	roduct	ion	1
2	Tec	hnique	es of NLO calculation	12
	2.1	Narro	w width approximation	12
		2.1.1	Helicity matrix elements of single top quark production	16
		2.1.2	Helicity matrix elements of top quark decay	17
	2.2	Regul	arization schemes and $\gamma_5$ problem	18
		2.2.1	Dimensional regularization scheme	19
		2.2.2	Dimensional reduction scheme	20
		2.2.3	Conversion between DREG and DRED	22
	2.3	Phase	space slicing method	26
3		O mat	rix elements of Single top quark production and decay	y 33
	3.1	catego	orizing the single top quark processes	33
	3.2	Form	factor formalism for SCV corrections	36
		3.2.1	NLO corrections to INIT	36
		3.2.2	NLO corrections to FNAL	37
		3.2.3	NLO corrections to LIGHT	39
		3.2.4	NLO corrections to HEAVY	39
		3.2.5	NLO corrections to top quark decay	40
	3.3		ty amplitudes of resolved contributions to single top quark pro- on and decay	41
		3.3.1	NLO corrections to INIT	41
		3.3.2	NLO corrections to FNAL	43

		3.3.3	NLO corrections to LIGHT	44
		3.3.4	NLO corrections to HEAVY	47
		3.3.5	NLO corrections to top quark decay	50
	3.4		SCV form factor of the single top quark production and decay	
		-	SS	51
		3.4.1	NLO corrections to INIT	51
		3.4.2	NLO corrections to FNAL	57
		3.4.3	NLO corrections to LIGHT	62
		3.4.4	NLO corrections to HEAVY	64
		3.4.5	NLO corrections to the decay process $t \to Wb' \ldots \ldots$	67
	3.5	Combi	ining the production and decay processes	68
4	Incl	lusive 1	rate of the single top process at NLO	72
	4.1	Theore	etical Cutoff Dependence	73
	4.2	Top qu	uark mass and scale dependence	76
		4.2.1	s-channel process	77
		4.2.2	t-channel process	78
	4.3	Inclusi	ive Cross Section	80
5	Phe	enomer	$oldsymbol{s}$ -channel	86
	5.1	Jet fin	nding algorithm	87
	5.2	Accep	tance Studies	88
	5.3	Single	Top Event Distributions	91
		5.3.1	Final State Object Distributions	93
		5.3.2	Event Reconstruction	99
		5.3.3	Kinematical and Spin Correlations	103
				104
		5.3.4	Distributions for three-jet event	113
			5.3.4.1 Kinematic Distribution of the Extra Jet	113
			5.3.4.2 Angular Correlation Between the Extra Jet and the Best-Jet	116
	5.4	Single		117
	5.5	_		119
6	Phe	enomer	$oxed{nology:} t ext{-channel}$	122
	6.1	Event	Topology	123
	6.2			126
	6.3	_		129

		6.3.1	Final St	ate Object Distributions	131
			6.3.1.1	Charged Lepton and Missing Transverse Energy	131
			6.3.1.2	Spectator Jet	133
			6.3.1.3	<i>b</i> Jet	136
			6.3.1.4	$H_T$ Distribution	139
		6.3.2	Event R	Reconstruction	140
		6.3.3	Top Qua	ark Polarization	146
		6.3.4	Distribu	tions for Three-jet Events	153
			6.3.4.1	Kinematic Distribution of the Extra Jet	156
			6.3.4.2	Angular Correlation Between the Extra Jet and the Best Jet	160
	6.4	Conclu	ision		161
7	Sun	nmary	and out	look	164
A	Hel	icity A	.mplitud	les	167
В	$A_h$ a	and $B_h$	in the	Crossing Functions	169
$\mathbf{C}$	Scal	lar fun	ctions		172
	C.1	Definit	tion		172
	C.2	Tensor	reductio	on	174
	C.3	UV-di	vergent p	earts of tensor integrals	175
	C.4	Scalar	two-poin	t function	176
	C.5	Scalar	three-po	int function	178
		C.5.1	Analytic	cal result of $C_0(p_1^2, p_2^2, 0, 0, 0)$	178
		C.5.2	Analytic	cal result of $C_0((p_1+p_2)^2,(-p_2)^2,0,m_t^2,0)$	180
D	Vir	tual Co	orrection	าร	183
	D.1	Virtua	l correcti	on to $W^{+*} \rightarrow \bar{q}q'$	183
	D.2	Virtua	l correcti	on to $W^{+*} \to t\bar{b}$	188
$\mathbf{E}$				Soft and Collinear	193
	E.1				193
		E.1.1	Soft con	tribution	193
				r contribution	197
	E.2	$W^* \rightarrow$	$tar{b}$		200

		Soft contribution Collinear contribution													
F	$\Gamma$ function		·	·	·	·		·		•	•	•		·	204
$\mathbf{B}^{i}$	bliography														206

# List of Figures

1.1	Implication of precision measurement of $m_t$ and $M_W$ on the indirect extraction of the Higgs boson mass. The Standard Model allows only the shaded region	3
1.2	Feynman diagrams of the single top quark production	9
2.1	The representative Feynman diagrams of the interference effects at the NLO. (a) virtual correction (b) real correction	13
2.2	Feynman diagrams of the Born level contribution to the production and decay of single top quark. (a) $s$ -channel (b) $t$ -channel	14
2.3	Feynman diagram for $q\bar{q'} \rightarrow W^+$	22
2.4	Illustration of the PSS method with one cutoff scale to describe the processes with initial state massless quarks. Here, only half of the real emission diagrams is shown. In this paper, we will assign the particle's momentum such that the initial state particle's momentum is incoming to the vertex while the final state particle's momentum is outgoing.	30
3.1	The way we organize our calculations at the NLO. The blobs in the diagrams denote the higher order QCD corrections, including both virtual and real emission contributions	35
3.2	Feynman diagrams of the real emission corrections to s-channel single top quark production	43
3.3	Feynman diagrams of the real emission corrections to the t-channel single top quark production	45
3.4	Feynman diagrams of the real emission corrections to top quark decay processes	50
3.5	Illustration for crossing the initial state partons into the final state in the process $q\bar{q}' \to W^*g$	53
3.6	The $s_{ar q g} - s_{q'g}$ plane for quark pair annihilation to virtual W-boson	
	showing the delineation into soft $(\mathcal{F}_2)$ and collinear $(\mathcal{F}_2)$ and resolved region $(\mathcal{F}_1)$	54

3.7	The $s_{tg}-s_{ar{b}g}$ plane for quark pair annihilation to virtual W-boson	
	showing the delineation into soft $(\mathcal{F}_2)$ and collinear $(\mathcal{F}_2)$ and resolved region $(\mathcal{F}_1)$	59
4.1	The theoretical cutoff $s_{min}$ dependence of the inclusive single top quark cross section at the Tevatron with $\mu_R = \mu_F = m_t$ for $m_t = 178 \text{GeV}$ . The decay branching ratio $t \to bW^+(\to e^+\nu)$ has been included. (a) s-channel (b) t-channel	75
4.2	Top quark mass as well as renormalization and factorization scale dependence of the inclusive s-channel single top quark cross section at Tevatron. The decay branching ratio of $t \to bW^+(\to e^+\nu)$ has been included	77
4.3	Inclusive s-channel single top quark cross section at Tevatron for $m_t=178$ GeV, versus the ratio of the factorization scale $\mu_F$ to its typical	
	value $\mu_0$ , where $\mu_0 = m_t$ and $\mu_0 = \sqrt{\hat{s}}$ , respectively. The decay branching ratio of $t \to bW^+(\to e^+\nu)$ has been included	78
4.4	Top quark mass dependence as well as renormalization and factorization scale dependence of the inclusive $t$ -channel single top quark cross section at the Tevatron. The decay branching ratio of $t \to bW^+(\to bW^+)$	
	$e^+ u$ ) has been included	79
4.5	Inclusive t-channel single top quark production cross section at the Tevatron for $m_t = 178$ GeV, versus the ratio of the factorization scale $\mu_F$ to its typical value $\mu_0$ , where $\mu_0 = m_t$ (solid line) and $\mu_0 = M_W$	
	(dashed line), respectively. The decay branching ratio of $t \to bW^+(\to$	
	$e^+ u$ ) has been included	80
5.1	Cross section and fraction of 3-jet events at NLO for varying jet $E_T$ cuts, requiring only that $n_{jets} \geq 2$ , and not making any cuts on the electron or neutrino. The upper figure shows the total cross section for events with 2 or 3 jets as a function of the jet $E_T$ cut for three different jet pseudo-rapidity cuts. The lower figure shows the fraction of 3-jet events as a function of the jet $E_T$ for different jet pseudo-rapidity cuts. The lowest threshold considered is 15 GeV	92
5.2	The transverse momentum $p_T$ (a) and pseudo-rapidity $\eta$ (b) distributions of the electron and the missing transverse energy $\not\!\!E_T$ (c) after selection cuts, comparing Born-level to $O(\alpha_s)$ and full NLO	94
5.3	Transverse momentum $p_T$ of the $b$ jet (left) and the $\bar{b}$ jet (right) after selection cuts, comparing Born-level to $O(\alpha_s)$ corrections. The bottom row shows the different $O(\alpha_s)$ contributions	96
5.4	Pseudo-rapidity $\eta$ of the $b$ -jet (left) and the $\bar{b}$ -jet (right) after selection cuts, comparing Born level to $O(\alpha_s)$ corrections	98
5.5	Total event transverse energy $H_T$ after selection cuts, comparing Born level to $O(\alpha_s)$ corrections.	98

5.6	Transverse momentum distribution of the $b$ jet from the top quark decay, for all events that pass the loose set of cuts (solid line), only for those events in which the $b$ jet is also the leading jet (dashed line), and only for events in which the $b$ jet is the best-jet (dotted line)	101
5.7	Invariant mass of the reconstructed $W$ and a jet object. This jet object is: the jet containing the $b$ quark from the top decay, using parton information (solid line); the best-jet identified using the method outlined in the main text (dashed line); the leading jet (dotted line)	102
5.8	Transverse momentum and rapidity of the reconstructed top quark, comparing Born-level to $O(\alpha_s)$ corrections	103
5.9	Transverse momentum difference between the best-jet and the non-best-jet (left) and pseudo-rapidity difference between the two (right) after selection cuts, comparing Born-level to $O(\alpha_s)$ corrections	104
5.10	Illustration of the correlation between the charged lepton from the top decay and the top quark spin, in the top quark rest frame	105
5.11	Top quark polarization in the helicity basis using the full parton information (left) and after event reconstruction (right) with selection cuts, comparing Born-level to $O(\alpha_s)$ corrections	109
5.12	Top quark polarization in the "optimal basis" using the full parton information (left) and after event reconstruction(right) with selection cuts, comparing Born-level to $O(\alpha_s)$ corrections	109
5.13	Transverse momentum (left) and pseudo-rapidity of the third jet after selection cuts for the various $O(\alpha_s)$ contributions	114
5.14	Distance between the third jet and the best-jet (left) and distance between the third jet and the non-best-jet (right) after selection cuts for the various $O(\alpha_s)$ corrections	115
5.15	Angular correlation $\cos\theta$ between the gluon and the b quark before any selection cuts using the full parton information (left) and between the third jet and the best-jet after selection cuts (right). The solid line shows all $O(\alpha_s)$ contributions except for the decay part, while the dashed line shows only the $O(\alpha_s)$ decay contribution	117
5.16	Invariant mass of the $(b$ -jet, $\bar{b}$ -jet) system after selection cuts, comparing Born-level to $O(\alpha_s)$ corrections	118
5.17	Angular distance $cos\theta$ between a b-tagged jet and the (b jet, $\bar{b}$ jet) system after selection cuts, comparing Born-level to $O(\alpha_s)$ corrections.	119
6.1	Pictorial illustration of the notation used in this paper	123
6.2	Representative diagrams of the real emission corrections for the t-channel single top process: (a) and (b) represent the real radiative corrections to the LIGHT quark line, while (c) and (d) represent the real radiative corrections to the HEAVY quark line. The NLO QCD corrections are indicated by the large shaded ellipse. Detailed Feynman diagrams can be found in Fig. 3.2 and Fig. 3.3	124

6.3	Cross section and fraction of three-jet events at NLO for varying jet $p_T$ cuts, requiring only that $n_{jets} \geq 2$ , and not making any cuts on the electron or neutrino. Shown is the total cross section for events with two or three jets as a function of the jet $E_T$ cut for three different jet pseudo-rapidity cuts (a) and the fraction of three-jet events as a function of the jet $p_T$ for different jet pseudo-rapidity cuts (b). The lowest threshold considered is 15 GeV	130
6.4	The transverse momentum $p_T$ (a) and pseudo-rapidity $\eta$ (b) distributions of the electron and the missing transverse energy $E_T$ (c) after selection cuts, comparing Born-level to $O(\alpha_s)$ corrections	132
6.5	Transverse momentum $p_T$ (a), energy $E$ (b) and the pseudo-rapidity $\eta$ (c) of the spectator jet after selection cuts, comparing Born-level to $O(\alpha_s)$ corrections	134
6.6	Each individual contribution of the $O(\alpha_s)$ corrections to the spectator jet pseudo-rapidity, summed (a), separately for the case when the incoming up-type quark is from the proton and anti-proton (b). Here, "PA" and "AP" denotes the initial state light quark originating from proton and anti-proton, respectively	136
6.7	Transverse momentum $p_T$ of the $b$ jet after selection cuts, comparing Born-level to $O(\alpha_s)$ corrections (a) and the individual $O(\alpha_s)$ contributions (b)	137
6.8	Pseudo-rapidity $\eta$ of the $b$ -jet after selection cuts, comparing Born level to $O(\alpha_s)$ corrections.	137
6.9	Momentum of the $b$ and $\bar{b}$ jets (a) and fraction of events with one or two $b$ -tagged jets as a function of the jet $p_T$ threshold, for both inclusive two-jet and exclusive three-jet events (b)	138
6.10	Total event transverse energy $H_T$ after selection cuts, comparing Born level to $O(\alpha_s)$ corrections (a) and the individual $O(\alpha_s)$ contributions (b)	139
6.11	Transverse momentum of the $b$ quark jet, for all events (solid histogram), only for those events for which the leading $b$ -tagged jet corresponds to the $b$ quark jet (dashed histogram), only for those events in which the best jet corresponds to the $b$ quark jet (dotted histogram), and only for those events in which the leading jet corresponds to the $b$ quark jet (dash-dotted histogram). The transverse momentum is shown for the inclusive two-jet sample (a) and for the exclusive three-jet sample (b)	141
6.12	Invariant mass of the reconstructed $W$ and a jet object. This jet object is: the jet containing the $b$ quark from the top decay, using parton information (solid line), the leading $b$ -tagged jet (dashed line), the best jet (dotted line), or the leading jet (dot-dashed line). The $W$ is reconstructed either using the standard neutrino $p_z^{\nu}$ constraint (a) or a top mass constraint (b)	144
6.13	Transverse momentum of the reconstructed top quark, comparing Born-level to $O(\alpha_s)$ corrections(a) and the individual $O(\alpha_s)$ contributions	1.45
	(b)	145

6.14	Rapidity of the reconstructed top quark, comparing Born-level to $O(\alpha_s)$ corrections(a) and the individual $O(\alpha_s)$ contributions (b)	145
6.15	Illustration of the three choices for the top quark spin basis. The circle denotes the top quark rest frame and the blue arrows denote the top quark spin direction	147
6.16	Top quark polarization in the helicity basis using the full parton information (a) and after event reconstruction with selection cuts (b), comparing Born-level to $O(\alpha_s)$ corrections. The Born-level and NLO curves have been normalized to the same area	148
6.17	Top quark polarization in the spectator basis using the full parton information (a) and after event reconstruction with selection cuts (b), comparing Born-level to $O(\alpha_s)$ corrections. The Born-level and NLO curves have been normalized to the same area	150
6.18	Top quark polarization in the beamline basis using the full parton information (a) and after event reconstruction with selection cuts (b), comparing Born-level to $O(\alpha_s)$ corrections. The Born-level and NLO curves have been normalized to the same area	151
6.19	Inclusive cross section and fraction of three-jet events at NLO for varying jet pseudo-rapidity cuts, after the loose selection cuts. Shown is the total cross section as a function of the jet pseudo-rapidity cut (a) and the fraction of two-jet and three-jet events as a function of the jet pseudo-rapidity cut (b)	155
6.20	Fraction of events with one or two $b$ -tagged jets for the inclusive sample and the exclusive three-jet sample as a function of the pseudo-rapidity cut on the $b$ -tagged jets (a), and fraction of events with two tagged jets as a function of the $p_T$ threshold on the $b$ -tagged jets for three different pseudo-rapidity cuts (b), after the loose selection cuts	156
6.21	Transverse momentum (a) and pseudo-rapidity (b) of the third jet after selection cuts for the various $O(\alpha_s)$ contributions	157
6.22	Separation between the third jet and the tagged jet (a) and between the third jet and the untagged jet (b) after selection cuts for the various $O(\alpha_s)$ corrections	158
6.23	Angular correlation $\cos\theta$ between the gluon and the b quark before any selection cuts using the full parton information (a) and between the third jet and the best jet after selection cuts (b). The solid line shows all $O(\alpha_s)$ contributions except for the decay part, while the dashed line shows only the $O(\alpha_s)$ decay contribution	161
C.1	The three-point green function with massless internal particles	178
C.2	The three-point green function with one massive internal particle	180
D.1	Feynman diagram for process $W^* \to q' \bar{q}$	183
D.2	Feynman diagram for process $W^* \to t\bar{b}$	188
D.3	Feynman diagram of the self-energy correction to top quark	190

E.1	Kinematics of $\bar{q}$ , $q'$	and $g$ in the rest frame of $W^*$	193
E.2	Kinematics of $\bar{q}, q'$	and q in the collinear region $q \parallel \bar{q}$ in $W^* \rightarrow \bar{q}q'q$ .	197

Images in this dessertation are presented in color.

## List of Tables

4.1	Inclusive single-top production cross section for different subprocesses, including the top quark decay branching ratio $t \to bW^+(\to e^+\nu)$	82
4.2	Inclusive t-channel single top production cross section for different subprocesses, including the top quark decay branching ratio $t \to bW^+(\to$	
	$e^+\nu$ )	83
5.1	The s-channel single-top production cross section and acceptance at the Tevatron (in fb) for different subprocesses under various scenario: (a) is for the loose version with $\eta_l^{max} = 2.5$ , $\eta_j^{max} = 3.0$ , and $R_{cut} = 0.5$ ,	
	(b) is for the loose version with a larger jet clustering cone size (and jet-lepton separation cut) of $R_{cut}=1.0$ , and (c) is for the tight version of cuts with $\eta_l^{max}=1.0$ , $\eta_j^{max}=2.0$ , and $R_{cut}=0.5$ . The first	
	two columns show the Born level and full NLO cross sections, the last three columns the contribution from the different $O(\alpha_s)$ processes. The decay branching ratio $t \to bW(\to e\nu)$ is included	89
5.2	Degree of polarization $\mathcal{D}$ , polarization fraction $\mathcal{F}$ , and asymmetry $\mathcal{A}$ for inclusive two-jet single top quark events, at the parton level (Parton) and after event reconstruction (Recon.), in the s-channel process. Here, $\mathcal{F}$ corresponds to $\mathcal{F}_{-}$ in the helicity basis for left-handed top quarks and to $\mathcal{F}_{+}$ in the optimal basis for top quarks with polarization along the direction of anti-proton three momentum, respectively. The $t\bar{b}g$ frame in the helicity basis denotes the c.m. frame of the incoming partons while $t\bar{b}$ frame denotes the rest frame of the reconstructed top	111
5.3	quark and $\bar{b}$ quark	111
	YUGIA	112

6.1	The t-channel single top production cross section at the Tevatron (in fb) for different subprocesses under various cut scenarios: (a) is the loose version with $\eta_l^{max} = 2.5$ , $\eta_j^{max} = 3.0$ , and $R_{cut} = 0.5$ , (b) is	
	the loose version with a larger jet clustering cone size (and jet-lepton separation cut) of $R_{cut}=1.0$ , and (c) is the tight version of cuts with $\eta_l^{max}=1.0$ , $\eta_j^{max}=2.0$ , and $R_{cut}=0.5$ . The first two columns	
	show the Born-level and full NLO cross sections, the last three columns show the contributions from the different $O(\alpha_s)$ processes. The decay branching ratio $t \to bW(\to e\nu)$ is included	128
6.2	Degree of polarization $\mathcal{D}$ , polarization fraction $\mathcal{F}$ , and asymmetry $\mathcal{A}$ for inclusive two-jet single top quark events, at the parton level (Parton) before cuts and after selection cuts and event reconstruction (Recon.), in the t-channel process. Here, $\mathcal{F}$ corresponds to $\mathcal{F}$ in the helicity basis for left-handed top quarks and to $\mathcal{F}_+$ in the spectator and beamline bases for top quarks with polarization along the direction of the spectator-jet and proton three momentum, respectively. Also, the $tq(j)$ -frame in the helicity basis denotes the c.m. frame of the incoming partons, while the $tq$ -frame denotes the rest frame of the top quark and spectator jet	152
6.3	Degree of polarization $\mathcal{D}$ , polarization fraction $\mathcal{F}$ , and asymmetry $\mathcal{A}$ for exclusive three-jet single top quark events, at parton level and after event reconstruction, in the $t$ -channel process. Here, $\mathcal{F}$ corresponds to $\mathcal{F}_{-}$ in the helicity basis for left-handed top quarks and to $\mathcal{F}_{+}$ in the spectator and beamline bases for top quarks with polarization along the direction of the spectator-jet and proton three momentum, respectively. The $tq(j)$ frame in the helicity basis denotes the c.m. frame of the incoming partons, while the $tq$ frame denotes the rest frame of the reconstructed top quark and light quark.	154

### Chapter 1

### Introduction

A major concern in today's High Energy Physics is to find the origin of the electroweak symmetry breaking (EWSB) and the flavor symmetry breaking. In the Standard Model (SM), both of them are related to the generation of mass terms; the first one for generating the mass of the electroweak interaction bosons (W and Z), and the second one for generating the hierarchical mass pattern of the three families of quarks and leptons. The SM Higgs mechanism can explain both symmetry breakings, but in doing so it leaves many other questions unanswered. Moreover, this mechanism predicts the existence of a fundamental spin zero particle (the Higgs boson) that so far has not been observed. Because the mass of the top quark is about the electroweak symmetry breaking scale, the interactions of the top quark may well provide critical information on the true nature of the electroweak symmetry breaking mechanism and give hints on the flavor symmetry breaking mechanism.

The discovery of the top quark at Fermilab's  $p\bar{p}$  collider Tevatron in 1995 by the CDF and D0 collaborations suggested the direct experimental confirmations of the three-generation structure of the SM and opened up the new field of top quark physics. It is interesting to point out that the top quark was already believed to exist even before its experimental discovery because of the theoretical consistency of the SM gauge theory (anomaly cancellation), consistency of b quark measurements with SM predictions, and consistency of precision measurements with the SM. The top quark is of particular importance in the SM for the following reasons:

1. Heavy mass: The most striking observed feature that sets the top quark apart from the other quarks is its very large mass. It is approximately forty times heavier than its partner, with a mass of 178 ± 4.3 GeV as measured from the Tevatron Run I data [1]. The precision measurement of the top quark mass (m<sub>t</sub>) is very important to the Higgs boson search because the masses of top quark, W-boson and Higgs boson are correlated through the radiative corrections in the SM. While m<sub>t</sub> is measured, the question of whether and to what extent it is possible to constrain the unknown Higgs boson mass (M<sub>H</sub>), has become of considerable interest. One example is the W-boson mass (M<sub>W</sub>) which receives quantum corrections proportional to m<sub>t</sub><sup>2</sup> and ln (M<sub>H</sub>) (in the MS framework) [2],

$$M_W = 80.3827 - 0.0579 \ln \left( \frac{M_H}{100 \,\text{GeV}} \right)$$

$$- 0.008 \ln^2 \left( \frac{M_H}{100 \,\text{GeV}} \right) + 0.543 \left( \left( \frac{m_t}{175 \,\text{GeV}} \right)^2 - 1 \right)$$

$$- 0.517 \left( \frac{\Delta_{had}^{(5)}(M_Z)}{0.0280} - 1 \right) - 0.085 \left( \frac{\alpha_s(M_Z)}{0.118} - 1 \right), \quad (1.1)$$

where  $m_t$ ,  $M_W$ , and  $M_H$  are expressed in GeV units. This is usually plotted as  $m_t$  vs.  $M_W$ , overlaid with bands that show the predicted  $M_H$ , as in Fig. 1.1. A "light" Higgs is favored, somewhere around 100 GeV, but with an uncertainty also of  $\mathcal{O}(100)$  GeV. The Higgs mass prediction extracted from precision measurements can be compared with the direct measurement of the Higgs mass at the LHC and the consistency of the Standard Model test.

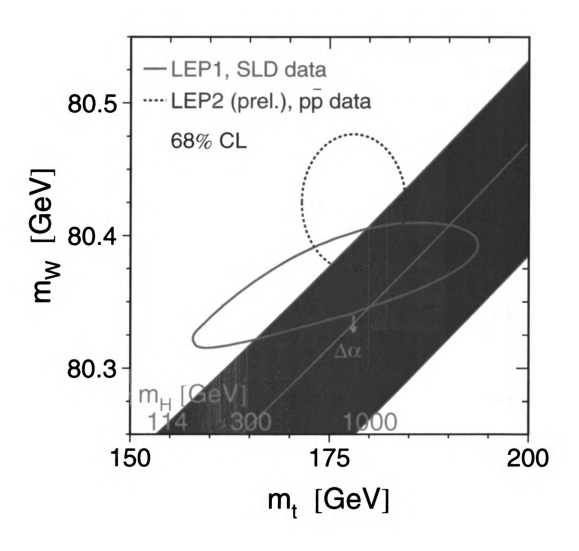


Figure 1.1: Implication of precision measurement of  $m_t$  and  $M_W$  on the indirect extraction of the Higgs boson mass. The Standard Model allows only the shaded region.

2. Short lifetime: The top quark decays before it can hadronize, since its lifetime

$$\Gamma_{\text{top}}^{-1} = (1.5 \,\text{GeV})^{-1} \sim 5 \times 10^{-25} \,\text{sec},$$

is much less than the QCD time scale

$$\Lambda_{\rm QCD}^{-1} = (200 \, {\rm MeV})^{-1} \sim 3 \times 10^{-24} \, {\rm sec.}$$

Therefore, there are no top mesons or baryons. As a result, the decay of top quarks offers a unique window on the properties of a bare quark free from the long-range effects of QCD, such as confinement. Since  $|V_{tb}| \sim 1$ , the top quark decays almost 100% of time into a W-boson and a b-quark via the weak interaction. Its decay width is, at the leading order,

$$\Gamma_t^{(0)}(t \to bW^+) = \frac{G_F m_t^3}{8\sqrt{2}\pi} |V_{tb}|^2 \lambda^{1/2} \left(1, \frac{m_b}{m_t}, \frac{M_W}{m_t}\right) \times \left[\left(1 - \frac{m_b^2}{m_t^2}\right)^2 + \left(1 + \frac{m_b^2}{m_t^2}\right) \frac{M_W^2}{m_t^2} - 2\frac{M_W^4}{m_t^4}\right]. \quad (1.2)$$

Here  $\lambda(x,y,z)=(x^2-y^2-z^2)^2-4y^2z^2$ . In the limit  $m_b\to 0$ , the tree level rate simplifies considerably, becoming

$$\Gamma_t^{(0)}(t \to bW^+) = \frac{G_F m_t^3}{8\sqrt{2}\pi} |V_{tb}|^2 \left(1 - \frac{M_W^2}{m_t^2}\right)^2 \left(1 + \frac{2M_W^2}{m_t^2}\right). \tag{1.3}$$

Since the top quark decays into a  $W^+$  and a b with a branching ratio (BR) close to one, top decays are distinguished by the W-boson decay products. The  $W^+$  will consequently decay into one of the three lepton doublets or one of the  $2N_C$  light quark doublets ( $u\bar{d}$  and  $c\bar{s}$ ). Hence, the hadronic decays ( $W^+ \to qq'$ ) are dominant (with BR  $\sim 6/9$ ). However, the leptonic decays ( $W^+ \to \ell^+ \nu_\ell$  with  $\ell = e, \mu, \tau$ ) generally provide a clean signature at a hadron collider.

3. Spin correlation: Because of the very short lifetime, the top quark decays before the strong interaction has time to depolarize its spin. (The spin-depolarization time,  $(\Lambda_{QCD}^2/m_t)^{-1} \approx (1.3 \, \text{MeV})^{-1}$ , is three orders of magnitude longer than the top quark lifetime [3].) Furthermore, the weak decay of the top quark is sensitive to its spin orientation; the angular distribution of the top quark's decay products acts as a spin analyzer. As a particle of exceptionally large mass, the polarization analyses of the top quark can shed light on its anomalous magnetic dipole moments, as well as on non-SM right-handed current admixtures to the decay amplitude. In the SM, the W-t-b vertex is entirely left-handed, which means that the top polarization information is passed on to its decay products, the W boson and b quark. Being on-shell, the W boson's helicity in top decay is very different from that in the decays of any other quark, where the W boson is highly virtual. The left-handed nature of the SM interaction demands that the produced W bosons be either transversely left-handed or longitudinally polarized when ignoring the b quark mass, and predicts the specific ratio of

$$\frac{f_0}{f_L} = \frac{m_t^2}{2m_W^2 + m_t^2} \simeq 70\%. \tag{1.4}$$

The degree of W polarization from top decays can be reconstructed by studying the angle between the W momentum and the charged lepton momentum in the W rest frame, because the W helicity is correlated with the momentum of the decay leptons: Right-handed polarized W bosons give rise to harder charged leptons than left-handed polarized W bosons.

Due to the interesting features mentioned above, the top quark physics has drawn much attention after its discovery. In fact, examining its production and decay characteristics and accurately measuring its mass, polarization and other properties have become one of the most important tasks of high energy physics in the last decade.

Several properties of the top quark were studied at the Tevatron during the Tevatron first run. For example,  $t\bar{t}$  pair production cross section and its kinematical properties, the top mass, tests of the SM t-b-W coupling via studies of W helicity in top decays and spin correlations in  $t\bar{t}$  production, etc. Needless to say, it will continue to be the major issue at the LHC in the future\*.

In hadronic interactions, the top quark is produced predominantly through the Quantum Chromodynamics interaction (QCD): by  $q\bar{q}$  annihilation  $(q\bar{q} \to t\bar{t})$  and by gluon fusion  $(gg \rightarrow t\bar{t})$ . Though it is possible to study the decay branching ratios of the top quark in  $t\bar{t}$  pairs, to test the coupling of top quark with bottom quark (b) and W gauge boson or to measure the width of the top quark in hadron collisions, it is best to study the single-top quark production. In contrast to the top quark pair production, the single top quark is produced through the electroweak interaction connecting top quark to the down-type quarks, with amplitudes proportional to the Cabibbo-Kabayashi-Maskawa (CKM) matrix elements. Furthermore, unlike the unpolarized top quark pairs produced at the Tevatron and LHC which are unpolarized beam machines, the top quark produced via single-top processes is highly polarized due to the left-handed nature of charged weak current interaction. Its polarization information remains among its decay products and can be studied from the angular distributions of its decay particles. Hence, measuring the rate of the single-top event can directly probe the electroweak properties of the top quark. For example, it can be used to measure the CKM matrix element  $V_{tb}$ , and to test the V-A structure of the top quark charged-current weak interaction, or to probe possible CP violation effects [4-6]. Apart from playing the role of a test of the Standard Model (SM), the precision measurement of single top quark events has additional importance in searching for new physics, because the charged-current top quark coupling (W-t-b)

<sup>\*</sup>LHC is the proton-proton Large Hadron Collider at CERN

might be particularly sensitive to certain new physics via new weak interactions or via loop effects, and new production mechanism can also contribute to the single top event rate [7–23].

Because of the unique features of single top quark physics, it has been extensively studied in the literature [18, 24-42]. Figure 1.2 shows the three separate single top quark production processes of interest at the hadron collider, which may be characterised by the virtuality of the W boson (of four momentum q) in the processes:

1. t-channel:  $q'b \rightarrow qt$  (including  $\bar{q}b \rightarrow \bar{q'}t$ ), cf. Fig. 1.2(a)

As the dominant process at the Tevatron and the LHC, the t-channel process involves a spacelike W boson ( $q^2 < 0$ ). The virtual W boson strikes a b quark in the proton sea, promoting it to a top quark. This process is also referred as W-gluon fusion, because the b quark ultimately arises from a gluon splitting to  $b\bar{b}$ , cf. Fig. 1.2(b).

2. s-channel:  $q'\bar{q} \to W^* \to t\bar{b}$  , cf. Fig. 1.2(c)

As the sub-dominant process at the Tevatron and smallest process at the LHC, the s-channel process involves a timelike W boson,  $q^2 > (m_t + m_b)^2 > 0$ . In order to detect this process, double b-tagging is needed to suppress the huge QCD backgrounds.

3. Associated production:  $bg \rightarrow tW^-$ , cf. Fig. 1.2(d)

As the smallest (negligible) process at the Tevatron and a sub-dominant process at the LHC, the Wt associated production process involves an on-shell W boson,  $q^2 = m_W^2$ . One of the initial partons is a b quark in the proton sea, as in the t-channel process.

These three single top quark production mechanisms probe the charged-current inter-

action in different  $q^2$  regions and are thus complementary to each other. Among the three processes, the largest cross section at both the Tevatron and the LHC is due to the t-channel. The next largest cross section is from the s-channel at the Tevatron, and from the tW associated production at the LHC. The s-channel production cross section is small at the LHC because it involves a quark-antiquark collision. On the other hand, associated production cross section is relatively large at the LHC because the gluon parton distribution functions (PDF) grow more rapidly with decreasing x than the light quark PDF. The s-channel and t-channel processes should be observed for the first time in Run II at the Tevatron; whereas the observation of associated production will likely have to await the LHC.

In Tevatron Run I, searches for single top quark production were performed by both the DØ [43] and CDF collaborations [44]. At the 95% confidence level, the DØ limit on the s-channel production is 17 picobarn (pb) and the CDF limit is 18 pb. At the same confidence level, the DØ limit on the t-channel production cross section is 22 pb and the CDF limit is 13 pb. Searches for single top quark production in Run II have begun, and the limits from CDF are 13.6 pb in the s-channel and 10.1 pb in the t-channel [45]. The s-channel and t-channel single top quark processes can be probed separately at the Tevatron by taking advantage of b-quark tagging using displaced vertices and differences in the kinematic distributions of the b-tagged and non-b-tagged jets. Usually, only one b-tagged jet can be expected in the t-channel case while two b-tagged jets can be expected in the s-channel case. This is because the b quark produced with the top quark tends to be collinear with the initial state gluon in the t-channel, giving it a large pseudo-rapidity  $(\eta)$  and low transverse momentum  $(p_T)$  and thus making it challenging to b-tag this jet experimentally. It is important to separate the two processes since they have different systematic uncertainties and different sensitivities to new physics [42].

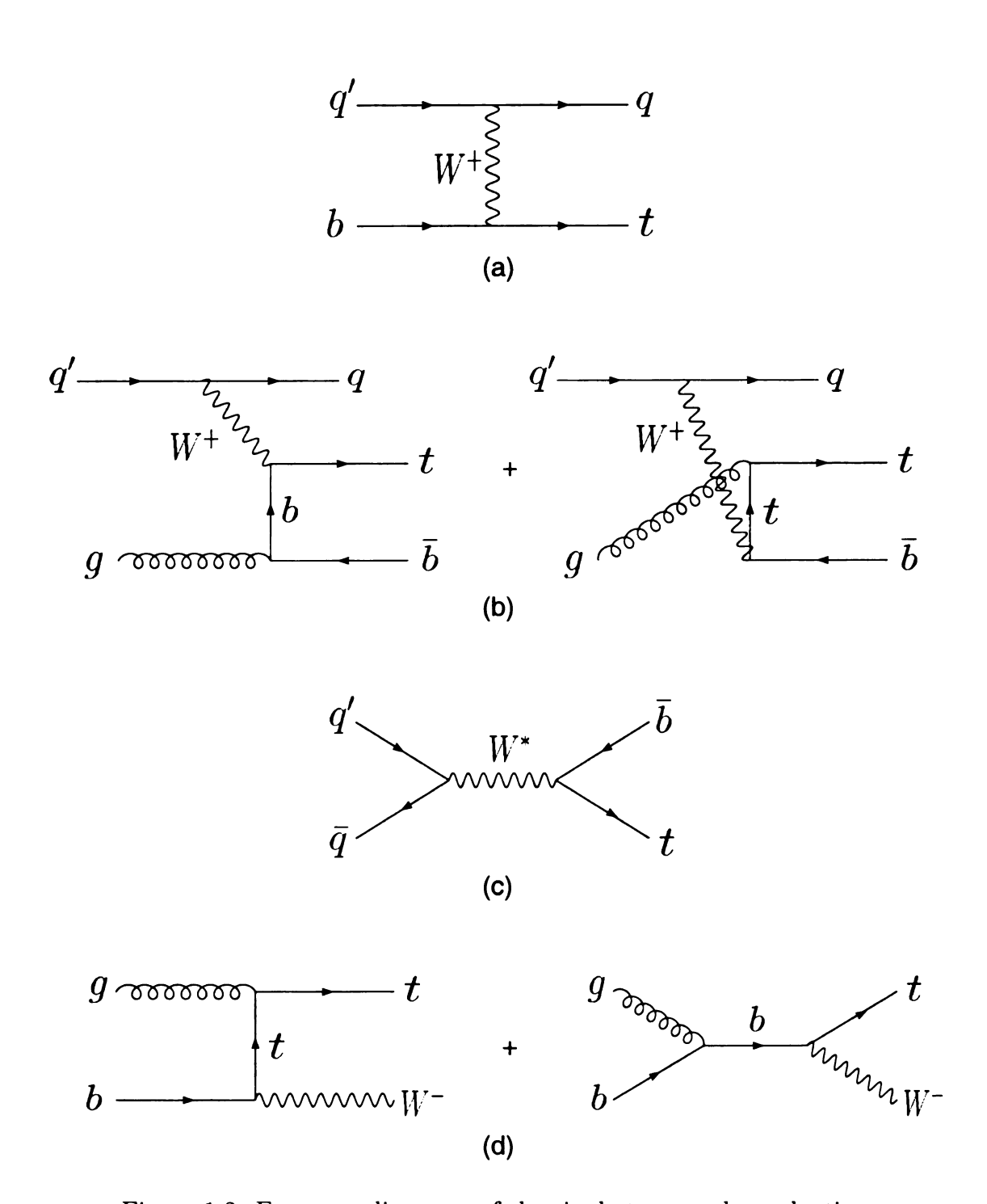


Figure 1.2: Feynman diagrams of the single top quark production

Furthermore, single top quark production is also a very important background to many searches for new physics. For example, the s-channel process is a significant background to Higgs searches at the Tevatron in the production process  $q\bar{q}' \to WH$  with decay  $H \to b\bar{b}$  [46–48] and other new physics searches [49]. At the LHC, the Wt associated production is an important background to Higgs searches in the decay channel  $H \to WW$  [37] and the primary charged Higgs boson production channel  $bg \to tH^{\pm}$  with  $H^{\pm} \to \tau \nu$  [50]. As the largest single top process, the t-channel production is an important background to many new physics searches.

The extraction of a signal is more challenging for single top quark production than for top pair production since there are fewer objects in the final state and the overall event properties are less distinct from the large W+jets background. Therefore, a calculation including higher order quantum chromodynamics (QCD) corrections is needed in order to make an accurate theoretical prediction. The next-to-leading order (NLO)  $O(\alpha_s)$  corrections to single top quark production have already been carried out in Refs. [31, 34], which shows an uncertainty on the total cross section of about 5% by varying the factorization and renormalization scales. For the schannel, multiple soft gluon resummation effects have been calculated [35]. In order to confront theory with experimental data, where kinematical cuts are necessary in order to detect a signal, it is crucial to accurately model event topologies of single top quark events. For this, Refs. [51–53] have calculated the differential cross sections for on-shell single top quark production. The complete NLO calculations including both the single top quark production and decay have been done independently by two groups recently [54–56]. In both calculations, the narrow width approximation was adopted in order to link top quark production with its consequent decay [54,55]. In Reference [56,57], we presented a detailed phenomenological analysis of the s-channel and t-channel single top quark production at the Tevatron, focusing on signal cross

sections and kinematical distributions.

The reminder of the thesis is organized as follows. In Chapter 2, we discuss a formalism which calculates the complete next-to-leading order QCD corrections to production and decay of single top quarks. In this formalism, the "modified" narrow width approximation is used to separate the production of the top quarks from their decay, and to incorporate the top quark width effects. In order to study the spin properties of the top quark, the helicity amplitude method is used to keep full spin information for all final state objects. In Chapter 3, we present a calculation of the next-to-leading order QCD corrections, with one-scale phase space slicing method, to single top quark production and decay process  $p\bar{p},pp \to t\bar{b} + X \to b\ell\nu\bar{b} + X$  at hadron colliders. Using the helicity amplitude method, the angular correlation of the final state partons and the spin correlation of the top quark are preserved. The effect of the top quark width is also examined. In order to regularize divergencies in the calculation, both the dimensional regularization (DREG) [58] and the dimensional reduction (DRED) [59] are used and the differences are shown in each individual form factor. In Chapter 4, we calculate the inclusive cross section and discuss the (renormalization / factorization) scale dependence and the top quark mass dependence of the cross section. In Chapter 5 and Chapter 6, the phenomenology of the s-channel and t-channel single top physics is discussed, respectively. In Appendixes, the details of the calculation are presented as well as other useful formulas.

### Chapter 2

### Techniques of NLO calculation

### 2.1 Narrow width approximation

Although the top quark width is proportional to  $m_t^3$  ( $\Gamma_t \simeq 1.5\,\mathrm{GeV}$ ), cf. Eq. 1.3, it is still much smaller than top quark mass ( $m_t = 178\,\mathrm{GeV}$ ). The characteristic time scale for the single top quark production is of order  $1/m_t$  while the time scale for the decay is  $1/\Gamma_t$ . Therefore, radiation in the production and decay stages are separated by a large time. This provides the motivation of using the narrow width approximation (NWA) to study the production and decay of top quark, in which the  $O(\alpha_s)$  corrections can be unambiguously assigned to both the single top quark production process and the top quark decay process.

In the usual NWA, the top quarks are always on mass shell and the width is identically zero. In that case gauge invariance requires only diagrams with one intermediate top quark in the single top processes. Once the top quark is allowed to have a finite width and be off-shell, non-resonant diagrams, those with the same final state but no intermediate top quarks, can also contribute. However, in the region of interest for single top physics, i.e. the region where the top quark is nearly on shell, the pole in the intermediate top quark propagator causes its contribution to dominate. A finite top width will also result in a new type of virtual NLO Feynman diagram in

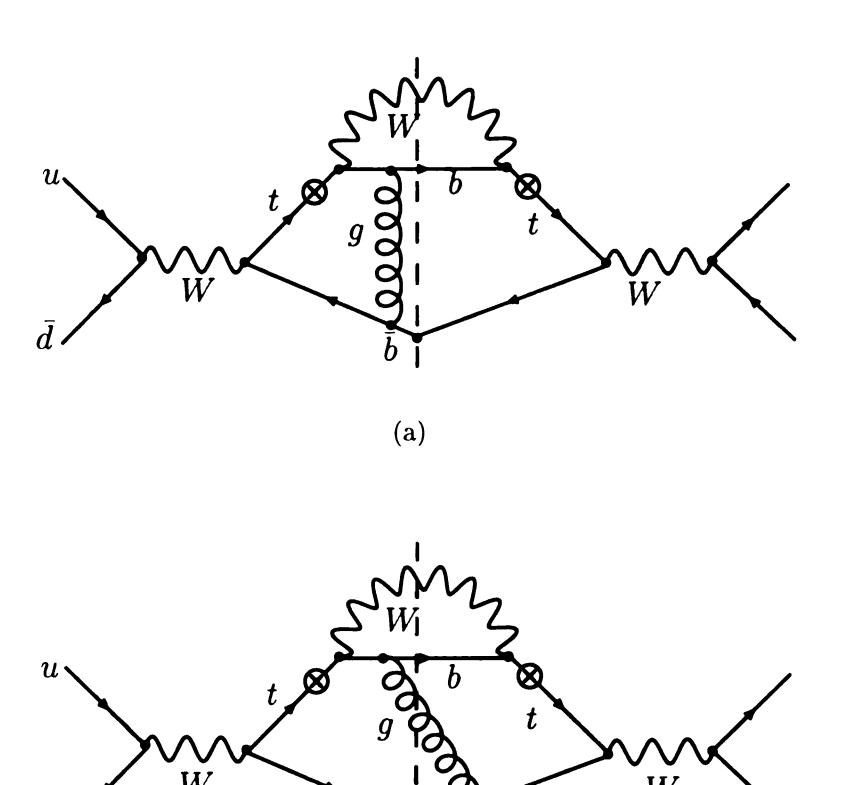


Figure 2.1: The representative Feynman diagrams of the interference effects at the NLO. (a) virtual correction (b) real correction

(b)

which a gluon line is connected from the anti-bottom quark (of top quark production process) to the bottom quark (of top decay), as shown in Fig. 2.1(a). There will also be interference between the gluons emitted in the production and the gluon emitted in the decay in the real NLO Feynman diagrams, as shown in Fig. 2.1(b). The potentially dangerous region for this diagram is the one in which the emitted gluon is soft therefore it is not confined to a time of order  $1/m_t$ . Those effects are nonfactorizable. Similar kind of effects also exists in  $e^+e^- \to W^+W^- \to 4f$  radiative corrections. It has been shown that the nonfactorizable effects are small for infrared safe variables,  $\mathcal{O}(\alpha_s\Gamma_t/m_t)$ , as long as the process is not near threshold [60–62].

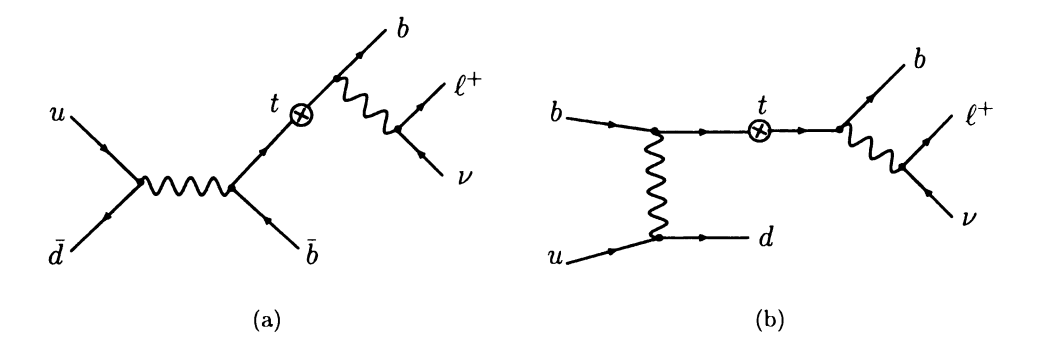


Figure 2.2: Feynman diagrams of the Born level contribution to the production and decay of single top quark. (a) s-channel (b) t-channel

The single top quark can be produced through s-channel and t-channel processes, as shown in Fig. 2.2(a) and Fig. 2.2(b), respectively. Using the NWA, we decompose the Born level processes depicted in Fig. 2.2 into two parts: the production and the decay, as indicated by the symbol  $\otimes$ . Both the production and the decay matrices are gauge invariant. Making use of the polarization information of the top quark, we can apply the NWA to correlate the top quark production with top quark decay processes by replacing the numerator of the top quark propagator  $(\not p_t + m_t)$  by  $\sum_{\lambda_t = \pm} u^{\lambda_t}(t) \bar{u}^{\lambda_t}(t)$ , where  $u^{\lambda_t}(t)$  is the Dirac spinor of the top quark with helicity  $\lambda_t$ , where  $\lambda_t = +$  or - for right-handed or left-handed top quark, respectively. Therefore, the scattering amplitude of the single top quark production and decay processes can be written as [7]

$$\mathcal{M} = \sum_{\lambda_t = \pm} \mathcal{M}^{dec}(\lambda_t) \mathcal{M}^{prod}(\lambda_t),$$

where  $\mathcal{M}(\lambda_t)$  is the helicity amplitude and  $\lambda_t$  is the helicity eigenvalue of the single top quark produced in the intermediate state. The matrix element squared can be written as the product of the production part and the decay part in the density matrix

formalism:

$$|\mathcal{M}|^2 = \sum_{\lambda_t, \, \lambda_t' = \pm} \mathcal{A}_{\lambda_t, \, \lambda_t'} \mathcal{B}_{\lambda_t, \, \lambda_t'}, \tag{2.1}$$

where

$$\mathcal{A}_{\lambda_t, \lambda_t'} = \mathcal{M}_{dec}^{\dagger}(\lambda_t) \mathcal{M}_{dec}(\lambda_t'), \tag{2.2}$$

$$\mathcal{B}_{\lambda_t, \lambda_t'} = \mathcal{M}_{prod}^{\dagger}(\lambda_t) \mathcal{M}_{prod}(\lambda_t'). \tag{2.3}$$

Besides the matrix elements, the phase space of the single top quark process can also be factorized into the top quark production and the top quark decay for a on-shell top quark in the NWA. We can write the denominator of the top quark propagator as

$$\int dp^2 \frac{1}{(p^2 - m_t^2)^2 + m_t^2 \Gamma_t^2} = \frac{\pi}{m_t \Gamma_t}.$$
 (2.4)

When the matrix element is calculated using the fixed  $m_t$  value, it is the usual NWA method. In this case, the invariant mass of the top quark decay particles will be equal to  $m_t$  (a fixed value) for all events. Reconstructing the top quark invariant mass from its decay particles is an important experimental task at the Tevatron and the LHC, it is desirable to have a theory calculation that would produce the invariant mass distribution of the reconstructed top quark mass with a Breit-Wigner resonance shape to reflect the non-vanishing decay width of the top quark (for being an unstable resonance). For that, we introduce the "modified NWA" method in our numerical calculation in which we generate a Breit-Wigner distribution for the to quark invariant mass in the phase space generator and then generated the squared matrix element according to Eq. 2.4 with  $m_t$  being the invariant mass generated by the phase space generator on the event-by-event basis. In the limit that the total decay

width of the top quark approaches to zero (i.e., much smaller than the top quark mass), the production and the decay of top quark can be factorized. Therefore, the S-matrix element for the production and the decay processes are separately gauge invariant with any value of top quark invariant mass. We find that the total event rate and the distribution of various kinematics variables (except the distribution of the reconstructed top quark invariant mass) calculated using the "modified NWA" method agree well with that using the NWA method. In the NWA method, the reconstructed top quark invariant mass distribution is a delta-function, i.e., taking a fixed value, while in the "modified NWA" method, it is almost a Breit-Wigner distribution.

Below, we give the explicit Born level helicity amplitudes of the single top quark production and decay, respectively.

#### 2.1.1 Helicity matrix elements of single top quark production

The helicity amplitudes for the s-channel single top quark production can be written as following:

$$\mathcal{M}_{s}^{prod}(\lambda_{t} = +) = \frac{2\langle t + |\bar{d}+\rangle\langle u + |\bar{b}-\rangle\omega_{-}^{t}}{s - m_{W}^{2}}, \tag{2.5}$$

$$\mathcal{M}_{s}^{prod}(\lambda_{t} = -) = \frac{2\langle t - |\bar{d}+\rangle\langle u + |\bar{b}-\rangle\omega_{+}^{t}}{s - m_{W}^{2}}, \tag{2.6}$$

where we have suppressed, for simplicity, the common factor  $\sqrt{2E_u}\sqrt{2E_{\bar{d}}}\sqrt{2E_b}$ , and the coupling constants  $\left(-ig/\sqrt{2}\right)^2$ . Here,  $s=(p_u+p_{\bar{d}})^2$ , g is the SU(2) coupling constant,  $m_W$  denotes the mass of W-boson, and  $\omega_{\pm}^t=\sqrt{E_t\pm|\vec{p_t}|}$ , where  $E_t$  and  $\vec{p_t}$  are the energy and momentum of the top quark, respectively. The meaning of the bra and ket in the above helicity amplitudes is summarized in Appendix A. We note that  $u,\bar{d},t$  and  $\bar{b}$  within the bra (<|) and ket (|>) denote the normalized three-momentum

of the particle, c.f. Eq. (A.1).

For the t-channel single top quark production process, the helicity amplitudes are given by

$$\mathcal{M}_{t}^{prod}(\lambda_{t} = +) = \frac{2\langle u + | b - \rangle \langle t + | d + \rangle \omega_{-}^{t}}{t - m_{W}^{2}}, \tag{2.7}$$

$$\mathcal{M}_{t}^{prod}(\lambda_{t} = -) = \frac{2\langle u + | b - \rangle \langle t - | d + \rangle \omega_{+}^{t}}{t - m_{W}^{2}}, \tag{2.8}$$

where we have also suppressed the common factor  $\sqrt{2E_u}\sqrt{2E_d}\sqrt{2E_b}$ , the coupling constants  $\left(-\frac{ig}{\sqrt{2}}\right)^2$ , and  $t=(p_u-p_d)^2$ .

#### 2.1.2 Helicity matrix elements of top quark decay

For the top quark decay process, the helicity amplitude are given by

$$\mathcal{M}^{dec}(\lambda_t = +) = \frac{-2\langle b' - | \nu + \rangle \langle e + | t + \rangle \omega_-^t}{p_W^2 - m_W^2 + i m_W \Gamma_W}, \tag{2.9}$$

$$\mathcal{M}^{dec}(\lambda_t = -) = \frac{-2\langle b' - | \nu + \rangle \langle e + | t - \rangle \omega_+^t}{p_W^2 - m_W^2 + i m_W \Gamma_W}, \tag{2.10}$$

where we have suppressed the common factor  $\sqrt{2E_e}\sqrt{2E_{\nu}}\sqrt{2E_{b'}}$ , the coupling con-

stants  $\left(-\frac{ig}{\sqrt{2}}\right)^2$ , and  $p_W$  and  $\Gamma_W$  denotes the 4-momentum and the total decay width of W-boson, respectively. For simplicity, we only consider the leptonic decay mode of W boson, i.e.  $W^+ \to \ell^+ \nu$ .

# 2.2 Regularization schemes and $\gamma_5$ problem

In the perturbative treatment of local quantum fields beyond the tree level, the occurrence of ultraviolet and infrared divergences has led to the development of various regularization schemes. Among these methods dimensional regularization (DREG) has become a standard tool. The most important feature of this scheme is the concept of analytic continuation of the dimension of space time to n (n = 4 for usual space time). This procedure of regularization has the advantage of preserving the local gauge invariance of the underlying Lagrangian, and permits us to treat, in a gauge invariant way, divergent Feynman integrals to all orders of perturbation theory [58]. In the context of supersymmetric theories, it has been shown that DREG will not display gauge invariance with respect to supersymmetry transformations. In order to treat Bose and Fermi degrees on the same footing, dimensional reduction (DRED) is proposed by Siegel [63] and has been further studied by other authors [64]. It considers the analytic continuation of all momenta to space-time dimensions  $n=4-2\varepsilon$ while the spin degrees of freedom stay in four-dimensional Minkowski space. The familiar four-dimensional Dirac algebra is then essentially maintained and a great technical advantage is obtained. The equivalence of the dimensional Reduction and the dimensional regularization has been proved to all orders in perturbation theory and for a general renormalizable theory [65].

The difference between DREG and DRED is how to treat the dimensional continuations when transferring from 4 dimensions to n dimensions. There are two parts to dimensional continuation: the continuation of the momenta and the continuation of  $\gamma$  matrices. The continuation of the momenta is unique, but there are various methods for continuing the  $\gamma$  matrices. The choice of latter defines which dimensional method is used.

# 2.2.1 Dimensional regularization scheme

In DREG one continues the metric tensor and the  $\gamma$  matrices to n dimensions,

$$g_n^{\mu\nu}g_{\mu\nu}^n = n,$$
 
$$\gamma^{\mu}\gamma^{\nu} + \gamma^{\nu}\gamma^{\nu} = 2g_n^{\mu\nu}.$$

Here,  $g_n^{\mu\nu}$  denotes the *n*-dimensional metric tensor. For unpolarized QCD processes, dimensional regularization preserves all the necessary invariance and symmetries for doing calculations to any order in  $\alpha_s$ . But in order to derive the fully differential cross section and study the spin correlation of the single top process, one must confront the basic problem of any polarized process, the ambiguity associated with defining the  $\gamma_5$  matrix, or  $\varepsilon^{\mu\nu\lambda\rho}$  tensor, in *n* dimensions. Because of the presence of the axial-vector current in the single top quark process, a prescription to handle the  $\gamma_5$  matrices in  $n = 4 - 2\epsilon$  dimensions has to be chosen. There exist two alternative definitions of the  $\gamma_5$  matrix in *n* dimensions.

1. Naive- $\gamma_5$  scheme [66]: taking the  $\gamma_5$  anti-commuting with all the other  $\gamma$ matrices

$$\gamma_5^2 = 1,$$

$$\left\{\gamma_5,\gamma_\mu\right\} = 0.$$

In this scheme, massless quark helicity is conserved, but there are known mathematical inconsistences if traces with only odd  $\gamma_5$  occur.

2. t'Hooft-Veltman scheme [58]: formally taking n>4 (with regards to the tensor algebra) and keeping the  $\gamma_5$  and  $\varepsilon^{\mu\nu\lambda\rho}$  in four dimensions so that

$$\left\{\gamma_5,\gamma_{\mu}\right\} = 0 : \mu \leq 4,$$

$$\left[\gamma_5, \gamma_\mu\right] = 0 : \mu > 4,$$

which follow from the definition

$$\gamma_5 = \frac{i}{4!} \varepsilon_{\mu_1 \mu_2 \mu_3 \mu_4} \gamma^{\mu_1} \gamma^{\mu_2} \gamma^{\mu_3} \gamma^{\mu_4},$$

where  $\varepsilon_{\mu_1\mu_2\mu_3\mu_4}=0$  for  $\mu_i>4$ , but it is the usual Levi-Civita tensor for  $\mu_i\leq 4$ .

#### 2.2.2 Dimensional reduction scheme

DRED is the most widely used scheme for preserving supersymmetry. The rules for dimensional reduction follow from viewing it as a compactification of a four-dimensional theory to n < 4:

1. As in ordinary dimensional regularization, all momentum integrals are integrated over n-component momenta. Any Kronecker  $\delta_{\mu}^{\nu}$ 's resulting from the integration are n-dimensional,

$$p_{\mu} \equiv p_{\mu}^{(n)},$$

$$g_{(n)}^{\mu\nu}g_{\mu\nu}^{(n)} = n.$$

This is necessary for maintaining gauge invariance.

2. All indices on the fields, and on corresponding matrices coming from the action, are treated as four-dimensional indices,

$$\gamma_{\mu} \equiv \gamma_{\mu}^{(4)}$$
.

This is for preserving supersymmetry.

We can decompose the four-dimensional space into the direct sum of n- and  $2\epsilon$ dimensional subspaces [67],

$$4 \equiv n \oplus (4-n) = n \oplus 2\epsilon.$$

Consequently, we may split the 4-dimensional Lagrangian into two pieces:

$$\mathcal{L}^{(4)} = \mathcal{L}^{(n)} + \mathcal{L}^{(2\epsilon)}.$$

The exact expressions of the Lagrangian are not shown here, but one should note that the conventional dimensional regularization amounts to using  $\mathcal{L}^{(n)}$  and discarding  $\mathcal{L}^{(2\epsilon)}$ , while the dimensional reduction include both. The additional contributions from  $\mathcal{L}^{(2\epsilon)}$  are precisely what is required to restore the supersymmetric Ward identities at one loop in supersymmetric theories. The orthogonality between these two subspaces,

$$g_{\lambda}^{(n)\mu}g_{\mu\nu}^{(2\epsilon)}\equiv 0,$$

enables us to get the following relations:

$$\left\{\gamma_{\mu}^{(2\epsilon)}, \not k\right\} = 0, \tag{2.11}$$

$$\left\{\gamma_{\mu}^{(2\epsilon)}, \gamma_{\nu}^{(n)}\right\} = 0, \tag{2.12}$$

$$\left\{ \gamma_{\mu}^{(2\epsilon)}, \gamma_{\nu}^{(4)} \right\} = 2g_{\mu\nu}^{(2\epsilon)},$$
 (2.13)

$$g_{\mu}^{(2\epsilon)\mu} = 0, \tag{2.14}$$

$$\gamma_{\mu}^{(2\epsilon)} \gamma^{(2\epsilon)\mu} = 2\epsilon. \tag{2.15}$$

As a result, any four-dimensional Kronecker  $\delta_{\mu}^{(4)\nu}$  contracted with a *n*-dimension momentum  $p_{\nu}^{(n)}$  yields a *n*-dimensional momentum,

$$\delta_{\mu}^{(4)\nu} p_{\nu}^{(n)} = p_{\mu}^{(n)}.$$

Similarly, for any four-dimensional vector,  $\varepsilon_{(4)}^{\mu}$ , the dot product with a *n*-dimensional vector yields a *n*-dimensional dot product,

$$\varepsilon_{(4)}^{\mu}p_{\mu}^{(n)}=\varepsilon_{(n)}^{\mu}p_{\mu}^{(n)}.$$

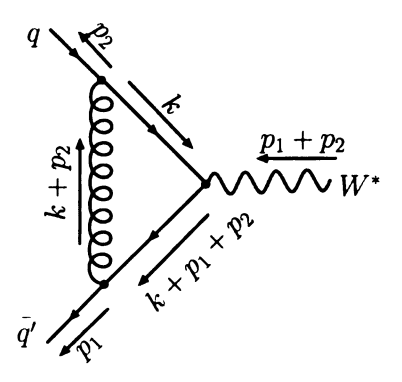


Figure 2.3: Feynman diagram for  $q\bar{q'} \rightarrow W^+$ .

#### 2.2.3 Conversion between DREG and DRED

There is no ambiguity of defining  $\gamma_5$  in the DRED scheme since all the  $\gamma$ -matrices are well defined in the four dimensions, but it inevitably requires certain ultraviolet counterterms to restore the gauge invariance in calculating the virtual corrections. The counterterms are the same in both unpolarized and polarized processes [68].

Let us use the Drell-Yan process  $(q\bar{q}' \to W^+)$ , as shown in Fig. 2.3, to illustrate it. In the DRED, the amplitude is

$$\mathcal{M} = -i\frac{g}{\sqrt{2}}g_s^2 C_F \int \frac{d^n k}{(2\pi)^n} \frac{\bar{v}(p_1)\gamma_{\rho}(\not k + \not p_1 + \not p_2)\gamma_{\mu} P_L \not k \gamma^{\rho} u(p_2)}{k^2(k+p_1)^2(k+p_1+p_2)^2} \epsilon^{*\mu}(q)$$

$$= -i\frac{g}{\sqrt{2}}g_s^2 C_F \int \frac{d^n k}{(2\pi)^n} \frac{\bar{v}(p_1)\gamma_{\rho}(\not k + \not p_1 + \not p_2)\gamma_{\mu} \not k \gamma^{\rho} u(p_2)}{k^2(k+p_1)^2(k+p_1+p_2)^2} P_L \epsilon^{*\mu}(q),$$

where  $q = p_1 + p_2$  and  $P_L = \frac{1 - \gamma_5}{2}$ . The tensor in numerator can be reduced as

$$n_{\mu} \equiv \gamma_{\rho} (\not k + \not p_{1} + \not p_{2}) \gamma_{\mu} \not k \gamma^{\rho}$$

$$= -4k_{\mu} \not k + 2\gamma_{\mu} \not k \not k + 2\gamma_{\mu} \not k \not q. \qquad (2.16)$$

After integrating over the virtual momentum k, we obtain

$$n_{\mu} = -4\gamma^{(4)\nu} g_{\mu\nu}^{(n)} C_{24} + 2\gamma_{\mu}^{(4)} \gamma_{\nu}^{(4)} \gamma_{\rho}^{(4)} g^{(n)\rho\nu} C_{24} + \text{finite}$$

$$= -\frac{1}{\epsilon} \underbrace{\gamma^{(4)\nu} g_{\mu\nu}^{(n)}}_{I} + \frac{1}{2\epsilon} \underbrace{\gamma_{\mu}^{(4)} \gamma_{\nu}^{(4)} \gamma_{\rho}^{(4)} g^{(n)\nu\rho}}_{II} + \text{finite}, \qquad (2.17)$$

where  $C_{24}$  is the Passarino-Veltman scalar function [69], cf. Appendix C. In the last step, we have used the property of  $C_{24}$  scalar function,  $C_{24} \propto 1/4\epsilon$ . As shown in the term I in Eq. 2.17, integrating over the virtual momentum generates  $g_{\mu\nu}^{(n)}$ , which will be contracted with four-dimensional  $\gamma$ -matrices. This can lead to a term  $\sim \gamma_{\mu}^{(2\epsilon)}$  which violates the gauge invariance, therefore needing a counterterm to remove it. For term II in Eq. 2.17, there is no need to introduce the counterterm because  $\gamma_{\mu}$  is already in four dimensions.

#### • Term I:

After introducing the counterterm  $\delta n_{\mu}$  as

$$\delta n_{\mu} = -\frac{1}{\epsilon} \gamma^{(4)\nu} (g_{\mu\nu}^{(4)} - g_{\mu\nu}^{(n)}), \tag{2.18}$$

we get

$$n_{\mu}(I) + \delta n_{\mu} = -\frac{1}{\epsilon} \gamma_{\mu}^{(4)}.$$
 (2.19)

#### • Term II:

Using the symmetry between the "dummy" index  $\nu$  and  $\rho$ , we rewrite the term II as

$$n_{\mu}(II) = \gamma_{\mu}^{(4)} \frac{1}{2} \left\{ \gamma_{\nu}^{(4)}, \gamma_{\rho}^{(4)} \right\} g^{(n)\nu\rho} = \gamma_{\nu}^{(4)} \left[ g_{\nu\rho}^{(n)} \oplus g_{\nu\rho}^{(2\epsilon)} \right] g^{(n)\nu\rho}$$
$$= \gamma_{\mu}^{(4)} n. \tag{2.20}$$

Substituting Eqs. 2.19 and 2.20 into Eq. 2.17, we obtain

$$n_{\mu} + \delta n_{\mu} = -\frac{1}{\epsilon} \gamma_{\mu}^{(4)} + \frac{1}{2\epsilon} \gamma_{\mu}^{(4)} (4 - 2\epsilon) + \text{finite}$$
$$= \frac{1}{\epsilon} \gamma_{\mu} - \gamma_{\mu} + \text{finite}.$$

It is very clear that the counterterm we introduced in Eq. 2.18 only gives a finite contribution, a constant "-1" always coming together with  $1/\epsilon$  or  $4C_{24}$ . Therefore, for the virtual correction, we can easily restore gauge invariance by replacing

$$4C_{24} \rightarrow 4C_{24} - 1.$$

In perturbative QCD, with the evaluation of the loop corrections one does not yet obtain the physical cross section. One has to add the real emission contribution as well to cancel the soft and collinear singular terms between the virtual and real corrections after trivial ultraviolet renormalization. The remaining collinear singularities are subtracted into the definition of parton distribution functions (PDFs), i.e. the physical cross sections of infrared safe quantities are obtained by folding the finite hard scattering cross section with PDFs. Although the analytic expressions for the soft and collinear contribution are universal (process independent), they depend on the regularization scheme used. In order to calculate the real emission contribution in n dimensions, we must first give the general form of n-dimensional Altarelli-Parisi splitting functions [70],  $P_{ij}^{(n)}(z)$ , related to the probability of parton j splitting into a collinear parton i having momentum fraction z, plus an arbitrary final state carrying the rest of the momentum. Hence, we may write the splitting in DREG scheme as

$$P_{ij}^{(n)}(z,\epsilon) \equiv P_{ij}^{(4)}(z) + \epsilon P_{ij}^{(2\epsilon)}(z),$$
 (2.21)

where  $P_{ij}^{(4)}(z)$  is the usual four-dimensional splitting function. In DRED,

$$P_{ij}^{DRED}(z,\epsilon) = P_{ij}^{(4)}(z),$$
 (2.22)

since all the spinors and vectors are handled in four dimensions. As an example, we present the relation between the Wilson coefficient functions of the Drell-Yan process  $q\bar{q}' \to W(g)$  in these two schemes:

$$C_{DREG}^{q\bar{q'}\to W(g)}(z) = C_{DRED}^{q\bar{q'}\to W(g)} \underbrace{-\frac{\alpha_s}{\pi} P_{qq}^{(2\epsilon)}(z) - \frac{\alpha_s}{\pi} P_{\bar{q'}\bar{q'}}^{(2\epsilon)}(z)}_{Real} + \underbrace{\frac{\alpha_s}{2\pi} C_F(-1)\delta(1-z)}_{Virtual}.$$
(2.23)

After adding the virtual correction counterterm and subtracting the  $\epsilon$ -term in the splitting kernel, we obtain the result in the DREG scheme which can be convoluted with the usual modified minimal subtraction ( $\overline{\rm MS}$ ) factorization scheme PDFs. In order to convert results calculated in DRED to the corresponding DREG  $\overline{\rm MS}$  results, one simply replaces

$$P_{ij}^{(4)}(z) \rightarrow P_{ij}^{(4)}(z) - \epsilon P_{ij}^{(2\epsilon)}(z)$$
 (2.24)

in the factorization counterterm. Bearing in mind that the usual PDFs are defined in the DREG ( $\overline{\rm MS}$ ) scheme, we need understand how to relate the DRED parton distribution functions to those in DREG ( $\overline{\rm MS}$ ). Noting that the bare parton distribution function,  $f_{i/A}^0(x)$ , is factorization scheme independent, we obtain

$$f_{i/A}^{(0)}(x) = f_{i/A}^{\overline{MS}}(x, \mu_F) - \frac{C_{\epsilon}}{\epsilon} \sum_{j} \frac{\alpha_s}{2\pi} \int_{x}^{1} \frac{dy}{y} f_{j/A}^{\overline{MS}}(x, \mu_F) P_{ij}^{(4)}(\frac{x}{y}),$$

$$f_{i/A}^{(0)}(x) = f_{i/A}^{DRED}(x, \mu_F) - \frac{C_{\epsilon}}{\epsilon} \sum_{j} \frac{\alpha_s}{2\pi} \int_{x}^{1} \frac{dy}{y} f_{j/A}^{DRED}(x, \mu_F) P_{ij}^{(n)}(\frac{x}{y}).$$
(2.25)

Hence, we derive

$$f_{i/A}^{DRED}(x,\mu_F)$$

$$= f_{i/A}^{\overline{MS}}(x,\mu_F)$$

$$-\frac{C_{\epsilon}}{\epsilon} \sum_{j} \frac{\alpha_s}{2\pi} \int_{x}^{1} \frac{dy}{y} \left\{ f_{j/A}^{\overline{MS}}(x,\mu_F) P_{ij}^{(4)}(\frac{x}{y}) - f_{j/A}^{DRED}(x,\mu_F) P_{ij}^{(n)}(\frac{x}{y}) \right\}$$

$$= f_{i/A}^{\overline{MS}}(x,\mu_F) - \sum_{j} \frac{\alpha_s}{2\pi} \int_{x}^{1} \frac{dy}{y} f_{j/A}^{\overline{MS}}(x,\mu_F) P_{ij}^{(2\epsilon)}(\frac{x}{y}) + \mathcal{O}(\alpha_s^2). \tag{2.26}$$

where  $\mu_F$  is the factorization scale and

$$C_{\epsilon} = \left(\frac{4\pi\mu_F^2}{m_W^2}\right)^{\epsilon} \frac{\Gamma(1-\epsilon)}{\Gamma(1-2\epsilon)}.$$

In Eq. 2.26 we have ignored the differences between  $f_{i/A}^{\overline{MS}}(x,\mu_F)$  and  $f_{j/A}^{DRED}(x,\mu_F)$  which come from the higher order contributions.

# 2.3 Phase space slicing method

The construction of a flexible event generator requires the generation of partonic final states with a minimal amount of implicit phase space integration. At the leading order this is trivial, but in the calculation of NLO QCD corrections, one generally encounters both ultraviolet (UV) and infrared (IR) (soft and collinear) divergences. The former divergences can be removed by proper renormalization of couplings and wave functions. We don't need to renormalize the couplings in our calculation because the Born level couplings do not involve QCD interactions. In order to handle the latter divergences, one has to consider both virtual and real corrections and carefully handle the cancellation of divergences between the soft and collinear contributions and the virtual corrections. The soft divergencies will cancel according to

the Kinoshita-Lee-Nauenberg (KLN) theorem [71,72], but some collinear divergencies remain uncancelled. In the case of considering the initial state partons, one needs to absorb additional collinear divergences to define the NLO parton distribution function of the initial state partons. After that, all the infrared-safe observables will be free of any singularities. To calculate the inclusive production rate, one can use dimensional regularization to regularize divergencies and adopt the modified minimal subtraction ( $\overline{\rm MS}$ ) factorization scheme to obtain the total rate. However, owing to the complicated phase space for multi-parton configurations, analytic calculations are in practice impossible for all but the simplest quantities. During the last few years, effective numerical computational techniques have been developed to calculate the fully differential cross section to NLO and above. There are, broadly speaking, two types of algorithm used for NLO calculations, differing in how they approximate the phase space and matrix elements in the neighborhood of divergent regions:

- 1. The phase space slicing (PSS) method is based on approximating the matrix elements and the phase space integration measure in boundary regions of phase space so integration may be carried out analytically [73–78].
- 2. The subtraction method is based on adding and subtracting counterterms designed to approximate the real emission amplitudes in the phase space boundary regions on the one hand, and to be integrable with respect to the momentum of an unresolved parton on the other [79–85].

The phase space slicing method makes use of a combination of analytic and Monte Carlo integration methods, which has many advantages over a purely analytic calculation. The Monte Carlo approach allows one to calculate any number of observables simultaneously by simply histogramming the appropriate quantities. Furthermore, it is easy to tailor the Monte Carlo calculation to different experimental conditions,

for example, detector acceptances, experimental cuts, and jet definitions. Also, with the Monte Carlo approach one can study the dependence of the cross section on the choice of scale and the size of higher order quantum corrections in different regions of phase space. The basic challenge is to design a program which retains the versatility inherent in a Monte Carlo approach while ensuring that all of the required cancellations of singularities still take place.

In this study, we use the phase space slicing method with one cutoff scale for which the universal crossing functions have been derived in Refs. [76–78]. The advantage of this method is that, after calculating the effective matrix elements with all the partons in the final state, we can use the generalized crossing property of the NLO matrix elements to calculate the corresponding s-channel or t-channel matrix elements numerically without requiring any further effort. The validity of this method is due to the property that both the phase space and matrix element for the initial and final state collinear radiation processes can be simultaneously factorized. Below, we briefly review the general formalism for the NLO calculation in PSS method with one cutoff scale.

The phase space slicing method with one cutoff scale introduces an unphysical parameter  $s_{\min}$  to separate the real emission correction phase space into two regions:

- 1. the resolved region in which the amplitude has no divergences and can be integrated numerically by Monte Carlo method;
- 2. unresolved region in which the amplitude contains all the soft and collinear divergences and can be integrated out analytically.

It should be emphasized that the notion of resolved/unresolved partons is unrelated to the physical jet resolution criterium or to any other relevant physical scale. In

the massless case, a convenient definition of the resolved region is given by the requirement  $s_{ij} > s_{min}$  for all invariants  $s_{ij} = (p_i + p_j)^2$ , where  $p_i$  and  $p_j$  are the 4-momenta of partons i and j, respectively. For the massive quarks, we follow the definition in Ref. [86] to account for masses, but still use the terminology "resolved" and "unresolved" partons. In the regions with unresolved partons, soft and collinear approximations of the matrix elements, which hold exactly in the limit  $s_{min} \to 0$ , are used. The necessary integrations over the soft and collinear regions of phase space can then be carried out analytically in  $d=4-2\epsilon$  space-time dimensions. One can thus isolate all the poles in  $\epsilon$  and perform the cancellation of the IR singularities between the real and virtual contributions and absorb the leftover singularities into the parton structure functions in the factorization procedure. After the above procedure, one takes the limit  $\epsilon \to 0$ . The contribution from the sum of virtual and unresolved region corrections is finite but  $s_{min}$  dependent. Since the parameter  $s_{min}$  is introduced in the theoretical calculation for technical reasons only and is unrelated to any physical quantity, the sum of all contributions (virtual, unresolved and resolved corrections) must not depend on  $s_{min}$ . The phase space slicing method is only valid in the limit that  $s_{\min}$  is small enough that a given jet finding algorithm (or any infrared-safe observable) can be consistently defined even after including the experimental cuts.

In general, the conventional calculation of the NLO differential cross section for a process with initial state hadrons  $H_1$  and  $H_2$  can be written as

$$d\sigma_{H_1H_2}^{NLO} = \sum_{a,b} \int dx_1 dx_2 f_a^{H_1}(x_1, \mu_F) f_b^{H_2}(x_2, \mu_F) d\widehat{\sigma_{ab}^{NLO}}(x_{1,x_2}, \mu_R), \qquad (2.27)$$

where a, b denote parton flavors and  $x_1, x_2$  are parton momentum fractions.  $f_a^H(x, \mu_F)$  is the usual NLO parton distribution function with the mass factorization scale  $\mu_F$  and  $\widehat{d\sigma_{ab}^{NLO}}(x_1, x_2, \mu_R)$  is the NLO hard scattering differential cross section with the renormalization scale  $\mu_R$ . The pictorial demonstration of Eq. (2.27) is shown in the

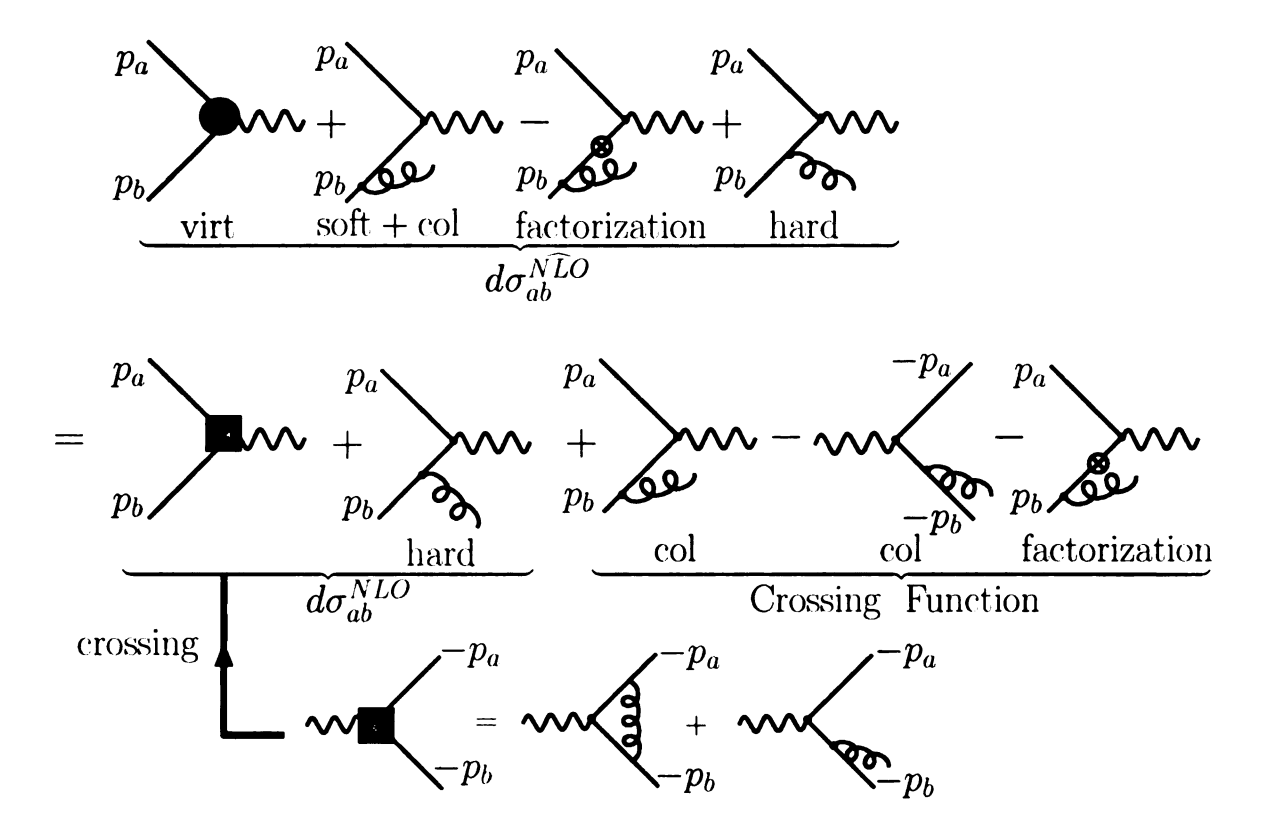


Figure 2.4: Illustration of the PSS method with one cutoff scale to describe the processes with initial state massless quarks. Here, only half of the real emission diagrams is shown. In this paper, we will assign the particle's momentum such that the initial state particle's momentum is incoming to the vertex while the final state particle's momentum is outgoing.

#### upper part of Fig. 2.4.

Contrary to the conventional calculation method, the PSS method with one cutoff scale will firstly cross the initial state partons into the final state, including the virtual corrections and unresolved real emission corrections. For example, to calculate the s-channel single top quark production at the NLO, we first calculate the radiative corrections to  $W^* \to q\bar{q}'(g)$ , as shown in the lower part of the Fig. 2.4, in which we split the phase space of the real emission corrections into the unresolved and resolved region. After we integrate out the unresolved phase space region, the net contribution of the virtual corrections and the real emission corrections in the unresolved phase space is finite but theoretical cutoff  $s_{min}$  dependent, which can be written as a form

factor (denoted by the box in Fig. 2.4) of the Born level vertex.

Secondly, we take the already calculated effective matrix elements with all the partons in the final state and use the universal "crossing function", which is the generalization of the crossing property of the LO matrix elements to NLO, to calculate the corresponding matrix elements numerically. Once we cross the needed partons to the initial state, the contributions from the unresolved collinear phase space regions are different from those with all the partons in the final state. These differences are included into the definition of the crossing function as well as the mass factorization effects, as shown in the middle part of Fig. 2.4. Here, we only present the explicit expressions of the crossing function, while the definition and detailed derivation of the crossing function can be found in Ref. [77]. After applying the mass factorization in a particular scheme, the crossing functions for an initial state parton a, which participates in the hard scattering processes, can be written in the form:

$$C_a^{\text{scheme}}(x, \mu_F, s_{min}) = \left(\frac{N_C}{2\pi}\right) \left[ A_a(x, \mu_F) \log \left(\frac{s_{min}}{\mu_F}\right) + B_a^{\text{scheme}}(x, \mu_F) \right], (2.28)$$

where

$$A_a(x,\mu_F) = \sum_p A_{p\to a}(x,\mu_F),$$
 (2.29)

$$B_a^{\text{scheme}}(x, \mu_F) = \sum_p B_{p \to a}^{\text{scheme}}(x, \mu_F),$$
 (2.30)

and  $N_C$  denotes the number of colors. The sum runs over  $p=q, \bar{q}, g$ . The functions A and B can be expressed as convolution integrals over the parton distribution functions and the explicit forms are shown in Appendix B. Although  $A_a$  is scheme independent,  $B_a$  does depend on the mass factorization scheme, and therefore so does the crossing function.

After introducing the crossing function, we can write the NLO differential cross section in the PSS method with one cutoff scale as

$$d\sigma_{H_1H_2}^{NLO} = \sum_{a,b} \int dx_1 dx_2 f_a^{H_1}(x_1, \mu_F) f_b^{H_2}(x_2, \mu_F) d\sigma_{ab}^{NLO}(x_1, x_2, \mu_R)$$

$$+ \alpha_s(\mu_R) \left[ C_a^{H_1}(x_1, \mu_F) f_b^{H_2}(x_2, \mu_F) + f_a^{H_1}(x_1, \mu_F) C_b^{H_2}(x_2, \mu_F) \right] d\sigma_{ab}^{LO}(x_1, x_2).$$

$$(2.31)$$

Here  $d\sigma_{ab}^{NLO}$  consists of the finite effective all-partons-in-the-final-state matrix elements, in which partons a and b have simply been crossed to the initial state, i.e. in which their momenta  $-p_a$  and  $-p_b$  have been replaced by  $p_a$  and  $p_b$ , as shown in the Fig. 2.4. The difference between  $d\sigma_{ab}^{NLO}$  and  $d\sigma_{ab}^{\widehat{NLO}}$  has been absorbed into the finite, universal crossing function  $C_a^H(x,\mu_F)$ . Defining a "effective" NLO parton distribution function  $\mathcal{F}_a^H(x)$  as

$$\mathcal{F}_{a}^{H}(x) = f_{a}^{H}(x, \mu_{F}) + \alpha_{s}(\mu_{R})C_{a}^{H}(x, \mu_{F}) + O(\alpha_{s}^{2}), \tag{2.32}$$

we can rewrite Eq. (2.31) in a simple form as

$$d\sigma_{H_1H_2}^{NLO} = \sum_{a,b} \int dx_1 dx_2 \mathcal{F}_a^{H_1}(x_1) \mathcal{F}_b^{H_2}(x_2) d\sigma_{ab}^{NLO}(x_1, x_2). \tag{2.33}$$

# Chapter 3

# NLO matrix elements of Single top quark production and decay processes

Beyond the leading order, an additional gluon will be radiated from the quark lines or appear as the initial parton in the single top quark process. Since the single top quark can only be produced through the electroweak interaction in the SM, we can further separate the single top quark processes into smaller gauge invariant sets, even at the NLO. Taking advantage of this property, in the first part of this Chapter we separate the s-channel and t-channel single top quark processes into smaller gauge invariant sets of diagrams to organize our calculations.

# 3.1 categorizing the single top quark processes

Here, we separate the NLO s-channel and t-channel single top quark processes into smaller gauge invariant sets of diagrams to organize our calculations. The s-channel diagrams at NLO consist of all the virtual correction diagrams as well as the Feynman diagrams of the following real correction processes:

$$q\bar{q}' \to W^* g \to \bar{b}gt(\to bW^+),$$
 (3.1)

$$qg \to W^* q' \to \bar{b}q' t (\to bW^+),$$
 (3.2)

$$g\bar{q}' \to W^* \bar{q} \to \bar{b}\bar{q}t(\to bW^+),$$
 (3.3)

$$q\bar{q}' \to W^* \to \bar{b}gt(\to bW^+),$$
 (3.4)

$$q\bar{q}' \to W^* \to \bar{b}t(\to bW^+g)$$
 (3.5)

with the gluon connected only to q, q' lines in (3.1)-(3.3) and the gluon connected only to  $t, \bar{b}$  lines in (3.4) and the gluon connected only to t, b lines in (3.5). We note that diagrams (3.2) and (3.3) do not include those in which the gluon line is connected to the final state  $\bar{b}$  and t line, for those are part of the NLO corrections to t-channel process as shown in Eqs. (3.8) and (3.9). To facilitate the presentation of our calculation, we separate the s-channel higher order QCD corrections (including both virtual and real corrections) into the following three categories:

- corrections to the initial state of the single top quark production (INIT), in which the gluon is only connected to the initial state light quark  $(q, \bar{q}')$  line,
- corrections to the final state of the single top quark production (FNAL), in which the gluon is only connected to the final state heavy quark  $(t, \bar{b})$  line of the single top quark production,
- corrections to the decay of the top quark (SDEC), in which the gluon is connected to the heavy quark (t, b) line of the top quark decay,

as illustrated in the upper part of Fig. 3.1 in which the blobs represent the higher order QCD corrections. The explicit real emission diagrams for the s-channel process can be found in Fig. 3.2.

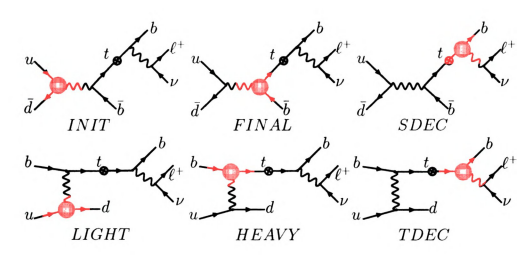


Figure 3.1: The way we organize our calculations at the NLO. The blobs in the diagrams denote the higher order QCD corrections, including both virtual and real emission contributions.

The NLO t-channel real correction processes for the top quark production and decay are

$$bq \to q'gt(\to bW^+),$$
 (3.6)

$$b\bar{q}' \rightarrow \bar{q}gt(\rightarrow bW^+),$$
 (3.7)

$$qg \rightarrow q'\bar{b}t(\rightarrow bW^+),$$
 (3.8)

$$\vec{q}'g \rightarrow \bar{q}\bar{b}t(\rightarrow bW^+),$$
 (3.9)

$$bg \to \bar{q}q't(\to bW^+),$$
 (3.10)

$$bq \rightarrow q't(\rightarrow bW^+g),$$
 (3.11)

$$b\bar{q}' \rightarrow \bar{q}t(\rightarrow bW^+q)$$
. (3.12)

Here the gluon is connected to both q,q' lines and  $t,\bar{b}$  lines in (3.6, 3.7), but only to t,b lines in (3.8, 3.9). In (3.10), we restrict the gluon to be connected only to q,q' lines. When the gluon in (3.10) is connected to t,b lines, it corresponds to the process  $bg \to tW$  with  $W \to \bar{q}q'$ , therefore it is not included here. As done in the s-channel case, we separate the processes (3.6-3.12) into the following categories:

• the one in which the gluon is connected to the q, q' light quark lines (LIGHT),

- the one in which the gluon is connected to the  $t, \bar{b}$  heavy quark lines (HEAVY),
- the one in which the gluon is radiated from the t, b heavy quark lines of the on-shell top quark decay processes (TDEC),

as illustrated in the lower part of Fig. 3.1. The explicit real emission diagrams for the t-channel process can be found in Fig. 3.3.

# 3.2 Form factor formalism for SCV corrections

As we pointed out in Sec. 2.3, NLO QCD corrections in the PSS method can be separated into two parts: (I) the resolved real emission corrections and (II) the virtual correction plus the unresolved real (soft+collinear) emission corrections, denoted by "SCV". After integrating out the virtual gluon and the unresolved partons, the SCV corrections can be written as form factors multiplying the Born level vertex. The form factors either modify the Born level coupling or give rise to new Lorentz structure of W coupling to fermions. In this section, we will write down the most general form factors of the single top quark processes and show their contribution to the helicity amplitudes for both the s-channel and the t-channel processes explicitly. It is worthwhile to mention that the form factor formalism presented here can be easily extended to study new physics models whose effects can also show up as the form factors.

#### 3.2.1 NLO corrections to INIT

Higher order QCD corrections to the diagrams labelled as INIT in Fig. 3.1 do not change the Lorentz structure of the  $W^* - u - d$  coupling. Therefore the most general

- the one in which the gluon is connected to the  $t, \bar{b}$  heavy quark lines (HEAVY),
- the one in which the gluon is radiated from the t, b heavy quark lines of the on-shell top quark decay processes (TDEC),

as illustrated in the lower part of Fig. 3.1. The explicit real emission diagrams for the t-channel process can be found in Fig. 3.3.

# 3.2 Form factor formalism for SCV corrections

As we pointed out in Sec. 2.3, NLO QCD corrections in the PSS method can be separated into two parts: (I) the resolved real emission corrections and (II) the virtual correction plus the unresolved real (soft+collinear) emission corrections, denoted by "SCV". After integrating out the virtual gluon and the unresolved partons, the SCV corrections can be written as form factors multiplying the Born level vertex. The form factors either modify the Born level coupling or give rise to new Lorentz structure of W coupling to fermions. In this section, we will write down the most general form factors of the single top quark processes and show their contribution to the helicity amplitudes for both the s-channel and the t-channel processes explicitly. It is worthwhile to mention that the form factor formalism presented here can be easily extended to study new physics models whose effects can also show up as the form factors.

#### 3.2.1 NLO corrections to INIT

Higher order QCD corrections to the diagrams labelled as INIT in Fig. 3.1 do not change the Lorentz structure of the  $W^* - u - d$  coupling. Therefore the most general

form of the initial state contribution can be rewritten as

$$\frac{ig}{\sqrt{2}}\gamma^{\mu}P_{L}I_{L},\tag{3.13}$$

where  $I_L$  denotes the effective form factor that includes the higher order corrections. Denoting the helicity amplitude as  $\mathcal{M}_{INIT}(\lambda_t)$  with t helicity  $\lambda_t=\pm 1$  and suppressing, for simplicity, the common factor  $\sqrt{2E_u}\sqrt{2E_{\bar{b}}}$ , the coupling factors  $\left(i\frac{g}{\sqrt{2}}\right)^2$  and the propagators

$$\frac{1}{s - m_W^2}$$

with  $s = (p_u + p_{\bar{d}})^2$ , we obtain the helicity amplitudes which include higher order corrections to the initial state of the s-channel single top quark production as following:

$$\mathcal{M}_{INIT}(+) = 2I_L \langle t + |\bar{d} + \rangle \langle u + |\bar{b} - \rangle \omega_-^t, \tag{3.14}$$

$$\mathcal{M}_{INIT}(-) = 2I_L \langle t - | \bar{d} + \rangle \langle u + | \bar{b} - \rangle \omega_+^t, \tag{3.15}$$

where  $\omega_{\pm}^t = \sqrt{E_t \pm |\overrightarrow{p_t}|}$ , c.f. Appendix A.

Needless to say, up to the NLO, the decay matrix elements in this case are taken to be the Born level ones as given in Eqs. (2.5) and (2.6).

#### 3.2.2 NLO corrections to FNAL

In the limit that the bottom quark mass is taken to be zero \*, the most general  $W^* - t - b$  coupling, labelled as FNAL in Fig. 3.1, is

$$\frac{ig}{\sqrt{2}} \left\{ \gamma_{\mu} (F_1^{L\star} P_L + F_1^{R\star} P_R) - \frac{(t_{\mu} - \bar{b}_{\mu})}{m_W} (F_2^{R\star} P_L + F_2^{L\star} P_R) \right\}, \tag{3.16}$$

<sup>\*</sup>We take the bottom quark mass to be zero throughout our calculation because  $(m_b/m_t)^2$  can be ignored numerically. Strictly speaking,  $\alpha_s \ln(m_b)$  terms have been included in the definition of NLO PDF.

where the star in the superscript indicates taking its complex conjugate. This is different from the coupling in Eq. (3.13) because the top quark mass is kept in the calculation, though the bottom quark mass is taken to be zero. Because the charged current interacts with massless quarks in the initial state, one can use the on-shell condition of the massless initial state quarks to rewrite Eq. (3.16) as

$$\frac{ig}{\sqrt{2}} \left\{ \gamma_{\mu} (F_1^{L\star} P_L + F_1^{R\star} P_R) + \bar{b}_{\mu} (F_2^{R\star} P_L + F_2^{L\star} P_R) \right\}, \tag{3.17}$$

where the  $m_W$  has been absorbed into form factors  $F_2^{R*}$  and  $F_2^{L*}$ . Denoting the helicity amplitude as  $\mathcal{M}_{FNAL}(\lambda_{\bar{b}}, \lambda_t)$ , we obtain the helicity amplitudes which include higher order corrections to the s-channel single top quark production as following:

$$\mathcal{M}_{FNAL}(-,-) = 2F_1^{L*} \langle t - | \bar{d} + \rangle \langle u + | \bar{b} - \rangle \omega_+^t$$

$$+ F_2^{R*} \langle \bar{d} - | \bar{b} | u - \rangle \langle t - | \bar{b} - \rangle \omega_-^t,$$
(3.18)

$$\mathcal{M}_{FNAL}(+,-) = 2F_1^{R*} \langle t - | u - \rangle \langle \bar{d} - | \bar{b} + \rangle \omega_{-}^{t}$$

$$+ F_2^{L*} \langle \bar{d} - | \bar{b} | u - \rangle \langle t - | \bar{b} + \rangle \omega_{+}^{t},$$
(3.19)

$$\mathcal{M}_{FNAL}(-,+) = 2F_1^{L*} \langle t+|\bar{d}+\rangle \langle u+|\bar{b}-\rangle \omega_-^t + F_2^{R*} \langle \bar{d}-|\bar{b}|u-\rangle \langle t+|\bar{b}-\rangle \omega_+^t,$$
(3.20)

$$\mathcal{M}_{FNAL}(+,+) = 2F_1^{R*} \langle t + | u - \rangle \langle \bar{d} - | \bar{b} + \rangle \omega_+^t$$

$$+ F_2^{L*} \langle \bar{d} - | \bar{b} | u - \rangle \langle t + | \bar{b} + \rangle \omega_-^t.$$
(3.21)

Again as before, we have suppressed the common factor  $\sqrt{2E_u}\sqrt{2E_{\bar{b}}}$ , the coupling factors  $\left(i\frac{g}{\sqrt{2}}\right)^2$ , and the propagators

$$\frac{1}{s - m_W^2}$$

with  $s = (p_u + p_{\bar{d}})^2$ .

#### 3.2.3 NLO corrections to LIGHT

The effective form factor for  $u-W^*-d$ , labelled as LIGHT in Fig. 3.1, takes the exact form as  $W^*-u-d$  in Eq. (3.13). Hence, the helicity amplitudes  $\mathcal{M}_{LIGHT}(\lambda_t)$  for the t-channel single top quark production are given as follows:

$$\mathcal{M}_{LIGHT}(+) = 2L_L \langle t + | d + \rangle \langle u + | b - \rangle \omega_{-}^t, \tag{3.22}$$

$$\mathcal{M}_{LIGHT}(-) = 2L_L \langle t - | d + \rangle \langle u + | b - \rangle \omega_+^t, \tag{3.23}$$

where  $L_L$  is the effective coupling induced by higher order corrections. Again, we have suppressed the common factor  $\sqrt{2E_u}\sqrt{2E_d}\sqrt{2E_b}$ , the coupling factors  $\left(i\frac{g}{\sqrt{2}}\right)^2$  and the propagators

$$\frac{1}{t - m_W^2}$$

with  $t = (p_u - p_d)^2$ .

#### 3.2.4 NLO corrections to HEAVY

The effective form factor for  $b-W^*-t$ , labelled as HEAVY in Fig. 3.1, takes the exact form as  $W^*-t-b$  in Eq. (3.17). Hence, the helicity amplitudes  $\mathcal{M}_{HEAVY}(\lambda_b, \lambda_t)$  for the t-channel single top quark production are given as follows:

$$\mathcal{M}_{HEAVY}(-,-) = 2H_1^{L*} \langle t - | d + \rangle \langle u + | b - \rangle \omega_+^t$$

$$- H_2^{R*} \langle d - | \not b | u - \rangle \langle t - | b - \rangle \omega_-^t, \qquad (3.24)$$

$$\mathcal{M}_{HEAVY}(+,-) = 2H_1^{R*} \langle t - | u - \rangle \langle d - | b + \rangle \omega_-^t$$

$$- H_2^{L*} \langle d - | \mathcal{M} u - \rangle \langle t - | b + \rangle \omega_+^t, \qquad (3.25)$$

$$\mathcal{M}_{HEAVY}(-,+) = 2H_1^{L*} \langle t+|d+\rangle \langle u+|b-\rangle \omega_-^t$$

$$- H_2^{R*} \langle d-|\not b|u-\rangle \langle t+|b-\rangle \omega_+^t, \qquad (3.26)$$

$$\mathcal{M}_{HEAVY}(+,+) = 2H_1^{R*} \langle t+|u-\rangle \langle d-|b+\rangle \omega_+^t - H_2^{L*} \langle d-|\not b|u-\rangle \langle t+|b+\rangle \omega_-^t,$$
(3.27)

where  $H_{1,2}^{L,R}$  denote the effective couplings induced by higher order corrections. Here,

we have suppressed the common factor  $\sqrt{2E_u}\sqrt{2E_d}\sqrt{2E_b}$ , the coupling factors  $\left(i\frac{g}{\sqrt{2}}\right)^2$  and the propagators

$$\frac{1}{t - m_W^2}$$
with  $t = (p_u - p_d)^2$ .

# 3.2.5 NLO corrections to top quark decay

The most general t-b-W coupling, labelled as DEC for both s-channel and t-channel processes, is

$$\frac{ig}{\sqrt{2}} \left\{ \gamma_{\mu} (D_1^L P_L + D_1^R P_R) - b'_{\mu} (D_2^R P_R + D_2^L P_L) \right\}, \tag{3.28}$$

where  $D_{1,2}^{L,R}$  denote the form factors which include higher order QCD corrections. Denoting the helicity amplitude as  $\mathcal{M}_{DEC}(\lambda_t, \lambda_{b'})$ , we obtain the helicity amplitudes which include higher order corrections to single top quark decay process as follows:

$$\mathcal{M}_{DEC}(-,-) = -2D_1^L \langle b' - | \nu + \rangle \langle e + | t - \rangle \omega_+^t$$

$$+ D_2^R \langle \nu - | b' | e - \rangle \langle b' - | t - \rangle \omega_-^t,$$
(3.29)

$$\mathcal{M}_{DEC}(+,-) = -2D_{1}^{L} \langle b'-|\nu+\rangle \langle e+|t+\rangle \omega_{-}^{t}$$

$$+ D_{2}^{R} \langle \nu-|\not b'|e-\rangle \langle b'-|t+\rangle \omega_{+}^{t},$$
(3.30)

$$\mathcal{M}_{DEC}(-,+) = -2D_1^R \langle b'+|e-\rangle \langle \nu-|t-\rangle \omega_-^t$$

$$+ D_2^L \langle \nu-| \not b'|e-\rangle \langle b'+|t-\rangle \omega_+^t,$$
(3.31)

$$\mathcal{M}_{DEC}(+,+) = -2D_1^R \langle b' + | e - \rangle \langle \nu - | t + \rangle \omega_+^t$$

$$+ D_2^L \langle \nu - | b' | e - \rangle \langle b' + | t + \rangle \omega_-^t,$$
(3.32)

where we ignore the common factor  $\sqrt{2E_e}\sqrt{2E_\nu}\sqrt{2E_{b'}}$ , the coupling factors  $\left(i\frac{g}{\sqrt{2}}\right)^2$  and the propagator

$$\frac{1}{(p_W^2 - m_W^2) + i m_W \Gamma_W}$$

with  $p_W = p_{e^+} + p_{\nu}$ .

The category SDEC (or TDEC) in Fig. 3.1 is obtained by convoluting the s-channel (t-channel) Born level helicity amplitudes (c.f. Eqs. (2.5) and (2.6) or Eqs. (2.7) and (2.8)) with the corresponding DEC amplitudes listed above.

# 3.3 Helicity amplitudes of resolved contributions to single top quark production and decay

Here, we present the helicity amplitudes of resolved corrections for each category defined in Sec. 4.3.

#### 3.3.1 NLO corrections to INIT

The Feynman diagrams of the initial state real emission corrections are shown in Figs. 3.2(a)-(f). At the NLO, a hard gluon can be radiated from initial state quark line, or a quark can be radiated from the gluon splitting. We separate the NLO INIT real emission corrections into three categories:

INI – A : 
$$q\bar{q}' \to W^*g \to t\bar{b}g$$
, including (a) and (b),

$$INI - B : qg \rightarrow W^*q' \rightarrow t\bar{b}q',$$
 including (c) and (d),

INI – C : 
$$\bar{q}'g \to W^*\bar{q} \to t\bar{b}\bar{q}$$
, including (e) and (f),

which are separately gauge invariant. Denoting the helicity amplitude as  $\mathcal{M}_{INI}^{A,B,C}(\lambda_t)$ , we calculate the helicity amplitudes for a given helicity state  $(\lambda_t)$  of the top quark, which are listed as follows.

The helicity amplitudes for INI A are:

$$\mathcal{M}_{INI}^{A}(+) = 2\omega_{-}^{t} \left\{ -\frac{\langle \bar{d}-|t-\rangle \langle \bar{b}+|\not p_{-} \not \mathcal{E}^{*}_{+}|u-\rangle}{p^{2}} + \frac{\langle \bar{b}+|u-\rangle \langle \bar{d}-|\not \mathcal{E}^{*}_{+} \not \mathcal{Q}_{-}|u-\rangle}{q^{2}} \right\},$$

$$(3.33)$$

$$\mathcal{M}_{INI}^{A}(-) = 2\omega_{+}^{t} \left\{ \frac{\langle \bar{d}-|t+\rangle \langle \bar{b}+| \not q_{-} \not g^{*}_{+}|u-\rangle}{p^{2}} - \frac{\langle \bar{b}+|u-\rangle \langle \bar{d}-| \not g^{*}_{+} \not q_{-}|t+\rangle}{q^{2}} \right\},$$

$$(3.34)$$

with  $p = p_u - p_g$  and  $q = p_{\bar{d}} - p_g$ .

The helicity amplitudes for INI B are:

$$\mathcal{M}_{INI}^{B}(+) = 2\omega_{-}^{t} \left\{ -\frac{\langle \bar{b}+|u-\rangle \langle d-|\not \in_{+}\not p_{-}|t-\rangle}{p^{2}} + \frac{\langle d-|t-\rangle \langle \bar{b}+|\not q_{-}\not \in_{+}|u-\rangle}{q^{2}} \right\},$$

$$\mathcal{M}_{INI}^{B}(-) = 2\omega_{+}^{t} \left\{ -\frac{\langle \bar{b}+|u-\rangle \langle \bar{d}-|\not \in_{+}\not p_{-}|t+\rangle}{p^{2}} \right\}$$
(3.35)

$$+\frac{\langle d-|t+\rangle \left\langle \bar{b}+|\not q_-\not e_+|u-\rangle}{q^2}\right\},\tag{3.36}$$

with  $p = p_g - p_d$  and  $q = p_g + p_u$ .

The helicity amplitudes for INI C are:

$$\mathcal{M}_{INI}^{C}(+) = 2\omega_{-}^{t} \left\{ -\frac{\langle \bar{b}+|\bar{u}-\rangle \langle \bar{d}-|\not e_{+}\not q_{-}|t-\rangle}{q^{2}} + \frac{\langle \bar{d}-|t-\rangle \langle \bar{b}+|\not p_{-}\not e_{+}|\bar{u}-\rangle}{p^{2}} \right\}, \tag{3.37}$$

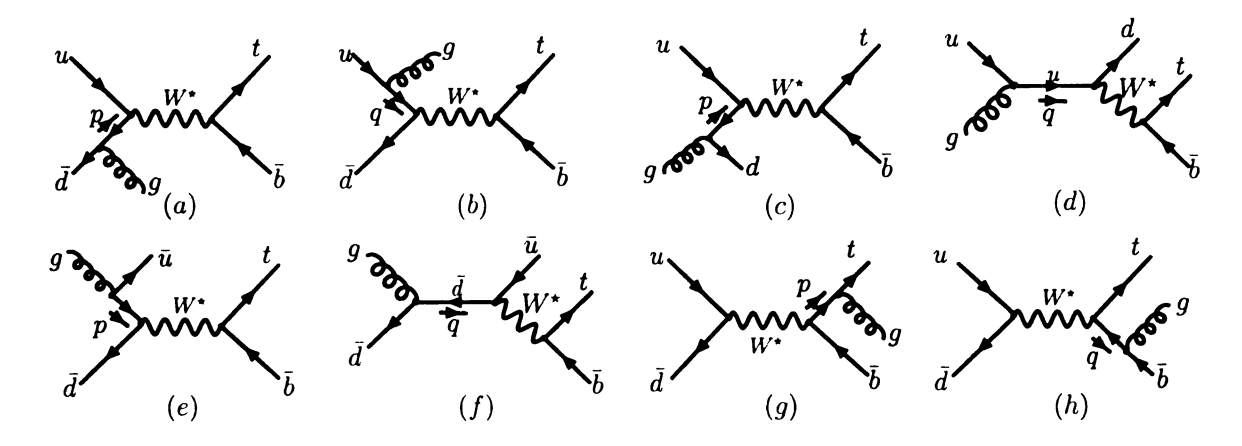


Figure 3.2: Feynman diagrams of the real emission corrections to s-channel single top quark production.

$$\mathcal{M}_{INI}^{C}(-) = 2\omega_{+}^{t} \left\{ -\frac{\langle \bar{b}+|\bar{u}-\rangle \langle \bar{d}-|\not \not e_{+}\not q_{-}|t+\rangle}{q^{2}} + \frac{\langle \bar{d}-|t+\rangle \langle \bar{b}+|\not p_{-}\not e_{+}|\bar{u}-\rangle}{p^{2}} \right\}, \tag{3.38}$$

with  $p = p_g - p_{\bar{u}}$  and  $q = p_g + p_{\bar{d}}$ .

Again, we have suppressed the common factor  $\sqrt{2E_u}\sqrt{2E_{\bar{d}}}\sqrt{2E_{\bar{b}}}$ , the coupling factors  $g_s\left(\frac{ig}{\sqrt{2}}\right)^2$ , and the propagator

$$\frac{1}{p_W^2 - m_W^2 + i m_W \Gamma_W}$$

in all the above equations. Here,  $p_W=p_t+p_{\bar{b}}$  and  $g_s$  is the coupling constant of the strong interaction.

#### 3.3.2 NLO corrections to FNAL

The Feynman diagrams for NLO real emission corrections to the final state of schannel top quark production process are shown in the Fig. 3.2(g) and (h). Denoting the helicity amplitude as  $\mathcal{M}_{FNAL}(\lambda_t)$ , then

$$\mathcal{M}_{FNAL}(+) = 2\omega_{-}^{t} \frac{\langle u+|\bar{b}-\rangle \langle t+|\not \xi^{*}+\not p_{-}|\bar{d}+\rangle}{p^{2}-m_{t}^{2}}$$

$$+ 2m_{t}\omega_{+}^{t} \frac{\langle u+|\bar{b}-\rangle \langle t+|\not \xi^{*}-|\bar{d}+\rangle}{p^{2}-m_{t}^{2}}$$

$$- 2\omega_{-}^{t} \frac{\langle t+|\bar{d}+\rangle \langle u+|\not q_{-}\not \xi^{*}+|\bar{b}-\rangle}{q^{2}}, \qquad (3.39)$$

$$\mathcal{M}_{FNAL}(-) = 2\omega_{+}^{t} \frac{\langle u+|\bar{b}-\rangle \langle t-|\not \xi^{*}+\not p_{-}|\bar{d}+\rangle}{p^{2}-m_{t}^{2}}$$

$$+ 2m_{t}\omega_{-}^{t} \frac{\langle u+|\bar{b}-\rangle \langle t-|\not \xi^{*}-|\bar{d}+\rangle}{p^{2}-m_{t}^{2}}$$

$$- 2\omega_{+}^{t} \frac{\langle t-|\bar{d}+\rangle \langle u+|\not q_{-}\not \xi^{*}+|\bar{b}-\rangle}{q^{2}}, \qquad (3.40)$$

with  $p=p_g+p_t$  and  $q=p_g+p_{\bar{b}}$ . We again suppressed the common factor  $\sqrt{2E_u}\sqrt{2E_{\bar{d}}}\sqrt{2E_{\bar{b}}}$ , the coupling constants  $g_s\left(\frac{ig}{\sqrt{2}}\right)^2$ , and the W boson propagator

$$\frac{1}{p_W^2 - m_W^2 + i m_W \Gamma_W}$$

with  $p_W = p_u + p_{\bar{d}}$ .

#### 3.3.3 NLO corrections to LIGHT

The Feynman diagrams, that generate real emission contributions through coupling a gluon to the light quark lines, are shown in Figs. 3.3(a) to (f). To facilitate our calculations, we separate the NLO LIGHT real emission corrections into the following

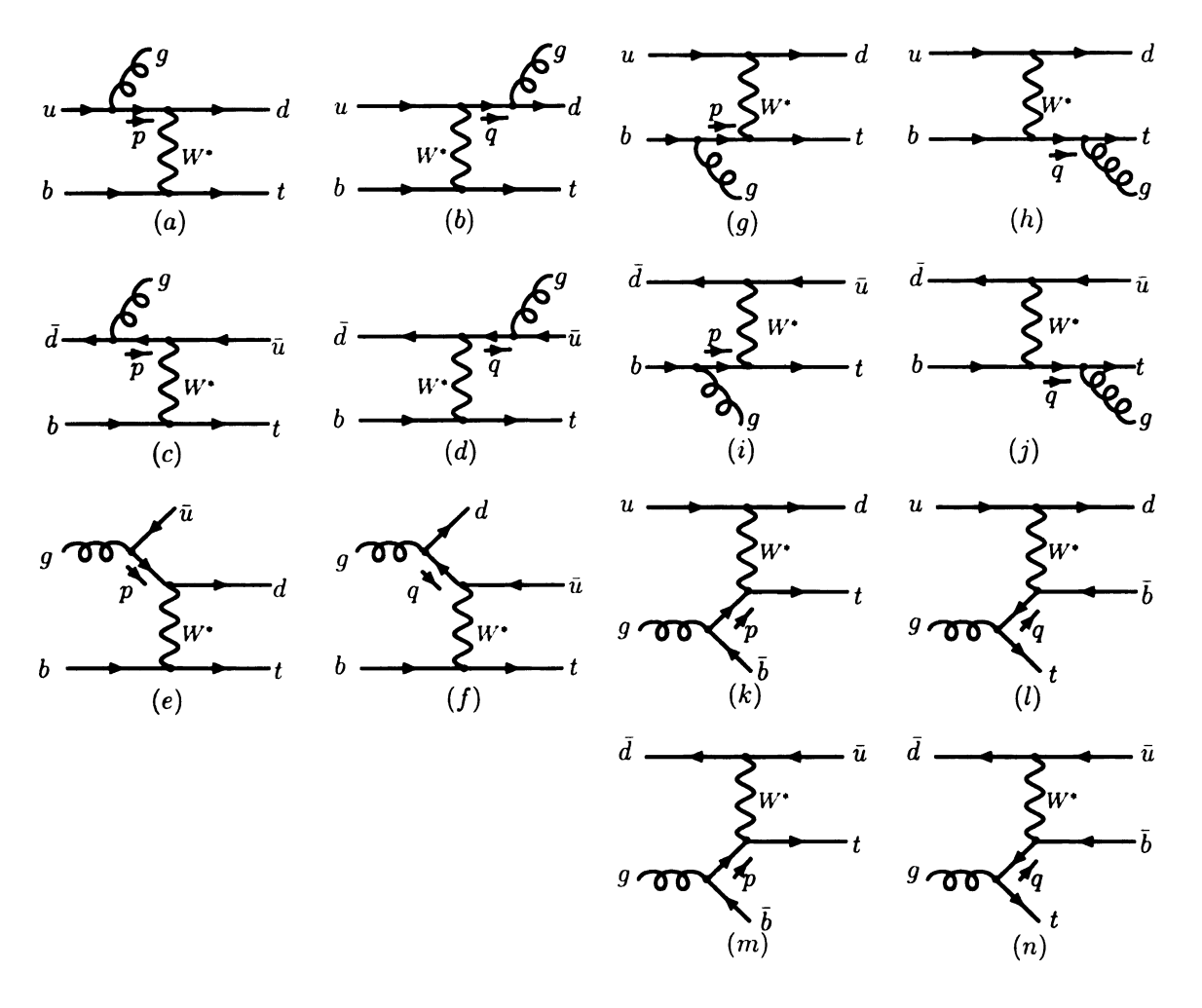


Figure 3.3: Feynman diagrams of the real emission corrections to the t-channel single top quark production

three categories:

LIGHT – A :  $bq \rightarrow q'gt$ , including (a) and (b),

LIGHT – B :  $b\bar{q}' \rightarrow \bar{q}gt$ , including (c) and (d),

LIGHT – C :  $bg \rightarrow \bar{q}q't$ . including (e) and (f).

Denoting the helicity amplitude as  $\mathcal{M}_{LIGHT}^{A,B,C}(\lambda_t)$ , then the helicity amplitudes for LIGHT-A are:

$$\mathcal{M}_{LIGHT}^{A}(+) \ = \ -2\omega_{-}^{t} \left\{ \frac{\left\langle d-|t-\right\rangle \left\langle b+|\not p_{-}\not \mathcal{E}^{*}_{+}|u-\right\rangle}{p^{2}} \right.$$

$$+\frac{\langle b+|u-\rangle \left\langle d-| \not\in^*+ \not q_-|t-\rangle}{q^2}\right\},\tag{3.41}$$

$$\mathcal{M}_{LIGHT}^{B}(-) = 2\omega_{+}^{t} \left\{ \frac{\langle d-|t+\rangle \langle b+| \not p_{-} \not \mathcal{E}^{*}_{+}|u-\rangle}{p^{2}} + \frac{\langle b+|u-\rangle \langle d-| \not \mathcal{E}^{*}_{+} \not q_{-}|t+\rangle}{q^{2}} \right\}, \tag{3.42}$$

with  $p = p_u - p_g$  and  $q = p_d + p_g$ .

The helicity amplitudes for LIGHT-B are:

$$\mathcal{M}_{LIGHT}^{B}(+) = 2\omega_{-}^{t} \left\{ \frac{\langle b+|\bar{u}-\rangle \langle \bar{d}-| \not \xi^{*}+\not p_{-}|t-\rangle}{p^{2}} + \frac{\langle \bar{d}-|t-\rangle \langle b+| \not q_{-} \not \xi^{*}+|\bar{u}-\rangle}{q^{2}} \right\}, \qquad (3.43)$$

$$\mathcal{M}_{LIGHT}^{B}(-) = -2\omega_{+}^{t} \left\{ \frac{\langle b+|\bar{u}-\rangle \langle \bar{d}-| \not \xi^{*}+\not p_{-}|t+\rangle}{p^{2}} + \frac{\langle \bar{d}-|t+\rangle \langle b+| \not q_{-} \not \xi^{*}+|\bar{u}-\rangle}{k^{2}} \right\}, \qquad (3.44)$$

with  $p = p_{\bar{d}} - p_g$  and  $q = p_{\bar{u}} + p_g$ .

The helicity amplitudes for LIGHT-C are:

$$\mathcal{M}_{LIGHT}^{C}(+) = -2\omega_{-}^{t} \left\{ -\frac{\langle d-|t-\rangle \langle b+|\not p_{-}\not \ell_{+}|\bar{u}-\rangle}{p^{2}} + \frac{\langle b+|\bar{u}-\rangle \langle d-|\not \ell_{+}\not k_{-}|t-\rangle}{k^{2}} \right\}, \qquad (3.45)$$

$$\mathcal{M}_{LIGHT}^{C}(-) = 2\omega_{+}^{t} \left\{ -\frac{\langle d-|t+\rangle \langle b+|\not p_{-}\not \ell_{+}|\bar{u}-\rangle}{p^{2}} + \frac{\langle b+|\bar{u}-\rangle \langle d-|\not \ell_{+}\not k_{-}|t+\rangle}{k^{2}} \right\}, \qquad (3.46)$$

with  $p = p_g - p_{\bar{u}}$  and  $q = p_g - p_d$ .

Again in all above equations, we suppressed the common factor  $\sqrt{2E_u}\sqrt{2E_d}\sqrt{2E_b}$ , the coupling constants  $g_s\left(\frac{ig}{\sqrt{2}}\right)^2$ , and the W boson propagator

$$\frac{1}{p_W^2 - m_W^2 + i m_W \Gamma_W}$$

with  $p_W = p_t - p_b$ .

#### 3.3.4 NLO corrections to HEAVY

The Feynman diagrams, that generate real emission contributions through coupling a gluon to the heavy quark lines, are shown in Figs. 3.3(g) to (n). We separate the NLO HEAVY real emission corrections into the following four categories:

$$\text{HEAVY} - A : bq \rightarrow q'gt$$
, including (g) and (h),

$${\rm HEAVY-B}~:~b ar q' o ar q gt,~~{\rm including}$$
 (i) and (j),

$$\text{HEAVY} - \text{C} : qg \rightarrow q'\bar{b}t, \quad \text{including (k)} \text{ and (l)},$$

$$\text{HEAVY} - D : \bar{q}'g \to \bar{q}\bar{b}t, \quad \text{including (m) and (n)}.$$

Denoting the helicity amplitude as  $\mathcal{M}_{HEAVY}^{A,B,C,D}(\lambda_t)$ , then the helicity amplitudes for HEAVY-A are:

$$\mathcal{M}_{HEAVY}^{A}(+) = 2\omega_{-}^{t} \frac{\langle u+|b-\rangle \langle t+| \, \mathscr{E}^{*}_{+} \, \mathscr{Q}_{-}|d+\rangle}{q^{2} - m_{t}^{2}}$$

$$+ 2 m_{t} \omega_{+}^{t} \frac{\langle u+|b-\rangle \langle t+| \, \mathscr{E}^{*}_{-}|d+\rangle}{q^{2} - m_{t}^{2}}$$

$$+ 2\omega_{-}^{t} \frac{\langle t+|d+\rangle \langle u+| \, \mathscr{P}_{-} \, \mathscr{E}^{*}_{+}|b-\rangle}{p^{2}}, \qquad (3.47)$$

$$\mathcal{M}_{HEAVY}^{A}(-) = 2\omega_{+}^{t} \frac{\langle u+|b-\rangle \langle t-| \, \mathscr{E}^{*}_{+} \, \mathscr{Q}_{-}|d+\rangle}{q^{2} - m_{t}^{2}}$$

$$+ 2 m_t \omega_-^t \frac{\langle u + |b - \rangle \langle t - | \mathscr{E}^*_- | d + \rangle}{q^2 - m_t^2}$$

$$+ 2 \omega_+^t \frac{\langle t - |d + \rangle \langle u + | \mathscr{P}_- \mathscr{E}^*_+ | b - \rangle}{n^2}, \qquad (3.48)$$

with  $p = p_b - p_g$  and  $q = p_g + p_t$ .

The helicity amplitudes for HEAVY-B are:

$$\mathcal{M}_{HEAVY}^{B}(+) = 2\omega_{-}^{t} \frac{\langle \bar{u}+|b-\rangle \langle t+|\cancel{\xi^{*}}+\cancel{q}_{-}|\bar{d}+\rangle}{q^{2}-m_{t}^{2}}$$

$$+ 2m_{t}\omega_{+}^{t} \frac{\langle \bar{u}+|b-\rangle \langle t+|\cancel{\xi^{*}}-|\bar{d}+\rangle}{q^{2}-m_{t}^{2}}$$

$$+ 2\omega_{-}^{t} \frac{\langle t+|\bar{d}+\rangle \langle \bar{u}+|\cancel{p}_{-}\cancel{\xi^{*}}+|b-\rangle}{p^{2}}, \qquad (3.49)$$

$$\mathcal{M}_{HEAVY}^{B}(-) = 2\omega_{+}^{t} \frac{\langle \bar{u}+|b-\rangle \langle t-|\cancel{\xi^{*}}+\cancel{q}_{-}|\bar{d}+\rangle}{q^{2}-m_{t}^{2}}$$

$$+ 2m_{t}\omega_{-}^{t} \frac{\langle \bar{u}+|b-\rangle \langle t-|\cancel{\xi^{*}}-|\bar{d}+\rangle}{q^{2}-m_{t}^{2}}$$

$$+ 2\omega_{+}^{t} \frac{\langle t-|\bar{d}+\rangle \langle \bar{u}+|\cancel{p}_{-}\cancel{\xi^{*}}+|b-\rangle}{p^{2}}, \qquad (3.50)$$

The helicity amplitudes for HEAVY-C are:

$$\mathcal{M}_{HEAVY}^{C}(+) = 2\omega_{-}^{t} \frac{\langle u+|\bar{b}-\rangle\langle t+|\not e_{+}\not q_{-}|d+\rangle}{q^{2}-m_{t}^{2}}$$

$$- 2m_{t}\omega_{+}^{t} \frac{\langle u+|\bar{b}-\rangle\langle t+|\not e_{-}|d+\rangle}{q^{2}-m_{t}^{2}}$$

$$- 2\omega_{-}^{t} \frac{\langle t+|d+\rangle\langle u+|\not p_{-}\not e_{+}|\bar{b}-\rangle}{p^{2}}, \qquad (3.51)$$

$$\mathcal{M}_{HEAVY}^{C}(-) = 2\omega_{+}^{t} \frac{\langle u+|\bar{b}-\rangle\langle t-|\not e_{+}\not q_{-}|d+\rangle}{q^{2}-m_{t}^{2}}$$

$$-2m_{t}\omega_{-}^{t}\frac{\langle u+|\bar{b}-\rangle\langle t-|\cancel{\cancel{e}}-|d+\rangle}{q^{2}-m_{t}^{2}}$$

$$-2\omega_{+}^{t}\frac{\langle t-|d+\rangle\langle u+|\cancel{\cancel{p}}-\cancel{\cancel{e}}+|\bar{b}-\rangle}{n^{2}},$$
(3.52)

where  $p = p_g - p_{\bar{b}}$  and  $q = p_g - p_t$ .

The helicity amplitudes for HEAVY-D are:

$$\mathcal{M}_{HEAVY}^{D}(+) = 2\omega_{-}^{t} \frac{\langle \bar{u}+|\bar{b}-\rangle \langle t+|\not \not -|\bar{d}+\rangle}{q^{2}-m_{t}^{2}}$$

$$- 2m_{t} \omega_{+}^{t} \frac{\langle \bar{u}+|\bar{b}-\rangle \langle t+|\not \not -|\bar{d}+\rangle}{q^{2}-m_{t}^{2}}$$

$$- 2\omega_{-}^{t} \frac{\langle t+|\bar{d}+\rangle \langle \bar{u}+|\not \not -|\not -|\bar{b}-\rangle}{p^{2}}, \qquad (3.53)$$

$$\mathcal{M}_{HEAVY}^{D}(-) = 2\omega_{+}^{t} \frac{\langle \bar{u}+|\bar{b}-\rangle \langle t-|\not \not -|\not -|\bar{d}+\rangle}{q^{2}-m_{t}^{2}}$$

$$- 2m_{t} \omega_{-}^{t} \frac{\langle \bar{u}+|\bar{b}-\rangle \langle t-|\not \not -|\bar{d}+\rangle}{q^{2}-m_{t}^{2}}$$

$$- 2\omega_{+}^{t} \frac{\langle \bar{u}+|\bar{b}-\rangle \langle t-|\not \not -|\bar{d}+\rangle}{q^{2}-m_{t}^{2}}$$

$$- 2\omega_{+}^{t} \frac{\langle t-|\bar{d}+\rangle \langle \bar{u}+|\not \not -|\not -|\bar{b}-\rangle}{p^{2}}, \qquad (3.54)$$

where  $p = p_g - p_{\bar{b}}$  and  $q = p_g - p_t$ .

Again in all above equations, we suppressed the common factor  $\sqrt{2E_u}\sqrt{2E_d}\sqrt{2E_b}$ , the coupling constants  $g_s\left(\frac{ig}{\sqrt{2}}\right)^2$ , and the W boson propagator

$$\frac{1}{p_W^2 - m_W^2 + i m_W \Gamma_W}$$

with  $p_W = p_u - p_d$ .

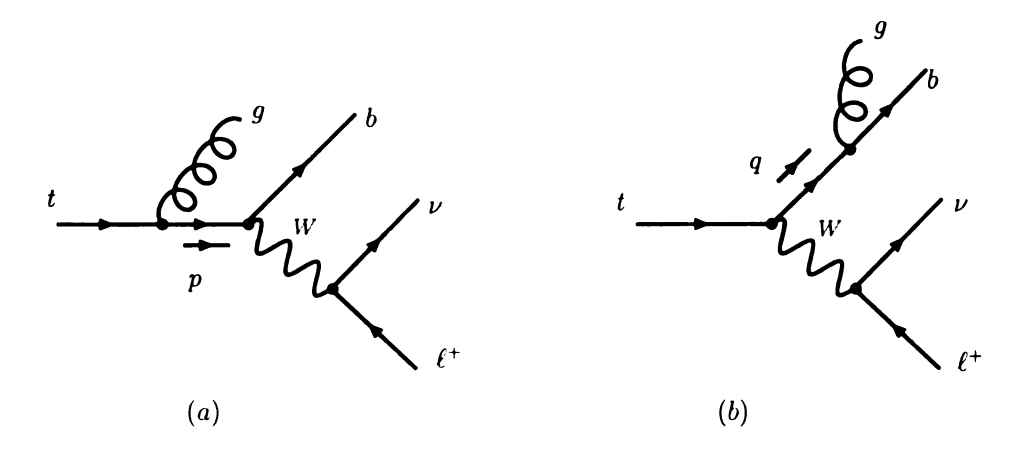


Figure 3.4: Feynman diagrams of the real emission corrections to top quark decay processes

## 3.3.5 NLO corrections to top quark decay

The Feynman diagrams for NLO real emission corrections to the top quark decay process are shown in Fig. 3.4. Denoting the helicity amplitude as  $\mathcal{M}_{DEC}(\lambda_t)$ , then

$$\mathcal{M}_{DEC}(+) = 2\omega_{-}^{t} \frac{\langle b - | \nu + \rangle \langle e + | \not p_{-} \not e_{+}^{*} | t + \rangle}{p^{2} - m_{t}^{2}}$$

$$+ 2m_{t} \omega_{+}^{t} \frac{\langle b - | \nu + \rangle \langle e + | \not e_{-}^{*} | t + \rangle}{p^{2} - m_{t}^{2}}$$

$$+ 2\omega_{-}^{t} \frac{\langle e + | t + \rangle \langle b - | \not e_{+}^{*} | \not e_{-} | \nu + \rangle}{q^{2}}, \qquad (3.55)$$

$$\mathcal{M}_{DEC}(-) = 2\omega_{+}^{t} \frac{\langle b - | \nu + \rangle \langle e + | \not p_{-} \not e_{+}^{*} | t - \rangle}{p^{2} - m_{t}^{2}}$$

$$+ 2m_{t} \omega_{-}^{t} \frac{\langle b - | \nu + \rangle \langle e + | \not e_{-}^{*} | t - \rangle}{p^{2} - m_{t}^{2}}$$

$$+ 2\omega_{+}^{t} \frac{\langle e + | t - \rangle \langle b - | \not e_{+}^{*} | \not q_{-} | \nu + \rangle}{q^{2}}, \qquad (3.56)$$

with  $p = p_t - p_g$  and  $q = p_b + p_g$ . We again suppressed the common factor  $\sqrt{2E_e}\sqrt{2E_\nu}\sqrt{2E_b}$ , the coupling constants  $g_s\left(\frac{ig}{\sqrt{2}}\right)^2$ , and the W boson propagator

$$\frac{1}{p_W^2 - m_W^2 + i m_W \Gamma_W}$$
with  $m_W = n_+ + n_W$ 

with  $p_W = p_{e^+} + p_{\nu}$ .

#### NLO SCV form factor of the single top quark 3.4 production and decay process

In this section the analytical results of the effective form factors are given in details together with the corresponding phase space boundary conditions which splice the phase space of real emission corrections into unresolved and resolved regions. Provided with such phase space boundary conditions, one can use the helicity amplitudes given in the previous section to perform numerical calculations. Since the unresolved regions of massless partons differ from the ones of massive partons, we consider both the massless and massive partons and present the detailed derivations of the SCV form factors in Sec. 3.4.1 and Sec. 3.4.2, respectively. For comparison, we present our results in both the DREG and DRED schemes. We note that the form factors and the crossing functions should be applied consistently in a given scheme.

#### 3.4.1NLO corrections to INIT

Let us first examine the initial state corrections to the s-channel single top quark process, c.f. Fig 3.1. After calculating the effective matrix element with all the partons in the final state, we cross the relevant partons into the initial state to obtain the needed matrix element. In dimension  $d=4-2\epsilon$ , the NLO matrix element for the vertex  $q - \bar{q}' - W^*$  can be written as

$$M_{\mu}^{q\bar{q}' \to W^*} = \frac{-ig}{\sqrt{2}} \bar{v}(\bar{q}') [f_1^{q\bar{q}' \to W^*} \gamma_{\mu}] P_L u(q), \qquad (3.57)$$

where  $u(q)(\bar{v}(\bar{q}'))$  is the wave function of  $q(\bar{q}')$ ,  $P_L = (1 - \gamma_5)/2$ . As usual, we have used the particle to label its momentum.

The calculation of the virtual corrections for the vertex  $q - \bar{q}' - W^*$  is straightforward and after renormalization it contributes

$$f_1^{q\bar{q}' \to W} = \frac{\alpha_s}{4\pi} C_F C_\epsilon \left\{ -\frac{2}{\epsilon^2} + \frac{2}{\epsilon} \ln \frac{\hat{s}}{m_t^2} - \frac{3}{\epsilon} + \frac{4\pi^2}{3} + 3 \ln \frac{\hat{s}}{m_t^2} - \ln^2 \frac{\hat{s}}{m_t^2} + I_{\text{scheme}}^{q\bar{q}' \to W(\text{virt})} \right\},$$
(3.58)

where  $\hat{s}=2p_q\cdot p_{\bar{q}'},\ C_F=4/3,\ C_\epsilon=\left(\frac{4\pi\mu^2}{m_t^2}\right)^\epsilon\Gamma(1+\epsilon)$  and the scheme dependent

term  $I_{\text{scheme}}^{q\bar{q}' \to W(\text{virt})}$  is

$$I_{\text{Scheme}}^{q\bar{q}' \to W(\text{virt})} = \begin{cases} -8 & \text{in DREG scheme,} \\ -7 & \text{in DRED scheme.} \end{cases}$$

We have neglected all the possible imaginary parts in the above result and also in what follows, since they do not contribute to cross sections up to the NLO. We also set  $m_b = 0$  throughout the this work. The detailed calculation is given in Appendix D.1. Note that the tree level amplitude corresponds to setting  $f_1^{q\bar{q}'\to W} = 1$  in Eq. (3.57).

In the phase space slicing method, the soft and collinear singularities in the virtual corrections, the poles of  $\epsilon$  in Eq. (3.58), should be cancelled by the unresolved real emission corrections from processes shown in Eqs. (3.1)-(3.3). Below, we will partition the phase space of the real emission corrections to calculate the unresolved contribution.

As an example, let us examine the  $q\bar{q} \to W^*g$  process. After crossing all the initial state partons of the process  $q\bar{q}' \to W^*g$  into the final state, the particles' momenta are assigned as in Fig. 3.5 which requires the crossed process  $W^* \to \bar{q}q'g$ .

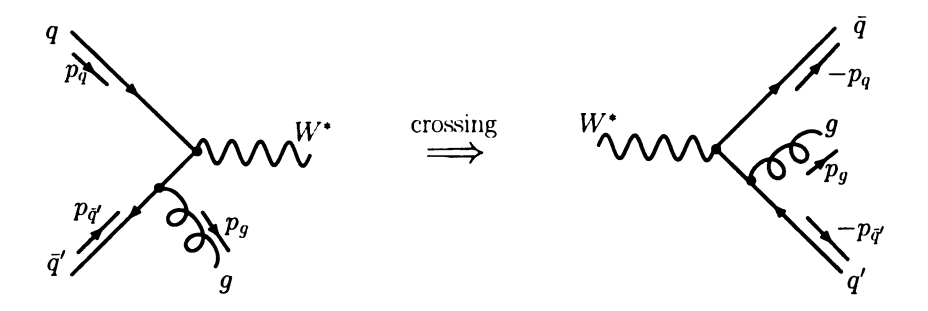


Figure 3.5: Illustration for crossing the initial state partons into the final state in the process  $q\bar{q}' \to W^*g$ .

Let us consider the whole phase space of the process  $W^* \to \bar{q}q'g$  as the identity and partition it into three regions as shown in Fig. 3.6:

$$1 \equiv \Theta(|s_{\bar{q}g}| + |s_{q'g}| - 2s_{min}) + \Theta(2s_{min} - |s_{\bar{q}g}| - |s_{q'g}|)$$

$$- \Theta(|s_{\bar{q}g}| - 2s_{min})\Theta(s_{min} - |s_{q'g}|) - \Theta(|s_{q'g}| - 2s_{min})\Theta(s_{min} - |s_{\bar{q}g}|)$$

$$+ \Theta(|s_{\bar{q}g}| - 2s_{min})\Theta(s_{min} - |s_{q'g}|) + \Theta(|s_{q'g}| - 2s_{min})\Theta(s_{min} - |s_{\bar{q}g}|)$$

$$= \mathcal{F}_1 + \mathcal{F}_2 + \mathcal{F}_3, \tag{3.59}$$

where

$$\mathcal{F}_{1} = \Theta(\left|s_{\bar{q}g}\right| + \left|s_{q'g}\right| - 2s_{min})$$

$$- \Theta(\left|s_{\bar{q}g}\right| - 2s_{min})\Theta(s_{min} - \left|s_{q'g}\right|)$$

$$- \Theta(\left|s_{q'g}\right| - 2s_{min})\Theta(s_{min} - \left|s_{\bar{q}g}\right|), \qquad (3.60)$$

$$\mathcal{F}_{2} = \Theta(2s_{min} - \left|s_{\bar{q}g}\right| - \left|s_{q'g}\right|), \qquad (3.61)$$

$$\mathcal{F}_{3} = \Theta(\left|s_{\bar{q}g}\right| - 2s_{min})\Theta(s_{min} - \left|s_{q'g}\right|)$$

(3.62)

Here  $\Theta$  is the Heaviside step function and  $s_{ij} = 2p_i \cdot p_j$  where  $p_i$  is the four-momentum of the particle i. In the phase space region constrained by function  $\mathcal{F}_1$  (resolved), there is no soft and collinear divergencies, therefore it can be calculated in four dimensions

+  $\Theta(\left|s_{q'q}\right| - 2s_{min})\Theta(s_{min} - \left|s_{\bar{q}g}\right|).$ 

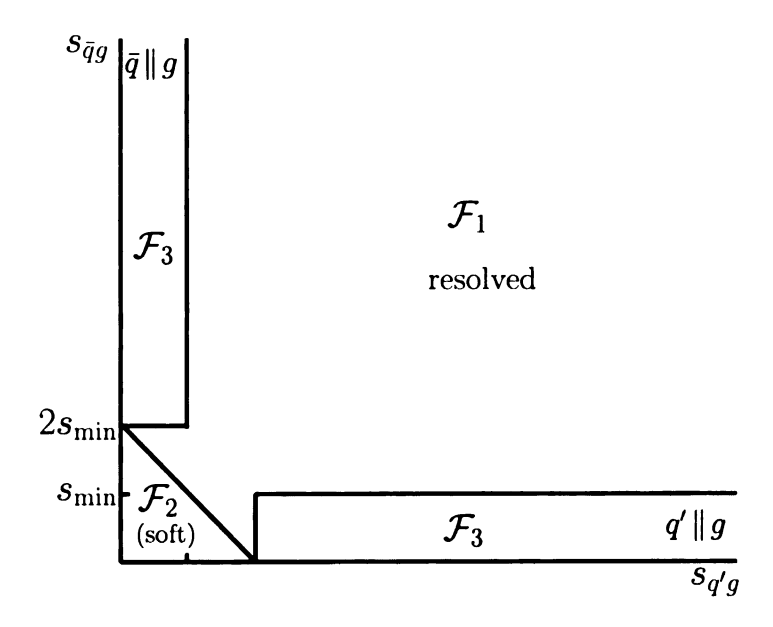


Figure 3.6: The  $s_{\bar{q}g} - s_{q'g}$  plane for quark pair annihilation to virtual W-boson showing the delineation into soft  $(\mathcal{F}_2)$  and collinear  $(\mathcal{F}_2)$  and resolved region  $(\mathcal{F}_1)$ .

numerically. The soft region is defined by the function  $\mathcal{F}_2$ , which has both the soft and collinear divergencies. The collinear regions are defined by the function  $\mathcal{F}_3$  as shown in Fig. 3.6 which only have the collinear singularities but no soft singularities. In the function  $\mathcal{F}_3$ , the first term denotes the collinear region of  $g \parallel q'$  and the second term represents the collinear region of  $g \parallel \bar{q}$ .

Under the soft approximation, i.e. in the soft region  $(\mathcal{F}_2)$ , the squared matrix element can be written as a factor multiplying the squared Born matrix element:

$$\Theta(2s_{min} - \left|s_{\bar{q}g}\right| - \left|s_{q'g}\right|) \left|\mathcal{M}(W^* \to \bar{q}q'g)\right|^2 \xrightarrow{p_g \to 0} \hat{f}_{soft}^{W^* \to \bar{q}q'g} \left|\mathcal{M}(W^* \to \bar{q}q')\right|,$$

where we have defined the eikonal factor  $\hat{f}_{soft}^{W^* \to \bar{q}q'g}$  as

$$\hat{f}_{soft}^{W^* \to \bar{q}q'g} = g_s C_F \mu^{2\epsilon} \frac{4(2p_{\bar{q}} \cdot p_{q'})}{(2p_{\bar{q}} \cdot p_q)(2p_{q'} \cdot p_q)}.$$

It is very simple to analytically integrate the eikonal factors in d dimensions over the soft gluon momentum. The detailed calculation is given in Appendix E.1.1. Here we

only present the final result of the soft factor:

$$I_{\text{soft}}^{W^* \to \bar{q}q'g} = \frac{g_s^2}{16\pi^2} \frac{C_F}{\Gamma(1-\epsilon)} \left(\frac{4\pi\mu_d^2}{s_{min}}\right)^2 \left\{ \frac{2}{\epsilon^2} - \frac{4\ln 2}{\epsilon} - \frac{2}{\epsilon} \ln\left(\frac{s_{min}}{\hat{s}}\right) + 4\ln^2 2 - \frac{\pi^2}{3} + \ln^2\left(\frac{s_{min}}{\hat{s}}\right) + 4\ln 2\ln\left(\frac{s_{min}}{\hat{s}}\right) \right\}.$$
(3.63)

In addition to being singular in the soft gluon region, the matrix elements are also singular in the collinear region  $(\mathcal{F}_3)$  where the matrix elements exhibit an overall factorization. In the limit  $g \parallel \bar{q}$ , we define

$$p_g \xrightarrow{g \parallel \bar{q}} (1 - \xi) p_h, \qquad p_{\bar{q}} \xrightarrow{g \parallel \bar{q}} \xi p_h,$$

with  $p_h = p_g + p_{\tilde{q}}$ . In this limit,

$$\Theta(\left|s_{q'g}\right| - 2s_{min})\Theta(s_{min} - \left|s_{\bar{q}g}\right|) \left|\mathcal{M}(W^* \to \bar{q}q'g)\right|^2 \xrightarrow{g \parallel \bar{q}} \hat{c}^{\bar{q}g \to \bar{q}} \left|\mathcal{M}(W^* \to \bar{q}q')\right|^2,$$

where the collinear factor  $\hat{c}^{\bar{q}g \to \bar{q}}$  is defined as

$$\hat{c}^{\bar{q}g \to \bar{q}} = g_s^2 \mu^{2\epsilon} C_F \frac{P^{\bar{q}g \to \bar{q}}(\xi)}{2p_g \cdot p_{\bar{q}}}.$$

The function  $P^{\bar{q}g \to \bar{q}}$  is related to the Altarelli-Parisi splitting function, which has some scheme dependence since one can treat the hard particle in either 4 or d dimensions. In this work, we adopt two schemes: the conventional DREG scheme where all the particles are treated in d-dimensions and the dimensional reduction (DRED) scheme,

$$P^{\bar{q}g \to \bar{q}}(\xi) = \begin{cases} 2 \frac{1 + \xi^2 - \epsilon (1 - \xi)^2}{1 - \xi}, & \text{in DREG scheme,} \\ 2 \frac{1 + \xi^2}{1 - \xi}, & \text{in DRED scheme.} \end{cases}$$
(3.64)

Integrating over the collinear phase space and also considering the contribution from the region  $p_g \parallel p_{g'}$ , we obtain the collinear factor (cf. Appendix E.1.2)

$$I_{\text{col}}^{W^* \to \bar{q}q'g} = \frac{g_s^2}{16\pi^2} \frac{C_F}{\Gamma(1-\epsilon)} \left(\frac{4\pi\mu_d^2}{s_{min}}\right)^{\epsilon}$$

$$\times \left\{ \frac{4}{\epsilon} \ln\left(\frac{2s_{min}}{\hat{s}}\right) + \frac{3}{\epsilon} - \frac{2\pi^2}{3} - 2\ln^2\left(\frac{2s_{min}}{\hat{s}}\right) + I_{\text{Scheme}}^{W^* \to \bar{q}q'(\text{col})} \right\}$$
(3.65)

where the scheme dependent factor  $I_{\text{Scheme}}^{W^* \to \bar{q}q'(\text{col})}$  is

$$I_{\text{Scheme}}^{W^* \to \bar{q}q'(\text{col})} = \begin{cases} 7 & \text{in DREG scheme,} \\ 6 & \text{in DRED scheme.} \end{cases}$$

Summing the soft and collinear factors and crossing the needed partons into the initial state, we get the contributions to  $\mathcal{M}^{q\bar{q}'\to W^*}$  from the unresolved real (soft-plus-collinear) corrections from processes (3.1)-(3.3) as following:

$$f_1^{q\bar{q}' \to W(\text{real})} = \frac{\alpha_s}{4\pi} C_F C_\epsilon \left\{ \frac{2}{\epsilon^2} - \frac{2}{\epsilon} \ln \frac{\hat{s}}{m_t^2} + \frac{3}{\epsilon} - \frac{4\pi^2}{3} + 2\ln^2 2 + 3\ln \frac{m_t^2}{s_{min}} - 2\ln^2 \frac{\hat{s}}{s_{min}} + \ln^2 \frac{\hat{s}}{m_t^2} + I_{\text{Scheme}}^{q\bar{q}' \to W(\text{real})} \right\}$$

where the scheme dependent term  $I_{\text{Scheme}}^{q\bar{q}' \to W(\text{real})}$  is

$$I_{\text{Scheme}}^{q\bar{q}' \to W(\text{real})} = \begin{cases} 7 & \text{in DREG scheme,} \\ 6 & \text{in DRED scheme.} \end{cases}$$

It is clear that the divergences of  $f_1^{q\bar{q}'\to W({\rm virt})}$  and  $f_1^{q\bar{q}'\to W({\rm real})}$  cancel with each other and the sum is finite and  $s_{min}$  dependent. The remaining unresolved real

corrections for  $q\bar{q}' \to W^*$  are included through the process independent, but  $s_{min}$  and factorization scheme dependent universal crossing functions.

The corrections from the resolved regions of processes (3.1)-(3.3) can be obtained by multiplying the following phase space slicing functions by the corresponding phase space elements and matrix element squares in the cross section calculations:

• For 
$$q\bar{q'} \to W^*g \to t\bar{b}g$$
 
$$\left[\Theta(\left|s_{gq}\right| + \left|s_{g\bar{q'}}\right| - 2s_{min}) - \Theta(\left|s_{gq}\right| - 2s_{min})\Theta(s_{min} - \left|s_{g\bar{q'}}\right|) - \Theta(\left|s_{g\bar{q'}}\right| - 2s_{min})\Theta(s_{min} - \left|s_{gq}\right|)\right]$$

• For 
$$qg \to W^*q' \to t\bar{b}q'$$
 
$$\left[1 - \Theta(s_{min} - \left|s_{gq'}\right|)\right]$$

• For 
$$g\bar{q}' \to W^*\bar{q} \to t\bar{b}\bar{q}$$
 
$$\left[1 - \Theta(s_{min} - \left|s_{g\bar{q}}\right|)\right]$$

The  $\Theta$  functions ensure the amplitude squares are finite in four dimensions. Therefore, they can be calculated numerically.

#### 3.4.2 NLO corrections to FNAL

Now we look at the final state corrections to  $W_{\mu}^* - t - \bar{b}$ . The NLO matrix element for the  $W^* - t - b$  vertex can be written as

$$\mathcal{M}_{\mu}^{W^* \to t\bar{b}} = \frac{-ig}{\sqrt{2}} \bar{u}(t) [f_1^{W^* \to t\bar{b}} \gamma_{\mu} + f_2^{W^* \to t\bar{b}} \frac{(p_t - p_{\bar{b}})_{\mu}}{m_t}] P_L v(\bar{b}). \tag{3.66}$$

The above formula is valid only when W boson is on-shell or off-shell but coupled to massless quarks because we have neglected term proportional to  $(p_t + p_{\bar{b}})_{\mu}$ . At

the tree level,  $f_1^{W \to t\bar{b}} = 1$  and  $f_2^{W \to t\bar{b}} = 0$ . At the NLO, the virtual corrections to  $f_1^{W \to t\bar{b}}$ ,  $f_2^{W \to t\bar{b}}$  are

$$f_{1}^{W \to t\bar{b}(\text{virt})} = \frac{\alpha_{s}}{4\pi} C_{F} C_{\epsilon} \left\{ -\frac{1}{\epsilon^{2}} - \frac{5}{2\epsilon} + \frac{2}{\epsilon} \ln \frac{\hat{s}_{1}}{m_{t}^{2}} + \pi^{2} + 2 \text{Li}_{2}(\frac{\hat{s}}{\hat{s}_{1}}) + 3 \ln \frac{\hat{s}_{1}}{m_{t}^{2}} - \frac{m_{t}^{2}}{\hat{s}} \ln \frac{\hat{s}_{1}}{m_{t}^{2}} - \ln^{2} \frac{\hat{s}_{1}}{m_{t}^{2}} + I_{\text{Scheme}}^{W \to t\bar{b}(\text{virt})} \right\},$$
(3.67)

$$f_2^{W \to t\bar{b}(\text{virt})} = \frac{\alpha_s}{4\pi} C_F C_\epsilon \left\{ \frac{m_t^2}{\hat{s}} \ln \frac{\hat{s}_1}{m_t^2} \right\}, \tag{3.68}$$

where  $\hat{s}=(p_t+p_{\bar{b}})^2$ ,  $\hat{s}_1=2p_t\cdot p_{\bar{b}}=\hat{s}-m_t^2$  and the scheme dependent term  $I_{\text{Scheme}}^{W\to t\bar{b}(\text{virt})}$  is

$$I_{\text{Scheme}}^{W \to t\bar{b}(\text{virt})} = \begin{cases} -6 & \text{in DREG scheme,} \\ -5 & \text{in DRED scheme.} \end{cases}$$

The detailed calculation of the virtual correction is given in Appendix D.2.

In the presence of a massive top quark, the structure of the collinear and soft poles of FINAL matrix elements is completely different from the massless case (INIT). The top quark mass serves as a regularizer for collinear singularities. Thus, the matrix element contains fewer singular structures. However, the presence of the top quark mass leads to more complicated phase space integrals. Again, let us consider the whole phase space of the process  $W^* \to t\bar{b}g$  as the identity and partition it into three regions as shown in Fig. 3.7:

$$1 \equiv \Theta(s_{tg} + s_{\bar{b}g} - 2s_{min}) + \Theta(2s_{min} - s_{tg} - s_{\bar{b}g})$$

$$+ \Theta(s_{tg} - 2s_{min})\Theta(s_{min} - s_{\bar{b}g}) - \Theta(s_{tg} - 2s_{min})\Theta(s_{min} - s_{\bar{b}g})$$

$$= \mathcal{F}_1 + \mathcal{F}_2 + \mathcal{F}_3, \tag{3.69}$$

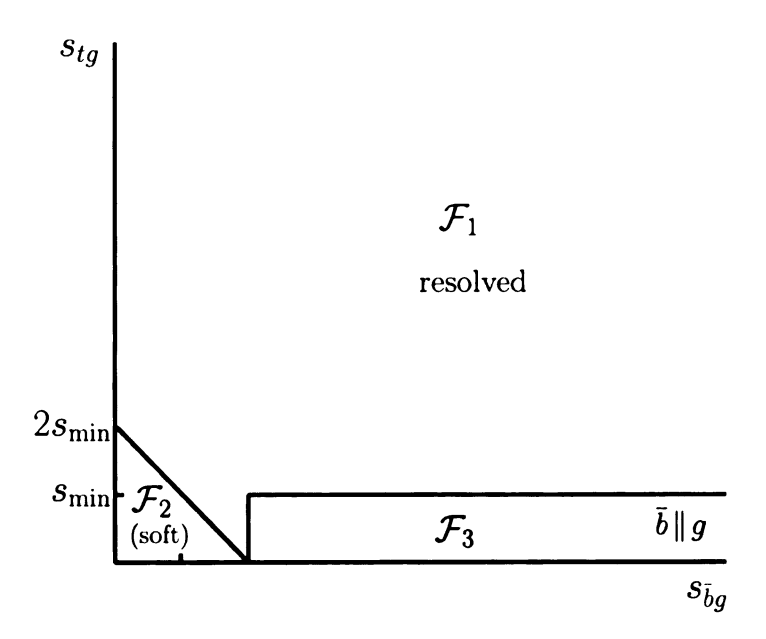


Figure 3.7: The  $s_{tg} - s_{\bar{b}g}$  plane for quark pair annihilation to virtual W-boson showing the delineation into soft  $(\mathcal{F}_2)$  and collinear  $(\mathcal{F}_2)$  and resolved region  $(\mathcal{F}_1)$ .

where

$$\mathcal{F}_{1} = \Theta(s_{tg} + s_{\bar{b}g} - 2s_{min}) - \Theta(s_{tg} - 2s_{min})\Theta(s_{min} - s_{\bar{b}g}), \tag{3.70}$$

$$\mathcal{F}_2 = \Theta(2s_{min} - s_{tg} - s_{\bar{b}q}), \tag{3.71}$$

$$\mathcal{F}_3 = \Theta(s_{tg} - 2s_{min})\Theta(s_{min} - s_{\bar{b}g}). \tag{3.72}$$

Here again, we divide the phase space of process  $W^* \to t\bar{b}g$  into three parts: the resolved region  $(\mathcal{F}_1)$ , the soft region  $(\mathcal{F}_2)$  and the collinear region  $(\mathcal{F}_3)$ . Moreover, the phase space boundary conditions are much simpler than the case of massless partons, c.f. Eqs. (3.60)-(3.62).

Under the soft approximation, in the soft region  $(\mathcal{F}_2)$ , the squared matrix element can be written as a factor multiplying the squared Born matrix element:

$$\Theta(2s_{min} - s_{tg} - s_{\bar{b}g}) \left| \mathcal{M}(W^* \to t\bar{b}g) \right|^2 \xrightarrow{p_g \to 0} \hat{f}_s^{W^* \to tbg} \left| \mathcal{M}(W^* \to t\bar{b}) \right|,$$

where we have defined the eikonal factor  $\hat{f}_s^{W^* \to t\bar{b}g}$  as:

$$\hat{f}_s^{W^* \to t\bar{b}g} = g_s C_F \mu^{2\epsilon} \frac{4(2p_t \cdot p_{\bar{b}})}{(2p_t \cdot p_g)(2p_{\bar{b}} \cdot p_g)} - \frac{4m_t^2}{(2p_t \cdot p_g)^2}.$$

Integrating the eikonal factors  $\hat{f}_s^{W^* \to t\bar{b}g}$  in d dimensions over the soft gluon momentum, we get the soft factor

$$I_{\text{soft}}^{W^* \to t\bar{b}g} = \frac{g_s^2}{16\pi^2} \frac{C_F}{\Gamma(1-\epsilon)} \left(\frac{4\pi\mu_d^2}{s_{min}}\right)^2 \left(\frac{s_{min}}{\hat{s}_1 + m_t^2}\right)^{-\epsilon}$$

$$\times \left\{\frac{1}{\epsilon^2} - -\frac{1}{\epsilon} \left[\ln\left(1 + \frac{\hat{s}_1}{m_t^2}\right) + 2\ln 2 - 1\right] - \frac{\pi^2}{6} + 2\ln^2 2 - 2\ln 2 + \left[2\ln 2 + \frac{\hat{s}_1 + 2m_t^2}{\hat{s}_1}\right] \ln\left(1 + \frac{\hat{s}_1}{m_t^2}\right) - \frac{1}{2}\ln^2\left(1 + \frac{\hat{s}_1}{m_t^2}\right) - 2\text{Li}_2\left(\frac{\hat{s}_1}{\hat{s}_1 + m_t^2}\right)\right\}. \tag{3.73}$$

In the collinear region  $(\mathcal{F}_3)$ , where  $g \parallel \bar{b}$ , the matrix elements exhibit an overall factorization as

$$\Theta(s_{tg} - 2s_{min})\Theta(s_{min} - s_{\bar{b}q}) \left| \mathcal{M}(W^* \to t\bar{b}g) \right|^2 \xrightarrow{g \parallel \bar{b}} \hat{c}^{\bar{b}g \to \bar{b}}(\xi) \left| \mathcal{M}(W^* \to t\bar{b}) \right|^2,$$

where the collinear factor  $\hat{c}^{\bar{b}g \to \bar{b}}$  is defined as:

$$\hat{c}^{\bar{b}g \to \bar{b}} = g_s^2 \mu^{2\epsilon} C_F \left[ \frac{P^{\bar{b}g \to b}(\xi)}{2p_{\bar{b}} \cdot p_g} - \frac{4m_t^2}{\left(2p_t \cdot p_g\right)^2} \right].$$

where  $P^{\bar{b}g \to \bar{b}}(\xi)$  is same as Eq. (E.16). Integrating over the collinear phase space, we

get the collinear factor

$$I_{\text{col}}^{W^* \to t\bar{b}g} = \frac{g_s^2}{16\pi^2} \frac{C_F}{\Gamma(1-\epsilon)} \left(\frac{4\pi\mu_d^2}{s_{min}}\right)^{\epsilon}$$

$$\times \left\{ \frac{2}{\epsilon} \left[ \ln^2 \left(\frac{2s_{min}}{\hat{s}}\right) + \frac{3}{4} \right] - \ln^2 \left(\frac{2s_{min}}{\hat{s}}\right) - \frac{\pi^2}{3} - \frac{m_t^2}{\hat{s}_1} + I_{\text{Scheme}}^{W^* \to t\bar{b}g(\text{col})} \right\}$$

$$(3.74)$$

where the scheme dependent factor  $I_{\text{Scheme}}^{W^* \to t\bar{b}g(\text{col})}$  is

$$I_{\text{Scheme}}^{W^* \to t\bar{b}g(\text{col})} = \begin{cases} \frac{7}{2} & \text{in DREG scheme,} \\ 3 & \text{in DRED scheme.} \end{cases}$$

Summing the soft and collinear factor, we get the contributions to  $\mathcal{M}^{W^* \to t\bar{b}}$  from the unresolved real (soft+collinear) corrections as follows:

$$\begin{split} f_1^{W^* \to t\bar{b}g(\text{real})} &= \frac{\alpha_s}{4\pi} C_F C_\epsilon \left\{ \frac{1}{\epsilon^2} + \frac{5}{2\epsilon} - \frac{2}{\epsilon} \ln \frac{\hat{s}_1}{m_t^2} - \frac{2\pi^2}{3} + \ln^2 2 - 2 \ln 2 \right. \\ &- 2 \text{Li}_2(\frac{\hat{s}_1}{\hat{s}}) - \frac{7}{2} \ln \frac{s_{min}}{m_t^2} + 2 \ln 2 \ln \frac{\hat{s}_1}{m_t^2} + \left(2 + \frac{2m_t^2}{\hat{s}_1}\right) \ln \frac{\hat{s}}{m_t^2} \\ &- \ln^2 \frac{\hat{s}}{m_t^2} - \ln^2 \frac{\hat{s}_1}{s_{min}} + 2 \ln \frac{\hat{s}_1}{m_t^2} \ln \frac{s_{min}}{m_t^2} - \frac{m_t^2}{\hat{s}_1} + I_{\text{Scheme}}^{W^* \to t\bar{b}g(\text{real})} \right\}, \end{split}$$

where the scheme dependent term  $I_{\text{Scheme}}^{W^* \to t\bar{b}g(\text{real})}$  is

$$I_{\text{Scheme}}^{W^* \to t \bar{b} g(\text{real})} = \begin{cases} \frac{7}{2} & \text{in DREG scheme,} \\ 3 & \text{in DRED scheme.} \end{cases}$$

The correction from the resolved regions of process (3.4) can be obtained by multiplying the following phase space slicing functions by the corresponding phase space elements and matrix element squares in the cross section calculations:

$$\left[\Theta(s_{tg}+s_{\bar{b}g}-2s_{min})-\Theta(s_{tg}-2s_{min})\Theta(s_{min}-s_{\bar{b}g})\right].$$

#### 3.4.3 NLO corrections to LIGHT

The NLO matrix element fro the  $q-W_{\mu}-q'$  vertex can be written as

$$M_{\mu}^{q \to W q'} = \frac{-ig}{\sqrt{2}} \bar{u}(q') [f_1^{q \to W q'} \gamma_{\mu} P_L] u(q), \qquad (3.75)$$

where  $u(q)(\bar{u}(q'))$  is the wave function of q(q'). The virtual correction to  $f_1^{q \to Wq'}$  is

$$f_{1}^{q \to Wq'(\text{virt})} = \frac{\alpha_{s}}{4\pi} C_{F} C_{\epsilon} \left\{ -\frac{2}{\epsilon^{2}} + \frac{2}{\epsilon} \ln(\frac{-\hat{t}}{m_{t}^{2}}) - \frac{3}{\epsilon} + \frac{\pi^{2}}{3} + 3\ln(\frac{-\hat{t}}{m_{t}^{2}}) - \ln^{2}(\frac{-\hat{t}}{m_{t}^{2}}) + I_{\text{scheme}}^{q \to Wq'(\text{virt})} \right\},$$
(3.76)

where  $\hat{t} = -2p_q \cdot p_{q'}$  and the scheme dependent term  $I_{\text{Scheme}}^{q \to Wq'(\text{virt})}$  is

$$I_{\text{Scheme}}^{q \to Wq'(\text{virt})} = \begin{cases} -8 & \text{in DREG scheme,} \\ -7 & \text{in DRED scheme.} \end{cases}$$

The tree level amplitude can be obtained by setting  $f_1^{q \to Wq'} = 1$ .

We now consider the unresolved real correction to  $f_1^{q \to Wq'}$ . There are two processes that contribute to  $q - W_{\mu} - q'$  vertex:

- $bq \rightarrow tq'g(I)$ , in which the gluon only connects with the light quark (q,q') line, c.f. Eqs. (3.6) and (3.7),
- $bg \rightarrow t\bar{q}q'$ , c.f. Eq. 3.10.

The soft and collinear divergent regions of  $bq \to tq'g(I)$  can be constrained by the function

$$\left[\Theta(2s_{min} - \left|s_{qg}\right| - \left|s_{q'g}\right|) + \Theta(\left|s_{qg}\right| - 2s_{min})\Theta(s_{min} - \left|s_{q'g}\right|) + \Theta(\left|s_{q'g}\right| - 2s_{min})\Theta(s_{min} - \left|s_{qg}\right|)\right].$$

In the above function, the first term constrains  $p_g$  to be soft and the second and third terms restrict  $p_g$  to be collinear with  $p_{q'}$  and  $p_q$ , respectively. The process  $bg \to t\bar{q}q'$  has only a collinear divergent phase space region which is projected by

$$\left[\Theta(s_{min} - \left|s_{\bar{q}g}\right|) + \Theta(s_{min} - \left|s_{q'g}\right|)\right],$$

in which the two terms require  $p_g$  to be collinear with  $p_q$  and  $p_{q'}$ , respectively. After performing all the above constrained phase space integrations analytically, one can get the contribution to  $f_1^{q \to Wq'}$  from the unresolved real emission corrections as:

$$f_1^{q \to Wq'(\text{real})} = \frac{\alpha_s}{4\pi} C_F C_\epsilon \left\{ \frac{2}{\epsilon^2} - \frac{2}{\epsilon} \ln(\frac{-\hat{t}}{m_t^2}) + \frac{3}{\epsilon} - \frac{4\pi^2}{3} + 2\ln^2 2 + 3\ln\frac{m_t^2}{s_{min}} - 2\ln^2(\frac{-\hat{t}}{s_{min}}) + \ln^2(\frac{-\hat{t}}{m_t^2}) + I_{\text{Scheme}}^{q \to Wq'(\text{real})} \right\},$$

where the scheme dependent term  $I_{\text{Scheme}}^{q \to Wq'(\text{real})}$  is

$$I_{\text{Scheme}}^{q \to Wq'(\text{real})} = \begin{cases} 7 & \text{in DREG scheme,} \\ 6 & \text{in DRED scheme.} \end{cases}$$

It is clear that the divergences of  $f_1^{q \to Wq'(\text{virt})}$  and  $f_1^{q \to Wq'(\text{real})}$  cancel with each other and the sum is finite and  $s_{min}$  dependent. The remaining unresolved real

corrections for  $q \to Wq'$  are included through the process independent, but  $s_{min}$  and factorization scheme dependent universal crossing functions.

The resolved phase spaces without divergent regions are obtained by multiplying by the following functions:

• For 
$$bq \to tq'g(I)$$
,
$$\left[\Theta(\left|s_{gq}\right| + \left|s_{q'g}\right| - 2s_{min})\right.$$

$$\left. -\Theta(\left|s_{gq}\right| - 2s_{min})\Theta(s_{min} - \left|s_{q'g}\right|)\right.$$

$$\left. -\Theta(\left|s_{q'g}\right| - 2s_{min})\Theta(s_{min} - \left|s_{gq}\right|)\right],$$

• For  $bg \to t\bar{q}q'$ ,

$$\left[1 - \Theta(s_{min} - \left|s_{q'g}\right|) - \Theta(s_{min} - \left|s_{\bar{q}g}\right|)\right].$$

#### 3.4.4 NLO corrections to HEAVY

The NLO matrix element for the  $b-W_{\mu}-t$  vertex can be written as

$$M_{\mu}^{bW \to t} = \frac{-ig}{\sqrt{2}} \bar{u}(t) [f_1^{bW \to t} \gamma_{\mu} + f_2^{bW \to t} \frac{(p_b + p_t)_{\mu}}{m_t}] P_L u(b). \tag{3.77}$$

The above formula is valid only when W boson is on-shell or off-shell but coupled to massless quarks because we have neglected term proportional to  $(p_t-p_b)_{\mu}$ . At leading-order,  $f_1^{bW\to t}=1$ ,  $f_2^{bW\to t}=0$ . At the NLO, the virtual corrections to

 $f_1^{bW o t}$  and  $f_2^{bW o t}$  are

$$\begin{split} f_1^{bW \to t (\text{virt})} &= \frac{\alpha_s}{4\pi} C_F C_\epsilon \left\{ -\frac{1}{\epsilon^2} - \frac{5}{2\epsilon} + \frac{2}{\epsilon} \ln(\frac{-\hat{t}_1}{m_t^2}) + 2 \text{Li}_2(\frac{\hat{t}}{\hat{t}_1}) \right. \\ &+ 3 \ln(\frac{-\hat{t}_1}{m_t^2}) - \frac{m_t^2}{\hat{t}} \ln(\frac{-\hat{t}_1}{m_t^2}) - \ln^2(\frac{-\hat{t}_1}{m_t^2}) + I_{\text{Scheme}}^{bW \to t (\text{virt})} \right\}, \\ f_2^{bW \to t (\text{virt})} &= \frac{\alpha_s}{4\pi} C_F C_\epsilon \left\{ \frac{m_t^2}{\hat{t}} \ln(\frac{-\hat{t}_1}{m_t^2}) \right\}, \end{split}$$

where  $\hat{t}_1 = \hat{t} - m_t^2 = -2p_b \cdot p_t$ , and the scheme dependent term  $I_{\text{Scheme}}^{bW \to t(\text{virt})}$  is

$$I_{\text{Scheme}}^{bW \to t(\text{virt})} = \begin{cases} -6 & \text{in DREG scheme,} \\ -5 & \text{in DRED scheme.} \end{cases}$$

We now consider the unresolved real correction to  $f_1^{bW \to t}$ . The unresolved real correction to  $f_1^{bW \to t}$  comes from the soft and collinear regions of the following three processes:

- $bq \rightarrow tq'g$  (II), in which the gluon only connect with the heavy quark (t,b) line, c.f. Eqs. (3.6) and (3.7),
- $qq \rightarrow tq'\bar{b}$ , c.f. Eq. (3.8),
- $\bar{q}'g \rightarrow \bar{q}\bar{b}t$ , c.f. Eq. (3.9).

The soft and collinear divergent regions of  $bq \to tq'g\left(II\right)$  are sliced out by

$$\left[\Theta(2s_{min} - |s_{bg}| - |s_{tg}|) + \Theta(|s_{tg}| - 2s_{min})\Theta(s_{min} - |s_{bg}|)\right].$$

The  $qg \to tq'\bar{b}$  and  $\bar{q}'g \to \bar{q}\bar{b}t$  processes both have the collinear divergent region restricted with  $\Theta(s_{min} - \left|s_{\bar{b}g}\right|)$ . After integrating out the soft and collinear regions,

we get the contribution to the form factor  $f_1^{bW \to t}$  from the unresolved real emission corrections as:

$$\begin{split} f_1^{bW \to t (\mathrm{real})} &= \frac{\alpha_s}{4\pi} C_F C_\epsilon \left\{ \frac{1}{\epsilon^2} + \frac{5}{2\epsilon} - \frac{2}{\epsilon} \ln \frac{-\hat{t}_1}{m_t^2} - \frac{2\pi^2}{3} + \ln^2 2 - 2 \ln 2 \right. \\ &- 2 \mathrm{Li}_2(\frac{-\hat{t}_1}{m_t^2 - \hat{t}_1}) - \frac{7}{2} \ln \frac{s_{min}}{m_t^2} + 2 \ln 2 \ln (\frac{-\hat{t}_1}{m_t^2}) \\ &+ (2 - \frac{2m_t^2}{\hat{t}_1}) \ln (1 - \frac{\hat{t}_1}{m_t^2}) - \ln^2 (1 - \frac{\hat{t}_1}{m_t^2}) - \ln^2 (\frac{-\hat{t}_1}{m_t^2}) \\ &- \ln^2 \frac{s_{min}}{m_t^2} + 4 \ln (\frac{-\hat{t}_1}{m_t^2}) \ln \frac{s_{min}}{m_t^2} + \frac{m_t^2}{\hat{t}_1} + I_{\mathrm{Scheme}}^{bW \to t (\mathrm{real})} \right\}, \end{split}$$

where the scheme dependent term  $I_{\text{Scheme}}^{\,bW \to t(\text{real})}$  is

$$I_{\text{Scheme}}^{bW \to t(\text{real})} = \begin{cases} \frac{7}{2} & \text{in DREG scheme,} \\ 3 & \text{in DRED scheme.} \end{cases}$$

and the remaining unresolved real corrections for  $bW \to t$  are included through the process independent, but  $s_{min}$  and factorization scheme dependent universal crossing functions.

The resolved phase spaces without divergent regions are obtained by multiplying by the following functions:

• For  $bq \rightarrow tq'g(II)$ :

$$\left[\Theta(|s_{bg}| + |s_{tg}| - 2s_{min}) - \Theta(|s_{tg}| - 2s_{min})\Theta(s_{min} - |s_{bg}|)\right],$$

• For  $qg \to tq'\bar{b}$ ,  $\bar{q}'g \to \bar{q}\bar{b}t$ :

$$\left[1-\Theta(s_{min}-\left|s_{\bar{b}g}\right|)\right].$$

## 3.4.5 NLO corrections to the decay process $t \to Wb'$

The NLO matrix element for the t - W - b' vertex can be written as

$$M_{\mu}^{t \to Wb} = \frac{-ig}{\sqrt{2}} \bar{u}(b') [f_1^{t \to Wb'} \gamma_{\mu} P_L + f_2^{t \to Wb'} \frac{(p_t + p_{b'})_{\mu}}{m_t} P_R] u(t), \qquad (3.78)$$

where  $P_R=(1+\gamma_5)/2$  and b' denotes bottom quark from top decay. At the tree level,  $f_1^{t\to Wb'}=1$ ,  $f_2^{t\to Wb'}=0$ . At the NLO, the virtual corrections to  $f_1^{t\to Wb'}$  and  $f_2^{t\to Wb'}$  are

$$f_{1}^{t \to Wb'(\text{virt})} = \frac{\alpha_{s}}{4\pi} C_{F} C_{\epsilon} \left\{ -\frac{1}{\epsilon^{2}} - \frac{5}{2\epsilon} + \frac{2}{\epsilon} \ln(1 - \beta_{W}) + 2 \text{Li}_{2} \left( \frac{\beta_{W}}{\beta_{W} - 1} \right) + \frac{3\beta_{W} - 1}{\beta_{W}} \ln(1 - \beta_{W}) - \ln^{2} (1 - \beta_{W}) + I_{\text{Scheme}}^{t \to Wb'(\text{virt})} \right\} (3.79)$$

$$f_{2}^{t \to Wb'(\text{virt})} = \frac{\alpha_{s}}{4\pi} C_{F} C_{\epsilon} \left\{ \frac{1}{\beta_{W}} \ln(1 - \beta_{W}) \right\}, \qquad (3.80)$$

where  $\beta_W = m_W^2/m_t^2$  and the scheme dependent term  $I_{\text{Scheme}}^{t \to Wb'(\text{virt})}$  is

$$I_{\text{Scheme}}^{t \to Wb'(\text{virt})} = \begin{cases} -6 & \text{in DREG scheme,} \\ -5 & \text{in DRED scheme.} \end{cases}$$

The unresolved real correction to  $f_1^{t\to Wb'}$  is obtained by integrating out the soft and collinear regions of  $t\to Wb'g$  which are sliced by

$$\left[\Theta(2s_{min} - \left|s_{tg}\right| - \left|s_{b'g}\right|) + \Theta(\left|s_{tg}\right| - 2s_{min})\Theta(s_{min} - \left|s_{b'g}\right|)\right]. \tag{3.81}$$

After integrating over the sliced region, we get the contribution to  $f_1^{t \to Wb'}$  as

$$f_{1}^{t \to Wb'(\text{real})} = \frac{\alpha_{s}}{4\pi} C_{F} C_{\epsilon} \left\{ \frac{1}{\epsilon^{2}} + \frac{5}{2\epsilon} - \frac{2}{\epsilon} \ln(1 - \beta_{W}) - \frac{2\pi^{2}}{3} + \ln^{2} 2 - 2 \ln 2 \right.$$

$$-2 \text{Li}_{2} \left( \frac{1 - \beta_{W}}{2 - \beta_{W}} \right) - \frac{7}{2} \ln \frac{s_{min}}{m_{t}^{2}} + 2 \ln 2 \ln(1 - \beta_{W})$$

$$+ \frac{4 - 2\beta_{W}}{1 - \beta_{W}} \ln(2 - \beta_{W}) - \ln^{2} (2 - \beta_{W}) - \ln^{2} (1 - \beta_{W})$$

$$- \ln^{2} \frac{s_{min}}{m_{t}^{2}} + 4 \ln(1 - \beta_{W}) \ln \frac{s_{min}}{m_{t}^{2}} - \frac{1}{1 - \beta_{W}} + I_{\text{Scheme}}^{t \to Wb'(\text{real})} \right\},$$

$$(3.82)$$

where the scheme dependent term  $I_{\text{Scheme}}^{t \to Wb'(\text{real})}$  is

$$I_{\text{Scheme}}^{t \to Wb'(\text{real})} = \begin{cases} \frac{7}{2} & \text{in DREG scheme,} \\ 3 & \text{in DRED scheme.} \end{cases}$$

The resolved region of  $t \to Wb'g$  is obtained by multiplying by the following function:

$$\left[\Theta(\left|s_{tg}\right| + \left|s_{b'g}\right| - 2s_{min}) - \Theta(\left|s_{tg}\right| - 2s_{min})\Theta(s_{min} - \left|s_{b'g}\right|)\right]. \tag{3.83}$$

We have checked the formulas of (3.78)-(3.83) by comparing the result of NLO correction to  $\Gamma(t \to Wb')$  with Ref. [87].

#### 3.5 Combining the production and decay processes

With those building blocks given in the above sections, the NLO QCD corrections to single top quark production and decay can be computed, keeping the full information on the spin configuration of the intermediate top quark state. The general differential hadronic cross section at NLO can be written as

$$d\sigma(H_{1}H_{2} \to YX)$$

$$= \sum_{a,b} \int dx_{1}dx_{2} \left\{ f_{a}^{H_{1}}(x_{1}, \mu_{F}) f_{b}^{H_{2}}(x_{2}, \mu_{F}) \times [d\sigma_{0}(ab \to Y) + d\sigma_{1}(ab \to Y)] \right.$$

$$+ \alpha_{s} f_{a}^{H_{1}}(x_{1}, \mu_{F}) C_{b}^{H_{2}}(x_{2}, \mu_{F}, s_{min}) d\sigma_{0}(ab \to Y)$$

$$+ \alpha_{s} C_{a}^{H_{1}}(x_{1}, \mu_{F}, s_{min}) f_{b}^{H_{2}}(x_{2}, \mu_{F}) d\sigma_{0}(ab \to Y) + (x_{1} \leftrightarrow x_{2}) \right\},$$

$$(3.84)$$

where  $d\sigma_0$  is the leading-order subprocess cross section,  $d\sigma_1$  is the  $O(\alpha_S)$  subprocess cross section.

We now consider the single top quark production subprocess  $ab \to t_{\lambda}h_1$  with  $t_{\lambda} \to W_{\rho}h_2$  and  $W_{\rho} \to l\nu$ . (Here,  $h_1$  and  $h_2$  stand for any single parton or multiple partons.  $\lambda$  and  $\rho$  are the top quark spin and W boson polarization indices.) In the frame work of NWA, the cross section can be written as

$$d\sigma(ab \to l\nu h_1 h_2) = \frac{1}{2\hat{s}} \left| \sum_{\lambda,\rho} M(ab \to t_\lambda h_1) M(t_\lambda \to W_\rho h_2) M(W_\rho \to l\nu) \right|^2$$

$$\times S_F \frac{1}{2m_t \Gamma_t} \frac{1}{2m_W \Gamma_W} d\Phi(ab \to th_1) d\Phi(t \to Wh_2) d\Phi(W \to \ell\nu),$$
(3.85)

where  $S_F$  is possible spin-color sum and averaging factor,  $d\Phi$ 's are the phase space elements

$$(2\pi)^4 \delta^4(P - \sum p_i) \prod \frac{d^3 \vec{p_i}}{2E_i(2\pi)^3}$$

We use  $\Gamma_t = \Gamma_t^0(t \to bW) + \Gamma_t^1(t \to bW)$  where  $\Gamma_t^1(t \to bW)$  is the  $O(\alpha_S)$  correction to the Born level decay width  $\Gamma_t^0(t \to bW)$  and  $\Gamma_W$  is the W boson total decay width.

The matrix element square can be calculated as follows. The sum over  $\rho$  is equivalent to the following replacement in  $M(t_{\lambda} \to W_{\rho}h_2)$ :

$$\varepsilon_W^{\mu} \to \frac{g}{2\sqrt{2}} \bar{u}_{\nu} \gamma^{\mu} (1 - \gamma_5) v_{\ell}. \tag{3.86}$$

We denote the result by  $M(t_{\lambda} \to W h_2)$ . Decomposing  $M(ab \to t_{\lambda} h_1)$  and  $M(t_{\lambda} \to W h_2)$  as

$$\mathcal{M}(ab \to t_{\lambda} h_1) = \bar{u}_{\lambda}(p_t) \mathcal{M}^{prd}, \tag{3.87}$$

$$\mathcal{M}(t_{\lambda} \to W h_2) = \mathcal{M}^{dec} u_{\lambda}(p_t), \tag{3.88}$$

when we separate the on-shell top quark spinors from both the production process and the decay process, we have

$$\left| \sum_{\lambda,\rho} \mathcal{M}(ab \to t_{\lambda} h_1) \mathcal{M}(t_{\lambda} \to W_{\rho} h_2) \mathcal{M}(W_{\rho} \to l\nu) \right|^2 = \left| \mathcal{M}^{dec}(\not p_t + m_t) \mathcal{M}^{prd} \right|^2.$$
(3.89)

In our calculations,  $\mathcal{M}^{dec}$  and  $\mathcal{M}^{prd}$  are calculated numerically using helicity amplitude approach and can be easily obtained from the formulas presented in this Chapter. Eqs. (3.86) and (3.89) guarantee that the spin and angular correlations of the decay products are preserved.

Denoting

$$d\Phi^{\text{LO}} = S_F \frac{1}{2m_t \Gamma_+^0} \frac{1}{2m_W \Gamma_W} d\Phi(ab \to th_1) d\Phi(t \to Wh_2) d\Phi(W \to \ell\nu), \quad (3.90)$$

$$d\Phi^{\rm NLO} = S_F \frac{1}{2m_t \Gamma_t} \frac{1}{2m_W \Gamma_W} d\Phi(ab \to th_1) d\Phi(t \to Wh_2) d\Phi(W \to \ell\nu), \quad (3.91)$$

the LO subprocess cross section is

$$d\sigma_0(ab \to l\nu h_1 h_2) = \frac{1}{2\hat{s}} |\mathcal{M}_0^{dec}(p_t + m_t)\mathcal{M}_0^{prd}|^2 d\Phi^{LO},$$
 (3.92)

where  $\mathcal{M}_0^{prd,dec}$  stands for the LO amplitude.

The NLO subprocess cross section is

$$d\sigma_{1}(ab \rightarrow l\nu h_{1}h_{2})$$

$$= \frac{1}{2\hat{s}} \left| \mathcal{M}_{0}^{dec}(\not p_{t} + m_{t}) \mathcal{M}_{1R}^{prd} \right|^{2} d\Phi^{LO}$$

$$+ \frac{1}{2\hat{s}} 2\Re \left[ \mathcal{M}_{0}^{dec}(\not p_{t} + m_{t}) \mathcal{M}_{1SCV}^{prd} (\mathcal{M}_{0}^{dec}(\not p_{t} + m_{t}) \mathcal{M}_{0}^{prd})^{\dagger} \right] d\Phi^{LO}$$

$$+ \frac{1}{2\hat{s}} 2\Re \left[ \mathcal{M}_{1SCV}^{dec}(\not p_{t} + m_{t}) \mathcal{M}_{0}^{prd} (\mathcal{M}_{0}^{dec}(\not p_{t} + m_{t}) \mathcal{M}_{0}^{prd})^{\dagger} \right] d\Phi^{NLO}$$

$$+ \frac{1}{2\hat{s}} \left| \mathcal{M}_{1R}^{dec}(\not p_{t} + m_{t}) \mathcal{M}_{0}^{prd} \right|^{2} d\Phi^{NLO}, \tag{3.93}$$

where  $M_{1SCV,1R}^{prd,dec}$  stands for the  $O(\alpha_s)$  amplitudes from soft+collinear+virtual and resolved real correction for the production and decay processes. The first term is the real NLO correction from production. The second term is the soft+collinear+virtual correction from production. The last two terms are from the top quark decay corrections. If no kinematical cut is applied, the last two terms cancel each other, which means there is no net correction to the cross section from the top quark decay. Because the virtual correction processes and real correction processes have different phase spaces  $d\Phi^{\rm LO}$  and  $d\Phi^{\rm NLO}$ , we calculate them separately using different Monte Carlo programs.

# Chapter 4

# Inclusive rate of the single top process at NLO

In order to be able to compare theoretical predictions with experimental results it is important to not only determine the total production rate of single-top events but also the rate of events passing kinematic cuts due to detector acceptances or the need for background suppression. Furthermore, reconstructing the top quark is critical to many of the physics goals of the Tevatron and the LHC. At the Tevatron Run II, experiments may hope for an accuracy of 2 GeV [88] in the top mass measurement. But the ability to achieve this accuracy depends on how well systematic effects - especially those associated with gluon radiation - are understood and controlled. It is therefore crucial to properly simulate final state particle distributions in single top events. In this chapter, we discuss inclusive production rates of the s-channel and t-channel single top quark processes and also examine their dependences upon the scale and top quark mass. The phenomenology of the single top physics, including the acceptance of the single top events under various kinematic cuts and distributions of final state particles with an emphasis on the effects of gluon radiation, is discussed in the next two chapters.

We present numerical results for the production of single-top events considering

the leptonic decay of the W-boson from the top quark decay at the upgraded Tevatron (a 1.96 TeV  $p\bar{p}$  collider). Unless otherwise specified, we use the NLO parton distribution function set CTEQ6M [89], defined in the  $\overline{MS}$  scheme, and the NLO (2-loop) running coupling  $\alpha_s$  with  $\Lambda_{\overline{MS}}$  provided by the PDFs. For the CTEQ6M PDFs,  $\Lambda_{\overline{MS}}^{(4)} = 0.326$  GeV for four active quark flavors. The values of the relevant electroweak parameters are:  $\alpha = 1/137.0359895$ ,  $G_{\mu} = 1.16637 \times 10^{-5} \, \mathrm{GeV^{-2}}$ ,  $m_t = 178\,{
m GeV}$  [1,90],  $m_W = 80.33\,{
m GeV},\ m_Z = 91.1867\,{
m GeV},\ {
m and}\ \sin^2\theta_W = 0.231.$ Thus, the square of the weak gauge coupling is  $g^2 = 4\sqrt{2}m_W^2G_\mu$ . Here, we focus our attention on the positively charged electron lepton (i.e., positron) only, though our analysis procedure also applies to the  $\mu$  lepton. Including the  $O(\alpha_s)$ corrections to  $W \to \bar{q}q'$ , the decay branching ratio of the W boson into leptons is  $Br(W \to \ell^+ \nu) = 0.108$  [91]. Unless otherwise specified, we will choose the top quark mass to be 178 GeV and the renormalization scale  $(\mu_R)$  as well as the factorization scale ( $\mu_F$ ) to be equal to the top quark mass  $m_t$ . The top quark mass and scale dependences of single top events are investigated in the second and third part of this section.

## 4.1 Theoretical Cutoff Dependence

The NLO QCD differential cross sections are calculated using the one-cutoff phase space slicing (PSS) method [76–78]. This procedure introduces a theoretical cutoff parameter  $(s_{min})$  in order to isolate soft and collinear singularities associated with real gluon emission subprocesses by partitioning the phase space into soft, collinear and hard regions such that

$$|\mathcal{M}^{r}|^{2} = |\mathcal{M}^{r}|_{soft}^{2} + |\mathcal{M}^{r}|_{collinear}^{2} + |\mathcal{M}^{r}|_{hard}^{2}.$$

$$(4.1)$$

In the soft and collinear regions the cross section is proportional to the Born-level cross section. Using dimensional regularization, we can evaluate the real gluon emission diagrams in n-dimensions under the soft gluon approximation in the soft region, or the collinear approximation in the collinear region, and can integrate out the corresponding phase space volume analytically. The resulting divergences are cancelled by virtual corrections or absorbed into the perturbative parton distribution functions in the factorization procedure. Since the cutoff is introduced in the calculation only for this technical reason and is unrelated to any physical quantity, the inclusive rate must not depend on it. In other words, the sum of all contributions, virtual, resolved, and unresolved corrections must be independent of  $s_{min}$ .

That the total rate is indeed insensitive to the value of  $s_{min}$  for a large range is illustrated in Fig. 4.1(a) and (b) for s-channel and t-channel process, respectively. The figure shows the sum of the virtual and unresolved real corrections (s+v) as well as the resolved contribution (real) to the s-channel and t-channel single top quark process as a function of  $s_{min}$ . Although the contributions from the individual pieces vary, their sum (total) remains essentially constant for a large range of  $s_{min}$ . It is necessary to point out that the value of  $s_{min}$  needs to be small enough so that the soft and collinear approximations are valid. If  $s_{min}$  is too large, then PSS method will not be valid. This is clearly shown in the large  $s_{min}$  region where the physical result, sum of s + v correction and the real correction, drops off rapidly, i.e. depending on the choice of  $s_{min}$ . Furthermore, the jet-finding algorithm and other infraredsafe experimental observables should also be defined in a way such that they are consistent with the choice of  $s_{min}$ , say, the value of  $s_{min}$  should be smaller than the jet definition cutoff. On the other hand, numerical cancellation in the Monte Carlo integration becomes unstable if  $s_{min}$  is too small. As shown in Fig. 4.1, the statistical error becomes larger as we choose the smaller value of  $s_{min}$  with the understanding the

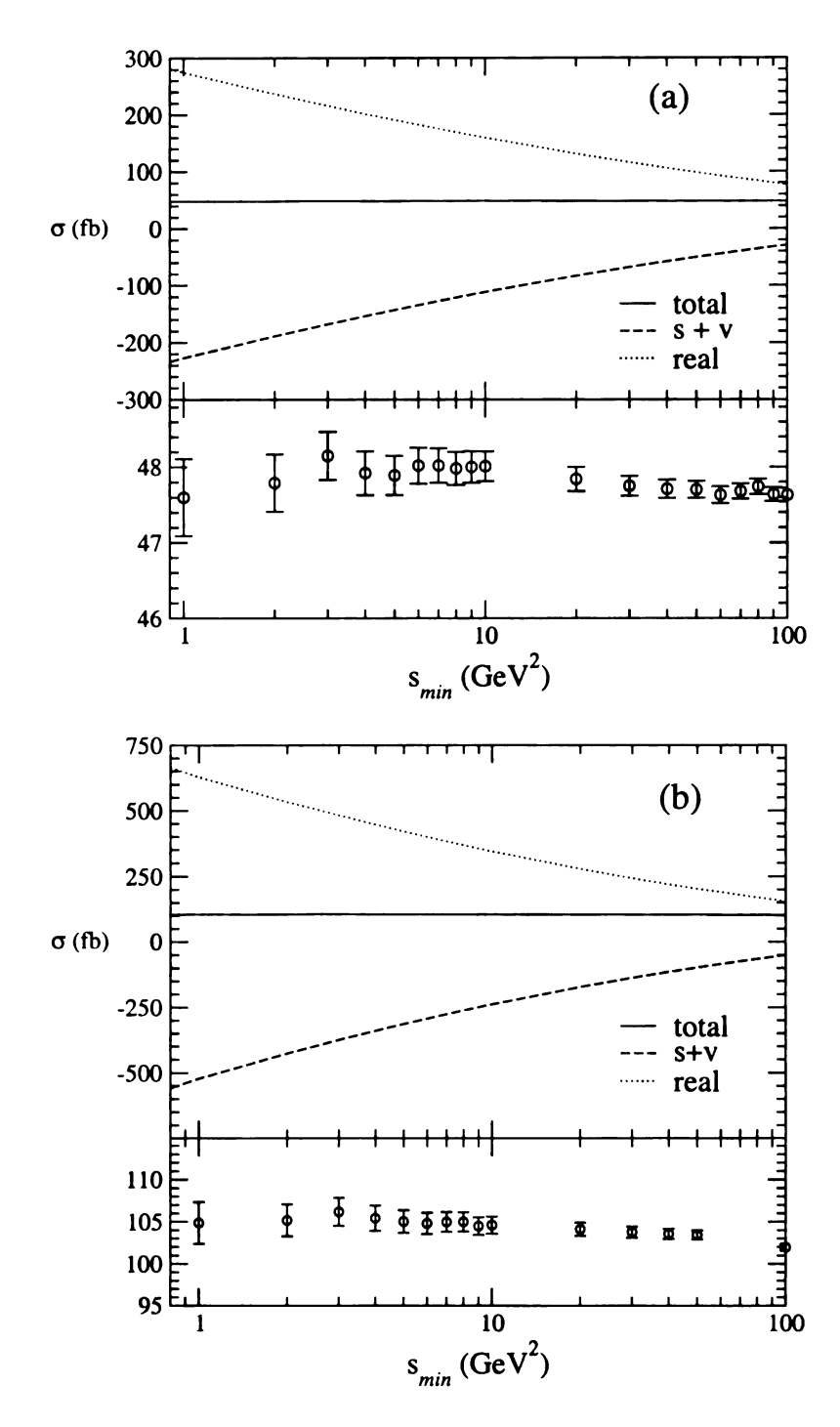


Figure 4.1: The theoretical cutoff  $s_{min}$  dependence of the inclusive single top quark cross section at the Tevatron with  $\mu_R = \mu_F = m_t$  for  $m_t = 178 \,\text{GeV}$ . The decay branching ratio  $t \to bW^+(\to e^+\nu)$  has been included. (a) s-channel (b) t-channel

same Monte Carlo event numbers are chosen. Therefore, an extremely long computing time is needed in order to get a stable numerical result in Monte Carlo calculation. In practice, one wants to choose the largest  $s_{min}$  possible within these constraints in order to minimize the processing time of the MC integration program. For our study, we found a value of  $s_{min} = 5 \,\text{GeV}^2$  to be appropriate for the s-channel process but a value of  $s_{min} = 1 \,\text{GeV}^2$  for studying the t-channel process. With the choices of  $\mu_R = \mu_F = m_t$  at the Tevatron, we obtain an inclusive cross section for the s-channel and t-channel single top (t only) processes (with W-boson decay branching ratio) of 47.9 femtobarn (fb) and 104.8 fb, respectively, which agrees with Ref. [54].

## 4.2 Top quark mass and scale dependence

To test the standard model and measure the CKM matrix element  $V_{tb}$ , one needs an accurate prediction of the single top quark production and decay to reduce the theoretical uncertainty. Examining the top quark mass dependence can provide information about how accurately the top quark mass must be measured in  $t\bar{t}$  events. Besides of the top quark mass, the choices of renormalization and factorization scales also contribute to the uncertainty of the theoretical prediction. The renormalization scale  $\mu_R$  is introduced when redefining the bare parameters in terms of the renormalized parameters, while the factorization scale  $\mu_F$  is introduced when absorbing the collinear divergence into the parton distribution functions. Therefore, both  $\mu_R$  and  $\mu_F$  are unphysical and the final predictions should not depend on them. However, since we work at a fixed order in perturbation theory, we indeed see dependences of the predicted cross section on  $\mu_R$  and  $\mu_F$ . The change due to varying the scale is formally of higher order. Since the single-top rate is very small at the Tevatron, it is very important to reduce the scale uncertainty in order to compare the theory prediction with experimental data. Below, we examine the top quark mass and the

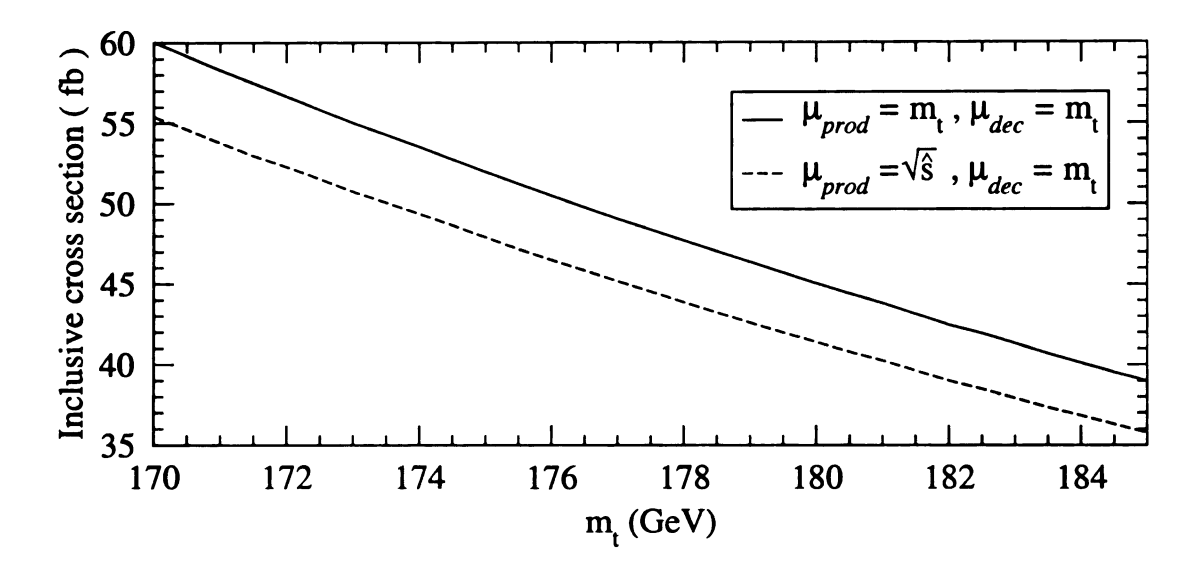


Figure 4.2: Top quark mass as well as renormalization and factorization scale dependence of the inclusive s-channel single top quark cross section at Tevatron. The decay branching ratio of  $t \to bW^+(\to e^+\nu)$  has been included.

scale dependence of the s-channel and t-channel single top quark events.

#### 4.2.1 s-channel process

As shown in Fig. 4.2, the cross section changes by about  $\pm 10\%$  when the top quark mass  $m_t$  is varied by its current uncertainty of about  $\mp 5\,\text{GeV}$ . Measuring the top quark mass to an uncertainty of  $1-2\,\text{GeV}$  will thus reduce the theoretical uncertainty on the single top cross section. The reduction in uncertainty of the s-channel single top production rate will improve the measurement of the CKM matrix element  $V_{tb}$ .

To examine the scale dependence of the s-channel single top quark production rate, we show in Fig. 4.2 the results of two typical scales; one is the top quark mass  $(\mu_F = \mu_R^{prod} = m_t)$ , shown as the solid-line, and another is the total invariant mass of the event  $(\mu_F = \mu_R^{prod} = \sqrt{\hat{s}})$ , shown as the dashed-line. For the decay of top quark, we take  $\mu_R^{dec} = m_t$  which gives similar results as the choice of  $\mu_R^{dec} = M_W$ . The band constrained by these two  $\mu_F$  scales represents a range of uncertainty due to the NLO predictions. The usual practice for estimating the yet-to-be calculated higher order

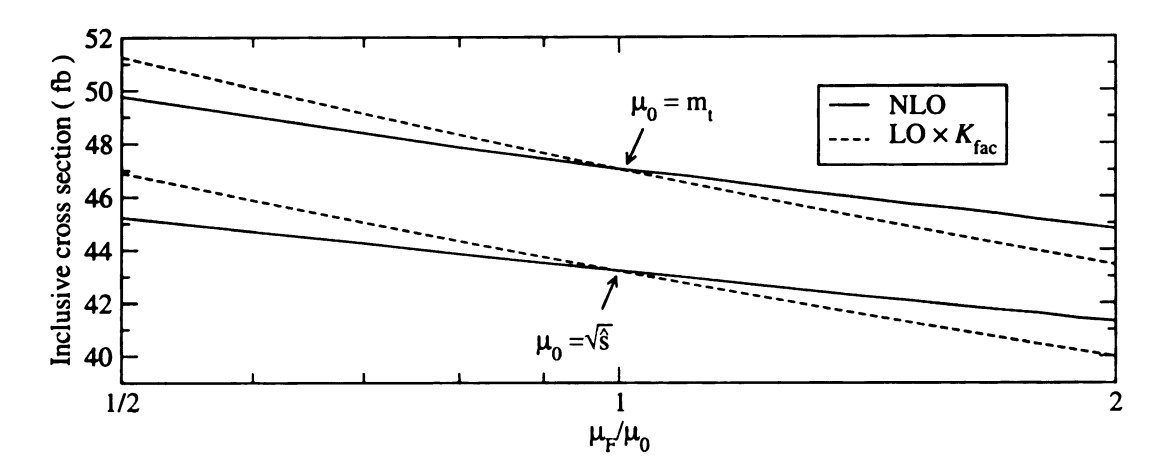


Figure 4.3: Inclusive s-channel single top quark cross section at Tevatron for  $m_t = 178$  GeV, versus the ratio of the factorization scale  $\mu_F$  to its typical value  $\mu_0$ , where  $\mu_0 = m_t$  and  $\mu_0 = \sqrt{\hat{s}}$ , respectively. The decay branching ratio of  $t \to bW^+(\to e^+\nu)$  has been included.

QCD correction to a perturbative cross section is to vary around the typical scale by a factor of 2, though in principle the "best" scale to be used for estimation cannot be determined without completing the higher order calculation. In Fig. 4.3 we show the total cross section of the s-channel single top production for a range of the scale  $\mu_F$  which, for simplicity, is set to be equal to  $\mu_R$ . We have multiplied a constant factor (the "K-factor") of 1.52 to the LO cross sections (shown as the dashed-line) in order to compare to the NLO ones (shown as the solid-line). It is clear that the NLO calculation reduces the scale dependence. For example, around  $\mu_F = m_t$ , the LO rate varies by +8.9% to -5.7% when scale is changed from  $\mu_F/2$  to  $2\mu_F$ , while the NLO rate varies by +7.6% to -4.7%. Similar results also hold for varying the scale around  $\mu_F = \sqrt{\hat{s}}$ .

#### 4.2.2 t-channel process

As shown in Fig. 4.4, the cross section changes by about  $\pm 9\%$  when the top quark mass  $m_t$  is varied by its current uncertainty of about  $\mp 5\,\text{GeV}$  around 178 GeV. It can also be seen that measuring the top quark mass to an uncertainty of  $1-2\,\text{GeV}$ 

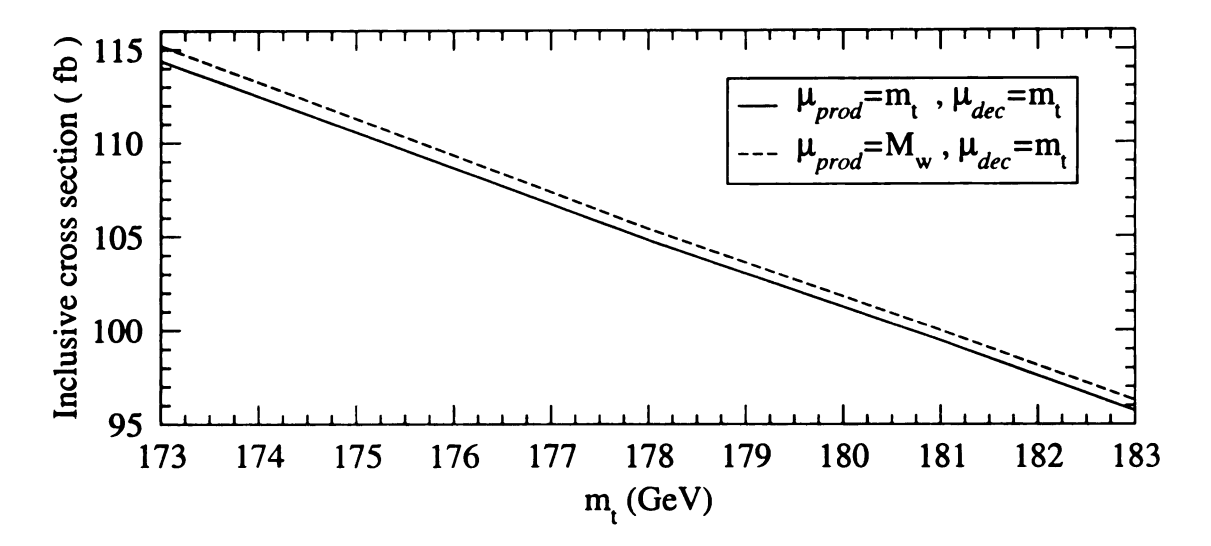


Figure 4.4: Top quark mass dependence as well as renormalization and factorization scale dependence of the inclusive t-channel single top quark cross section at the Tevatron. The decay branching ratio of  $t \to bW^+(\to e^+\nu)$  has been included.

will reduce the theoretical uncertainty on the single top cross section correspondingly. The reduction in uncertainty on the t-channel single top production rate will improve the measurement of the CKM matrix  $V_{tb}$ .

In order to examine the scale dependence of the t-channel single top production rate, we show in Fig. 4.4 the results of two typical scales: one is the top quark mass ( $\mu_F = \mu_R^{prod} = m_t$ ), shown as the solid line, the other is the W boson mass ( $\mu_F = \mu_R^{prod} = M_W$ ), shown as the dashed line. For the decay of top quark, we take  $\mu_R^{dec} = m_t$ , which gives similar results as the choice of  $\mu_R^{dec} = M_W$ . The band constrained by these two  $\mu_F$  scales represents a range of uncertainty due to the NLO predictions. The usual practice for estimating the yet-to-be calculated higher order QCD correction to a perturbative cross section is to vary around the typical scale by a factor of 2, though in principle the "best" scale to be used for estimation cannot be determined without completing the higher order calculation. In Fig. 4.5 we show the total cross section of the t-channel single top production for a range of the scale  $\mu_F$  which, for simplicity, is set to be equal to  $\mu_R$ . We have multiplied the LO cross

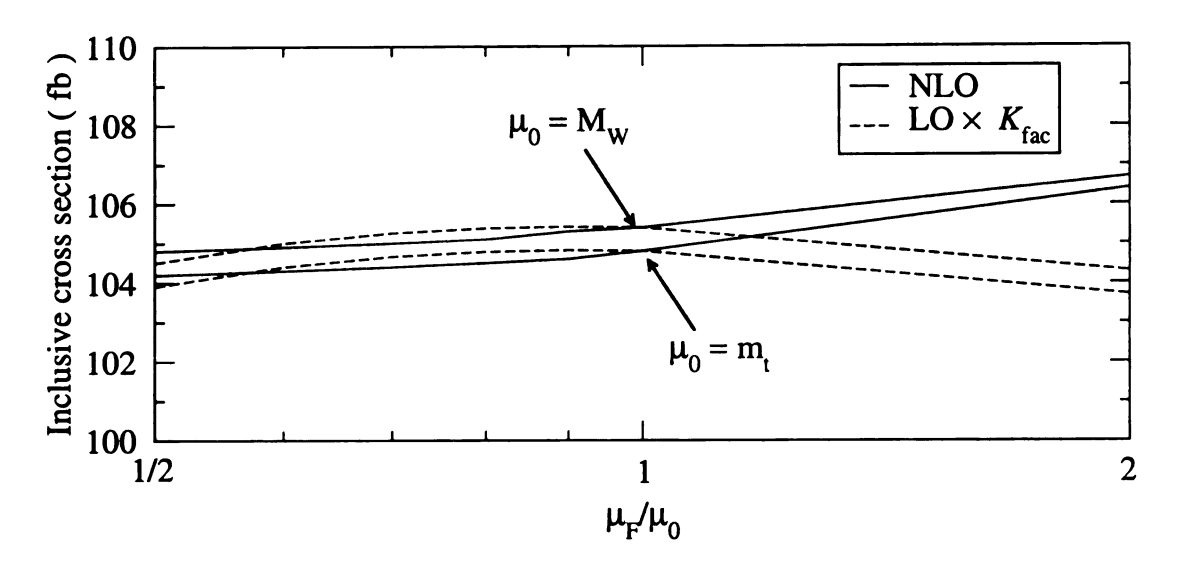


Figure 4.5: Inclusive t-channel single top quark production cross section at the Tevatron for  $m_t = 178$  GeV, versus the ratio of the factorization scale  $\mu_F$  to its typical value  $\mu_0$ , where  $\mu_0 = m_t$  (solid line) and  $\mu_0 = M_W$  (dashed line), respectively. The decay branching ratio of  $t \to bW^+(\to e^+\nu)$  has been included.

sections by a constant factor (the "K-factor") of 1.04 (shown as the dashed line) in order to compare to the NLO ones (shown as the solid-line). It is clear that the NLO calculation reduces the scale dependence. For example, when the scale is changed from  $\mu_F/2$  to  $2\mu_F$  around  $\mu_F=m_t$ , the LO rate varies by -0.9% to -1.0% while the NLO rate varies only by -0.6% to +1.3%. Similar results also hold for varying the scale around  $\mu_F=M_W$ .

#### 4.3 Inclusive Cross Section

To facilitate the calculation, the higher-order QCD corrections to the s-channel processes can be divided into three separate gauge invariant sets: the corrections from the initial state of top quark production (INIT), the corrections from the final state of top quark and  $\bar{b}$  quark (FINAL), and the corrections from the top quark decay (DEC). For the t-channel processes, we can also divide the higher-order QCD corrections into three separate gauge invariant sets: corrections from the light quark line of top quark production (LIGHT), corrections from the heavy quark line of top quark production (HEAVY), and corrections from the top quark decay (TDEC). The explicit diagrams and definitions for these three sets can be found in . The inclusive cross section as well as the individual  $O(\alpha_s)$  contributions are listed in Table 4.1 and Table 4.2 for the s-channel and t-channel processes, respectively. The effect of the finite widths of the top quark and W-boson has been included. We use a "modified" narrow width approximation (MNWA) in the calculation instead of the usual narrow width approximation (NWA). In the usual NWA, the effect of the Breit-Wigner resonance propagator reduces to a delta function in the limit of vanishing top quark width, i.e.

$$\int dp^2 \frac{1}{\left(p^2 - m_t^2\right)^2 + m_t^2 \Gamma_t^2} = \frac{\pi}{m_t \Gamma_t} \delta\left(p^2 - m_t^2\right).$$

Therefore, the invariant mass of the top quark decay particles will be exactly equal to  $m_t$  (a fixed value). To model the reconstructed top quark invariant mass from its decay particles with a Breit-Wigner resonance shape to reflect the non-vanishing decay width of the top quark (an unstable resonance), we introduced the MNWA method in our numerical calculation in which we generate a Breit-Wigner distribution for the top quark invariant mass in the phase space generator and then calculate the squared matrix element with  $m_t$  being the invariant mass generated by the phase space generator on the event-by-event basis. We find that the total event rate and the distributions of various kinematic variables (except the distribution of the reconstructed top quark invariant mass) calculated using the "modified NWA" method agree well with that using the NWA method. In the NWA method, the reconstructed top quark invariant mass distribution is a delta-function, while in the "modified NWA" method, it is almost a Breit-Wigner distribution. The reason that the "modified NWA" method does not generate a perfect Breit-Wigner shape in the distribution of the top quark invariant mass is because the initial state parton luminosities (predominantly due

	Cross Section	Fraction of
	(fb)	NLO (%)
Born Level	31.2	65.0
$O(\alpha_s)$ initial	10.7	22.3
$O(lpha_s)$ final	5.5	11.5
$O(lpha_s)$ decay	0.57	1.19
$O(\alpha_s)$ sum	16.8	35.0
NLO	47.9	100

Table 4.1: Inclusive single-top production cross section for different subprocesses, including the top quark decay branching ratio  $t \to bW^+(\to e^+\nu)$ .

to valence quarks) for the s-channel single-top process drop rapidly at the relevant Bjorken-x range, where  $\langle x \rangle \simeq \frac{m_t}{\sqrt{s}} \sim 0.1$ . As shown in Table 4.1, the total  $O(\alpha_s)$  QCD corrections increase the Born level cross section of the single top quark event by 54%. The INIT correction dominates over the FINAL and SDEC corrections, due to the enhancement from collinear physics. The contribution from the SDEC corrections is furthermore suppressed by almost a factor of 20 compared to the INIT corrections. Different from the s-channel process, as one expects, the dominant  $O(\alpha_s)$  corrections to the t-channel processes come from the heavy quark line rather than from the light quark line. This is because the bulk part of the radiative corrections originating from the light quark line have been absorbed into the definition of the light quark PDFs. The TDEC contribution is very small compared to the LIGHT and HEAVY contributions.

In both s-channel and t-channel processes, the corrections to the top quark decay

	Cross Section	Fraction of
	(fb)	NLO (%)
Born -level	99.2	94.6
$O(\alpha_s)$ HEAVY	5.56	5.31
$O(\alpha_s)$ LIGHT	1.03	0.98
$O(\alpha_s)$ TDEC	-0.81	-0.77
$O(lpha_s)$ sum	5.54	5.28
NLO	104.8	

Table 4.2: Inclusive t-channel single top production cross section for different subprocesses, including the top quark decay branching ratio  $t \to bW^+(\to e^+\nu)$ .

processes (i.e. SDEC and TDEC) are very small compared to the other higher order corrections. This can be understood from Eq. 3.93 and is explained below. When calculating the NLO QCD corrections to the top quark decay process, we must use the NLO top quark decay width in order to restore the correct top quark decay branching ratio. With the narrow width approximation, the NLO differential cross section of the top quark decay process is given by

$$d\sigma_{\rm NLO}^{\rm decay} = d\sigma_{\rm LO}^{\rm production} \times \frac{\pi}{\Gamma_t^{\rm NLO}} \times d\Gamma_{\rm NLO}^{\rm decay}, \tag{4.2}$$

where

$$\begin{split} d\Gamma_{\text{NLO}}^{\text{decay}} &= d\Gamma_0^{\text{decay}} + d\Gamma_1^{\text{decay}}, \\ \Gamma_t^{\text{NLO}} &= \Gamma_t^0 + \Gamma_t^1. \end{split}$$

Here  $\Gamma_t^0$  denotes the Born-level top quark decay width,

$$\Gamma_t^0 = \frac{G_F m_t^3}{8\sqrt{2}\pi} |V_{tb}|^2 \left(1 - \frac{M_W^2}{m_t^2}\right)^2 \left(1 + \frac{2M_W^2}{m_t^2}\right) 
= \frac{G_F m_t^3}{8\sqrt{2}\pi} |V_{tb}|^2 \beta_W^4 (3 - 2\beta_W^2),$$
(4.3)

where we have defined  $\beta_W = (1 - M_W^2/m_t^2)^{1/2}$ , the velocity of the  $W^+$  in the top quark rest frame.  $\Gamma_t^1$  denotes the NLO correction to the top quark decay width [87],

$$\Gamma_t^1 = \Gamma_t^{(0)} \times \frac{C_F \alpha_s}{2\pi} \delta_{QCD},\tag{4.4}$$

where

$$\delta_{QCD} = 2 \frac{(1 - \beta_W^2)(2\beta_W^2 - 1)(\beta_W^2 - 2)}{\beta_W^4(3 - 2\beta_W^2)} \ln(1 - \beta_W^2) - \frac{9 - 4\beta_W^2}{3 - 2\beta_W^2} \ln \beta_W^2$$

$$+ 2 \text{Li}_2 \beta_W^2 - 2 \text{Li}_2 (1 - \beta_W^2) - \frac{9 - 4\beta_W^2}{3 - 2\beta_W^2} \ln \beta_W^2. \tag{4.5}$$

In our calculation,  $\Gamma_t^0 = 1.695 \, \text{GeV}$  and  $\Gamma_t^{\text{NLO}} = 1.558 \, \text{GeV}$  for  $m_t = 178 \, \text{GeV}$ . The  $O(\alpha_s)$  decay part includes only the  $O(\alpha_s)$  QCD correction in Eq. 4.2,

$$d\sigma_{O(\alpha_s)}^{\rm DEC} = d\sigma_{\rm LO}^{\rm production} \times \frac{\pi}{\Gamma_t^{\rm NLO}} \times d\Gamma_1^{\rm decay}.$$
 (4.6)

We obtain

$$\frac{\pi}{\Gamma_t^{\text{NLO}}} = \frac{\pi}{\Gamma_t^0 + \Gamma_t^1} = \frac{\pi}{\Gamma_t^0 \left(1 + \frac{\Gamma_t^1}{\Gamma_t^0}\right)} \approx \frac{\pi}{\Gamma_t^0} \left(1 - \frac{\Gamma_t^1}{\Gamma_t^0}\right) + O(\alpha_s^2). \tag{4.7}$$

Expanding Eq. 4.2 up to  $O(\alpha_s)$ , we get

$$d\sigma_{\text{NLO}}^{\text{decay}} = d\sigma_{\text{LO}}^{\text{production}} \times \frac{\pi}{\Gamma_t^0} \left( 1 - \frac{\Gamma_t^1}{\Gamma_t^0} \right) \times \left( d\Gamma_0^{\text{decay}} + d\Gamma_1^{\text{decay}} \right)$$

$$= d\sigma_{\text{LO}}^{\text{production}} \times \frac{\pi}{\Gamma_t^0} \times d\Gamma_0^{\text{decay}}$$

$$- d\sigma_{\text{LO}}^{\text{production}} \times \frac{\pi}{\Gamma_t^0} \times \frac{\Gamma_t^1}{\Gamma_t^0} \times d\Gamma_0^{\text{decay}} + d\sigma_{\text{LO}}^{\text{production}} \times \frac{\pi}{\Gamma_t^0} \times d\Gamma_1^{\text{decay}}.$$

$$(4.8)$$

The first term in Eq. 4.8 belongs to the Born level contribution, and both the second and third terms belong to the  $O(\alpha_S)$  decay contribution. The net contribution of the second and third terms should be exactly zero in order to respect the top quark decay branching ratio (to be one), after we integrate out the phase space of the top quark decay products. As shown in Table 4.1, there is a small remaining DEC contribution, which is due to higher order contributions:

- The  $O(\alpha_s^2)$  term, which is dropped in the expansion in Eq. 4.8, will give about a 1% contribution which is positive.
- A mismatch exists between  $\int d\Gamma_1^{\text{decay}}$  and  $\Gamma^1$ , since we use a Breit-Wigner distribution of the top quark mass modulated by its decay width in the MNWA method rather than using a fixed mass (which indicates an on-shell top quark).

This DEC contribution will become sizable once we use a jet finding algorithm to define infrared-safe observables and impose the kinematic cuts. This is especially the case for three-jet events which can only come from the real emission corrections. However, the decay contribution cannot be very large because the large top quark mass has already set the scale for the top quark decay which will be shown later.

# Chapter 5

# Phenomenology: s-channel

In this Chapter we explore the final state objects of s-channel single top events. Although the W-boson from the top quark decay can decay in both leptonic and hadronic modes, we only focus on the leptonic decay mode in this study because the all-jet production mode of single top events is difficult to observe experimentally. Therefore, the signature of s-channel single top events that is accessible experimentally consists of one charged lepton, missing transverse energy together with two or three jets. Since we are studying the effect of NLO QCD radiative corrections on the production rate and the kinematic distributions of single top events at the parton level in this work, we are not including any detector effects, such as jet energy resolution or b-tagging efficiency. Only the kinematic acceptance of the detector is considered. Since the Tevatron is  $p\bar{p}$  collider, and  $p\bar{p}$  is a CP eigenstate, the production cross sections for  $b\bar{t}(j)$  at the Tevatron are the same as those for  $t\bar{b}(j)$  (when ignoring the small CP violation effect induced by the CKM mixing matrix in quarks). For simplicity we therefore only show distributions of the s-channel single-top events in this work in which a t quark (not including  $\bar{t}$ ) decays into  $W^+(\to \ell^+\nu)$  and b quark.

#### 5.1 Jet finding algorithm

To meaningfully discuss the effect of gluon radiation in single top events, we have to define a jet as an infrared-safe observable. At a crude level, high transverse energy  $(E_T)$  jets are quite obvious and the precise definition hardly matters. However, if we want to make a quantitative measurement of a jet cross section to compare to next-to-leading order theory, then the definition does matter. There are several possibilities for a definition that is infrared safe: (a) the "fixed-cone" algorithm, used by UA2 [92]; (b) the "iterative-cone" algorithm, used by CDF [93] and DØ [94] collaborations at Fermilab; (c) the " $K_T$ " algorithm, under study by CDF and DØ [95, 96]; (d) the "EKS" algorithm, used in NLO one-jet and two-jet inclusive calculations [97]. The numerical stability of several jet algorithms commonly used in experiments has been investigated in Ref. [98]. In this study, we adopt the cone-jet algorithm which is organized as follows:

- 1. Build a sorted list of all clusters (in this case the final state b and  $\bar{b}$  quarks plus a light quark or gluon from the  $O(\alpha_s)$  correction), decreasing in transverse energy  $E_T$ .
- 2. Select the highest  $E_T$  cluster from the cluster list and draw a cone of radius R around its axis. Call this a jet and calculate the transverse jet energy and a new jet axis by summing over the 4-momenta of all clusters inside the cone.
- 3. Remove all clusters in the cone from the cluster list and move the newly constructed jet to the jet list.
- 4. Apply the appropriate minimum transverse energy and rapidity cuts to the entries in the jet list to create the final state list of jets.

More specifically, we adopt the E-scheme cone-jet (4-momenta of particles in one cone are simply added to form a jet) with radius  $R = \sqrt{\Delta \eta^2 + \Delta \phi^2}$  to define b,  $\bar{b}$  and possibly extra g or q (or  $\bar{q}$ ) jets, where  $\Delta \eta$  and  $\Delta \phi$  are the separation of particles in the pseudo-rapidity  $\eta$  and the azimuthal angle  $\phi$ . For reference, we shall consider both R = 0.5 or R = 1.0. The same R-separation will also be applied to the separation between the lepton and each jet.

## 5.2 Acceptance Studies

In this study, we adopt the cone-jet algorithm. For reference, we shall consider both R=0.5 and R=1.0 \*. The kinematic cuts imposed on the final state objects are:

$$P_T^{\ell} \ge 15 \,\text{GeV}$$
 ,  $|\eta_{\ell}| \le \eta_{\ell}^{max}$ ,  
 $E_T \ge 15 \,\text{GeV}$  ,  $|\eta_j| \le \eta_j^{max}$ ,  
 $\Delta R_{\ell j} \ge R_{cut}$  ,  $\Delta R_{jj} \ge R_{cut}$  (5.1)

where the jet cuts are applied to both the b- and  $\bar{b}$ -jet as well as any gluon or light anti-quark jet in the final state. Two lepton pseudo-rapidity cuts are considered here: a loose version with  $\eta_\ell^{max}=2.5$ ; and a tight version with  $\eta_\ell^{max}=1.0$ . Similarly, loose and tight cuts are also considered for the jet pseudo-rapidity,  $\eta_j^{max}=3.0$  and  $\eta_j^{max}=2.0$ , respectively. The minimum transverse energy cuts on the lepton as well as the jets is 15 GeV. Each event is furthermore required to have at least one lepton and two jets passing all selection criteria. The cut on the separation in R between the lepton and the jets as well as between different jets is given by  $R_{cut}$  which is is chosen to be 0.5 (or 1.0).

<sup>\*</sup>In this study, we have checked that at the parton level using the Durham  $k_T$  algorithm [95,96] leads to similar conclusion.

		Cross section					Acceptance	
		(fb)				(%)		
		LO	NLO	INIT	FINAL	DEC	LO	NLO
(a)	$tar{b} + tar{b}j$	22.7	32.3	6.6	3.0	0.16	72	67.4
	$t\bar{b} + t\bar{b}j, \ E_{Tj} > 30 \text{GeV}$	17.8	24.8	5.5	1.7	-0.16	57	52
	$tar{b}j$	0.0	10.6	6.2	2.6	1.8	0.0	22.1
	$t\bar{b}j, E_{Tj} > 30 \mathrm{GeV}$	0.0	3.5	2.2	0.92	0.33	0.0	7.3
(b)	$t\bar{b}+t\bar{b}j$	19.0	21.7	2.0	1.4	-0.54	60.9	45.3
	$  t\bar{b} + t\bar{b}j, E_{Tj} > 30 \text{GeV}$	14.8	16.7	1.8	0.70	-0.48	47.4	34.9
	$tar{b}j$	0.0	5.6	3.9	1.1	0.56	0.0	11.7
	$t\bar{b}j, E_{Tj} > 30 \mathrm{GeV}$	0.0	1.9	1.4	0.40	0.08	0.0	4.0
(c)	$tar{b}+tar{b}j$	14.7	21.4	4.4	2.2	0.13	47	44.7
	$  t\bar{b} + t\bar{b}j, E_{Tj} > 30 \text{GeV}$	12.2	16.9	3.6	1.3	-0.17	39	35.3
	$tar{b}j$	0.0	6.4	3.6	1.7	1.1	0.0	13.4
	$t\bar{b}j, E_{Tj} > 30 \text{GeV}$	0.0	2.3	1.5	0.65	0.23	0.0	4.8

Table 5.1: The s-channel single-top production cross section and acceptance at the Tevatron (in fb) for different subprocesses under various scenario: (a) is for the loose version with  $\eta_l^{max} = 2.5$ ,  $\eta_j^{max} = 3.0$ , and  $R_{cut} = 0.5$ , (b) is for the loose version

with a larger jet clustering cone size (and jet-lepton separation cut) of  $R_{cut}=1.0$ , and (c) is for the tight version of cuts with  $\eta_l^{max}=1.0$ ,  $\eta_j^{max}=2.0$ , and  $R_{cut}=0.5$ . The first two columns show the Born level and full NLO cross sections, the last three columns the contribution from the different  $O(\alpha_s)$  processes. The decay branching ratio  $t \to bW(\to e\nu)$  is included.

In Table 5.1, we show the single-top production cross sections in femtobarns as well as acceptances for different subprocesses for several sets of cuts. We apply the  $E_T$  cuts listed in Eq. (5.1) and study three separate sets of values:

- loose cuts with small  $R_{cut}$ :  $\eta_l^{max}=2.5,\,\eta_j^{max}=3.0,\,{\rm and}\,\,R_{cut}=0.5,$
- loose cuts with large  $R_{cut}$ :  $\eta_l^{max} = 2.5, \eta_j^{max} = 3.0$ , and  $R_{cut} = 1.0$ ,
- tight cuts with small  $R_{cut}$ :  $\eta_l^{max} = 1.0$ ,  $\eta_j^{max} = 2.0$ , and  $R_{cut} = 0.5$ .

A larger value for  $R_{cut}$  reduces the acceptance significantly mainly because more events fail the lepton-jet separation cut. While this is only a 16% reduction at Bornlevel, the difference grows to 33% at NLO. Hence, a smaller cone size is preferred to keep the acceptance at a high level. For events with at least three jets, imposing a harder cut on the transverse momentum of the third jet ( $E_{Tj} > 30\,\text{GeV}$ ) only decreases the contribution from INIT and FINAL corrections by a factor of 3. By contrast, this cut reduced the contribution from the SDEC correction by a factor of more than five because the top quark mass sets the scale for the top quark decay contribution rather than the invariant mass of system. A tighter cut on jet  $E_T$  also reduces the relative contribution from the SDEC contribution in the 3-jet bin. The  $E_T$  spectrum of the gluon from the DEC contribution is softer because the available phase space is limited by the top quark mass, which can also be seen below in Fig. 5.13.

Fig. 5.1 shows how the observed cross section changes as a function of the jet  $E_T$  cut when applying the loose set of cuts, including a requirement of at least 2 jets. The cross section (and thus the acceptance) doesn't change very much until the jet  $E_T$  threshold reaches about 25 GeV because the b- and  $\bar{b}$ -jets typically have high  $E_T$ . The figure also shows that a jet pseudo-rapidity cut of  $|\eta| < 2$  or  $|\eta| < 3$  does not impact the overall acceptance; the cross section only decreases significantly when

restricting jets to the very central region ( $|\eta| < 1$ ). This implies not only that  $\eta$  cuts on jets should be large when separating single top events from the large backgrounds, but also that b-tagging needs to be efficient over a large  $\eta$  range (at least  $|\eta| \lesssim 2$ ) to be able to detect s-channel single top signal events.

The dependence of the fraction of 2-jet events and 3-jet events on the jet  $E_T$  cut is also shown in Fig. 5.1. At Born-level, there are only 2-jet events, whereas  $O(\alpha_s)$  corrections can produce an additional soft jet. The fraction of events with these additional jets is low only for very high jet  $E_T$  thresholds. For typical jet  $E_T$  thresholds considered by experiments of 15 GeV to 25 GeV these jets add a significant contribution. As expected, the effect is not quite as large when only jets within a very small  $\eta$  range are considered because the extra jet typically has higher  $\eta$ . In order to study  $O(\alpha_s)$  effects it is thus important to set the jet  $\eta$  cut as high as possible and the jet  $E_T$  cut as low as possible.

As mentioned before, the event rate for single top events is small and it is important for experiments to maximize their acceptance. We will thus use the loose set of cut values for the following discussion:  $\eta_l^{max} = 2.5$ ,  $\eta_j^{max} = 3.0$ , and  $R_{cut} = 0.5$ ,  $E_{Tj}^{min} = 15$  GeV, c.f. Eq (5.1).

# 5.3 Single Top Event Distributions

In this section, we study the kinematic properties of single top quark events. For the s-channel process at the Born level, two b-jets (the b from the top quark decay and the  $\bar{b}$  produced with the top) appear in the final state and cannot be distinguished from each other experimentally. A prescription is needed to identify which of the two jets corresponds to the b quark from the top decay. At NLO, an addition jet is radiated, which further complicates the reconstruction of the top quark. This is because the

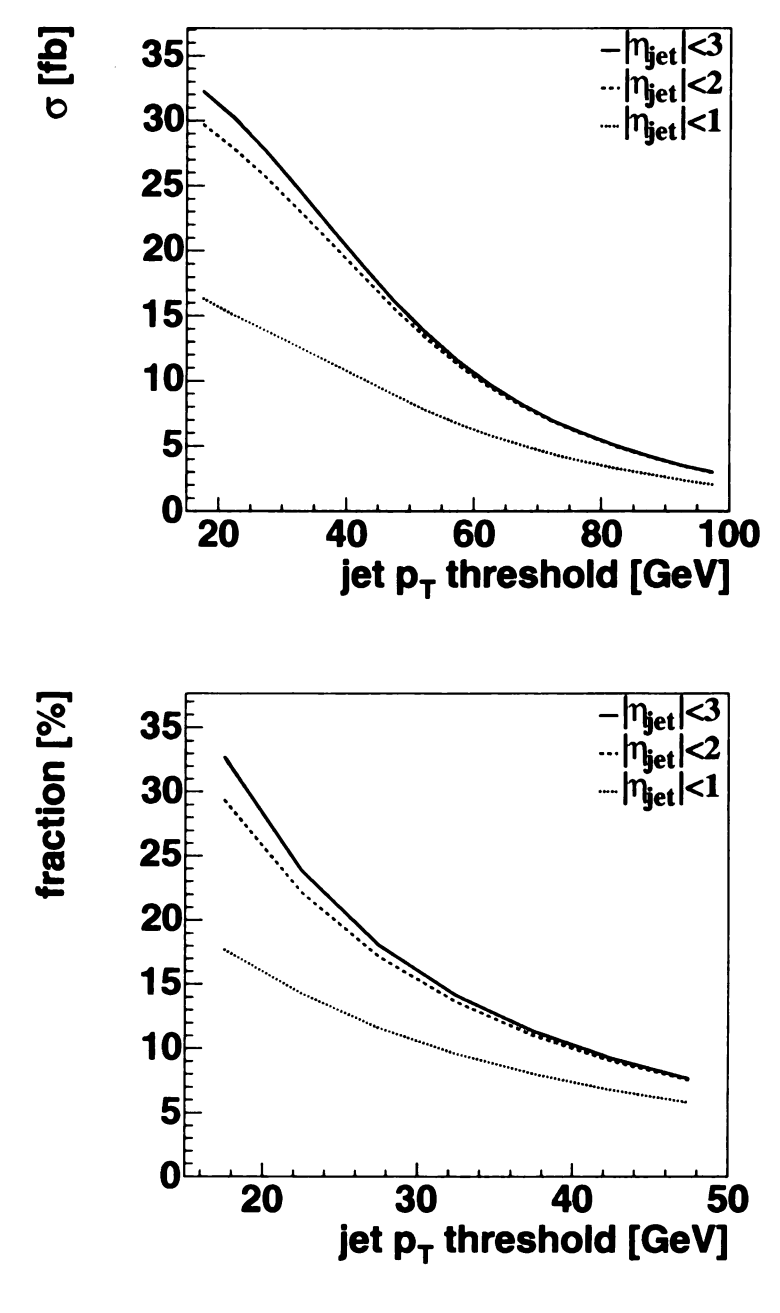


Figure 5.1: Cross section and fraction of 3-jet events at NLO for varying jet  $E_T$  cuts, requiring only that  $n_{jets} \geq 2$ , and not making any cuts on the electron or neutrino. The upper figure shows the total cross section for events with 2 or 3 jets as a function of the jet  $E_T$  cut for three different jet pseudo-rapidity cuts. The lower figure shows the fraction of 3-jet events as a function of the jet  $E_T$  for different jet pseudo-rapidity cuts. The lowest threshold considered is 15 GeV.

additional jet can come from either the production or the decay of the top quark. Production-stage emission occurs before the top quark goes on shell and decay-stage emission occurs only after the top quark goes on shell. In production emission events, the W boson and b quark momenta will combine to give the top quark momentum, while in the decay emission event the gluon momentum must also be include to reconstruct the top quark momentum. To find the best prescription of classifying the gluon jet correctly, we first examine various kinematic distributions of the final state particles. We then investigate two top quark reconstruction prescriptions: the leading jet algorithm and the best-jet algorithm. Having chosen a prescription, the effects of NLO corrections on distributions concerning the reconstructed top quark are studied, in particular spin correlations between the final state particles. Finally, we explore the impact of the radiated jet in exclusive 3-jets events.

### 5.3.1 Final State Object Distributions

In this section we examine various kinematical distributions of final state objects after event reconstruction and after applying the loose set of cuts, c.f. Table 5.1(a) and Eq. (5.1). We study inclusive 2-jet events in this section because they give more reliable infrared-safe predictions.

Fig. 5.2 shows the transverse momentum of the electron and the missing transverse momentum  $E_T$ . As expected because they are leptons and not quarks, the change in shape when going from Born-level to  $O(\alpha_s)$  is not very large for the electron or the neutrino where the  $O(\alpha_s)$  corrections have the same shape and peak position as the Born-level contribution. The pseudo-rapidity distribution of the electron is also given in Fig. 5.2. This distribution widens at  $O(\alpha_s)$  and shifts slightly to more positive values of  $\eta$ , but again the effect is not very large. We note that the peak position of the  $E_T$  distribution is at a higher value than that of the electron  $p_T$  because the

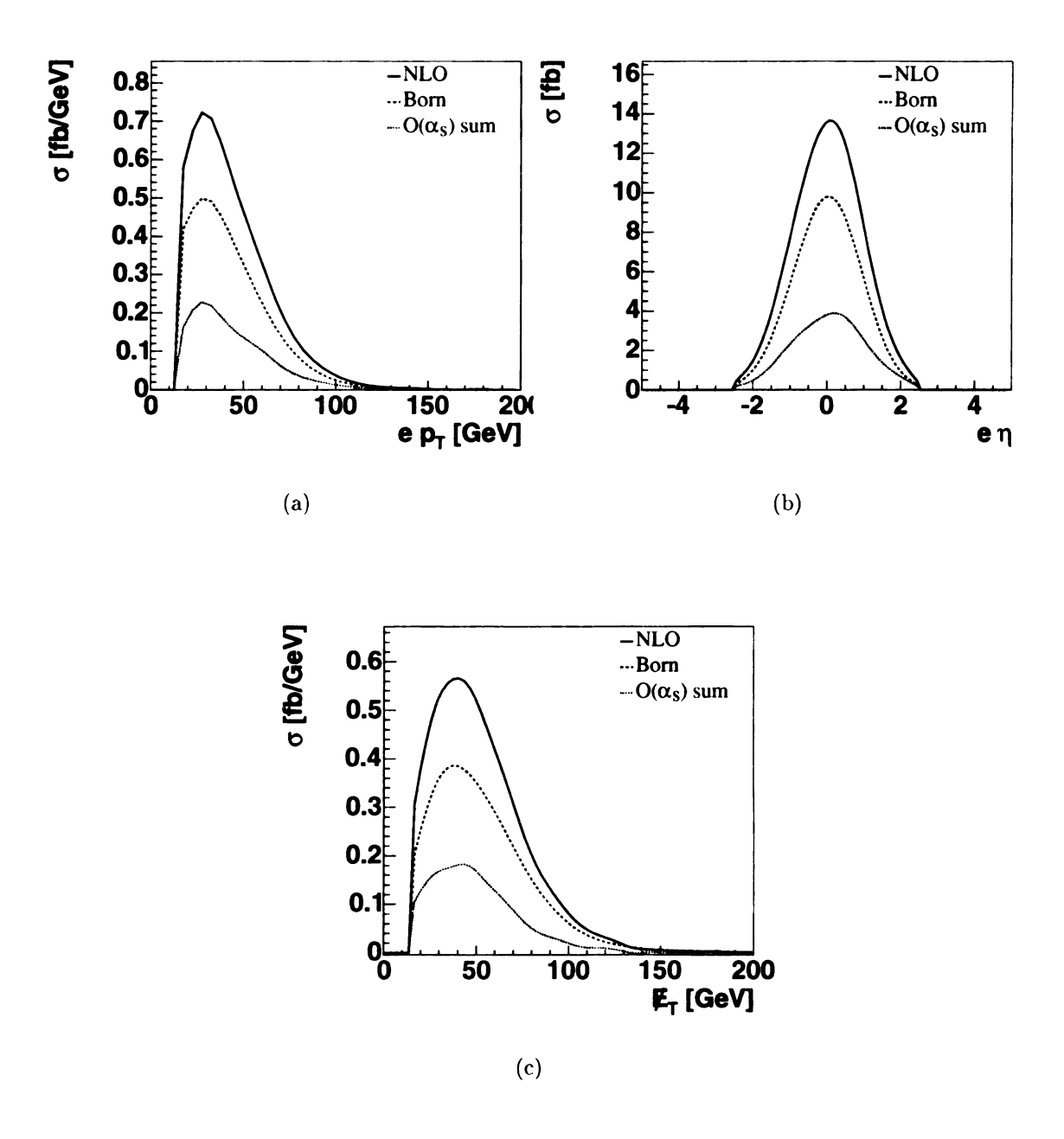


Figure 5.2: The transverse momentum  $p_T$  (a) and pseudo-rapidity  $\eta$  (b) distributions of the electron and the missing transverse energy  $\not\!\!E_T$  (c) after selection cuts, comparing Born-level to  $O(\alpha_s)$  and full NLO.

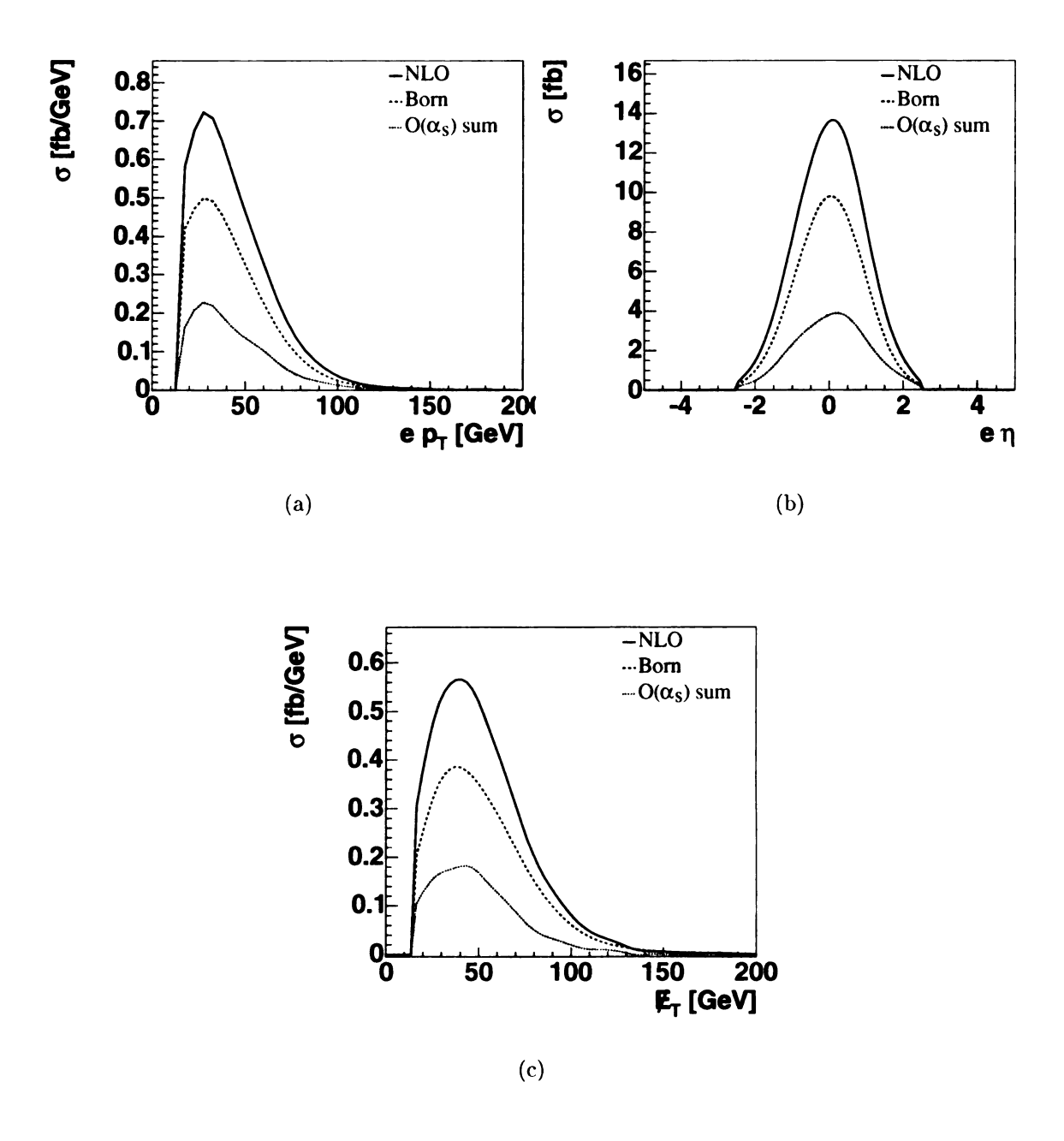


Figure 5.2: The transverse momentum  $p_T$  (a) and pseudo-rapidity  $\eta$  (b) distributions of the electron and the missing transverse energy  $E_T$  (c) after selection cuts, comparing Born-level to  $O(\alpha_s)$  and full NLO.

neutrino from the W-boson decay moves preferentially along the direction of the top quark. This is due to the left-handed nature of the charged current interaction and can easily be seen when examining the spin correlation between the charged lepton and the top quark in the top quark rest frame. We will comment more on this subject in Sec. 5.3.3.

Compared to the lepton and neutrino, the effect of the  $O(\alpha_s)$  corrections on the reconstructed b-jet and  $\bar{b}$ -jet is more pronounced. Fig. 5.3 shows a comparison of the  $E_T$  distributions of these two jets between the Born level and the  $O(\alpha_s)$  contributions. Though it is not possible to distinguish between the b- and  $\bar{b}$ -jet experimentally, it is nevertheless instructive to consider their  $E_T$  distributions individually. At the Bornlevel, the transverse momentum of the b-jet peaks higher and drops off faster than that of the  $\bar{b}$ -jet, resulting in similar mean  $E_T$  for the two (68 GeV for the b-jet and 71 GeV for the b-jet). Since the b-jet is produced in association with the heavy top quark, it has a long tail into the high  $p_T$  region to balance the top quark. The  $p_T$ distribution of the b-jet (from top quark decay) on the other hand is predominantly controlled by the top quark mass and therefore peaks at  $\sim m_t/3$ . The NLO QCD corrections broaden the LO transverse momentum distributions and shift the peak positions to lower values. The result for the mean of the distribution depends on the cuts that are applied because the different  $O(\alpha_s)$  corrections have different effects; in the case of the loose cuts both distributions have a mean of 66 GeV at  $O(\alpha_s)$ . The INIT correction shifts the mean of the b-jet  $p_T$  distribution up while the FINAL and DEC corrections tend to shift it down. The  $\bar{b}$ -jet  $p_T$  distribution receives a large contribution from the FINAL corrections and a negligible contribution from the DEC corrections, as expected. When a gluon is radiated from (t, b) quark line, it prefers to move along the b-jet direction due the collinear enhancement and therefore shifts the  $\bar{b}$ -jet  $p_T$  distribution to the small  $p_T$  region, as shown in Fig. 5.3(d). For

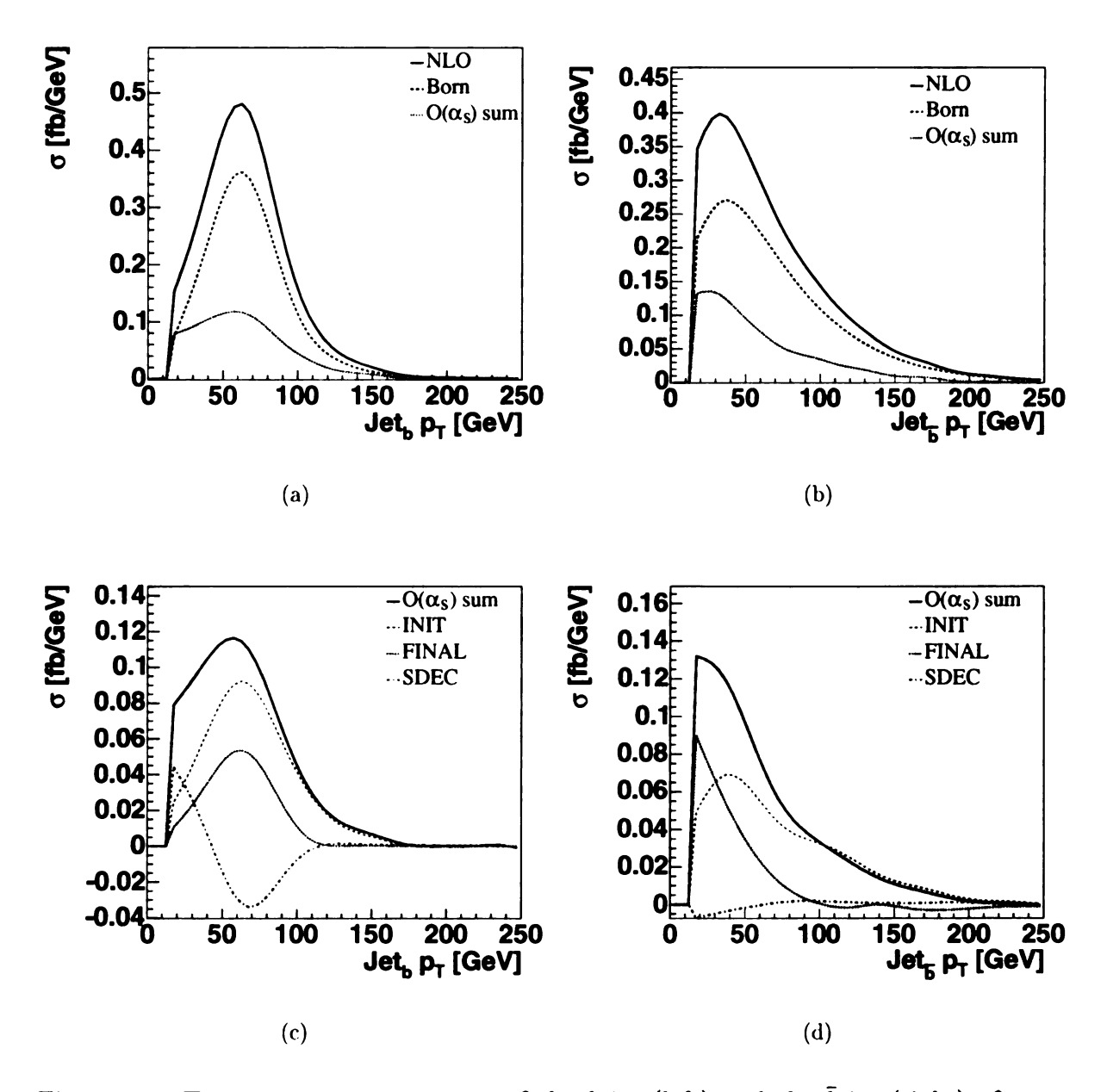


Figure 5.3: Transverse momentum  $p_T$  of the b jet (left) and the  $\bar{b}$  jet (right) after selection cuts, comparing Born-level to  $O(\alpha_s)$  corrections. The bottom row shows the different  $O(\alpha_s)$  contributions.

the same reason, the DEC correction to the b-jet  $p_T$  distribution also peaks around 60 GeV (the Born level peak position), but it provides a negative contribution, cf. Fig. 5.3(c). Furthermore, because the FINAL corrections are larger in size than the DEC corrections, the resulting shift to the low  $p_T$  region is stronger for the  $\bar{b}$ -jet than the b-jet.

This shift in the  $\eta$  distribution of the  $\bar{b}$ -jet, when comparing the Born level to  $O(\alpha_s)$ , is also evident in Fig. 5.4, where in particular the FINAL correction shifts the distribution to more central pseudo-rapidities. The top quark is so heavy that it is mostly produced in the central rapidity region and thus its partner  $\bar{b}$ -jet also peaks around a pseudo-rapidity of zero. We note that the pseudo-rapidity distribution of the b-jet is slightly asymmetric at the Born level, denoted by the red dotted line in Fig. 5.4, favoring negative pseudo-rapidity. This is similar to the lepton pseudorapidity asymmetry observed in the  $p\bar{p} \to W^+ \to \ell^+ \nu$  events due to the ratio of the down-quark and up-quark parton distributions inside the proton and anti-proton. The b-jet coming from the top quark decay follows the top quark moving direction and therefore favors a slightly positive pseudo-rapidity, denoted by the solid line in the Fig. 5.4. The  $O(\alpha_s)$  corrections, in particular the FINAL correction, shift the  $\bar{b}$ -jet to more central regions. The shape of the b-jet pseudo-rapidity distribution remains almost unchanged compared to Born-level because it comes from the top quark decay. Therefore we expect to see an asymmetry between  $\eta_b$  and  $\eta_{\bar{b}}$ , shown below after full event reconstruction.

The impact that the different  $O(\alpha_s)$  corrections have on the  $p_T$  of the jets is also reflected in event-wide energy variables such as the total transverse energy  $(H_T)$  in the event, defined as

$$H_T = p_T^{lepton} + \not\!\!E_T + \sum_{jets} p_T^{jet}. \tag{5.2}$$

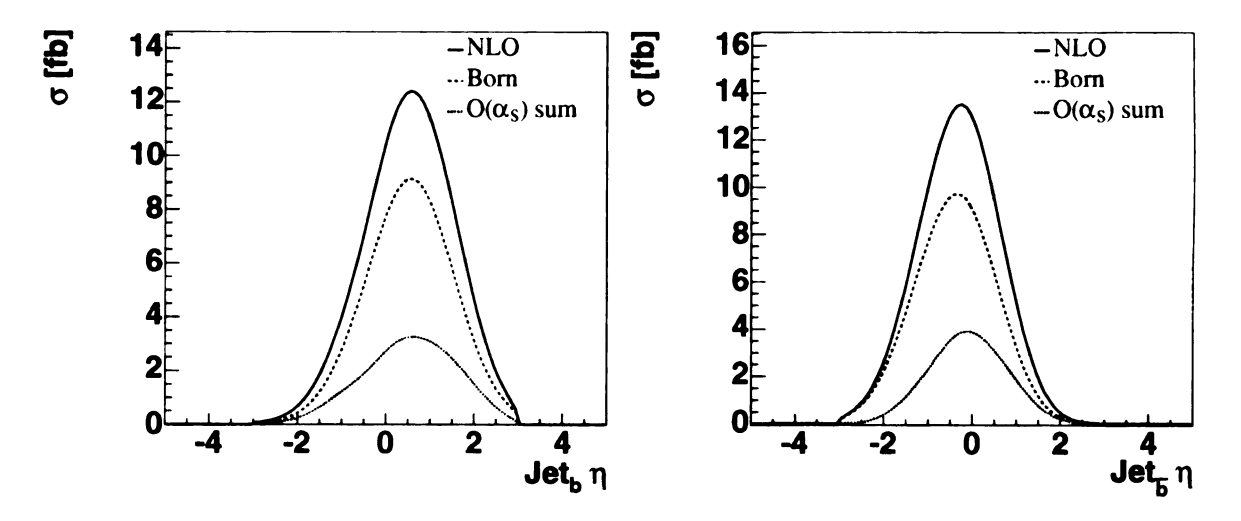


Figure 5.4: Pseudo-rapidity  $\eta$  of the *b*-jet (left) and the  $\bar{b}$ -jet (right) after selection cuts, comparing Born level to  $O(\alpha_s)$  corrections.

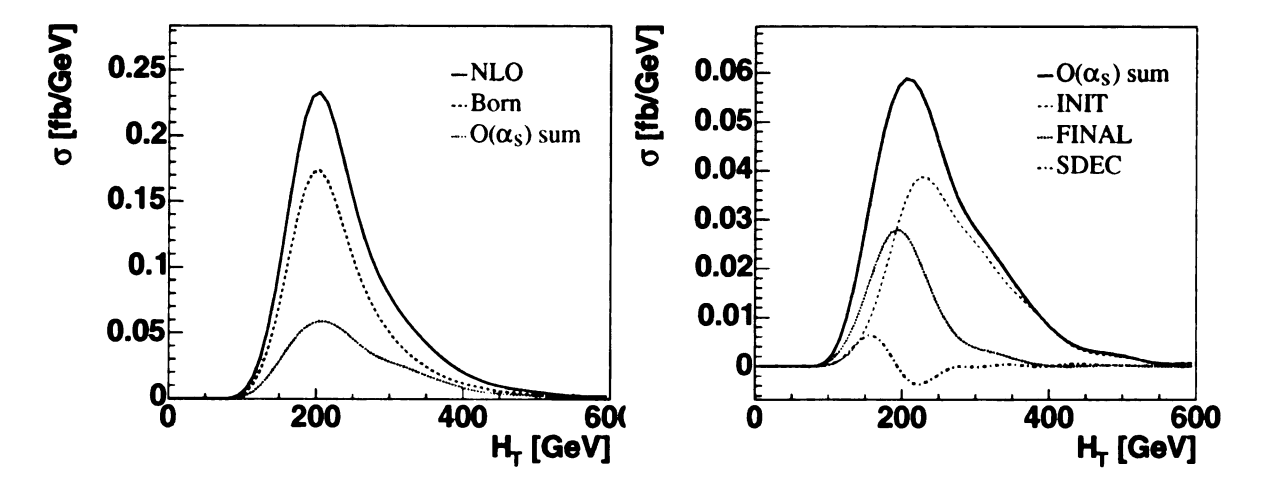


Figure 5.5: Total event transverse energy  $H_T$  after selection cuts, comparing Born level to  $O(\alpha_s)$  corrections.

The distribution of  $H_T$  for the s-channel single top events is shown in Fig. 5.5. Similar to the b- and  $\bar{b}$ -jet  $p_T$  distributions, the FINAL and DEC contributions shift the  $H_T$  distributions down, while the INIT contribution shifts it up. This is expected because the INIT correction contributes additional energy to the event in the form of a third jet.

#### 5.3.2 Event Reconstruction

When selecting single-top events we would like to take advantage not only of simple single-object kinematics but also of correlations between objects. For that we need to reconstruct the event completely, not just the final state jets but also intermediate particles, in particular the W-boson and the top quark.

The W-boson can be reconstructed from the final state electron and the observed missing transverse energy  $\mathcal{E}_T$ . The lack of information about the beam-direction component of the neutrino momentum  $(p_z^{\nu})$  that would prevent this reconstruction is overcome by requiring the invariant mass of the electron-neutrino system to be equal to the mass of the W-boson. This additional constraint yields two possible solutions for  $p_z^{\nu}$ , and typically, both of them are physical solutions for a signal event. In our analysis, we follow the prescription in the Ref. [99] to choose the solution which has the smaller  $|p_Z^{\nu}|$ . This picks the correct  $p_z^{\nu}$  in about 70% of the events passing the loose set of cuts.

To reconstruct the top quark, the reconstructed W-boson then needs to be combined with the b-jet from the top quark decay. The challenge that has to be overcome in this case is to identify the correct jet as the b-jet. Several different methods have been used in the past to select this jet. The simplest method is to choose the highest- $E_T$  jet in the event (leading jet). Another possibility that can be used when b-tagging is available experimentally is to choose the b-tagged jet in the event. However, neither of these methods is very successful in s-channel single top production because both the b quark from the top decay and the  $\bar{b}$  quark produced with the top quark have high  $E_T$  and central pseudo-rapidities. While the  $E_T$  distributions are different for b- and  $\bar{b}$ -jets, Fig. 5.3 shows that they differ both in peak position and in shape. For jet  $E_T$  values above 100 GeV, the leading jet is actually more likely to be from the  $\bar{b}$ 

quark. The leading jet corresponds to the b from the top about 55% of the time in the sample after loose cuts.

A more effective method to identify which jet corresponds to the b quark from the top decay is to make use of the known top quark mass that is measured in  $t\bar{t}$  events. In this "best-jet" algorithm, the Wj combination that gives an invariant mass closest to the true top mass is chosen as the reconstructed top quark. The jet thus identified is called "best-jet" [43].

If an additional jet is produced in the decay  $O(\alpha_s)$  contribution, then the best-jet method will not be able to reconstruct a top quark at all. We therefore need to extend the best-jet algorithm to also include 2-jet pairs when forming a top quark. In other words, candidates include not only Wj but also Wjj. The list of systems for which the invariant mass is evaluated and from which the best-jet is chosen thus consists of:  $(W, jet_1)$ ,  $(W, jet_2)$ ,  $(W, jet_1, jet_3)$ ,  $(W, jet_2, jet_3)$ . The jet (or 2-jet system) that is thus chosen will be called the "best-jet". Once we have identified the b-jet from the top quark decay, we can assign one of the other jets to the  $\bar{b}$  quark produced with the top. We choose this "non-best-jet" also from the leading two jets and assign the label to whichever of the two jets was not identified as the "best-jet".

This method identifies the b-jet properly about 80% of the time. The effectiveness of the best-jet algorithm is mainly limited by the efficiency of the W-boson identification method; if the W-boson is not reconstructed properly, then identifying the b quark from the top decay becomes a random pick. Fig. 5.6 shows the dependence of this efficiency on the transverse momentum of the b-jet. As expected, the leading jet corresponds to the b quark from the top quark decay mostly when the transverse momentum of the b-jet is very large. The best-jet algorithm in comparison shows

<sup>&</sup>lt;sup>†</sup>The combination  $(W, jet_1, jet_2)$  is not considered because it is very unlikely for the gluon jet to be one of the leading two jets due to its generally low  $p_T$  and because the gluon jet will not be b-tagged.

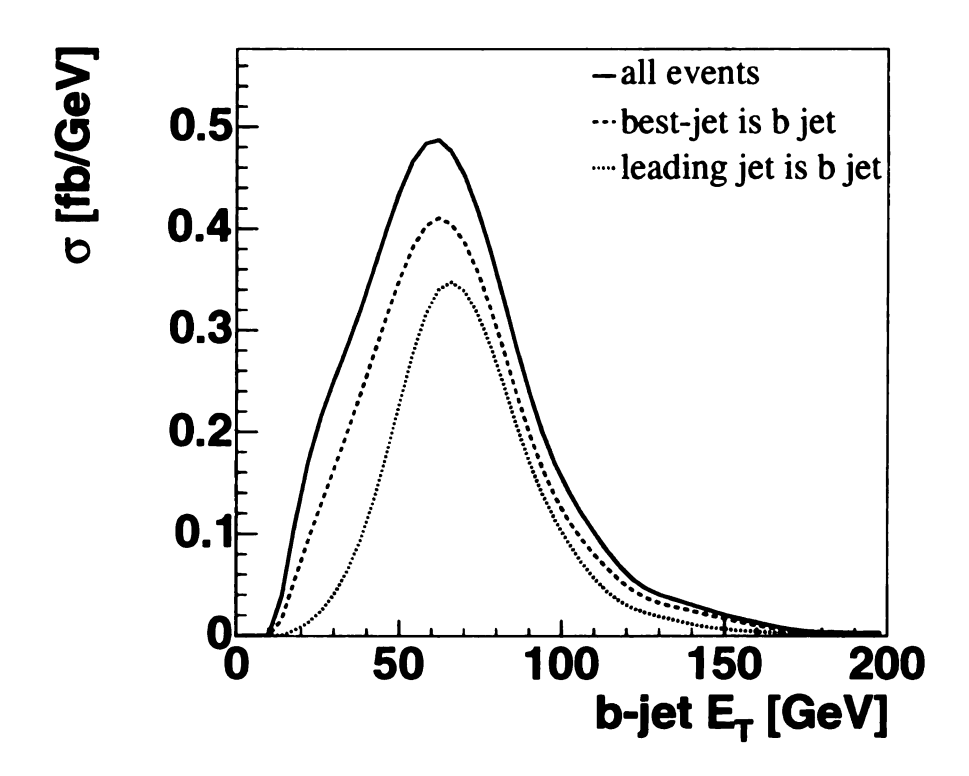


Figure 5.6: Transverse momentum distribution of the b jet from the top quark decay, for all events that pass the loose set of cuts (solid line), only for those events in which the b jet is also the leading jet (dashed line), and only for events in which the b jet is the best-jet (dotted line).

high efficiency for all transverse momenta.

Fig. 5.7 shows the invariant mass of the reconstructed top quark, comparing the different methods to identify the b quark from the top decay. For the b-jet curve in Fig. 5.7, parton-level information is used to identify which of the final state jets contains the b quark from the top decay. If this b quark produced a gluon in decay-stage emission, this resulting extra jet is also included when reconstructing the top quark. For the leading jet curve, only the highest  $E_T$  jet in each event is used.

The top quark width is larger than it would be at parton level even though no smearing was applied in this study. This is the result of using the reconstructed kinematics of the W- boson (in particular the neutrino z-momentum) rather than parton-level information. Furthermore, since the same reconstructed W-boson was

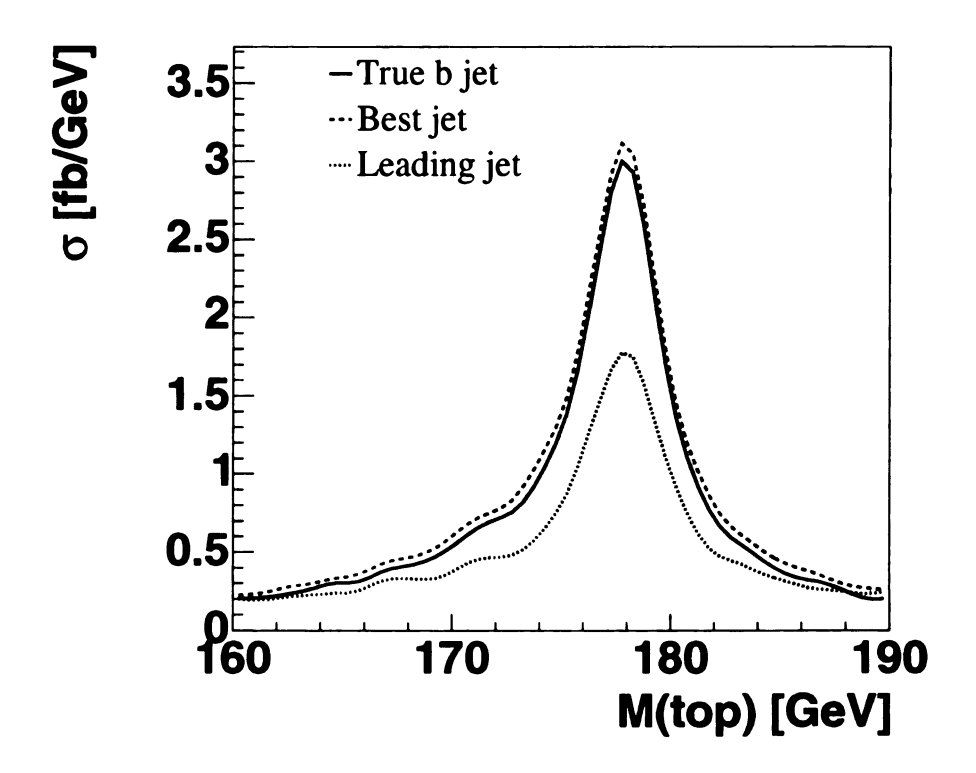


Figure 5.7: Invariant mass of the reconstructed W and a jet object. This jet object is: the jet containing the b quark from the top decay, using parton information (solid line); the best-jet identified using the method outlined in the main text (dashed line); the leading jet (dotted line).

used in each case, differences between the individual curves are solely due to which jet is chosen to reconstruct the top quark. Furthermore, because parton-level information is used for the *b*-jet curve, it functions as a reference and upper limit for the other methods.

As expected, using the leading jet gives a peak at the invariant mass of the top quark with a height of about half the b-jet peak. The best-jet algorithm by contrast shows approximately the same width and height as the b-jet curve. This is the result of two competing effects, to be discussed in order. On the one hand the best-jet algorithm identifies the correct jet only in some fraction of the events because the W-boson itself is mis-reconstructed part of the time, thus reducing the height of the curve. On the other hand the algorithm chooses an invariant mass close to 178 GeV

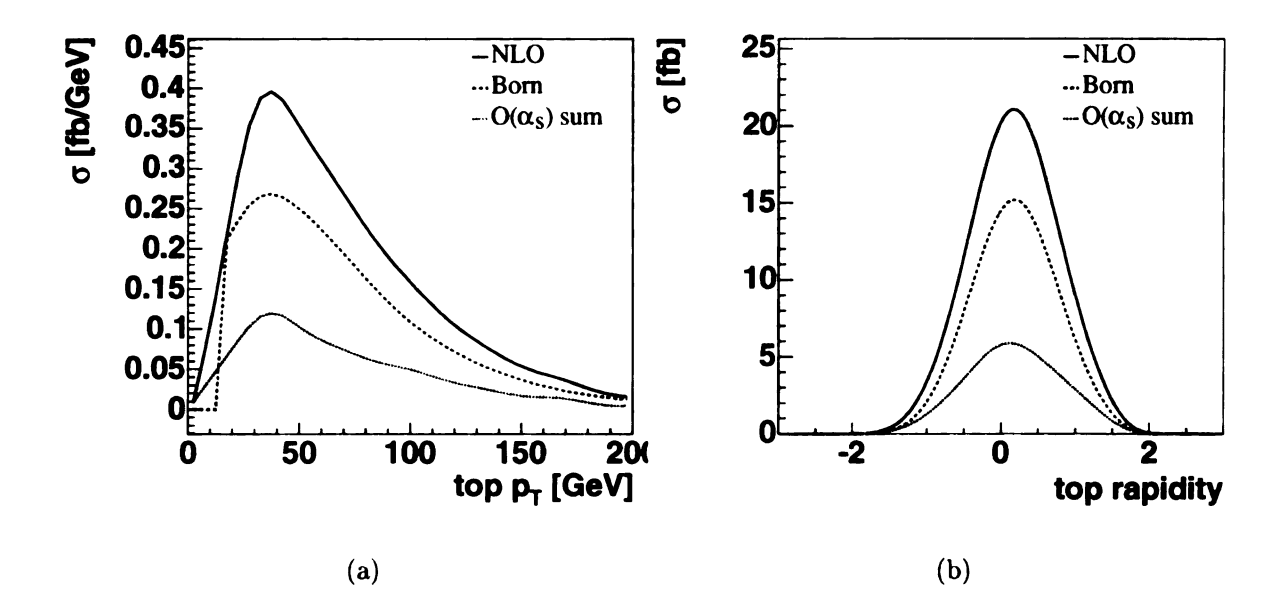


Figure 5.8: Transverse momentum and rapidity of the reconstructed top quark, comparing Born-level to  $O(\alpha_s)$  corrections.

and thus tends to bring mis-reconstructed events closer to 178 GeV. The latter effect is slightly larger than the former, hence the best-jet curve is slightly higher than the b-jet curve in Fig. 5.7.

Fig. 5.8 shows the transverse momentum and rapidity of the top quark reconstructed from the W and the best-jet. Using the best-jet in this case results in distributions that are very similar to those obtained using the true b-jet from the top quark decay.

## 5.3.3 Kinematical and Spin Correlations

Having identified the b-jet from the top quark decay through the best-jet algorithm, we can now study correlations expected from event kinematics. In the s-channel single top events, there is a strong correlation between the kinematics of the b and  $\bar{b}$  quarks at the Born level. This correlation is modified by gluon radiation in the production and decay of the top quark. Fig. 5.9 shows how  $O(\alpha_s)$  effects change the

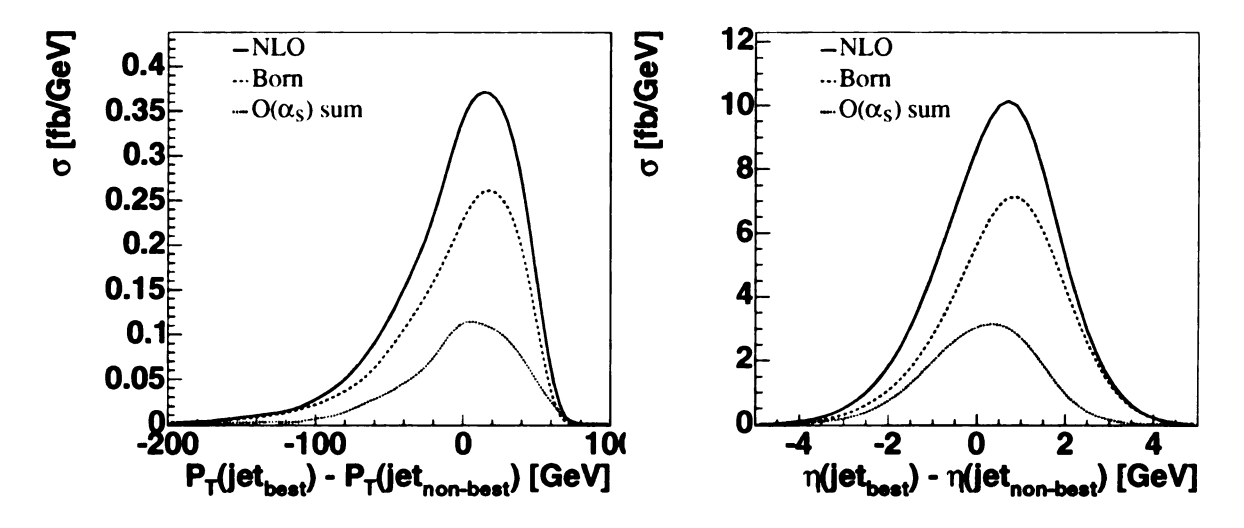


Figure 5.9: Transverse momentum difference between the best-jet and the non-best-jet (left) and pseudo-rapidity difference between the two (right) after selection cuts, comparing Born-level to  $O(\alpha_s)$  corrections.

momentum difference and the pseudo-rapidity difference between the best-jet and the non-best-jet.

The transverse momentum difference is not affected very much. While the  $O(\alpha_s)$  corrections affect both the b-jet and the  $\bar{b}$ -jet and tend to make the distribution broader, this is a small change compared to the overall width of the distribution. The  $O(\alpha_s)$  corrections have a larger affect on the pseudo-rapidity difference, shifting the distribution to more central values and making it broader. Both effects are mainly due to the FINAL and DEC corrections, which tend to weaken the correlation between the b-jet and the  $\bar{b}$ -jet.

#### 5.3.3.1 Top Polarization

In the SM, the top quark produced in single top quark events is highly polarized, and this polarization can in principle be measured. The top quark is by far the heaviest known fermion and the only known fermion with a mass at the electroweak symmetry-breaking scale. Thus, it is hoped that a detailed study of top quark coupling to other

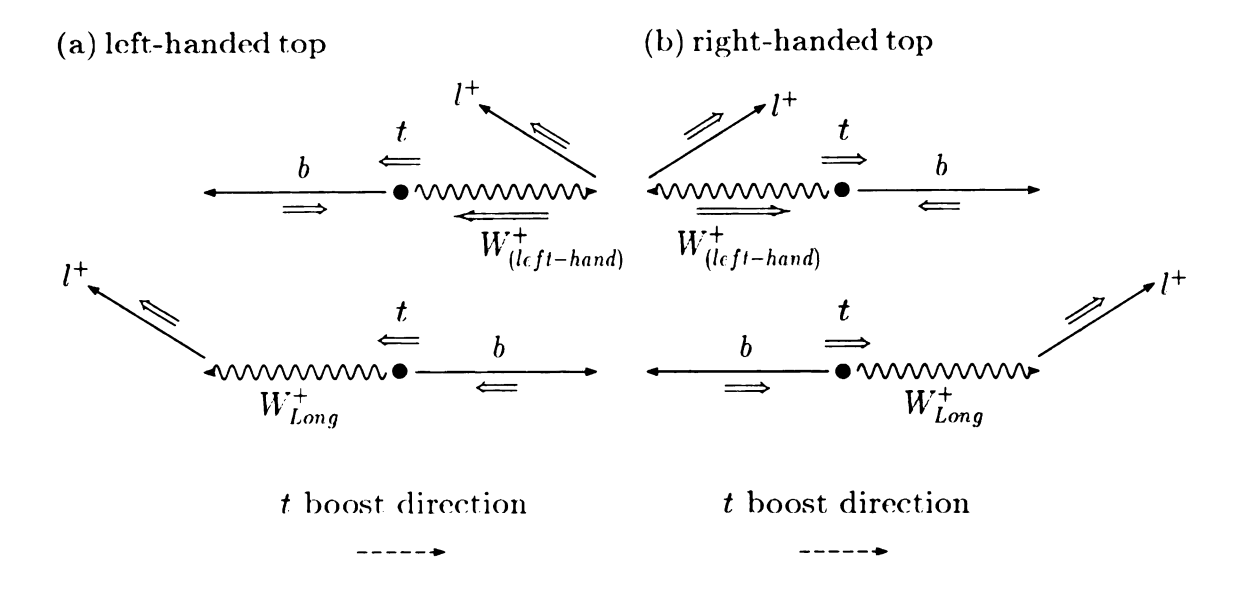


Figure 5.10: Illustration of the correlation between the charged lepton from the top decay and the top quark spin, in the top quark rest frame.

particles will be of great utility in determining if the SM mechanism for electroweak symmetry-breaking is the correct one, or if new physics is responsible [100]. Angular correlations among the decay products of polarized top quarks provide a useful handle on these couplings.

Although the top quark is produced via the left-handed charged current, there is no reason to believe that the helicity basis will give the best description of the top quark spin. Choosing an appropriate basis could maximize spin correlation effects. Two definitions for the polarization have been studied in the literature for s-channel processes, differing by the reference frame used to define the polarization: One calculation uses the helicity basis, another the so-called "optimal" basis [101,102]. Both work in the top quark rest frame, but they have different reference axis for the top quark spin, cf. Fig. 6.15. In the more common helicity basis the top quark spin is measured along the top quark direction of motion in the center of mass (c.m.) frame which is chosen as the frame of the (reconstructed top quark, non-best-jet) system after event reconstruction. In the optimal basis (beamline basis) we can maximize

the spin correlations by taking advantage of the fact that the top quark produced through the s-channel single top quark processes is almost 100% polarized along the direction of the d-type quark. In the discussion below, we will examine the polarization of single top quark events in both cases. The particular strength and weaknesses of both methods were discussed in Ref. [42]. In the discussion below, we will examine the polarization of single top quark events in these two bases.

It has been pointed out that among the decay products of top quark the charged lepton is maximally correlated with the top quark spin [101, 102]. We can thus obtain the most distinctive distribution by plotting the angle between the spin axis and the charged lepton in the top quark rest frame. Before examining this spin correlation effect for a particular process or in a particular basis, it is worthwhile to give a schematic picture. Due to helicity conservation and the left-handedness of charged current interactions, the W-boson from the top quark decay can be either longitudinally or left-handed polarized. This is true for a massless b quark and diagrammatically shown in Fig. 5.10. The figure shows the preferred moving direction of the lepton from a polarized W-boson in the rest frame of a polarized top quark. When the  $W^+$  is left-handed polarized, the fact that the b quark must be left-handed forces it to move along the direction of the top quark polarization, cf. the upper part of Fig. 5.10(a). The  $W^+$  thus moves against this direction. When the  $W^+$  decays, the charged anti-lepton  $(e^+)$  must be right-handed, hence it prefers to move against the  $W^+$  direction, in the same direction as the top quark polarization. When the  $W^+$ is longitudinally polarized, it prefers to move in the same direction as the top spin, c.f. the lower part of Fig. 5.10(a). Its decay products prefer to align along the  $W^+$ polarization, and since the  $W^+$  is boosted in the direction of the top quark polarization, the charged anti-lepton again prefers to move along the top quark spin axis. Since in both cases the charged anti-lepton moves against the top quark direction of motion, the neutrino from the  $W^+$  decay will be harder than the charged anti-lepton, as shown in Fig. 5.2(c). Similarly, the preferred moving direction of the charged anti-lepton from a right-handed polarized top quark is illustrated in Fig. 5.10(b). For simplicity, we will continue to use the phrase "charged lepton" when referring to the charged anti-lepton from the W decay.

In the helicity basis, the polarization of the top quark is examined as the angular distribution  $(\cos \theta_{hel})$  of the lepton in the c.m. frame of the incoming partons relative to the moving direction of the top quark in the same frame. The angular correlation in this frame is given by

$$\cos \theta_{hel} = \frac{\vec{p_t} \cdot \vec{p_\ell}^*}{|\vec{p_t}||\vec{p_\ell}^*|},\tag{5.3}$$

where  $\vec{p_t}$  is the top quark three-momentum defined in the c.m. frame of the two incoming partons, and  $\vec{p_\ell}^*$  is the charged lepton three-momentum defined in the rest frame of the top quark. For a left-handed top quark, the angular correlation of the lepton  $\ell^+$  is given by  $(1 - \cos \theta_{hel})/2$ , and for a right-handed top quark, it is  $(1 + \cos \theta_{hel})/2$ .

In order to study the top polarization in helicity basis, the c.m. frame needs to be reconstructed in order to define the top quark momentum. Due to additional jet radiation, the determination of the c.m. frame at NLO is more complicated than at the Born-level. The additional radiation will also blur the spin correlation, therefore, choosing the appropriate frame will reduce this effect. In this study, two options for reconstructing the c.m. frame are investigated:

1.  $t\bar{b}(j)$ -frame: the c.m. frame of the incoming partons. This is the rest frame of all the final state objects (reconstructed top quark and all others jets). In exclusive two-jet events, this frame is the same as that at the Born-level, i.e.

reconstructed from summing over momentum of the top quark and non-best-jet. In exclusive three-jet events, this frame is reconstructed by summing over the 4-momenta of top quark, non-best-jet, and the third-jet from the parton level calculation.

2.  $t\bar{b}$ -frame: the c.m. frame of the top quark and non-best-jet. In this case, even in the exclusive three-jet events, the reference frame is constructed by summing over only the 4-momenta of the top quark and non-best-jet. Note that this differs from the  $t\bar{b}(j)$ -frame only in exclusive three-jet events.

As shown in Table 5.2 and discussed below, the degree of top polarization is larger in the tq-frame than in the tq(j)-frame. Therefore, in the figures below we only display the top quark polarization in the tq-frame.

Fig. 5.11 shows that this linear relationship for  $\cos \theta_{hel}$  is indeed a valid description for s-channel single top events at the parton level. The figure also shows that the top quark is not completely polarized in the helicity basis, and that this polarization is weakened further when including  $O(\alpha_s)$  corrections. After reconstruction the effect of the lepton-jet separation cut can be seen as a drop-off of the  $\cos \theta_{hel}$  distribution close to a value of -1.

In the "optimal" basis, the relevant angular correlation for the s-channel process is  $\cos \theta_{opt}$ , defined as

$$\cos \theta_{opt} = \frac{\vec{p}_{\bar{p}}^* \cdot \vec{p}_{\ell}^*}{|\vec{p}_{\bar{p}}^*||\vec{p}_{\ell}^*|}, \tag{5.4}$$

where  $\vec{p}_{\vec{p}}^{*}$  is the anti-proton three-momentum in the top quark rest frame and  $\vec{p}_{\ell}^{*}$  is the lepton three-momentum in the top quark rest frame. In this analysis, we orient the coordinate system such that the protons travel in the positive z direction; the anti-protons travel in the negative z direction. For a top quark polarized along the anti-

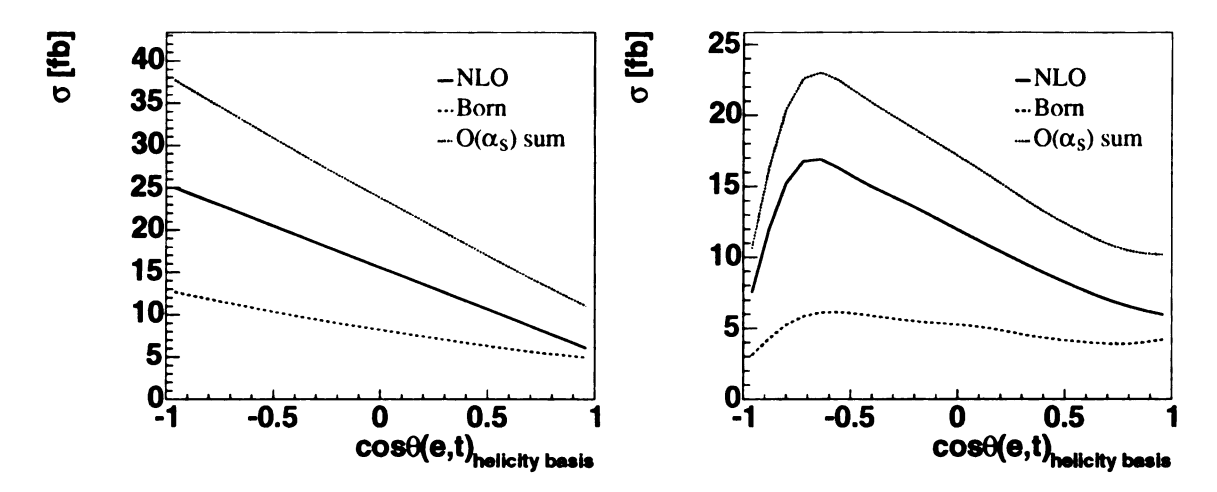


Figure 5.11: Top quark polarization in the helicity basis using the full parton information (left) and after event reconstruction (right) with selection cuts, comparing Born-level to  $O(\alpha_s)$  corrections.

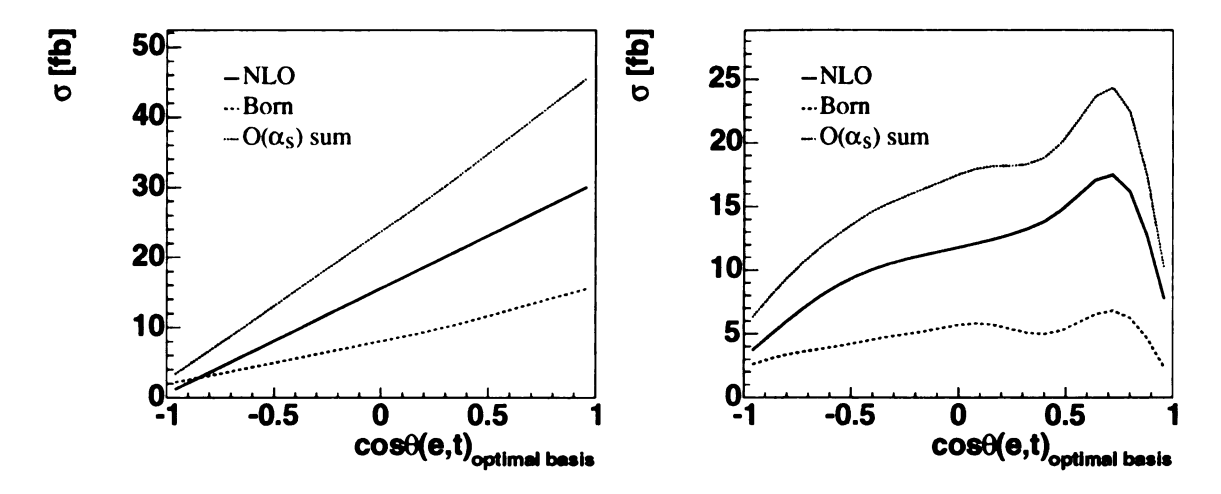


Figure 5.12: Top quark polarization in the "optimal basis" using the full parton information (left) and after event reconstruction(right) with selection cuts, comparing Born-level to  $O(\alpha_s)$  corrections.

proton moving direction, the angular distribution of the lepton  $\ell^+$  is  $(1 + \cos \theta_{opt})/2$ , while for a top quark polarized along the proton moving direction it is  $(1 - \cos \theta_{opt})/2$ . Fig. 5.12 shows that this linear relationship for  $\cos \theta_{opt}$  is a valid description for schannel single top events at the parton level. Moreover, in contrast to the helicity basis, the top quark is almost completely polarized in the "optimal basis" at parton level, and the  $O(\alpha_s)$  corrections don't change this picture very much.

However, in this case the event reconstruction itself has a significant effect on the distribution. The reconstructed  $\cos \theta_{opt}$  distribution also shows a drop-off, in this case at high  $\cos \theta_{opt}$ , which is due to the  $\eta$  cut on the lepton.

To better quantify the change in polarization, it is useful to define the degree of polarization  $\mathcal{D}$  of the top quark. This is given as the ratio

$$\mathcal{D} = \frac{N_{-} - N_{+}}{N_{-} + N_{+}},\tag{5.5}$$

where  $N_{-}$   $(N_{+})$  is , the number of left-hand (right-hand) polarized top quarks in the helicity basis. Similarly, in the optimal basis,  $N_{-}$   $(N_{+})$  is the number of top quarks with polarization against (along) the direction of the anti-proton three momentum in the top quark rest frame  $\vec{p}_{\bar{p}}^{*}$ . The angular distribution is then given by [103]

$$\frac{1}{\sigma} \frac{d\sigma}{d(\cos \theta)} = \frac{N_{-}}{N_{-} + N_{+}} \frac{1 + \cos \theta}{2} + \frac{N_{+}}{N_{-} + N_{+}} \frac{1 - \cos \theta}{2}$$
$$= \frac{1}{2} (1 + D \cos \theta_{i}).$$

A simple algebra leads to the following identity:

$$\mathcal{D} = 3 \int_{-1}^{1} x \frac{d\sigma}{\sigma dx} dx, \qquad (5.6)$$

where  $\frac{d\sigma}{\sigma dx}$  is the normalized differential cross section as a function of the polar angle x. Here, x denotes  $\cos\theta_{hel}$  in the helicity basis and  $\cos\theta_{opt}$  in the "optimal basis". Based on the degree of polarization  $\mathcal{D}$ , we can easily get the spin fractions  $\mathcal{F}_{\pm}$  as:

$$\mathcal{F}_{-} = \frac{N_{-}}{N_{-} + N_{+}} = \frac{1 + \mathcal{D}}{2},$$

$$\mathcal{F}_{+} = \frac{N_{+}}{N_{-} + N_{+}} = \frac{1 - \mathcal{D}}{2}.$$
(5.7)

Note that  $\mathcal{F}_{-}(\mathcal{F}_{+})$  is the fraction of left-handed (right-handed) polarized top quarks in the helicity basis. Similar, in the optimal basis,  $\mathcal{F}_{-}(\mathcal{F}_{+})$  is the fraction of top quarks

		$\mathcal{D}$		$\mathcal{F}$		A	
		LO	NLO	LO	NLO	LO	NLO
Helicity basis:	$\operatorname{Parton}(tar{b}(j) ext{-frame})$	0.63	0.54	0.82	0.77	0.32	0.27
	${ m Parton}(tar{b} ext{-frame})$	0.63	0.58	0.82	0.79	0.32	0.29
	Recon. $(t\bar{b}(j)$ -frame)	0.46	0.37	0.73	0.68	0.21	0.21
	Recon. $(t\bar{b}$ -frame)	0.46	0.37	0.73	0.68	0.26	0.21
Optimal basis:	Parton	-0.96	-0.92	0.98	0.96	-0.48	-0.46
	Recon.	-0.48	-0.42	0.74	0.71	-0.24	-0.21

Table 5.2: Degree of polarization  $\mathcal{D}$ , polarization fraction  $\mathcal{F}$ , and asymmetry  $\mathcal{A}$  for inclusive two-jet single top quark events, at the parton level (Parton) and after event reconstruction (Recon.), in the s-channel process. Here,  $\mathcal{F}$  corresponds to  $\mathcal{F}_{-}$  in the helicity basis for left-handed top quarks and to  $\mathcal{F}_{+}$  in the optimal basis for top quarks with polarization along the direction of anti-proton three momentum, respectively. The  $t\bar{b}g$  frame in the helicity basis denotes the c.m. frame of the incoming partons while  $t\bar{b}$  frame denotes the rest frame of the reconstructed top quark and  $\bar{b}$  quark.

with polarization against (along) the direction of the anti-proton three momentum in the top quark rest frame.

We can also define the asymmetry A of the distribution as

$$\mathcal{A} = \frac{\int_{-1}^{0} d\sigma(\cos\theta) - \int_{0}^{1} d\sigma(\cos\theta)}{\int_{-1}^{0} d\sigma(\cos\theta) + \int_{0}^{1} d\sigma(\cos\theta)}.$$
 (5.8)

It is easy to check that without imposing any kinematic cuts,  $D=2\mathcal{A}$ . Furthermore, the ratio of top quarks with spin along the basis direction will be  $r_{\uparrow}=0.5-\mathcal{A}$  when no cuts are applied. However, when cuts are imposed, the two relations break down.

Table 5.2 shows that the relationship  $\mathcal{D}=2\mathcal{A}$  indeed holds at parton level (within rounding errors) and is still approximately true at  $O(\alpha_s)$ . We present our result at

		$\mathcal{D}$	$\mathcal{F}$	$\mathcal{A}$
Helicity basis:	icity basis: Parton level ( $t\bar{b}g$ frame)		0.72	0.25
	Parton level $(tar{b} \ { m frame})$	0.49	0.74	0.27
	Reconstructed events $(tar{b}g$ frame)	0.36	0.68	0.21
	Reconstructed events $(tar{b} \ { m frame})$	0.37	0.68	0.21
optimal basis:	imal basis: Parton level		0.91	-0.45
	Reconstructed events	-0.38	0.69	-0.19

Table 5.3: Degree of polarization  $\mathcal{D}$ , polarization fraction  $\mathcal{F}$ , and asymmetry  $\mathcal{A}$  for exclusive three-jet single top quark events, at parton level and after event reconstruction, in the s-channel process. Here,  $\mathcal{F}$  corresponds to  $\mathcal{F}_{-}$  in the helicity basis for left-handed top quarks and to  $\mathcal{F}_{+}$  in the optimal bases for top quarks with polarization along the direction of anti-proton three momentum, respectively. The  $t\bar{b}g$  frame in the helicity basis denotes the c.m. frame of the incoming partons while the  $t\bar{b}$  frame denotes the rest frame of the reconstructed top quark and  $\bar{b}$  quark.

the parton level, both before and after event reconstruction. We found that at the parton level stage the "optimal basis" presents a significant improvement over the the helicity basis at both the Born level and NLO. The top quark is almost completely polarized in the optimal basis. However, after event reconstruction both bases give almost the same spin fractions. This is a result of the constraint on the W mass when reconstructing the neutrino. This constraint has the effect that the gain from using the optimal basis is lost again and the helicity basis is equivalent to the optimal basis in terms of polarization. Furthermore, the  $O(\alpha_s)$  corrections reduce the polarization already at the parton level in both the helicity and optimal basis. The result of exclusive three-jet events is shown in Table 5.3.

Before concluding this section, we note that the relative amounts of productionand decay-stage emission depend sensitively on the kinematic cuts applied. Also, we do not show the transverse momentum distribution of the  $t\bar{b}$  pair or their azimuthal angle separation because those distributions are sensitive to multiple gluon radiations, and they can only be reliable predicted using a resummed calculation [35].

#### 5.3.4 Distributions for three-jet event

As shown in Fig. 5.1, a large fraction of the events passing the loose selection cuts contains three jets. In this section we focus on the properties of the additional jet.

#### 5.3.4.1 Kinematic Distribution of the Extra Jet

Initial- and final-state emission of additional gluons occurs before the top quark goes on shell and can thus be considered as "production-stage emission", while decay-stage emission occurs only after the top quark goes on shell. In principle, an event with an extra jet can thus be classified as production-stage or decay-stage by looking at the invariant mass of the decay products. In production-stage emission events, the W-boson and b-quark momenta will combine to give the top momentum. In decay-stage emission events, the gluon momentum must also be included to reconstruct the top momentum. This interpretation is exact at the parton level in the narrow width approximation. Finite top width effects can blur it due to interference between production-and decay-stage emission. This classification is nevertheless still useful in our case because the top width of 1.5 GeV is small compared to the hard gluon  $E_T$  cut imposed in the MC calculations. It should be kept in mind that in an experiment, the production-decay distinction is further blurred by the experimental jet energy resolution and ambiguities associated with properly assigning partons to jets and the like.

Fig. 5.13 shows the transverse momentum distribution as well as the pseudorapidity distribution for the third jet in 3-jet events. This jet corresponds to the

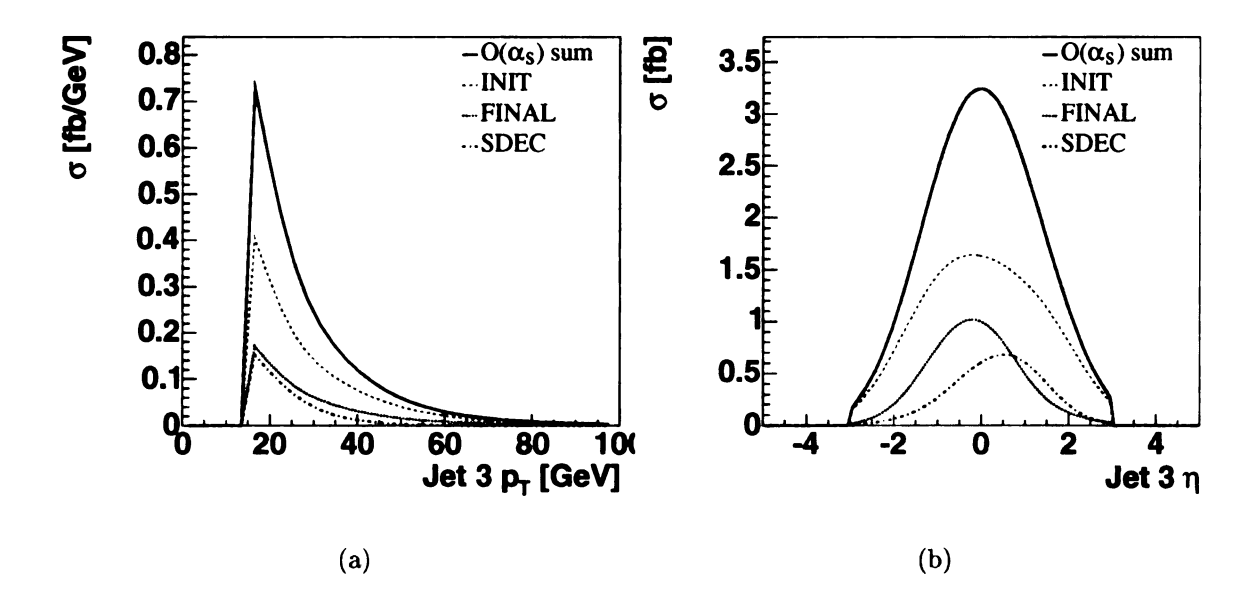


Figure 5.13: Transverse momentum (left) and pseudo-rapidity of the third jet after selection cuts for the various  $O(\alpha_s)$  contributions.

gluon in about 70% of the events after the loose set of cuts.

Note that production-stage emission is dominant over decay-stage emission because the decay contribution is determined not by the collider energy, but by the phase space of a 178 GeV top-quark decay. As expected, the  $E_T$  distribution is steeply falling for all contributions, but it extends to much higher  $E_T$  values for production-stage emission. The smaller values of  $E_T$  to which decay emission is constrained are again a consequence of the top decay kinematics. Recall that the top quarks are produced with relatively modest transverse momentum (cf. Fig. 5.8), so that gluons from the decay do not receive much of a boost. Note also that an increase in the  $E_T$  cut on the jet would result in a further reduction in relative size of the decay contribution compared to production. Fig. 5.13 also shows the distribution in pseudo-rapidity of the extra jet. Initial-state emission is relatively flat in pseudo-rapidity, as compared to the more central decay emission. This is consistent with our intuition that decay-stage radiation, being associated with the final-state

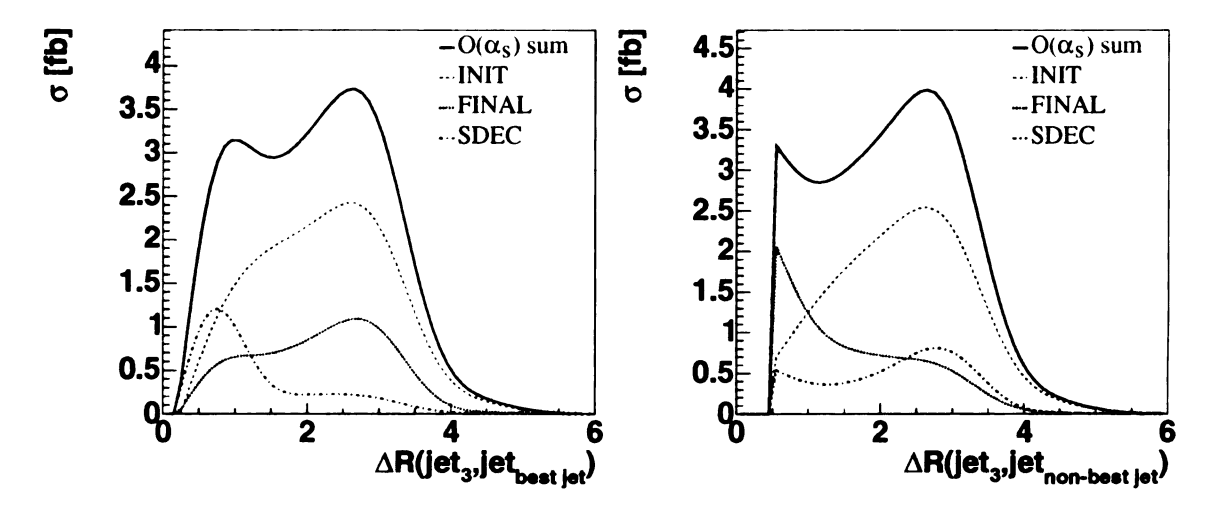


Figure 5.14: Distance between the third jet and the best-jet (left) and distance between the third jet and the non-best-jet (right) after selection cuts for the various  $O(\alpha_s)$  corrections.

particles - which tend to appear in the central pseudo-rapidity region - is also likely to be produced centrally. But this decay contribution is small and production-stage radiation dominates even in the central region. Also, final-state emission and decay emission have a tendency to follow the direction of the  $\bar{b}$ -jet and b-jet respectively, hence the decay  $O(\alpha_s)$  contribution peaks at a positive  $\eta$  value while the final state  $O(\alpha_s)$  contribution peaks at a negative  $\eta$  value, c.f. Fig. 5.4.

This tendency of decay-stage radiation to be associated with the final-state b quarks might lead one to expect that if the extra jet is "near" the b-jet it should be included in the mass reconstruction, and if it is not then it should be excluded. Fig. 5.14, which shows the distribution in  $\Delta R$  between the extra-jet and the best-jet, confirms that the decay-stage radiation peaks close to the best-jet, and production-stage radiation peaks farther away. Unfortunately, the production contribution is so large that it dominates even at the low  $\Delta R$  cutoff. A higher  $E_T$  cut on the jet would make this situation even worse. The best choice of what is "near" the b quark will therefore balance the competing effects of decay emission falling outside the cone and

production emission falling inside the cone. In Fig. 5.14, the equivalent distribution in  $\Delta R$  between the extra jet and the non-best-jet is also shown, where the production-stage radiation peaks close to the non-best-jet due to the effect of gluon radiation in the final state.

Tuning a prescription for dealing with the extra jet in s-channel single top events is further complicated because effects of multiple emission, hadronization, and detector resolutions will affect the result.

Finally, we point out that the above conclusion does not strongly depend on the choice of jet algorithm. We have checked that at the parton level using the Durham  $k_T$  algorithm [95, 96] leads to similar conclusion on the relative importance of the production- and decay-stage gluon emission.

#### 5.3.4.2 Angular Correlation Between the Extra Jet and the Best-Jet

While we cannot use the angular distance between the gluon jet and the b-jet to distinguish production-stage emission from decay-stage emission, it is nevertheless possible to separate the two using the best-jet algorithm.

The left-hand side of Fig. 5.15 shows the angular correlation  $\cos\theta$  between the gluon and the b quark at parton level before cuts. The right-hand side of the same figure shows the same correlation after event reconstruction between the third jet and the best-jet. In this case there is a clear separation between production-stage and decay-stage emission and the best-jet algorithm can be used to separate the two because only those events are included in the plot for which the best-jet algorithm consists of exactly two jets.

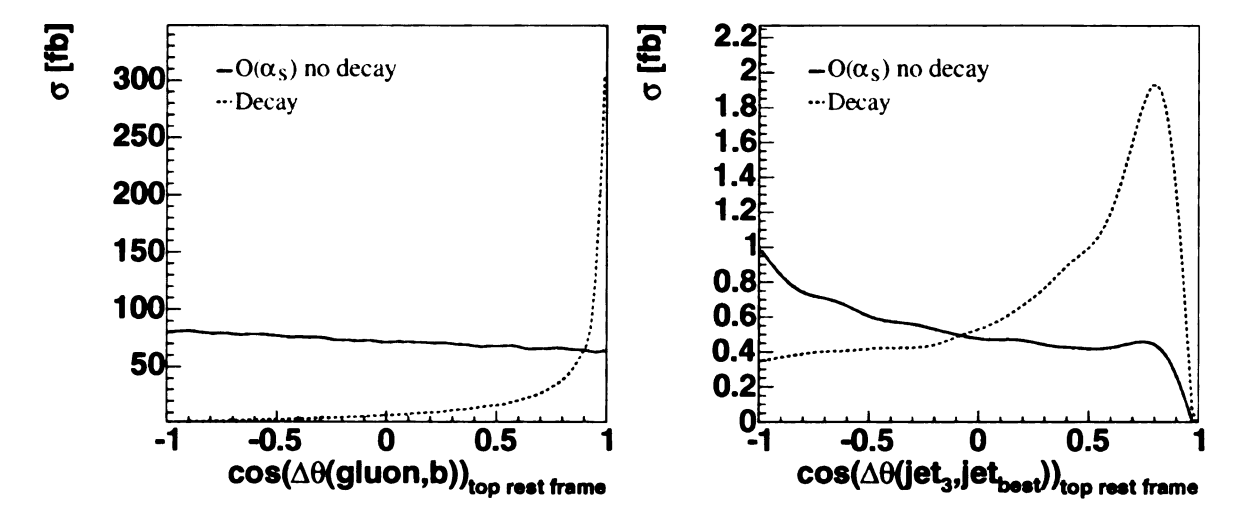


Figure 5.15: Angular correlation  $\cos\theta$  between the gluon and the b quark before any selection cuts using the full parton information (left) and between the third jet and the best-jet after selection cuts (right). The solid line shows all  $O(\alpha_s)$  contributions except for the decay part, while the dashed line shows only the  $O(\alpha_s)$  decay contribution.

# 5.4 Single Top Production as Background to SM Higgs Searches

The s-channel single top quark process also contributes as one of the major backgrounds to the SM Higgs searching channel  $q\bar{q} \to WH$  with  $H \to b\bar{b}$ . In this case it is particularly important to understand how  $O(\alpha_s)$  corrections will change distributions around the Higgs mass region.

Because of the scalar property of the Higgs boson, its decay products b and  $\bar{b}$  have symmetric distributions. Fig. 5.16 shows the invariant mass distribution of the b-jet,  $\bar{b}$ -jet pair. For a Higgs signal, this invariant mass of the two reconstructed b-tagged jets would correspond to a plot of the reconstructed Higgs mass. Thus, understanding this invariant mass distribution will be important to reach the highest sensitivity for Higgs boson searches at the Tevatron. The figure shows that at  $O(\alpha_s)$ , the invariant mass distribution not only peaks at lower values than at Born-level, it also drops off faster. This change in shape is particularly relevant in the region focused on by

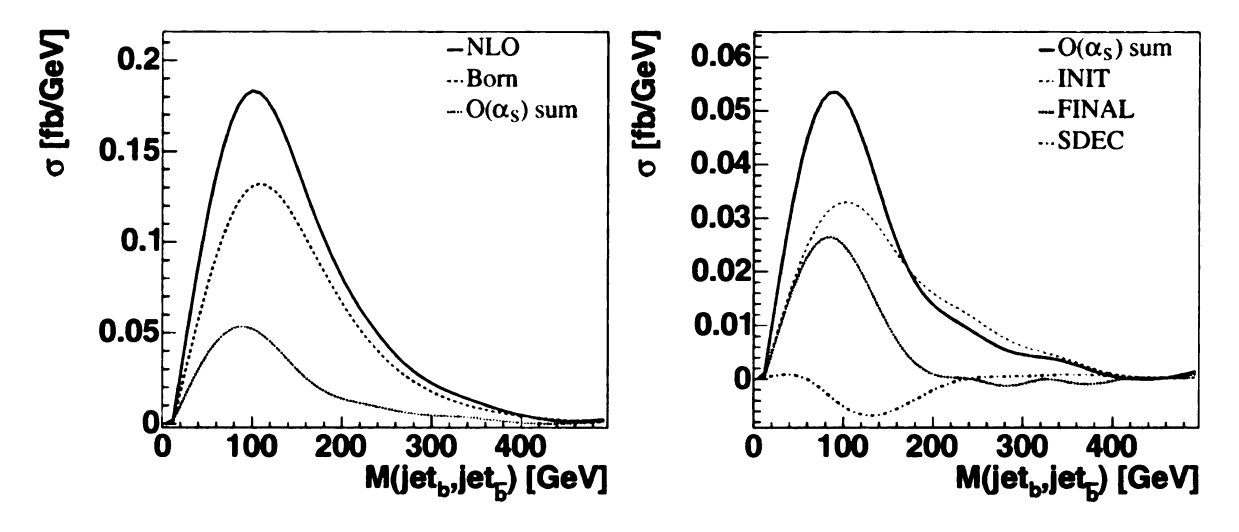


Figure 5.16: Invariant mass of the (b-jet,  $\bar{b}$ -jet) system after selection cuts, comparing Born-level to  $O(\alpha_s)$  corrections.

SM Higgs boson searches of  $80 \le m_{b\bar{b}} \le 140 {\rm GeV}$  which is also at the fb level. In particular the DEC contribution, while small overall, has a sizable effect in this region of the invariant mass and will thus have to be considered in order to make reliable background predictions for the Higgs boson searches.

Other kinematic distributions are also changing in shape when going from Born-level to  $O(\alpha_s)$ . Fig. 5.17 shows the distribution of  $cos\theta$  for the two b-tagged jets, where  $\theta$  is the angle between the direction of a b-tagged jet and the direction of the (b-jet,  $\bar{b}$ -jet) system, in the rest frame of the (b-jet,  $\bar{b}$ -jet) system. Experiments cannot distinguish between the b- and the  $\bar{b}$ -jets, we therefore include both the b-jet and the  $\bar{b}$ -jet in the graph. This distribution is generally flat at Born-level, with a drop-off at high  $cos\theta$  due to jet clustering effects, and a drop-off at negative  $cos\theta$  due to kinematics. The  $O(\alpha_s)$  corrections change this distribution significantly and result in a more forward peak of the distribution, similar to what is expected in Higgs boson production.

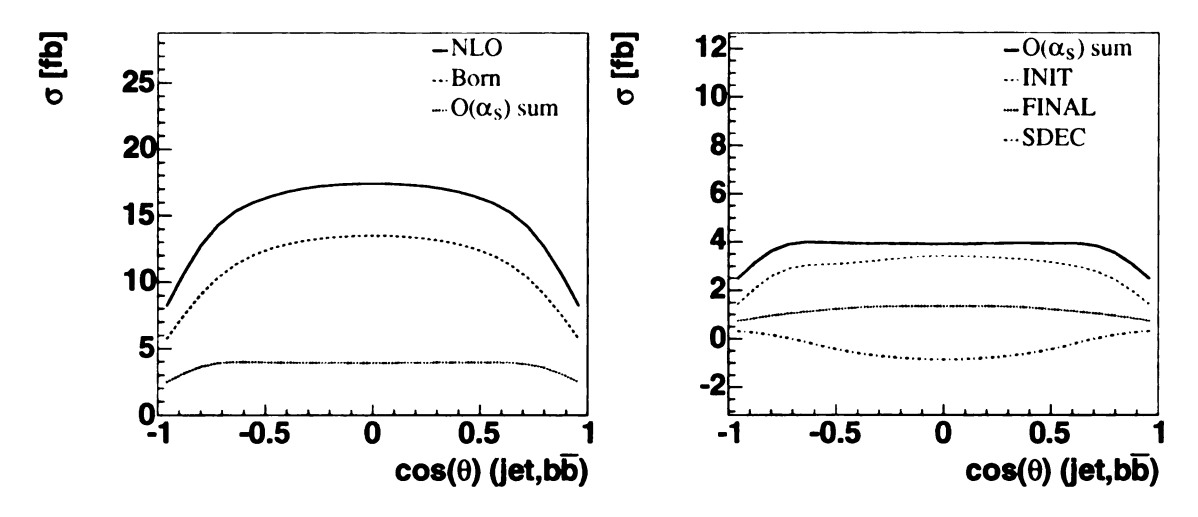


Figure 5.17: Angular distance  $cos\theta$  between a b-tagged jet and the (b jet,  $\bar{b}$  jet) system after selection cuts, comparing Born-level to  $O(\alpha_s)$  corrections.

### 5.5 Conclusion

We have presented a next-to-leading order study of s-channel single top quark events at the Tevatron, including  $\mathcal{O}(\alpha_s)$  QCD corrections to both the production and decay of the top quark. To obtain an accurate prediction of the inclusive rate of s-channel single top production, a "modified" narrow width approximation was adopted to link the production of the top quark with its decay (and thus preserve top quark spin information) instead of the usual narrow width approximation. In the former, a Breit-Wigner distribution of top quark mass is generated in the phase space generator of the Monte Carlo program, and the generated mass is also used to calculate the scattering matrix elements. Hence, the effect of the top quark width is included. In the latter, a fixed value of top quark mass is used. The impact of kinematical cuts on the acceptances has been studied for several different sets of cuts. We found that the difference between Born level and NLO acceptances is about 5% for two different sets of  $p_T$  and  $p_T$  cuts. This difference becomes significantly larger when changing the jet clustering cone size and jet-lepton separation cut  $R_{cut}$  from 0.5 to 1.0. Consequently,

a constant K-factor cannot be used to normalize Born-level distributions to NLO, especially for large values of  $R_{cut}$ .

We categorize the  $\mathcal{O}(\alpha_s)$  contributions to the s-channel single top process into three gauge invariant sets: the initial state corrections, the final state corrections and the top quark decay corrections. The  $\mathcal{O}(\alpha_s)$  corrections are significant in size and contribute over 40% of the inclusive cross section at NLO, a large fraction of which in events with three reconstructed jets in the final state. They also affect the shape of some of the important kinematical distributions that might be used experimentally to separate the s-channel single top signal from the various backgrounds. Among the higher order QCD corrections, the initial state correction dominates over the corrections from the final state and top decay processes in all inclusive single particle kinematical distributions. This implies that in particular the initial state soft gluon resummation effects need to be modeled properly in single top event generators. We have also found that the  $\mathcal{O}(\alpha_s)$  decay contribution, while small in size, has a significant impact on several distributions.

In order to study top quark properties such as the top quark polarization, we need to reconstruct the top quark by combining the reconstructed W boson with one of the jets in the event. There is an ambiguity in the choice of jet for this reconstruction due to the presence of two b jets in the event (the quark from the top quark decay and the  $\bar{b}$  quark produced with the top quark). We use two different methods to resolve this ambiguity: the leading jet (highest  $p_T$  jet) and the best-jet (giving a Wj invariant mass closest to 178 GeV). Our study shows that the best-jet algorithm identifies the correct jet in about 80% of the events while the leading jet is the correct jet in only 55% of the events. We thus choose the best-jet algorithm to explore kinematical correlations in the event.

The top spin correlation is examined in both the helicity basis and optimal basis. At parton level, without any kinematical cuts, both bases show strong correlations, with a polarization fraction of 98% in the optimal basis and 82% in the helicity basis. The measured polarization as well as the difference in fraction of polarization between the optimal basis and the helicity basis is reduced after event reconstruction due to the event selection cuts and the top quark reconstruction procedure (imperfect W reconstruction). It is further reduced by the  $\mathcal{O}(\alpha_s)$  corrections, resulting in a fraction of polarization of about 70% in both basis at NLO.

As a major irreducible background to  $W^{\pm}H$  searches, the s-channel single top quark process needs to be well understood in order to discover the Higgs boson or set a bound on the Higgs boson mass. We showed that the  $O(\alpha_s)$  corrections have an effect on distributions that are used in  $W^{\pm}H$  searches, in particular in the Higgs mass region 115 GeV  $\leq m_H \leq$  130 GeV. The contribution from the top quark decay process, has a sizable effect in this region of the invariant mass distribution of the b and  $\bar{b}$  jets. The decay contribution also affects the shape of other kinematical distributions, and reliable background predictions in Higgs boson searches will therefor need to include higher order QCD corrections.

# Chapter 6

# Phenomenology: t-channel

In this chapter we explore the final state objects of t-channel single top quark events. Although the W-boson from the top quark decay can decay in both leptonic and hadronic modes, we focus only on the leptonic decay mode in this study because the all-jet production mode of single top quark events is difficult to observe experimentally. Therefore, the signature of t-channel single top quark events which is accessible experimentally consists of one charged lepton, missing transverse energy, together with two or three jets. Since we are studying the effects of NLO QCD radiative corrections on the production rate and the kinematic distributions of single top quark events at the parton level in this work, we do not include any detector effects, such as jet energy resolution or b-tagging efficiency. Only an approximation of kinematic acceptances of a generic detector are considered. Since the Tevatron is  $p\bar{p}$  collider, and  $p\bar{p}$  is a CP-even state, the production cross sections for  $q\bar{t}(j)$  at the Tevatron are the same as those for  $t\bar{q}(j)$  (when ignoring the small CP violation effect induced by the CKM mixing matrix in quarks). For simplicity we therefore only consider distributions of t-channel single top quark events in this work in which a t quark (not including  $\bar{t}$ ) decays into  $W^+(\to \ell^+ \nu)$  and a b quark. In this section, we first present the event topology of the t-channel single top process, and then introduce a jet finding algorithm and the various kinematical cuts in order to study the acceptance.

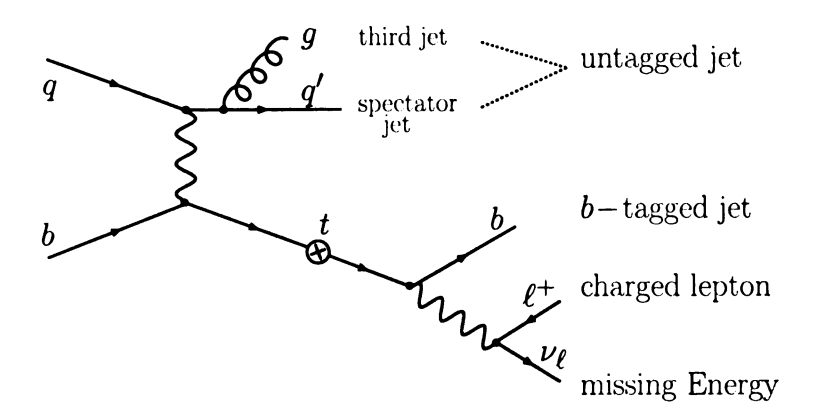


Figure 6.1: Pictorial illustration of the notation used in this paper.

## 6.1 Event Topology

At tree level, the collider signature of the t-channel single top process includes two jets (one b-tagged jet from the b quark from the top quark decay, and one non-b-tagged jet from the light quark), one charged lepton, and missing transverse energy  $(\cancel{E}_T)$  in the final state. This signature becomes more complicated beyond tree level, as Fig. 6.1 indicates. The light quark jet is also called "spectator jet", and the label "untagged jet" refers to all jets which do not contain a b or  $\bar{b}$  quark.

At NLO, besides the charged lepton and  $E_T$ , there may be two jets (one *b*-tagged jet and one untagged jet) as for the Born-level, or there may be three jets. The flavor composition of the three-jet final state depends on the origin of the third jet. When it is a gluon or anti-quark (cases (a-c) in Fig. 6.2), there is one *b*-tagged jet and two untagged jets. When it is a  $\bar{b}$  quark (case (d) in Fig. 6.2, also called *W*-gluon fusion), there are two *b*-tagged jets and one untagged jet. Therefore, prescriptions are needed to identify the *b* jet from the top quark decay and the light quark jet produced with the top quark.

In our study, we differentiate the following three cases:

1. Born-level-type exclusive two-jet events (containing the b quark and the light

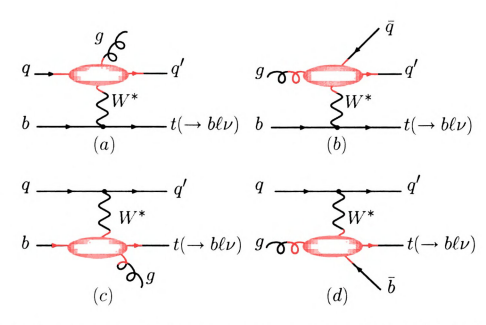


Figure 6.2: Representative diagrams of the real emission corrections for the t-channel single top process: (a) and (b) represent the real radiative corrections to the LIGHT quark line, while (c) and (d) represent the real radiative corrections to the HEAVY quark line. The NLO QCD corrections are indicated by the large shaded ellipse. Detailed Fevnman diagrams can be found in Fig. 3.2 and Fig. 3.3.

#### quark):

In Born-level type events, i.e. without an additional hard jet, the final state is given by the b jet from the top quark decay and the light quark jet produced with the top quark. Experimentally, this configuration is easily reconstructed because the b-tagged jet is identified as the b quark, and the untagged jet is assigned to the spectator jet. We note that in our phenomenology study to be presented in Sec. 6.3 we shall concentrate on inclusive two-jet events and exclusive three-jet events.

Exclusive three-jet events with one b jet (containing the b quark, the light quark, and a gluon or anti-quark):

When the radiated gluon is reconstructed as a separate jet in the LIGHT, TDEC, or HEAVY corrections, the final state contains one b jet and two other jets. As shown later, the transverse momentum and energy differences can be used to separate the spectator jet from the gluon jet (third jet). The transverse momentum of the spectator jet, which comes from the initial quark (q) after emitting the effective W-boson, peaks around  $\sim M_W/2$ , thus its energy is large. In comparison, the transverse momentum of the gluon jet is small. Due to the collinear enhancement, the resolved gluon jet prefers to move along the beam line direction at smaller transverse momentum  $(p_T)$  for both the LIGHT and HEAVY corrections, and along the b quark moving direction for the TDEC correction.

3. Exclusive three-jet events with one b jet and one  $\bar{b}$  jet (containing the b quark, the light quark, and a  $\bar{b}$  quark):

This final state is produced in the W-gluon fusion process, case (d) of Fig. 6.2. In this case, the spectator jet can be uniquely identified, but the b jet from the top decay cannot because heavy flavor tagging algorithms do not distinguish b jets from  $\bar{b}$  jets experimentally. Although the likelihood of tagging two b-jets is smaller than that of tagging a single b-jet, requiring two b-tagged jets will suppress the QCD and W+jets backgrounds significantly. We again can use transverse momentum differences to separate b jets from  $\bar{b}$  jets. The b jet from the top quark decay has a transverse momentum peaking around  $m_t/3$ , while the  $\bar{b}$  jet from gluon splitting tends to move along the beam line (the gluon-moving direction) due to the collinear enhancement and is much softer. These kinematic differences also enable us to separate the t-channel process from the s-channel process, recalling that in the s-channel process, both the b jet and the  $\bar{b}$  jet are preferentially produced at central rapidity and large  $p_T$ .

The unique signature of the t-channel single top process is the spectator jet in the forward direction, which can help to suppress the copious backgrounds, such as  $Wb\bar{b}$ 

and  $t\bar{t}$  production. Studying the kinematics of this spectator jet is important in order to have a better prediction of the acceptance of t-channel single top quark events and of the distribution of several important kinematic variables. In this work, we study the impact of the NLO QCD corrections on the kinematic properties of the spectator jet. As pointed out in Ref. [26], in the effective-W approximation, a high-energy t-channel single top quark event is dominated by a longitudinal W boson and the b quark fusion diagram. It is the same effective longitudinal W boson that dominates the production of a heavy Higgs boson at high energy colliders via the W-boson fusion process. For a heavy SM Higgs boson, the longitudinal W boson fusion process dominates the Higgs boson production rate. Therefore, it is also important to study the kinematics of the spectator jet in t-channel single top quark events in order to have a better prediction for the kinematics of Higgs boson events via the WW fusion process, i.e.  $q\bar{q}(WW) \to Hq'\bar{q}'$  at hadron colliders.

# 6.2 Acceptance

In order to meaningfully discuss the effects of gluon radiation in single top quark events, we must define a jet as an infrared-safe observable. In this study, we adopt the cone-jet algorithm [92] as explained in Chapter 5.1. More specifically, we adopt the E-scheme cone-jet approach (4-momenta of particles in a cone are simply added to form a jet) with radius  $R = \sqrt{\Delta\eta^2 + \Delta\phi^2}$  in order to define b, q and possibly extra  $g, \bar{q}$ , or  $\bar{b}$  jets, where  $\Delta\eta$  and  $\Delta\phi$  are the separation of particles in the pseudo-rapidity  $\eta$  and the azimuthal angle  $\phi$ , respectively. For reference, we shall consider both R=0.5 and R=1.0. The same R-separation will also be applied to the separation between the lepton and each jet.

The kinematic cuts imposed on the final state objects are:

$$P_T^{\ell} \ge 15 \,\mathrm{GeV}$$
 ,  $|\eta_{\ell}| \le \eta_{\ell}^{max}$ ,  
 $E_T \ge 15 \,\mathrm{GeV}$  ,  $|\eta_j| \le \eta_j^{max}$ ,  
 $E_T^j \ge 15 \,\mathrm{GeV}$  ,  $|\eta_j| \le \eta_j^{max}$ ,  
 $\Delta R_{\ell j} \ge R_{cut}$  ,  $\Delta R_{jj} \ge R_{cut}$ , (6.1)

where the jet cuts are applied to both the b- and light quark jets as well as any gluon or antiquark jet in the final state. Two lepton pseudo-rapidity cuts are considered here: a loose version with  $\eta_{\ell}^{max} = 2.5$  and a tight version with  $\eta_{\ell}^{max} = 1.0$ . Similarly, loose and tight cuts are also considered for the jet pseudo-rapidity,  $\eta_{j}^{max} = 3.0$  and  $\eta_{j}^{max} = 2.0$ , respectively. The minimum transverse energy cuts on the lepton as well as the jets is 15 GeV. Each event is furthermore required to have at least one lepton and two jets passing all selection criteria. The cut on the separation in R between the lepton and the jets as well as between different jets is given by  $R_{cut}$  which is is chosen to be 0.5 (or 1.0).

In Table 6.1, we show the single top production cross sections in fb for the loose and tight set of cuts listed in Eq. (6.1) for the different subprocesses. A larger value for  $R_{cut}$  reduces the acceptance significantly mainly because more events fail the lepton-jet separation cut. While this is only a 13% reduction at the Born-level, the difference grows to 25% at NLO. Hence, a smaller cone size is preferred in order to keep the acceptance at a high level. For events with at least three jets, imposing a harder cut on the transverse momentum of each jet ( $E_{Tj} > 30 \,\text{GeV}$ ) decreases the contribution from the LIGHT and HEAVY corrections by a factor of 3 to 4, but the contribution from the TDEC correction by more than a factor 6. This large reduction occurs because the top quark mass sets the scale for the top quark decay contribution rather than the invariant mass of tq' system, resulting in a softer jet  $E_T$  spectrum for

σ [fb]		LO	NLO	Heavy	Light	Decay
Tevatron (a)	tq + tqj	65.6	64.0	4.9	-3.4	-0.59
	$tq + tqj, E_{Tj} > 30 \text{GeV}$	46.3	44.0	4.2	-3.3	-1.7
	tqj		25.3	15.5	5.1	4.8
	$tqj, E_{Tj} > 30 \mathrm{GeV}$		7.4	5.4	1.3	0.75
Tevatron (b)	tq + tqj	56.8	48.1	-0.45	-4.4	-2.2
	$tq + tqj, E_{Tj} > 30 \text{GeV}$	40.1	33.3	0.0	-3.3	-2.1
	tqj		14.8	10.8	2.2	1.7
	$tqj, E_{Tj} > 30 \text{GeV}$		4.5	3.7	0.58	0.20
Tevatron (c)	tq + tqj	31.1	34.0	5.8	-2.8	0.82
	$tq + tqj, E_{Tj} > 30 \text{GeV}$	24.4	24.2	3.8	-2.7	-0.7
	tqj		11.4	6.7	2.4	2.3
	$tqj, E_{Tj} > 30 \text{GeV}$		3.9	2.8	0.74	0.41

Table 6.1: The t-channel single top production cross section at the Tevatron (in fb) for different subprocesses under various cut scenarios: (a) is the loose version with  $\eta_l^{max} = 2.5$ ,  $\eta_j^{max} = 3.0$ , and  $R_{cut} = 0.5$ , (b) is the loose version with a larger

jet clustering cone size (and jet-lepton separation cut) of  $R_{cut}=1.0$ , and (c) is the tight version of cuts with  $\eta_l^{max}=1.0$ ,  $\eta_j^{max}=2.0$ , and  $R_{cut}=0.5$ . The first two columns show the Born-level and full NLO cross sections, the last three columns show the contributions from the different  $O(\alpha_s)$  processes. The decay branching ratio  $t \to bW(\to e\nu)$  is included.

the TDEC correction (cf. Fig. 6.21, to be discussed in Sec. 6.3.4).

Figure 6.3 shows how the observed cross section changes as a function of the jet  $E_T$  cut when applying the loose set of cuts, including a requirement of there being at least two jets in the event. The figure also shows the dependence of the fraction of two-jet events and three-jet events on the jet  $E_T$  cut. At the Born-level, there are only two-jet events, whereas  $O(\alpha_s)$  corrections can produce an additional soft jet. The fraction of events with these additional jets is low only for very high jet  $E_T$  thresholds. For typical jet  $E_T$  thresholds considered by experiments of 15 GeV to 25 GeV these jets add a significant contribution. As expected, the effect is not quite as large when only jets within a very small  $\eta$  range are considered because the extra jet typically has higher  $\eta$ . In order to study  $O(\alpha_s)$  effects it is thus important to set the jet  $\eta$  cut as high as possible and the jet  $E_T$  cut as low as possible.

As mentioned before, the event rate for single top quark events is small and it is important for experiments to maximize their acceptance. We will thus use the loose set of cut values for the following discussion:  $\eta_l^{max} = 2.5$ ,  $\eta_j^{max} = 3.0$ , and  $R_{cut} = 0.5$ ,  $E_{Tj}^{min} = 15$  GeV, cf. Eq. (6.1).

## 6.3 Single Top Quark Event Distributions

In this section we examine the kinematic properties of single top quark events. As discussed in the previous section, the signature of the t-channel process includes at least one b-tagged jet, one untagged jet, one charged lepton, and missing energy. At the Born-level, it is straightforward to identify the single top final state using the b-tagged jet and the reconstructed W boson to reconstruct the top quark and identifying the spectator jet as the light quark. At NLO, however, an additional jet is radiated, which will complicate the reconstruction of the top quark final state. First, this is

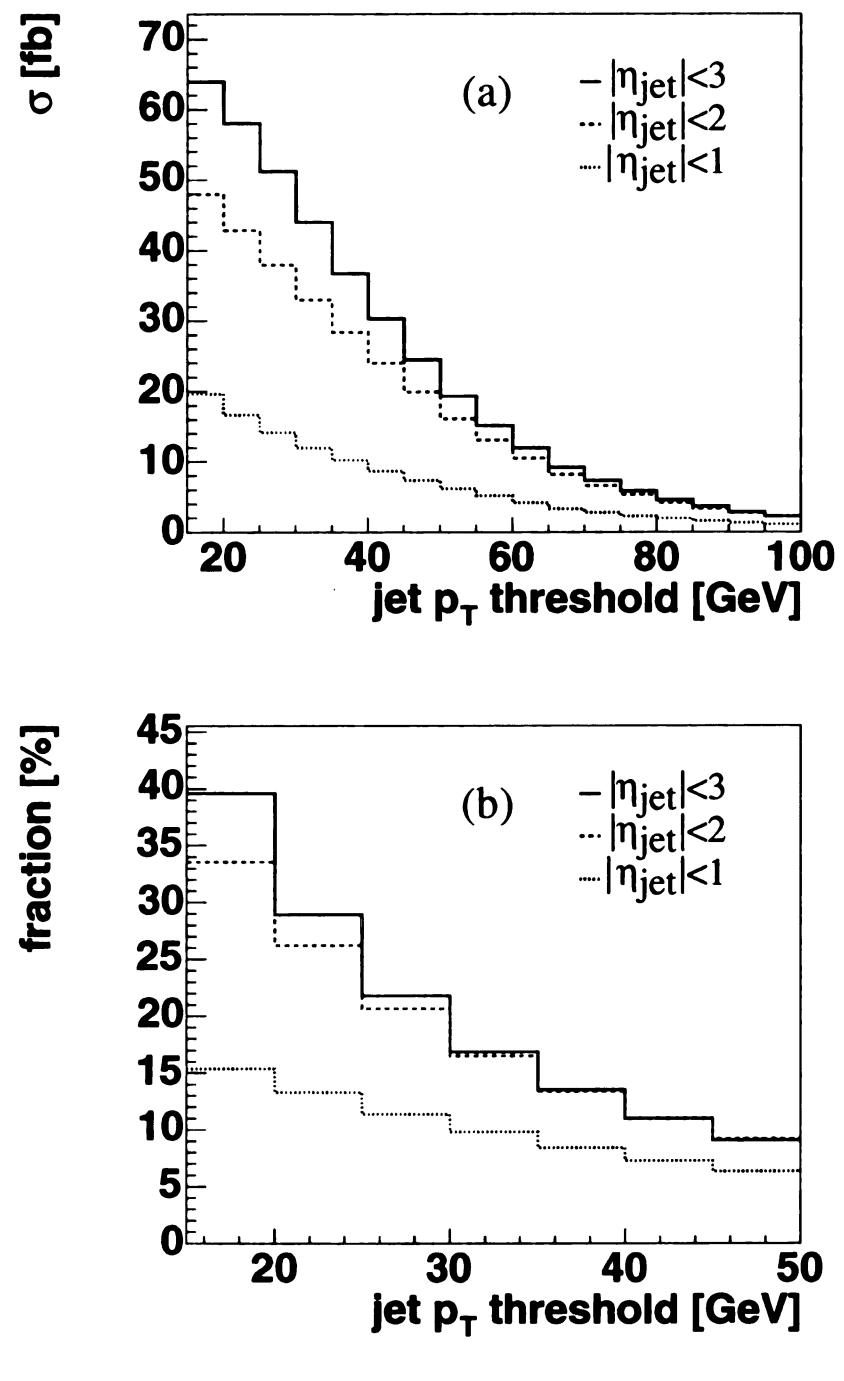


Figure 6.3: Cross section and fraction of three-jet events at NLO for varying jet  $p_T$  cuts, requiring only that  $n_{jets} \geq 2$ , and not making any cuts on the electron or neutrino. Shown is the total cross section for events with two or three jets as a function of the jet  $E_T$  cut for three different jet pseudo-rapidity cuts (a) and the fraction of three-jet events as a function of the jet  $p_T$  for different jet pseudo-rapidity cuts (b). The lowest threshold considered is 15 GeV.

because the additional jet can be either a b-tagged jet or an untagged jet. When it is the b-tagged jet, we need to select the correct b quark from the two possible jets in the finial state to reconstruct the top quark. When it is the untagged jet, we need to select the correct spectator jet. Second, the additional untagged jet can come from either the production or the decay of the top quark. Production-stage emission occurs before the top quark goes on shell and decay-stage emission occurs only after the top quark goes on shell. In production emission events, the W boson and b quark momenta will combine to give the top quark momentum, while in the decay emission event the gluon momentum must also be included in order to reconstruct the top quark momentum properly. To find the best prescription for identifying the correct b jet and spectator jet, we first examine various kinematic distributions of the final state particles. We then investigate two top quark reconstruction prescriptions: using the leading b-tagged jet and the best jet algorithm. Choosing the b-tagged jet prescription, we can also improve the reconstruction efficiency for the W boson. We then study the effects of NLO corrections on distributions concerning the reconstructed top quark, in particular spin correlations between the final state particles. Finally, we explore the impact of the radiated jet in exclusive three-jets events. We use only the loose set of cuts to maximize the efficiency when examining the distributions and efficiencies in detail.

## 6.3.1 Final State Object Distributions

### 6.3.1.1 Charged Lepton and Missing Transverse Energy

In this section we examine various kinematic distributions of final state objects after event reconstruction and after applying the loose set of cuts, cf. Table 4.2 and Eq. (6.1). We concentrate on inclusive two-jet events in this section because they give more reliable infrared-safe predictions.

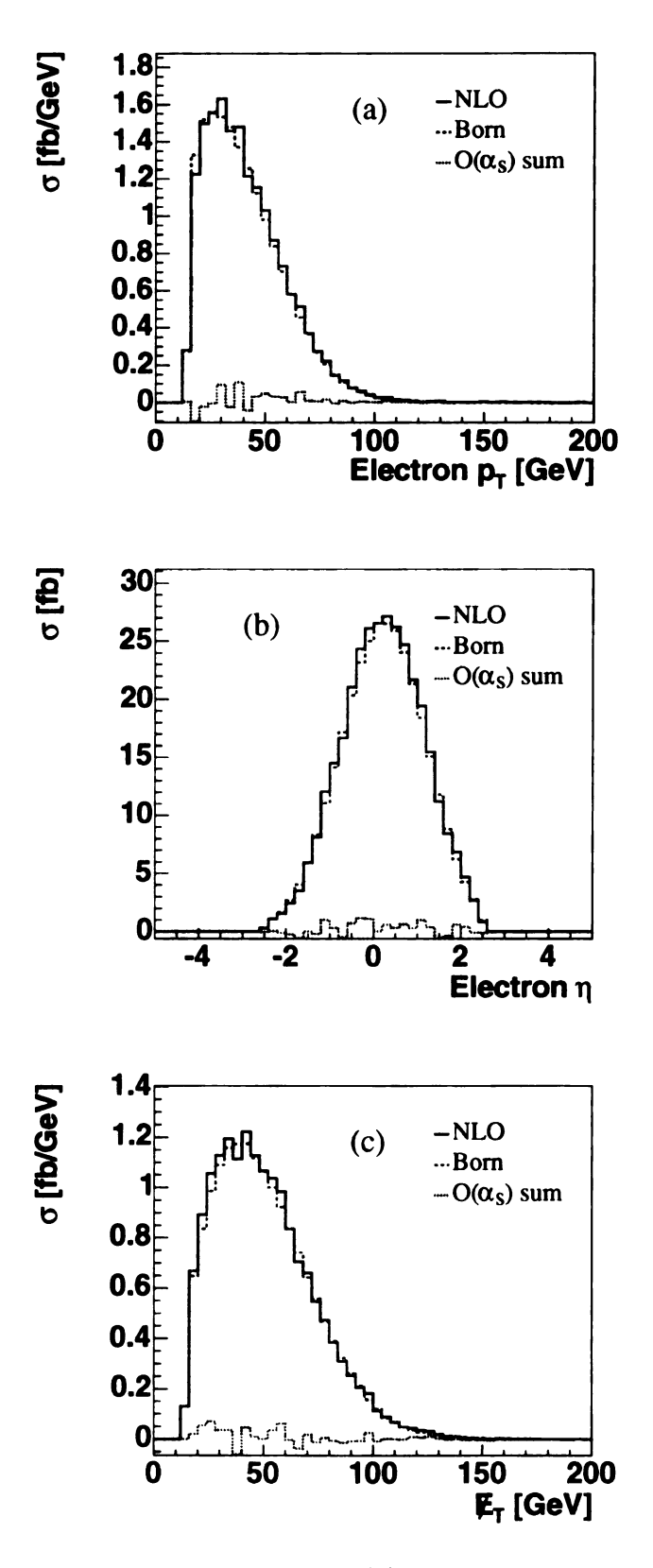


Figure 6.4: The transverse momentum  $p_T$  (a) and pseudo-rapidity  $\eta$  (b) distributions of the electron and the missing transverse energy  $\not\!\!E_T$  (c) after selection cuts, comparing Born-level to  $O(\alpha_s)$  corrections.

Figures 6.4 (a) and (c) show the transverse momentum of the electron and the missing transverse energy  $\mathbb{E}_T$ , respectively. As expected, because they are leptons and not quarks, the change in shape when going from Born-level to NLO is not very large for the electron or the missing transverse energy. The pseudo-rapidity distribution of the electron is given in Fig. 6.4(b). This distribution widens at NLO, but again the effect is small because the overall  $O(\alpha_s)$  contribution to the event rate is small, cf. Table 4.2. We note that the peak position of the  $\mathbb{E}_T$  distribution is at a higher value than that of the electron  $p_T$  because the neutrino from the W-boson decay moves preferentially along the direction of the top quark. This is due to the left-handed nature of the charged current interaction and can easily be seen when examining the spin correlations between the charged lepton and the top quark in the top quark rest frame. We will comment more on this subject in Sec. 6.3.3.

### 6.3.1.2 Spectator Jet

The differences between the s-channel and t-channel single top processes at the Born-level are that the former has two b-taggable jets in the final state (the b quark and the  $\bar{b}$  quark) while the latter only has one b-taggable jet and also has one light quark jet. This untagged jet (spectator jet) is a unique feature of the t-channel process which can be used to disentangle t-channel single top quark events from the copious backgrounds. Therefore, its kinematic distributions need to be well studied, especially the impact of  $O(\alpha_s)$  corrections on the features which make this jet a unique signature, such as the spectator jet pseudo-rapidity, cf. Fig. 6.5.

The pseudo-rapidity distribution of the spectator jet is asymmetric because the Tevatron is a  $p\bar{p}$  collider [26]. In order to produce a heavy top quark decaying to a positively charged lepton, the valence quark from the proton is most important, implying that the light quark will tend to move in the proton direction. We define

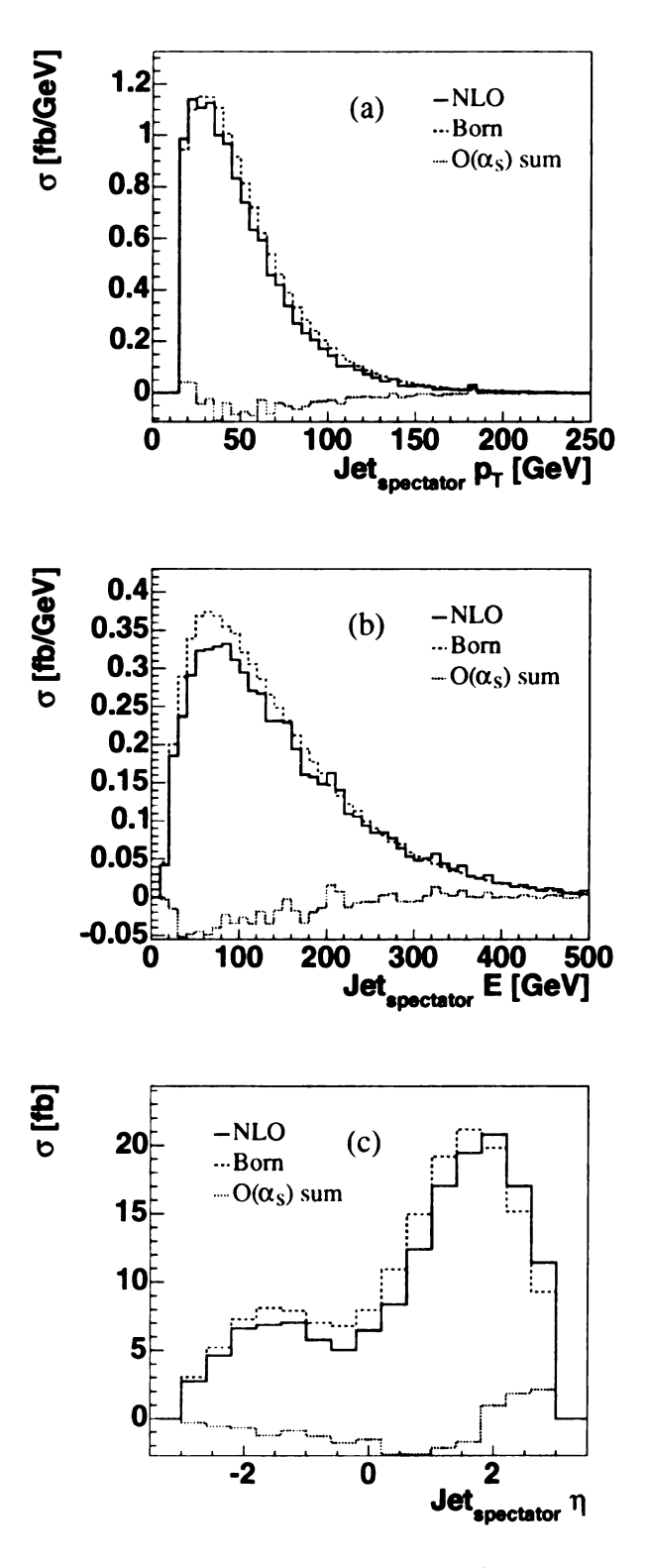


Figure 6.5: Transverse momentum  $p_T$  (a), energy E (b) and the pseudo-rapidity  $\eta$  (c) of the spectator jet after selection cuts, comparing Born-level to  $O(\alpha_s)$  corrections.

the positive z-direction to be the proton direction in the laboratory frame, thus the pseudo-rapidity of the spectator jet will tend be positive. Similarly, the spectator jet in an anti-top quark event produced from the t-channel process will preferably be at a negative pseudo-rapidity due to the large anti-up quark parton distribution inside the antiproton. The  $O(\alpha_s)$  corrections shift the spectator jet to even more forward pseudo-rapidities due to additional gluon radiation. However, since the  $O(\alpha_s)$  corrections are small compared to the Born-level contribution, the spectator jet pseudorapidity distribution only shifts slightly. As Fig. 6.6 shows, the LIGHT and HEAVY contributions have almost opposite behavior. The former shifts the spectator jet to even higher pseudo-rapidities, while the later shifts it more to the central rapidity region. This behavior is due to two different effects, as illustrated in Fig. 6.6 (b), in which "PA" denotes that the light quarks come from the proton while the bottom quarks from the anti-proton and vice versa for "AP". After separating the contributions by whether the light quark is from the proton or the antiproton, it can be seen that the HEAVY corrections shift the proton contribution down and the antiproton contribution up due to the slight change in acceptance caused by the additional jet. The LIGHT corrections show the opposite tendency. For the TDEC contribution, all corrections have similar shapes and the sum of them leaves the spectator jet pseudo-rapidity unchanged, as expected. After summing the negative soft-plusvirtual corrections with the real emission corrections, we obtain the result shown in Fig. 6.5, which shows that the  $O(\alpha_s)$  correction shifts the spectator jet to be in even more forward direction.

Besides its forward rapidity, the spectator jet also has large transverse momentum. Since it comes from the initial state quark after emitting the effective W boson, the transverse momentum peaks around  $\sim M_W/2$ , cf. Fig. 6.5. By comparison, the third jet is most often much softer, we can thus use  $p_T$  of the jet to identify the the

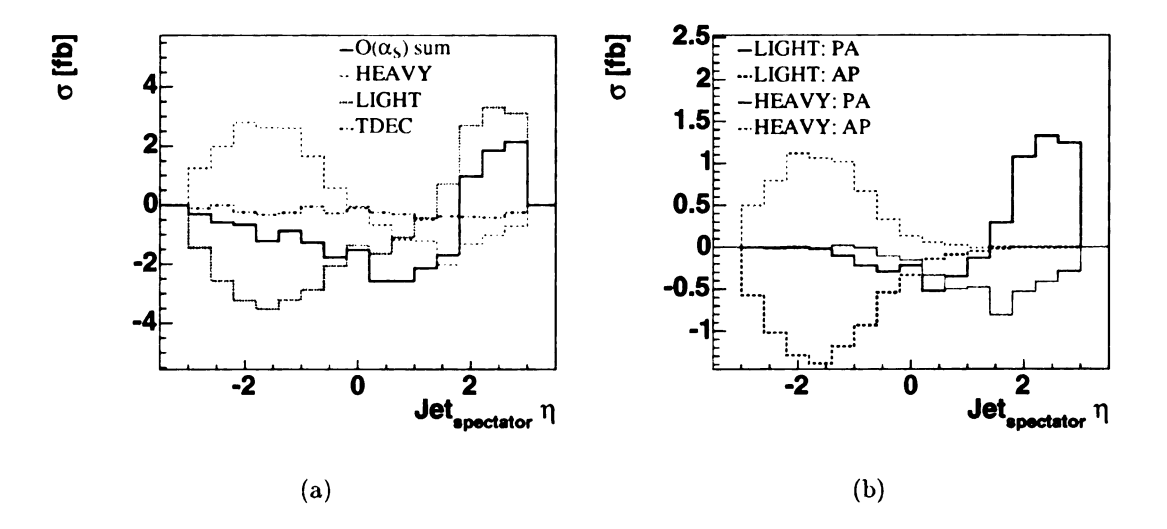


Figure 6.6: Each individual contribution of the  $O(\alpha_s)$  corrections to the spectator jet pseudo-rapidity, summed (a), separately for the case when the incoming up-type quark is from the proton and anti-proton (b). Here, "PA" and "AP" denotes the initial state light quark originating from proton and anti-proton, respectively.

spectator jet when considering exclusive three-jet events.

### **6.3.1.3** *b* Jet

Compared to the lepton and  $E_T$ , the effects of the  $O(\alpha_s)$  corrections on the reconstructed b jet are more pronounced. Figure 6.7 shows a comparison of the b jet  $p_T$  distribution between the Born-level and  $O(\alpha_s)$  corrections. The  $p_T$  distribution of the b jet is predominantly determined by the top quark mass and therefore peaks at  $\sim m_t/3$ . The NLO QCD corrections broaden the transverse momentum distribution and shift the peak position to lower values. The location of the mean of the distributions depends on the cuts that are applied because the different  $O(\alpha_s)$  corrections have different effects: in the case of the loose cuts it increases from 64 GeV at the Born-level to 62 GeV at full NLO. The LIGHT corrections shift the mean of the b jet  $p_T$  distribution up, the HEAVY corrections leave it mostly unchanged, and the

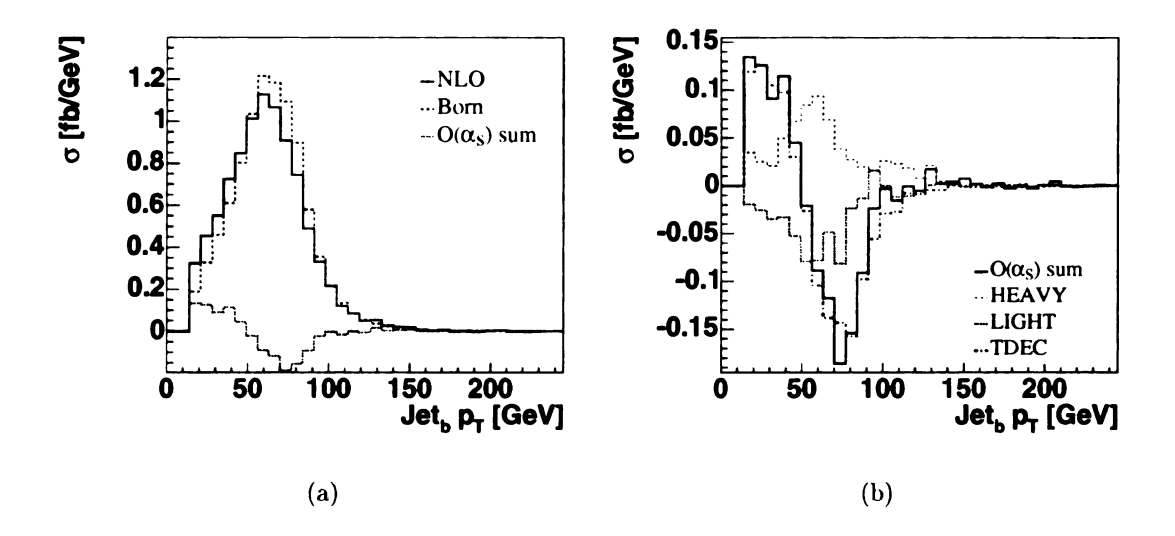


Figure 6.7: Transverse momentum  $p_T$  of the b jet after selection cuts, comparing Born-level to  $O(\alpha_s)$  corrections (a) and the individual  $O(\alpha_s)$  contributions (b).

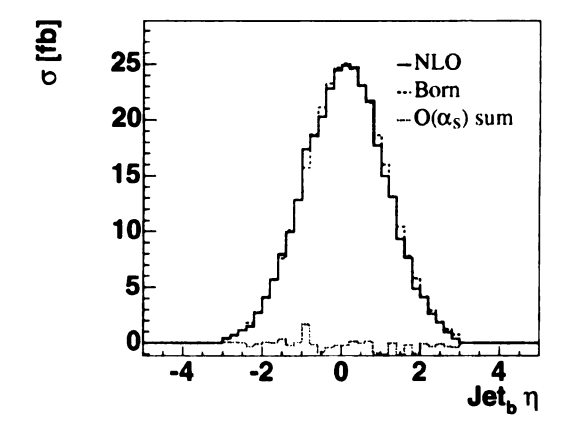


Figure 6.8: Pseudo-rapidity  $\eta$  of the *b*-jet after selection cuts, comparing Born level to  $O(\alpha_s)$  corrections.

TDEC corrections tend to shift it down. The b jet  $p_T$  distribution receives a large contribution from the TDEC corrections, as expected. When a gluon is radiated from the top quark decay, it tends to move along the b jet direction due to collinear enhancements and therefore shifts the b jet  $p_T$  distribution to the small  $p_T$  region, as shown in Fig. 6.7.

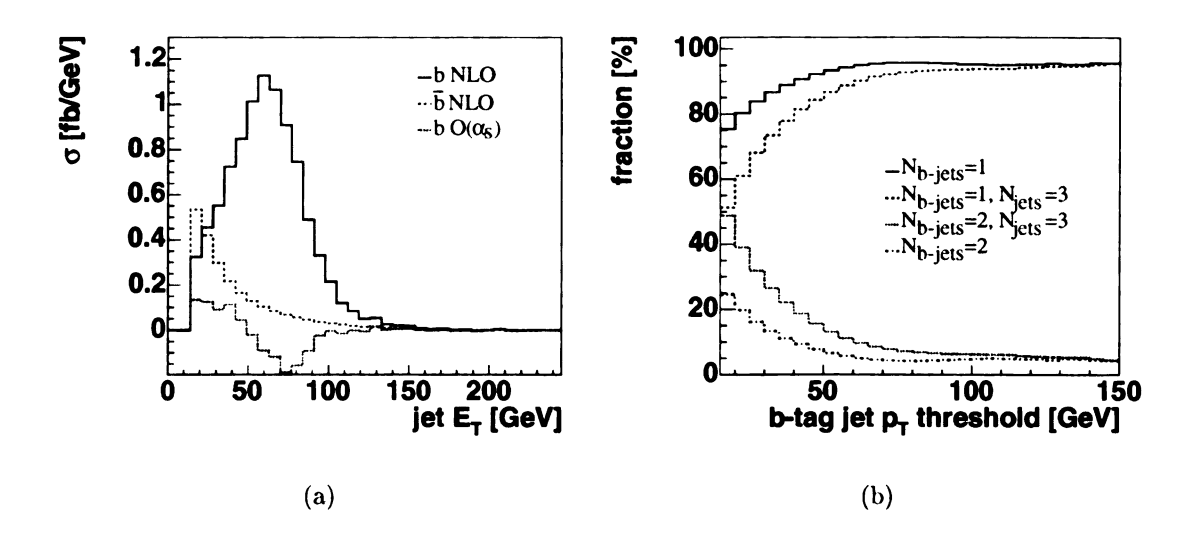


Figure 6.9: Momentum of the b and  $\bar{b}$  jets (a) and fraction of events with one or two b-tagged jets as a function of the jet  $p_T$  threshold, for both inclusive two-jet and exclusive three-jet events (b).

The b jet pseudo-rapidity distribution is less affected by the  $O(\alpha_s)$  corrections, as can be seen in Fig. 6.8. The top quark is so heavy that it is mostly produced in the central rapidity region and thus the b jet from its decay also peaks around a pseudo-rapidity of zero. The shape of the b jet pseudo-rapidity distribution remains almost unchanged compared to the Born-level because it comes from the top quark decay.

Figure 6.9 compares the momentum of the b jet and the  $\bar{b}$  jet at NLO and examines the fraction of events containing one or two b-tagged jets in the final state. Events with both b and  $\bar{b}$  jets originate from the W-gluon fusion subprocess,  $qg \to q'\bar{b}t(\to bW(\to \ell^+\nu))$ . While the fraction of events with two b-tagged jets is high for low jet  $p_T$ , it drops quickly. For a jet  $p_T$  above 50 GeV, the fraction of events with both b and  $\bar{b}$  jets is less than 5%. Figure 6.9 also shows that for exclusive three-jet events, the fraction of events with two b-tagged jets is much higher. About half of the events contain two b-tagged jets for the lowest threshold of 15 GeV, and the fraction only

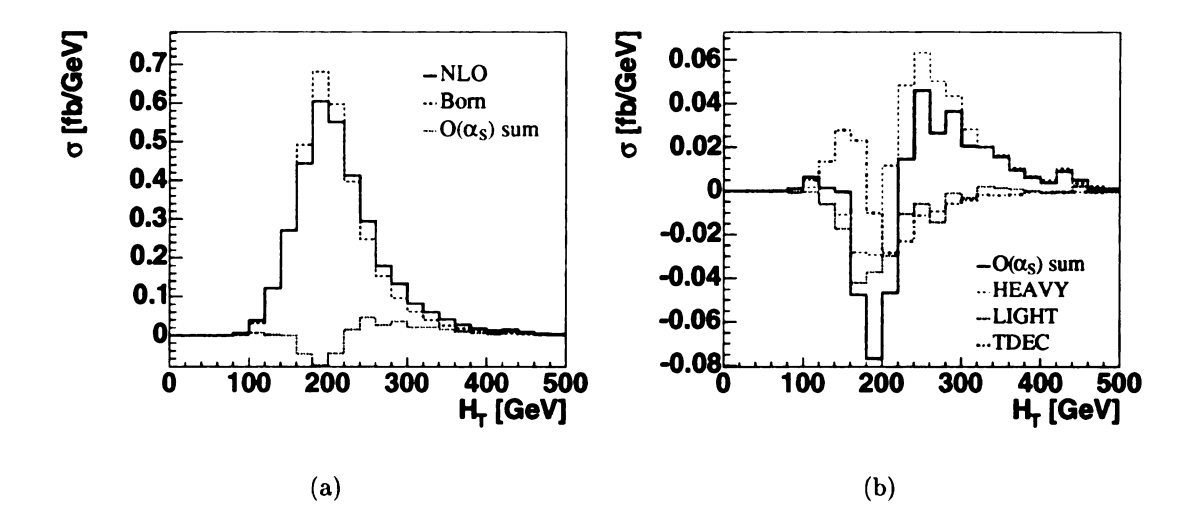


Figure 6.10: Total event transverse energy  $H_T$  after selection cuts, comparing Born level to  $O(\alpha_s)$  corrections (a) and the individual  $O(\alpha_s)$  contributions (b).

goes down to 5% when the jet  $p_T$  reaches about 140 GeV.

## **6.3.1.4** $H_T$ Distribution

The impact that different  $O(\alpha_s)$  corrections have on the  $p_T$  of the jets is also reflected in event-wide energy variables such as the total transverse energy in the event  $(H_T)$ , defined as

$$H_T = p_T^{lepton} + \not\!\!E_T + \sum_{jets} p_T^{jet}. \tag{6.2}$$

The distribution of  $H_T$  for t-channel single top quark events is shown in Fig. 6.10. The Born-level  $H_T$  distribution peaks around 200 GeV. Both the HEAVY and LIGHT contributions decrease the height of the peak and shift it to higher values, and all three  $O(\alpha_s)$  contributions broaden the distribution.

### 6.3.2 Event Reconstruction

When analyzing single top quark events we would like to take advantage not only of simple single-object kinematics but also of correlations between objects. In order to take full advantage of the correlations, we need to reconstruct the event completely, not just the final state jets but also intermediate particles, in particular the W-boson and the top quark.

The W boson can be reconstructed from the final state electron and the observed missing transverse energy,  $E_T$ . The lack of information about the beam-direction component of the neutrino momentum  $(p_z^{\nu})$  that would prevent this reconstruction is typically overcome by requiring that the invariant mass of the electron-neutrino system be equal to the mass of the W boson. This additional constraint results in two possible solutions for  $p_z^{\nu}$ . One usually follows the prescription given in Ref. [99] of choosing the solution which has the smaller  $|p_z^{\nu}|$ . This picks the correct  $p_z^{\nu}$  in about 70% of the events. The price paid for this method is that the W boson will blur the spin correlation in the reconstructed single top quark event. We will see later that we can improve on this by using a top mass constraint.

In order to reconstruct the top quark, the reconstructed W boson then needs to be combined with the b jet from the top quark decay. The challenge to overcome here is the proper identification of the b jet. In the s-channel single top process, we used the "best-jet" algorithm to find the correct b jet among the two possible b-tagged jets in the final state, making use of the known top quark mass ( $m_t = 178 \,\text{GeV}$ ) [56]. The effectiveness of the best-jet algorithm is mainly limited by the efficiency of the W boson identification method; if the W boson is not reconstructed properly, then identifying the b jet from the top quark decay becomes a random choice.

Unlike the s-channel processes, inclusive two-jet events of the t-channel single

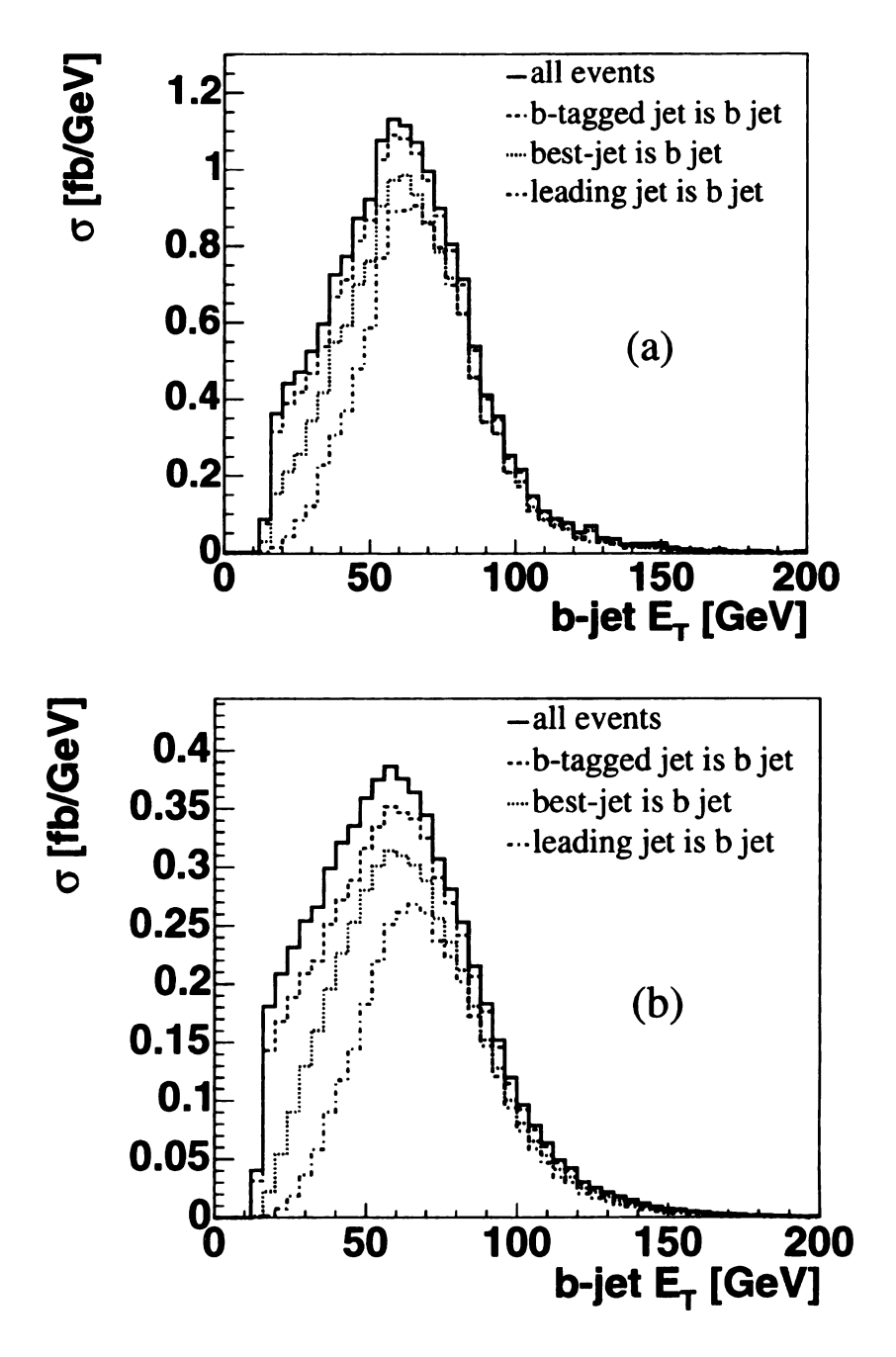


Figure 6.11: Transverse momentum of the b quark jet, for all events (solid histogram), only for those events for which the leading b-tagged jet corresponds to the b quark jet (dashed histogram), only for those events in which the best jet corresponds to the b quark jet (dotted histogram), and only for those events in which the leading jet corresponds to the b quark jet (dash-dotted histogram). The transverse momentum is shown for the inclusive two-jet sample (a) and for the exclusive three-jet sample (b).

top processes typically only contain one b-tagged jet in the final state, corresponding to the b quark from the top quark decay. Figure 6.11 shows a comparison of three different algorithms to identify the b jet from the top quark decay: a) using the leading jet (highest  $p_T$ ) in the event, b) using the leading b-tagged jet in the event, and c) using the best jet. The leading jet in this case could be either the b jet or the light quark jet, thus the efficiency for identifying the b-jet from top quark decay with method a) is rather low. The leading b-tagged jet is either the b jet from the top quark decay or the  $\bar{b}$  jet originating from the W-gluon fusion subprocess. Figure 6.11 shows that the leading b-tagged jet corresponds to the b quark from the top decay most of the time: it identifies the b quark correctly in 95% of the events in the inclusive sample after the loose selection cuts. We expect the efficiency to drop in the three-jet sample because of the additional  $\bar{b}$  quark in the final state. However, as shown in Fig. 6.9, the b jet from the top quark decay is much harder than the  $\bar{b}$  jet radiated from the initial state gluon. As a result, the leading b-tagged jet corresponds to the b quark from the top quark decay in 90% of the exclusive three-jet events. Figure 6.11 shows that this fraction is slightly smaller for low b jet  $p_T$  values, and reaches 100%above about 100 GeV. By comparison, the best jet corresponds to the b quark in only 80% of the events in the inclusive sample and about 72% of the events in the exclusive three-jet sample. We therefore choose the method of identifying the leading b-tagged jet as the b quark from the top decay. Having identified the b quark in this manner with no additional assumptions allows us to use it to reconstruct the top quark and the W boson more accurately, in particular to determine the longitudinal momentum of the neutrino  $(p_z^{\nu})$ . We reconstruct the W boson as above using a W mass constraint. We then identify the proper neutrino  $p_z^{\nu}$  by choosing the solution for which the invariant mass of the reconstructed W and the leading b-tagged jet is closest to the true top quark mass, i.e. 178 GeV.

This method identifies the correct neutrino  $p_z^{\nu}$  about 92% of the time at the Born-level and about 84% of the time at NLO. These efficiencies are slightly smaller than the b quark identification efficiencies shown in Fig. 6.11 due to the finite widths of the W boson and the top quark.

Figure 6.12 shows the invariant mass of the reconstructed top quark, comparing the different methods to identify the b quark and the W boson from the top quark decay. The top quark width is larger than it would be at parton level even though no kinematic smearing was applied in this study to mimic the detector effect. This is the result of using the reconstructed kinematics of the W boson (in particular the neutrino z-momentum) rather than parton level information. Furthermore, since the same reconstructed W boson was used for all curves in Fig. 6.12, differences among the individual curves are solely due to the jet choice used to reconstruct the top quark. Finally, because parton level information is used for the b jet curve, it functions as a reference and upper limit for the other methods.

Figure 6.12(a) shows the top mass reconstructed with the W boson using the standard method of choosing the smaller  $|p_z^{\nu}|$ . As expected, using the leading jet gives the worst performance, and using the leading b-tagged is a better choice. Given this choice for the neutrino, however, the best jet algorithm looks best because for those cases where the neutrino has been mis-reconstructed, the best jet algorithm sometimes chooses the wrong jet and thus it falsely appears to give well reconstructed top mass because the algorithm chooses an invariant mass close to 178 GeV. Figure 6.12(b) shows the top mass reconstructed with the W boson reconstructed from a top mass constraint. The overall height of the mass peak is higher in Fig. 6.12(b) than in Fig. 6.12(a), indicating that this method is able to reconstruct the W boson and b jet correctly more often. It can also be seen that for this choice of W boson reconstruction, we can properly reconstruct the true top quark with the leading b-

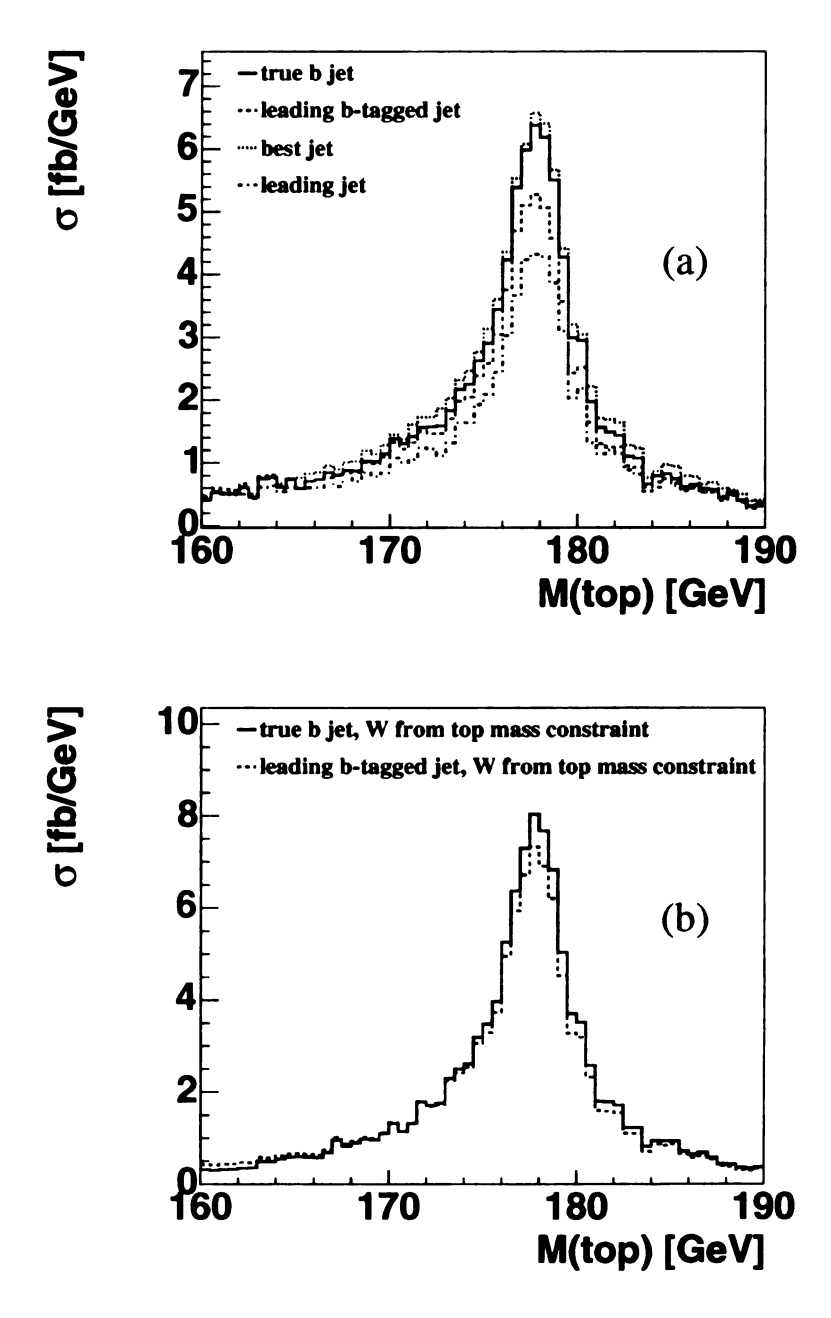


Figure 6.12: Invariant mass of the reconstructed W and a jet object. This jet object is: the jet containing the b quark from the top decay, using parton information (solid line), the leading b-tagged jet (dashed line), the best jet (dotted line), or the leading jet (dot-dashed line). The W is reconstructed either using the standard neutrino  $p_z^{\nu}$  constraint (a) or a top mass constraint (b).

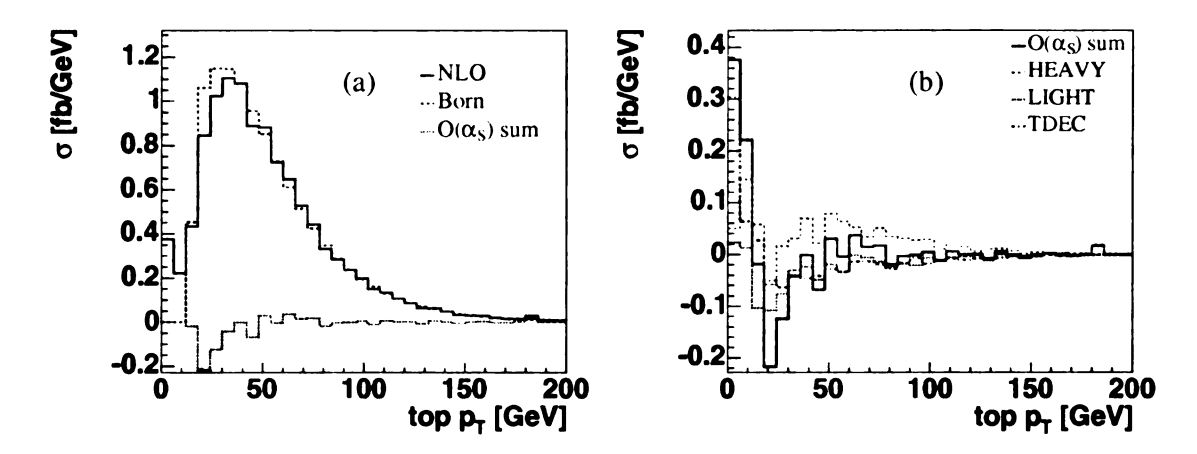


Figure 6.13: Transverse momentum of the reconstructed top quark, comparing Born-level to  $O(\alpha_s)$  corrections(a) and the individual  $O(\alpha_s)$  contributions (b).

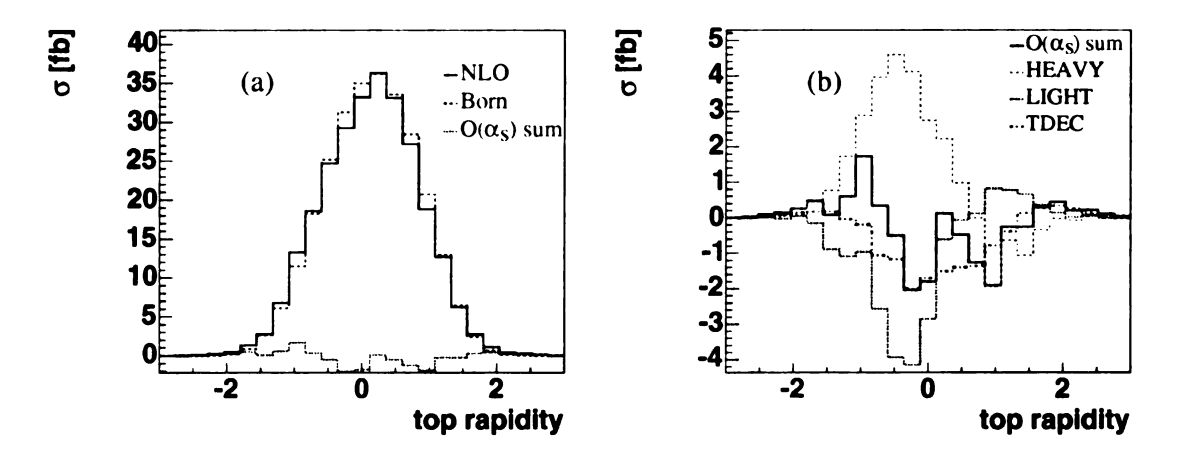


Figure 6.14: Rapidity of the reconstructed top quark, comparing Born-level to  $O(\alpha_s)$  corrections(a) and the individual  $O(\alpha_s)$  contributions (b).

tagged jet with very high efficiency. Using the leading b-tagged jet together with a top mass constraint to reconstruct the W boson gives the best reconstructed top quark and is the most efficient event reconstruction algorithm for t-channel single top quark events. We will henceforth focus on this algorithm.

Figure 6.13 shows the transverse momentum of the top quark reconstructed from the leading b-tagged jet together with the top mass constraint to reconstruct the W boson, hence, to determine  $p_z^{\nu}$ . The LIGHT and HEAVY corrections tend to shift

the top quark  $p_T$  to higher values, while the TDEC correction lowers it as expected. The different  $O(\alpha_s)$  corrections have only a small effect on the top quark rapidity shown in Fig. 6.14, similar to the b jet above. The HEAVY correction tends to shift the top quark to negative rapidities, while the LIGHT correction tends to shift it to positive rapidities, resulting in a net effect of only a small change in rapidity.

### 6.3.3 Top Quark Polarization

Having identified the b jet from the top quark decay and the W boson, we can now study correlations expected from event kinematics. As noted in the previous section, we shall focus on the study of top quark polarization using the leading b-tagged jet and the top mass constraint for the W boson, because it reconstructs the final state correctly with the highest efficiency.

Three polarization bases have been studied in the literature for the t-channel process, and they differ by the reference frame used to define the polarization: the helicity basis, the beamline basis, and the so-called "spectator" basis [104]. All three work in the top quark rest frame, but they have different reference axis for the top quark spin, cf. Fig. 6.15. In the more commonly used helicity basis, the top quark spin is measured along the top quark direction of motion in the center of mass frame which is chosen as the frame of the (reconstructed top quark, spectator jet) system after event reconstruction. In the beamline basis, the top quark spin is measured along the incoming proton direction. In the spectator basis we can maximize spin correlations by taking advantage of the fact that the top quark produced through the t-channel single top processes is almost 100% polarized along the direction of the spectator quark. In the discussion below, we will examine the polarization of single top quark events in these three bases.

As same as the s-channel study, two options for reconstructing the c.m. frame in

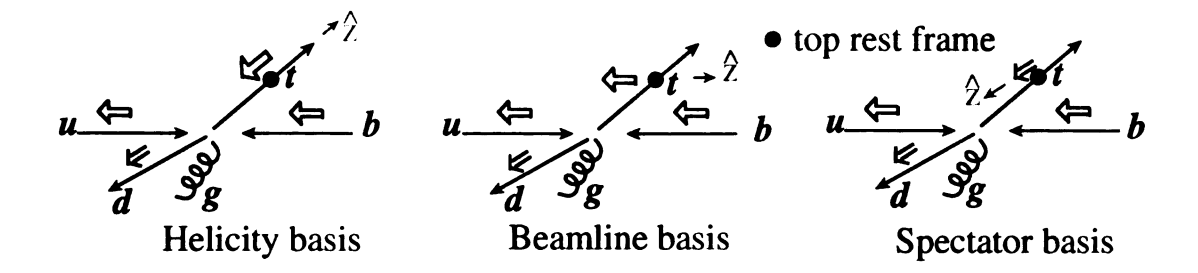


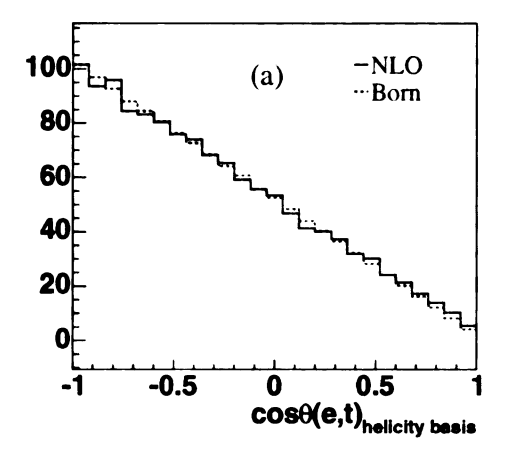
Figure 6.15: Illustration of the three choices for the top quark spin basis. The circle denotes the top quark rest frame and the blue arrows denote the top quark spin direction.

the helicity basis are investigated:

- 1. tq(j)-frame: the c.m. frame of the incoming partons. This is the rest frame of all the final state objects (reconstructed top quark and all others jets). In exclusive two-jet events, this frame is the same as the c.m. frame at the Born-level, i.e. reconstructed from summing over momentum of the top quark and spectator jet. In exclusive three-jet events, this frame is reconstructed by summing over the 4-momenta of top quark, spectator jet, and the third-jet from our parton level calculation.
- 2. tq-frame: the c.m. frame of the top quark and spectator jet. In this case, even in exclusive three-jet events, the reference frame is constructed by summing over only the 4-momenta of the top quark and spectator jet. Note that this differs from the tq(j)-frame only in exclusive three-jet events.

As shown in Table 6.2 and discussed below, the degree of top polarization is larger in the tq-frame than in the tq(j)-frame. Therefore, in the figures below we only display the top quark polarization in the tq-frame.

In the helicity basis, the polarization of the top quark is examined as the angular distribution ( $\cos \theta_{hel}$ ) of the lepton in the c.m. frame relative to the moving direction



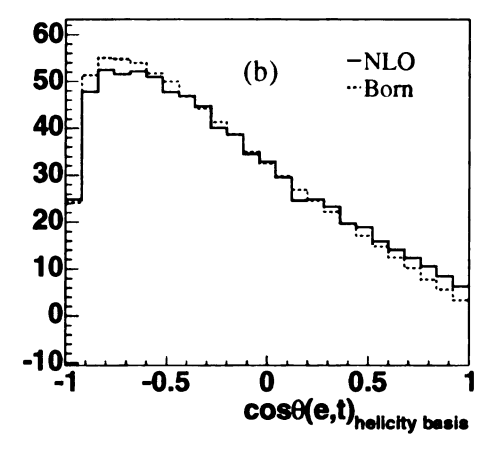


Figure 6.16: Top quark polarization in the helicity basis using the full parton information (a) and after event reconstruction with selection cuts (b), comparing Born-level to  $O(\alpha_s)$  corrections. The Born-level and NLO curves have been normalized to the same area.

of the top quark in the same frame. The angular correlation in this frame is given by

$$\cos \theta_{hel} = \frac{\vec{p_t} \cdot \vec{p_\ell}^*}{|\vec{p_t}||\vec{p_\ell}^*|},\tag{6.3}$$

where  $\vec{p}_{\ell}^*$  is the charged lepton three-momentum defined in the rest frame of the top quark, whose three momentum is denoted as  $\vec{p}_t$ , which is in turn defined in the c.m. frame. For a left-handed top quark, the angular correlation of the lepton  $\ell^+$  is given by  $(1-\cos\theta_{hel})/2$ , and for a right-handed top quark, it is  $(1+\cos\theta_{hel})/2$ . Figure 6.16(a) shows that this linear relationship for  $\cos\theta_{hel}$  is indeed a valid description for t-channel single top quark events at the parton level. The figure also shows that the top quark is not completely polarized in the helicity basis, and that this polarization is only slightly weakened when including  $O(\alpha_s)$  corrections. Figure 6.16 (b) shows that this weakening is amplified after event reconstruction, where the effect of the lepton-jet separation cut can also be seen, as a drop-off of the  $\cos\theta_{hel}$  distribution close to a value of -1.

In the "spectator" basis, the relevant angular correlation for the t-channel process

is  $\cos \theta_{spec}$ , defined as

$$\cos \theta_{spec} = \frac{\vec{p}_{spec}^* \cdot \vec{p}_{\ell}^*}{|\vec{p}_{spec}^*||\vec{p}_{\ell}^*|}, \tag{6.4}$$

where  $\vec{p}_{spec}^*$  is the spectator jet three-momentum in the top quark rest frame and  $\vec{p}_{\ell}^*$  is the lepton three-momentum in the top quark rest frame. Although this basis picks the wrong spin axis direction for the  $d\bar{b}$  and  $b\bar{d}$  initial states, it is correct most of the time at the Tevatron collider. This is because the Tevatron is a  $p\bar{p}$  collider which means that the production rate of  $p\bar{p}(ub,bu)\to dt$  is much larger than  $p\bar{p}(\bar{d}b)\to \bar{u}t$ . The large slope found in Fig. 6.17 shows that the spectator basis indeed results in a large degree of correlation for t-channel single top quark events at the parton level. The slope shown in Fig. 6.17(a) is opposite to that in Fig. 6.16(a) due to the fact that the spin quantization axis points in opposite directions for the two basis, cf. Fig. 6.15. The degree of polarization of the top quark is larger than that in the helicity basis, and the  $O(\alpha_s)$  corrections blur the spin correlation effects only slightly, both at parton level and after event reconstruction. The reconstructed  $\cos\theta_{spec}$  distribution again shows a drop-off due to the lepton-jet separation cut, in this case at high  $\cos\theta_{spec}$ .

In the "beamline" basis, the relevant angular correlation for the t-channel process is  $\cos \theta_{beam}$ , defined as

$$\cos \theta_{beam} = \frac{\vec{p}_p^* \cdot \vec{p}_\ell^*}{|\vec{p}_p^*||\vec{p}_\ell^*|},\tag{6.5}$$

where  $\vec{p}_p^*$  is the proton three-momentum in the top quark rest frame and  $\vec{p}_\ell^*$  is the lepton three-momentum in the top quark rest frame. In this analysis, we orient the coordinate system such that protons travel in the positive z direction and anti-protons travel in the negative z direction. For a top quark polarized along the proton moving direction, the angular distribution of the lepton  $\ell^+$  is  $(1 + \cos \theta_{beam})/2$ , while for a top quark polarized along the anti-proton moving direction it is  $(1 - \cos \theta_{beam})/2$ .

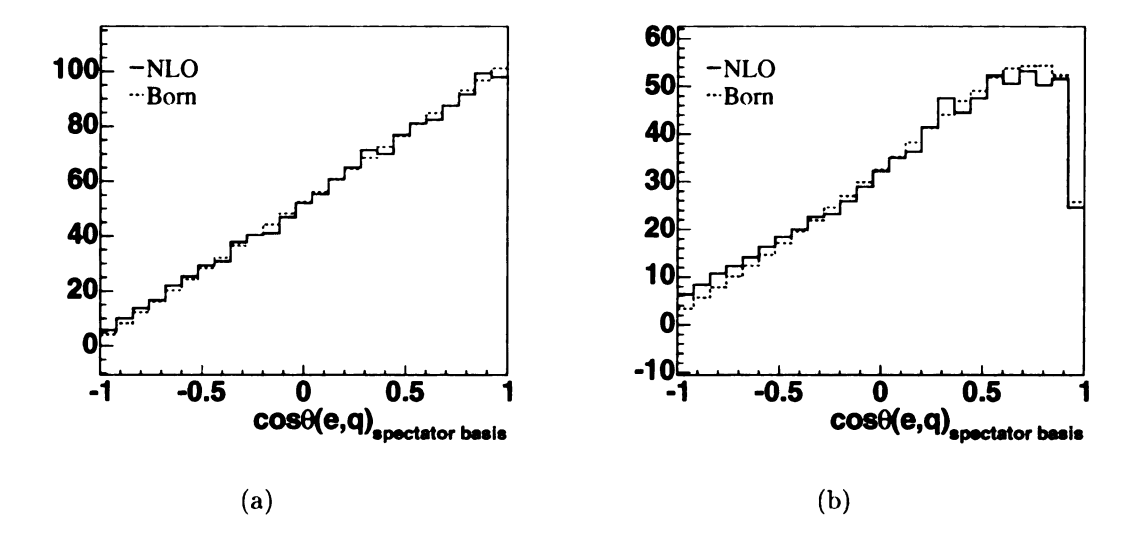


Figure 6.17: Top quark polarization in the spectator basis using the full parton information (a) and after event reconstruction with selection cuts (b), comparing Bornlevel to  $O(\alpha_s)$  corrections. The Born-level and NLO curves have been normalized to the same area.

Figure 6.18 shows that this linear relationship for  $\cos \theta_{beam}$  is a valid description for t-channel single top quark events at the parton level. However, the top quark is less polarized in the beamline basis at parton level. In this case, the  $O(\alpha_s)$  corrections actually improve the spin correlation effects at parton level. After event reconstruction the situation is similar as before, the spin correlation is further reduced and shows a drop-off close to 1.

To better quantify the change in polarization, we use the degree of polarization  $\mathcal{D}$  and the spin fractions  $\mathcal{F}_{\pm}$  of the top quark which are defined in Sec. 5.3.3.1, cf. Eqs. 5.5 and 5.7. We also examine the asymmetry  $\mathcal{A}$  of the distribution which is defined in Eq. 5.8. It is easy to check that without imposing any kinematic cuts,  $D=2\mathcal{A}$ . Furthermore, the ratio of top quarks with spin along the basis direction will be  $r_{\uparrow}=0.5-\mathcal{A}$  when no cuts are applied. However, when cuts are imposed, these two relations break down. Table 6.2 shows that the relationship  $\mathcal{D}=2\mathcal{A}$  indeed holds

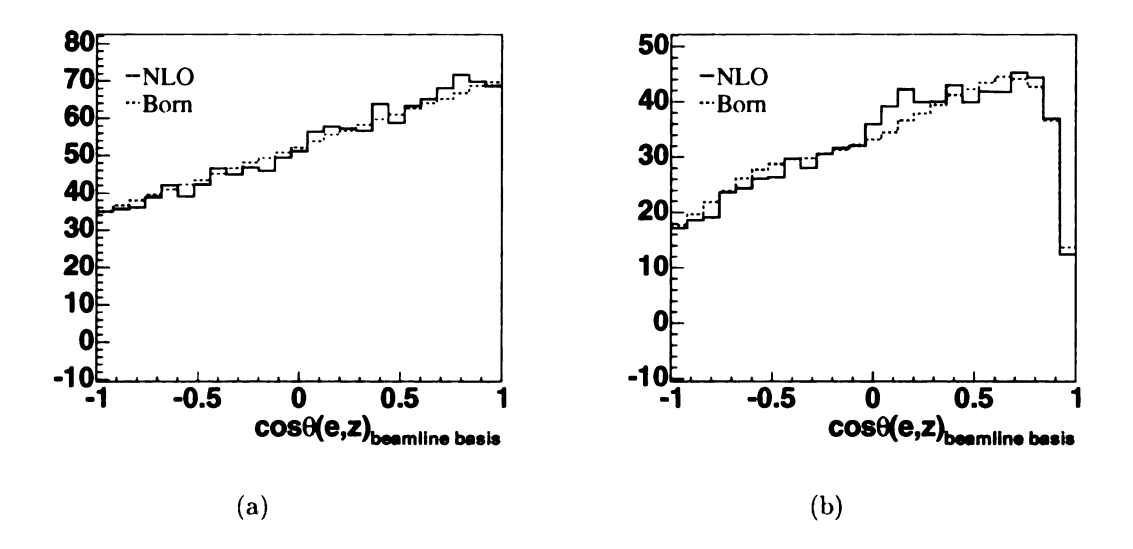


Figure 6.18: Top quark polarization in the beamline basis using the full parton information (a) and after event reconstruction with selection cuts (b), comparing Bornlevel to  $O(\alpha_s)$  corrections. The Born-level and NLO curves have been normalized to the same area.

at parton level (within rounding errors) and is still approximately true at  $O(\alpha_s)$ .

In Table 6.2, we present our results for inclusive two-jet events at the parton level before selection cuts and after the loose set of cuts and event reconstruction (cf. Sec. 6.3.2). The result of exclusive three-jet events is shown in Table 6.3.

• We note that in the helicity basis, the degree of top quark polarization is larger in the tq-frame than in the tq(j)-frame (the usual c.m. frame of the incoming partons) at the parton level. The degree of top quark polarization is 94% in the tq-frame and only 74% in tq(j)-frame. This is due to the fact the degree of top quark polarization in inclusive two-jet events is a mixture of contributions from both exclusive two-jet events and exclusive three-jet events. Table 6.3 shows that for exclusive three-jet events, the degree of top quark polarization is larger in the tq-frame than in the tq(j)-frame. This reduction in the degree of polarization for the tq(j)-frame is due to events in which the additional jet is produced

		$\mathcal{D}$		$\mathcal{F}$		A	
		LO	NLO	LO	NLO	LO	NLO
Helicity basis:	Parton(tq(j)-frame)	0.96	0.74	0.98	0.87	0.48	0.37
	$Parton(tq ext{-frame})$	0.96	0.94	0.98	0.97	0.48	0.47
	$\operatorname{Recon.}(tq(j)\operatorname{-frame})$	0.84	0.73	0.92	0.86	0.46	0.41
	Recon. $(tq$ -frame)	0.84	0.75	0.92	0.88	0.46	0.42
Spectator basis:	Parton	-0.96	-0.94	0.98	0.98	-0.48	-0.47
	Recon.	-0.85	-0.77	0.93	0.89	-0.46	-0.42
Beamline basis:	Parton	-0.34	-0.38	0.67	0.69	-0.17	-0.19
	Recon.	-0.30	-0.32	0.65	0.66	-0.17	-0.20

Table 6.2: Degree of polarization  $\mathcal{D}$ , polarization fraction  $\mathcal{F}$ , and asymmetry  $\mathcal{A}$  for inclusive two-jet single top quark events, at the parton level (Parton) before cuts and after selection cuts and event reconstruction (Recon.), in the t-channel process. Here,  $\mathcal{F}$  corresponds to  $\mathcal{F}_{-}$  in the helicity basis for left-handed top quarks and to  $\mathcal{F}_{+}$  in the spectator and beamline bases for top quarks with polarization along the direction of the spectator-jet and proton three momentum, respectively. Also, the tq(j)-frame in the helicity basis denotes the c.m. frame of the incoming partons, while the tq-frame denotes the rest frame of the top quark and spectator jet.

before the exchange of the virtual W boson. After event reconstruction, the two frames give almost the same degree of top quark polarization.

• We find that at the parton level stage, there is very little difference between the helicity basis (using the tq-frame) and the spectator basis, and that both of them give significantly better polarization than the beamline basis both at Born-level and NLO. The top quark is almost completely polarized in the helicity and spectator bases, and the  $O(\alpha_s)$  corrections only degrade that picture slightly.

The similarity between these two bases is due to the fact that the degree of polarization of the top quark is dominated by exclusive two-jet events for which these two bases are equivalent, cf. the Born-level results in Table 6.2. After event reconstruction for the inclusive two-jet sample, the degree of polarization is reduced as expected in both the helicity and spectator bases.

- In the beamline basis, the polarization actually increases when going from Born-level to NLO, but it is still much lower than in the other two bases. After event reconstruction, the degree of polarization is also reduced.
- In the exclusive three-jet sample, the degree of polarization is further reduced because the third-jet affects the kinematics of either spectator jet or the top quark. The helicity basis with tq-frame gives almost the same degree of polarization as the spectator basis.

Our study shows that the helicity basis (using the tq-frame) and the spectator basis are equally good to study the top quark polarization. Unlike the s-channel process in which the W-boson is not perfectly reconstructed in the best-jet algorithm and thus the polarization measurement was significantly degraded after event reconstruction, using the leading b-tagged jet and the top mass constraint gives excellent final state reconstruction in the t-channel process, and the degree of top quark polarization is only somewhat degraded after event reconstruction.

## 6.3.4 Distributions for Three-jet Events

As shown in Fig. 6.3, a large fraction of the events passing the loose selection cuts contain three jets. In this section we focus on the properties of these three-jet events and the additional jet.

		$\mathcal{D}$	$\mathcal{F}$	$\mathcal{A}$
Helicity basis:	Parton level $(tq(j)$ -frame)	0.65	0.83	0.35
	Parton level $(tq$ -frame)	0.78	0.89	0.43
	Reconstructed events $(tq(j)$ -frame)	0.63	0.81	0.34
	Reconstructed events ( $tq$ -frame)	0.70	0.85	0.38
Spectator basis:	Parton level	-0.78	0.89	-0.42
	Reconstructed events	-0.70	0.85	-0.38
Beamline basis:	Parton level	-0.26	0.63	-0.16
	Reconstructed events	-0.27	0.63	-0.16

Table 6.3: Degree of polarization  $\mathcal{D}$ , polarization fraction  $\mathcal{F}$ , and asymmetry  $\mathcal{A}$  for exclusive three-jet single top quark events, at parton level and after event reconstruction, in the t-channel process. Here,  $\mathcal{F}$  corresponds to  $\mathcal{F}_-$  in the helicity basis for left-handed top quarks and to  $\mathcal{F}_+$  in the spectator and beamline bases for top quarks with polarization along the direction of the spectator-jet and proton three momentum, respectively. The tq(j) frame in the helicity basis denotes the c.m. frame of the incoming partons, while the tq frame denotes the rest frame of the reconstructed top quark and light quark.

In events containing two untagged jets, we can use the  $p_T$  of the untagged jet to pick up the spectator jet. When the  $\bar{b}$  jet from the initial state gluon splitting in the W-gluon fusion process is mis-tagged, it will also contribute an untagged jet to the event. For simplicity, we will assume fully efficient, perfect b-tagging here and consider events with single b-tags and double b-tags separately.

From Fig. 6.3 it is clear that the jet multiplicity at NLO depends strongly on the jet  $p_T$  cut. Figure 6.19 shows that it also depends strongly on the jet pseudorapidity cut. The dependence of the total cross section on the jet pseudorapidity cut is different between the Born-level and NLO, mostly as a result of the third jet.

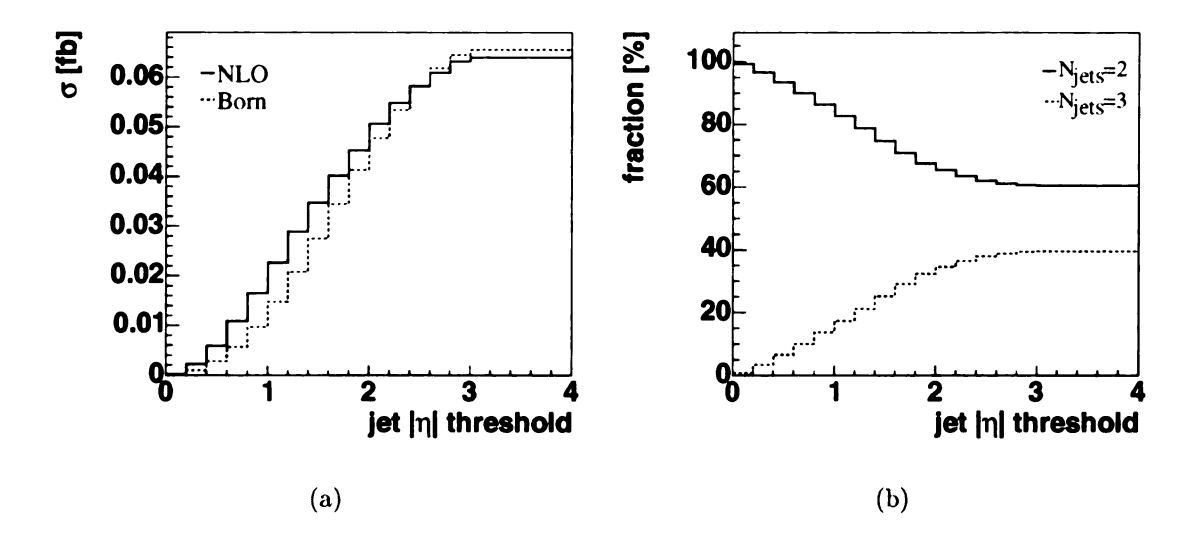


Figure 6.19: Inclusive cross section and fraction of three-jet events at NLO for varying jet pseudo-rapidity cuts, after the loose selection cuts. Shown is the total cross section as a function of the jet pseudo-rapidity cut (a) and the fraction of two-jet and three-jet events as a function of the jet pseudo-rapidity cut (b).

Figure 6.3 also shows that not only the cross section but also the jet multiplicity depends strongly on the jet pseudo-rapidity cut. Only for jet pseudo-rapidity cuts above 3 are cross section and jet multiplicities stable.

The fraction of b-tagged jets also depends strongly on the jet  $p_T$  cut, as shown in Fig. 6.9. There is a large fraction of events in which the third jet comes from the  $\bar{b}$  quark, especially for low b-tag  $p_T$  thresholds. This can also be seen in Fig. 6.20, which shows the dependence of the fraction of events with 1 b-tag and 2 b-tags as a function of the cut on the b-tagged jet  $p_T$  and  $\eta$ . As before, the fraction of events with 2 b-tagged jets is stable only for pseudo-rapidity thresholds above 3. At that point, about one quarter of the inclusive events contain two b-tagged jets, and half of the exclusive three-jet events contain two b-tagged jets. In the following analysis, we shall require at least one b-tagged jet in the event and do not distinguish the identity of the third jet, unless specified otherwise.

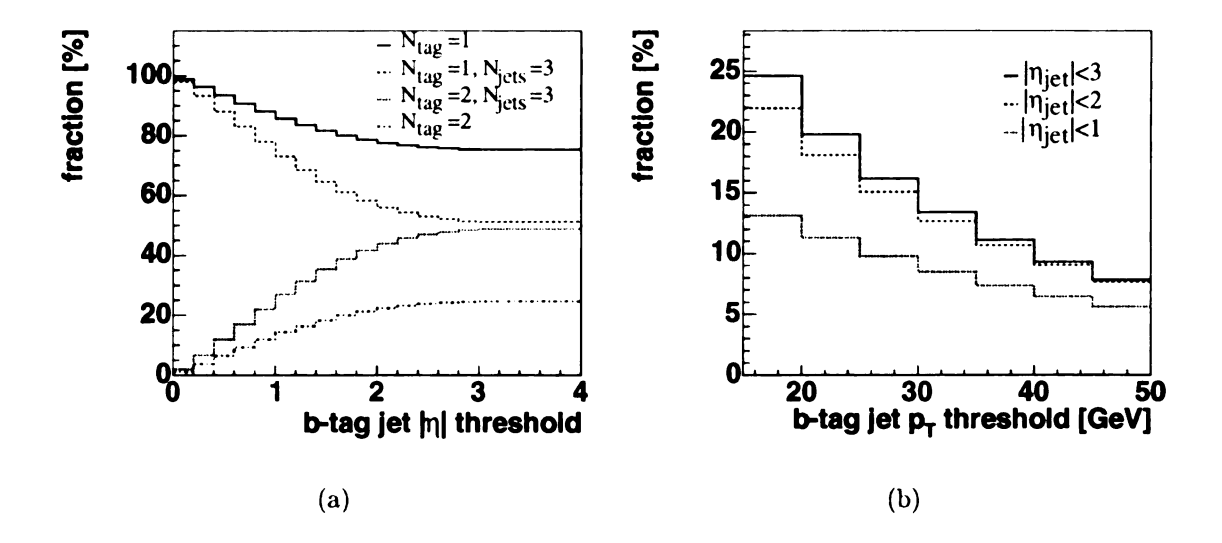


Figure 6.20: Fraction of events with one or two b-tagged jets for the inclusive sample and the exclusive three-jet sample as a function of the pseudo-rapidity cut on the b-tagged jets (a), and fraction of events with two tagged jets as a function of the  $p_T$  threshold on the b-tagged jets for three different pseudo-rapidity cuts (b), after the loose selection cuts.

#### 6.3.4.1 Kinematic Distribution of the Extra Jet

Initial- and final-state emission of additional gluons occurs before the top quark goes on shell and can thus be considered as "production-stage emission", while decay-stage emission occurs only after the top quark goes on shell. In principle, an event with an extra jet can thus be classified as production-stage or decay-stage by looking at the invariant mass of the decay products. In production-stage emission events, the W boson and b quark momenta will combine to give the top quark momentum. In decay-stage emission events, the gluon momentum must also be included to reconstruct the top quark momentum. This interpretation is exact at the NLO parton level in the narrow width approximation. Finite top width effects can blur the above classification due to interference between production- and decay-stage emission. This classification is nevertheless still useful in our case because the top width of 1.5 GeV is

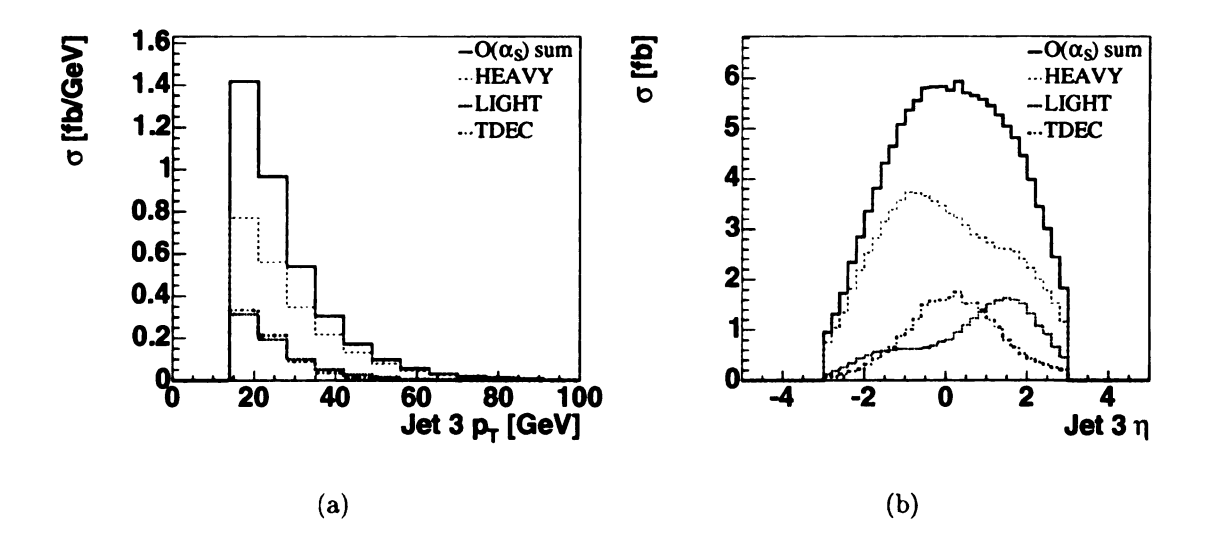


Figure 6.21: Transverse momentum (a) and pseudo-rapidity (b) of the third jet after selection cuts for the various  $O(\alpha_s)$  contributions.

small compared to the hard gluon  $E_T$  cut imposed in the MC calculations. It should be kept in mind that in an actual experiment, the production-decay distinction is further blurred by the experimental jet energy resolution and ambiguities associated with properly assigning partons to jets.

Figure 6.21 shows the transverse momentum distribution as well as the pseudorapidity distribution of the third jet in three-jet events. This jet corresponds to the gluon in about 70% of the events after the loose set of cuts. The transverse momentum distribution of the third jet for those events where that jet corresponds to the  $\bar{b}$  quark (from W-gluon fusion subprocess) can be seen in Fig. 6.9. It comprises about 80% of the HEAVY correction after imposing the loose selection cuts, which dominates over LIGHT and TDEC radiative corrections.

As expected, the  $E_T$  distribution is steeply falling for all contributions, but it extends to much higher  $p_T$  values for HEAVY emission. The smaller values of  $E_T$  to which TDEC emission is constrained are again a consequence of the available

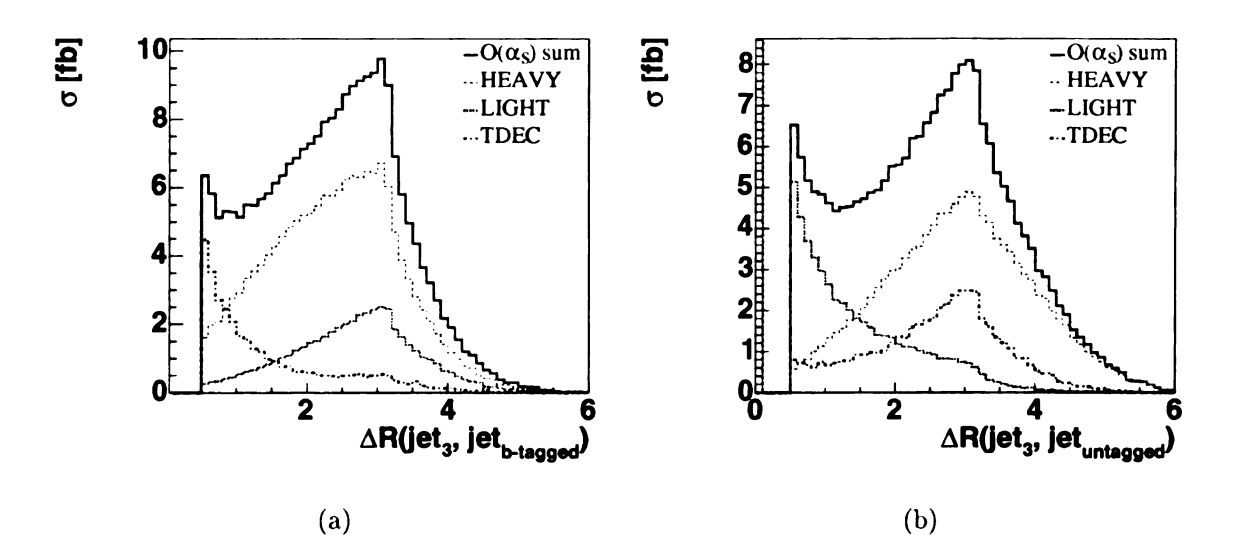


Figure 6.22: Separation between the third jet and the tagged jet (a) and between the third jet and the untagged jet (b) after selection cuts for the various  $O(\alpha_s)$  corrections.

phase space from the top quark decay. Recall that the top quarks are produced with relatively modest transverse momentum (cf. Fig. 6.13), so that gluons from the decay do not receive much of a boost. Note also that an increase in the  $p_T$  cut on the jet would result in a further reduction in relative size of the decay contribution compared to production. Figure 6.21 also shows the distribution in pseudo-rapidity of the extra jet. The third jet radiated from the LIGHT and HEAVY quark lines has a relative larger magnitude in its (non-symmetric) rapidity, as compared to the more central TDEC emission. This is consistent with our intuition that decay-stage radiation, dominated by the gluon radiated from the bottom quark which tends to appear in the central pseudo-rapidity region, is also likely to be produced centrally. However, this TDEC contribution is small and the HEAVY radiation dominates even in the central region.

This tendency of decay-stage radiation to be associated with the final-state b quark might lead one to expect that if the extra jet is "near" the b jet it should be included in

the top quark reconstruction, and if it is not then it should be excluded. Figure 6.22, which shows the angular separation  $\Delta R$  between the extra jet and the leading b-tagged-jet as well as the leading untagged jet, confirms that the decay-stage radiation peaks close to the leading b-tagged jet, and production-stage radiation peaks farther away. Figure 6.22(a) clearly shows that the decay contribution dominates in the low  $\Delta R$  region. This is different from the s-channel single top process, in which the production contribution dominates over decay emission even in the small  $\Delta R$  region, cf. Fig. 5.14. A higher  $p_T$  cut on the jet would make this situation worse because it would increase the relative size of the production emission.

Nevertheless, the figure suggests that it might be possible to further improve the top quark reconstruction for exclusive three-jet events. In this work, we have been using the leading b-tagged jet to identify the b quark from the top quark decay, and constraints on  $m_t$  and  $M_W$  to obtain the correct  $p_z^{\nu}$ . With this procedure the final state can be reconstructed accurately about 84 % of the time in inclusive two-jet events, cf. Fig. 6.11. Part of the efficiency loss is due to the gluon radiated in TDEC emission, and Fig. 6.22 indicates that some of this loss could be reclaimed by including the third jet in the top quark reconstruction if it is close to the b-tagged jet. The actual cut on  $\Delta R$  would need to be tuned to maximize the top quark reconstruction efficiency. However, tuning a prescription for dealing with the extra jet in t-channel single top quark events is complicated because the effects of multiple emission, hadronization, and detector resolutions will affect the result. For simplicity, we thus chose not to include the third jet in the top quark reconstruction algorithm used in this work.

In Fig. 6.22(b), the equivalent distribution in  $\Delta R$  between the extra jet and the untagged jet is also shown, where the LIGHT quark line radiation peaks close to the untagged jet as expected from gluon radiation in the final state. Obviously, the

radiation of the HEAVY quark line is dominated by initial state radiation, therefore, its contribution to  $\Delta R(j_3, j_{\rm untagged})$  is small in the region of small  $\Delta R$ . The peak at zero in this distribution corresponds to events containing two *b*-tagged jets in the the W-gluon fusion subprocess.

#### 6.3.4.2 Angular Correlation Between the Extra Jet and the Best Jet

As discussed above, the  $\Delta R$  separation between the third jet and the leading b-tagged jet can be used to distinguish decay-stage emission from production-stage emission. It was shown in Chapter 5 that the best-jet algorithm is effective in reconstructing the s-channel single top quark event, while retaining the top quark polarization information, but can also distinguish the decay-stage gluon radiation from the production-stage radiation by studying which jets are chosen as the best jets. Similarly, we can also study the correlations between the extra jet and the best jet in t-channel single top quark events using the best jet algorithm.

Figure 6.23 (a) shows the angular correlation  $\cos \theta$  between the radiated parton (gluon or  $\bar{b}$ ) and the b quark at parton level before cuts. Figure 6.23 (b) shows the same correlation after event reconstruction between the third jet and the best jet. Only events for which the best jet algorithm chooses a two-jet system are included in the figure. In this case there is a clear separation between production-stage and decay-stage emission, and the best jet algorithm can be used to separate the two. This approach thus allows a detailed experimental study of the radiation pattern in top quark decays in the t-channel single top quark events.

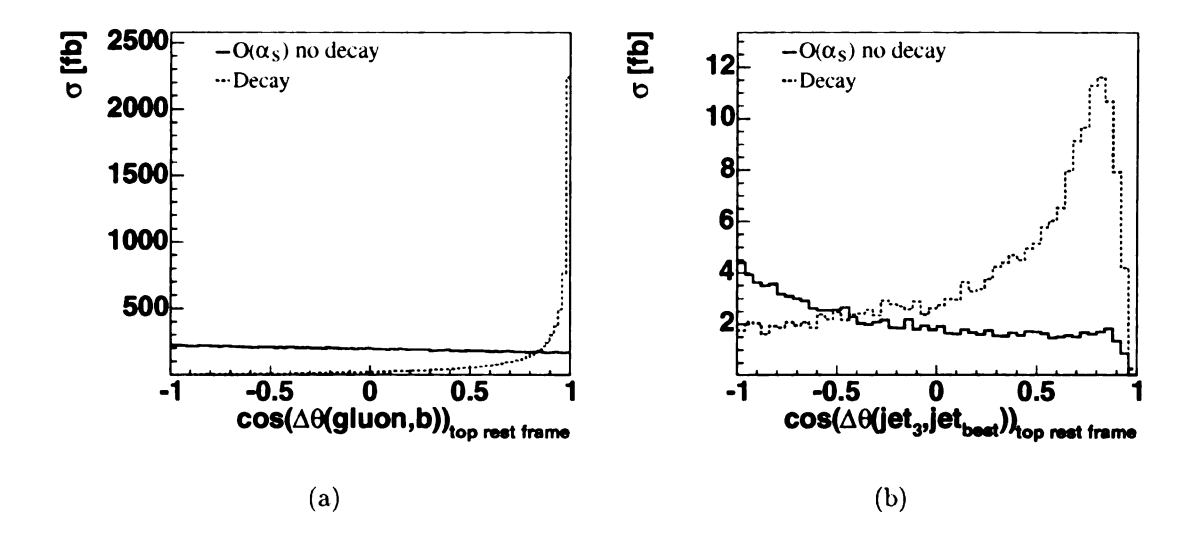


Figure 6.23: Angular correlation  $\cos \theta$  between the gluon and the b quark before any selection cuts using the full parton information (a) and between the third jet and the best jet after selection cuts (b). The solid line shows all  $O(\alpha_s)$  contributions except for the decay part, while the dashed line shows only the  $O(\alpha_s)$  decay contribution.

#### 6.4 Conclusion

We have presented a next-to-leading order study of t-channel single top quark events at the Tevatron, including  $O(\alpha_s)$  QCD corrections to both the production and decay of the top quark. To obtain an accurate prediction of the inclusive rate of t-channel single top quark production, a modified narrow width approximation has been adopted to link the production of the top quark with its decays (thus preserving top quark spin information) instead of the usual narrow width approximation. The impact of kinematical cuts on the acceptances has been studied for several different sets of cuts. We found that the acceptances are sensitive to the  $\Delta R_{\rm cut}$  we imposed on the jet cone size and the lepton isolation. With the choice of  $\Delta R_{\rm cut} = 0.5$ , we found that the difference between the Born-level and NLO acceptances is about 10% for a loose cut set (a) and  $3 \sim 6\%$  for a tight cut set (c). The above difference becomes significantly larger when changing  $\Delta R_{\rm cut}$  from 0.5 to 1.0.

We categorize the  $O(\alpha_s)$  contributions to the t-channel single top process into three gauge invariant sets: the light quark line corrections, the heavy quark line corrections and the top quark decay corrections. The  $O(\alpha_s)$  corrections are small in size and contribute about 5.5% of the inclusive cross section at NLO. They do however modify the event kinematics and in particular result in a large fraction of events containing three reconstructed jets in the final state for the loose set of kinematic cuts. The acceptance for t-channel single top quark events and this fraction of 3-jet events depend strongly on the pseudo-rapidity cut on the jets. Although the radiative corrections to the inclusive t-channel single top production rate are small, they affect the shape of some of the important kinematic distributions that can be used experimentally to separate the t-channel single top signal from the various backgrounds, such as the pseudo-rapidity distribution of the spectator jet. We find that the  $O(\alpha_s)$  LIGHT and HEAVY corrections have almost opposite contributions to various pseudo-rapidity distributions, due to the difference in the parton distribution functions between the valence quarks and sea quarks. The former shifts the spectator jet to even higher pseudo-rapidities, while the later shifts it to more central pseudorapidity regions. The summed contributions cause the spectator jet to be even more forward which will change the prediction of the acceptance for t-channel single top quark events. Also, a large fraction of three jet events contain two b-jets due to the collinear enhancement in the W+g fusion process. This implies that higher order corrections need to be calculated in order to correctly predict the behavior of the b-jet in the small  $p_T$  region.

In order to study top quark properties such as the top quark polarization, induced from the effective t-b-W couplings, we need to reconstruct the top quark by combining the reconstructed W boson with the b-tagged jet. Most of the t-channel single top quark events contain only one b-jet in the final state. Thus, we can use the leading

b-tagged jet algorithm to identify the b-jet in the final state, rather than the best-jet algorithm which is more appropriate for the s-channel. We found that the leading b-tagged jet algorithm effectively picks up the correct b-jet in the event. Since this algorithm makes no assumptions about the other particles in the event, we can use it to also determine the longitudinal momentum of the neutrino  $(p_z^{\nu})$  accurately through a top quark mass constraint. Information about the reconstructed final state can be used to explore correlations between different objects in the event. After reconstruction of the top quark event, we study spin correlations in the top quark decay in three different bases: the helicity basis, the spectator basis, and the beamline basis. We find that the degree of top polarization is very large, especially in the helicity and spectator bases. This is true even after event reconstruction because we are able to reconstruct the top quark final state almost perfectly. As one expects, the degree of top polarization is reduced slightly by the  $O(\alpha_s)$  corrections, both at parton level and after event reconstruction with the loose selection cuts. We also note that using the tq-frame (the rest frame of the reconstructed top quark and spectator jet) in the helicity basis gives almost the same degree of polarization as in the spectator basis.

### Chapter 7

## Summary and outlook

The primary puzzle confronting particle physicists today is the understanding of the electroweak symmetry breaking, responsible for the large masses of the weak bosons and the top quark. As the heaviest particle by far in the standard model, the top quark provides a perfect laboratory to study EWSB. In the hadron collisions, the top quark will be produced in many channels. As well as the  $t\bar{t}$  pair production channel, the top quark may be produced singly in associated with other particles. At the tree level, there are three modes: the s-channel, the t-channel and the Wt associated production channel. In contrast to the top quark pair production, the single top is produced through the electroweak interaction with amplitudes proportional to the Cabibbo-Kabayashi-Maskawa matrix element. Due to the left-handed nature of charged weak current interaction, the top quark produced via single-top processes is highly polarized and its polarization information remains among its decay products. The new physics effects can change the spin correlation in the single top event via the quantum corrections as well. Therefore, careful examination of the single top production and its decay characteristics, and precision measurement of th top spin information can test the standard model and may lead to the discovery of new physics beyond the standard model.

In this study, we present a complete next-to-leading order calculations to the s-channel and t-channel single top quark production and decay process at hadron colliders. Using the helicity amplitude method, the angular correlations of the final state particles and the spin correlation of the top quark are preserved. We also discuss the phenomenology of the single top physics at the Tevatron and find the following interesting results:

- 1. The s-channel single particle inclusive rate (with acceptance) is dominated by the initial state contribution, while the t-channel single particle inclusive rate is dominated by the heavy quark line contribution.
- With the loose kinematical cuts to maximize the acceptances, the full NLO kinematics needs to be studied. A constant K-factor with LO kinematics will not work.
- 3. In order to reconstruct top quark event, the best-jet algorithm is better in the s-channel process, while the leading b-tagged jet algorithm is best in the t-channel process.
- 4. The spin correlation of the single top event have been examined in many spin bases:

s-channel: Helicity basis and Optimal basis,

t-channel: Helicity basis, Beamline basis and Spectator basis.

We note that the higher order QCD corrections change the kinematical and spin correlations largely. After event reconstruction, the Optimal basis gives almost the same degree of polarization of the top quark as the Helicity basis  $(t\bar{b}$ -frame) in the s-channel processes, while the Spectator basis gives almost the same degree of polarization of the top quark as the Helicity basis (tq-frame) in the t-channel processes.

5. The NLO QCD corrections to the s-channel single-top process is very important to the SM Higgs boson search via  $q\bar{q}' \to W^{\pm}H$  precess. In particular, the NLO contribution from top quark decay process has to be included to make more reliable prediction on the background.

At present, discovery of the single top event has become the major focus of Run II of the Tevatron. And it will continue to be one of the most important goals at the LHC. In five years, single top physics will go from discovery (Tevatron) to precision measurement (LHC).

# Appendix A

## Helicity Amplitudes

In this appendix we briefly summarize our method for calculating the helicity amplitudes. The method breaks down the algebra of four-dimensional Dirac spinors and matrices into equivalent two-dimensional ones. In the Weyl basis, Dirac spinors have the form

$$\left(\begin{array}{c} \psi_+ \\ \psi_- \end{array}\right)$$
,

where for fermions and anti-fermions

$$\psi_{\pm} = \begin{cases} v_{\pm}^{(\lambda=1)} = \pm \omega_{\mp} \chi_{-1/2} & , \\ v_{\pm}^{(\lambda=-)} = \mp \omega_{\pm} \chi_{1/2} & , \end{cases}$$

with  $\omega_{\pm} = \sqrt{E \pm |\vec{p}|}$ , where E and  $\vec{p}$  are the energy and momentum of the fermion, respectively. The  $\chi_{\lambda/2}$ 's are eigenvectors of the helicity operator

$$h = \hat{p} \cdot \sigma$$
, with  $\hat{p} = \vec{p}/|\vec{p}|$ ,

where eigenvalue  $\lambda = 1$  is for "spin-up" and  $\lambda = -1$  is for "spin-down" fermion.

$$\chi_{1/2} \equiv |\hat{p}+\rangle = \begin{pmatrix} \cos\theta/2 \\ e^{i\phi}\sin\theta/2 \end{pmatrix}, \quad \chi_{-1/2} \equiv |\hat{p}-\rangle = \begin{pmatrix} -e^{i\phi}\sin\theta/2 \\ \cos\theta/2 \end{pmatrix}, \tag{A.1}$$

where we introduce the shorthand notations  $|\hat{p}\pm\rangle$  for  $\chi_{\pm 1/2}$ . Gamma matrices in the Weyl basis have the form

$$\gamma^0 = \begin{pmatrix} 0 & 1 \\ 1 & 0 \end{pmatrix}, \quad \gamma^j = \begin{pmatrix} 0 & -\sigma_j \\ \sigma_j & 0 \end{pmatrix}, \quad \gamma^5 = \begin{pmatrix} 1 & 0 \\ 0 & -1 \end{pmatrix},$$

where  $\sigma_j$  are the Pauli  $2\times 2$  spin matrices. In the Weyl basis,  $\not\!\!p$  takes the form

$$\not\!p\equiv p_{\mu}\gamma^{\mu}=\left(\begin{array}{cc}0&p_{0}+\vec{\sigma}\cdot\vec{p}\\p_{0}-\vec{\sigma}\cdot\vec{p}&0\end{array}\right)\equiv\left(\begin{array}{cc}0&\not\!p_{+}\\\not\!p_{-}&0\end{array}\right)\equiv p_{\mu}\left(\begin{array}{cc}0&\gamma_{+}^{\mu}\\\gamma_{-}^{\mu}&0\end{array}\right)$$

where

$$\gamma_{\pm}^{\mu} = (1, \mp \vec{\sigma}).$$

# Appendix B

# $A_h$ and $B_h$ in the Crossing Functions

There are four independent  $A_{p\to hX}(x,\mu_F)$  and  $B_{p\to hX}^{\text{Scheme}}(x,\mu_F)$ , respectively (we suppress  $\mu_F$  in the following expressions) in the process independent, but  $s_{min}$  and factorization scheme dependent crossing functions:

$$A_{g \to gg}(x) = \left[ \frac{33 - 2n_f}{18} + 2\ln(1 - x) \right] f_g^H(x)$$

$$+ 2 \int_x^1 dz f_g^H(x/z) \left[ \frac{1 - z}{z^2} + 1 - z \right]$$

$$+ 2 \int_x^1 dz \frac{f_g^H(x/z) - f_g^H(x)}{1 - z},$$
(B.1)

$$A_{q \to qg}(x) = \left[\frac{2}{3} + \frac{8}{9}\ln(1-x)\right] f_q^H(x)$$

$$+ \frac{4}{9} \int_{x}^{1} dz \frac{(1+z^{2})/z f_{q}^{H}(x/z) - 2 f_{q}^{H}(x)}{1-z}, \tag{B.2}$$

$$A_{g \to q\bar{q}}(x) = \frac{1}{6} \int_{x}^{1} dz f_{g}^{H}(x/z) \frac{z^{2} + (1-z)^{2}}{z},$$
 (B.3)

$$A_{q \to gq}(x) = \frac{4}{9} \int_{x}^{1} dz f_{q}^{H}(x/z) \frac{1 + (1-z)^{2}}{z^{2}},$$
 (B.4)

$$\begin{split} B^{\overline{MS}}_{g \to gg}(x) &= \left[ \frac{\pi^2}{3} - \frac{67}{18} + \frac{5n_f}{27} + \ln^2(1-x) \right] f_g^H(x) \\ &+ 2 \int_x^1 dz \, f_g^H(x/z) \ln(1-z) \left[ \frac{1-z}{z^2} + 1 - z \right] \\ &+ 2 \int_x^1 dz \ln(1-z) \frac{f_g^H(x/z) - f_g^H(x)}{1-z}, \end{split} \tag{B.5} \\ B^{\overline{MS}}_{q \to qg}(x) &= \left[ \frac{8}{9} (\frac{\pi^2}{6} - \frac{7}{4}) + \frac{4}{9} \ln^2(1-x) \right] f_q^H(x) \\ &+ \frac{4}{9} \int_x^1 dz \, f_q^H(x/z) \frac{1-z}{z} \\ &+ \frac{4}{9} \int_x^1 dz \ln(1-z) \frac{(1+z^2)/z f_q^H(x/z) - 2 f_q^H(x)}{1-z}, \tag{B.6} \\ B^{\overline{MS}}_{g \to qq}(x) &= \frac{1}{6} \int_x^1 dz \, f_g^H(x/z) \left[ \frac{z^2 + (1-z)^2}{z} \ln(1-z) + 2(1-z) \right], \tag{B.7} \\ B^{\overline{MS}}_{q \to gg}(x) &= \frac{4}{9} \int_x^1 dz \, f_q^H(x/z) \left[ \frac{1 + (1-z)^2}{z^2} \ln(1-z) + 1 \right], \tag{B.8} \\ B^{DRED}_{q \to qg}(x) &= \left[ \frac{8}{9} (\frac{\pi^2}{6} - \frac{3}{2}) + \frac{4}{9} \ln^2(1-x) \right] f_q^H(x) \\ &- \frac{4}{9} \int_x^1 dz \, f_q^H(x/z) \frac{1-z}{z} \\ &+ \frac{4}{9} \int_x^1 dz \ln(1-z) \frac{(1+z^2)/z f_q^H(x/z) - 2 f_q^H(x)}{1-z}, \tag{B.10} \end{split}$$

where  $n_f$  is the flavor number,  $f_h^H(x)$  is the parton distribution function of parton h inside hadron H. In the above, we have set  $N_c = 3$ . The subscript  $\overline{\rm MS}$  indicates the

(B.12)

 $B_{g \to q\bar{q}}^{\mathrm{DRED}}(x) = \frac{1}{6} \int_{0}^{1} dz f_{g}^{H}(x/z) \left[ \frac{z^{2} + (1-z)^{2}}{z} \ln(1-z) - 2(1-z) \right],$ 

 $B_{q \to qq}^{\text{DRED}}(x) = B_{q \to qq}^{\bar{M}S}(x),$ 

results in the  $\overline{\rm MS}$  DREG scheme while the subscript DRED indicates the results in the DRED scheme.

## Appendix C

### Scalar functions

### C.1 Definition

We define the one-point, two-point, three-point and four-point functions as [69, 105]

$$\mu^{2\epsilon} \int \frac{d^n \ell}{(2\pi)^n} \frac{1}{\ell^2 - m^2} = \frac{i}{16\pi^2} A_0(m), \tag{C.1}$$

$$\mu^{2\epsilon} \int \frac{d^n \ell}{(2\pi)^n} \frac{1, \ell_\mu, \ell_\mu \ell_\nu}{(\ell^2 - m_1^2) \left[ (\ell + k)^2 - m_2^2 \right]} = \frac{i}{16\pi^2} B_0, B_\mu, B_{\mu\nu}(k, m_1, m_2)$$
 (C.2)

$$\mu^{2\epsilon} \int \frac{d^n \ell}{(2\pi)^n} \frac{\ell^2, \ell^2 \ell_\mu}{(\ell^2 - m_1^2) \left[ (\ell + k)^2 - m_2^2 \right]} = \frac{i}{16\pi^2} \tilde{B}_0, \tilde{B}_\mu(k, m_1, m_2)$$
 (C.3)

$$\mu^{2\epsilon} \int \frac{d^n \ell}{(2\pi)^n} \frac{1, \ell_{\mu}, \ell_{\mu} \ell_{\nu}}{(\ell^2 - m_1^2) \left[ (\ell + k)^2 - m_2^2 \right] \left[ (\ell + k + s)^2 - m_3^2 \right]}$$

$$=\frac{i}{16\pi^2}C_0, C_{\mu}, C_{\mu\nu}(k, s, m_1, m_2, m_3) \tag{C.4}$$

$$\mu^{2\epsilon} \int \frac{d^{n}\ell}{(2\pi)^{n}} \frac{1, \ell_{\mu}, \ell_{\mu}\ell_{\nu}, \ell_{\mu}\ell_{\nu}\ell_{\alpha}, \ell_{\mu}\ell_{\nu}\ell_{\alpha}\ell_{\beta}}{(\ell^{2} - m_{1}^{2})\left[(\ell + k)^{2} - m_{2}^{2}\right]\left[(\ell + k + s)^{2} - m_{3}^{2}\right]\left[(\ell + k + s + p)^{2} - m_{4}^{2}\right]}$$

$$= \frac{i}{16\pi^2} D_0, D_{\mu}, D_{\mu\nu}, D_{\mu\nu\alpha}, D_{\mu\nu\alpha\beta}(k, s, p, m_1, m_2, m_3, m_4)$$
 (C.5)

The integration formula of the scalar functions  $A_0$ ,  $B_0$ ,  $B_1$ ,  $C_0$  and  $D_0$  are given

as follows:

$$A_0(m) = m^2 \left[ \Delta - \ln \frac{m^2}{\mu^2} + 1 \right],$$
 (C.6)

$$B_n(p_1, m_1, m_2) = (-1)^n \left[ \frac{\Delta}{n+1} - \int_0^1 dx \, x^n \ln \frac{x^2 p_1^2 - x(p_1^2 + m_1^2 - m_2^2) + m_1^2}{\mu^2} \right], \tag{C.7}$$

$$C_0(p_1, p_2, m_1, m_2, m_3) = \int_0^1 dx \int_0^x dy \frac{1}{ax^2 + by^2 + cxy + dx + ey + f},$$
 (C.8)

where

$$\Delta = \frac{1}{\epsilon} - \gamma_E + \ln 4\pi,$$

$$a = -p_2^2, \ b = -p_1^2, \ c = -2p_1 \cdot p_2, \ d = -m_2^2 + m_3^2 + p_2^2,$$

$$e = -m_1^2 + m_2^2 + p_1^2 + 2p_1 \cdot p_2, \ f = -m_3^2,$$
(C.9)

and the four-point scalar function is given by

$$D_{0}(p_{1}, p_{2}, p_{3}, m_{1}, m_{2}, m_{3}, m_{4}) = \int_{0}^{1} dx \int_{0}^{x} dy \int_{0}^{y} dz \frac{1}{\left[ax^{2} + by^{2} + gz^{2} + cxy + hxz + jyz + dx + ey + kz + f\right]^{2}},$$
(C.10)

where

$$a = p_3^2, b = p_2^2, g = p_1^2,$$

$$c = 2p_2 \cdot p_3, h = 2p_1 \cdot p_3, j = 2p_1 \cdot p_2,$$

$$d = m_3^2 - m_4^2 - p_3^2, e = m_2^2 - m_3^2 - 2p_2 \cdot p_3 - p_2^2,$$

$$k = m_1^2 - m_2^2 - 2p_1 \cdot p_2 - 2p_1 \cdot p_3 - p_1^2, f = m_4^2.$$

### C.2 Tensor reduction

Lorentz covariance of the integrals allows to decompose the tensor integrals into tensors constructed from the external momenta and the metric tensor  $g_{\mu\nu}$  with the scalar coefficients. The explicit Lorentz decompositions for the vector and tensor integrals  $B_{\mu}$ ,  $C_{\mu}$  and  $C_{\mu\nu}$  are given below. We are not going to show the four-point function because our calculation does not involve the box diagrams, but they can be found in Ref. [106].

For the two-point functions we have the relations

$$B_{\mu}(\ell, m_1, m_2) = \ell_{\mu} B_1(\ell, m_1, m_2), \tag{C.11}$$

$$B_1(\ell, m_1, m_2) = \frac{1}{2\ell^2} \left[ A_0(m_1) - A_0(m_2) - (\ell^2 + m_1^2 - m_2^2) B_0(\ell, m_1, m_2) \right]$$
 (C.12)

$$B_{\mu\nu}(\ell, m_1, m_2) = \ell_{\mu}\ell_{\nu}B_{21} + g_{\mu\nu}B_{22}, \tag{C.13}$$

$$B_{21}(\ell, m_1, m_2) = \frac{1}{3\ell^2} \left[ A_0(m_2) - m_1^2 B_0 - 2(\ell^2 + m_1^2 - m_2^2) B_1 - \frac{m_1^2 + m_2^2}{2} + \frac{\ell^2}{6} \right],$$
(C.14)

$$B_{22}(\ell, m_1, m_2) = \frac{1}{6} \left[ A_0(m_2) + 2m_1^2 B_0 + (\ell^2 + m_1^2 - m_2^2) B_1 + m_1^2 + m_2^2 - \frac{\ell^2}{3} \right],$$
(C.15)

$$\tilde{B}_{\mu}(\ell, m_1, m_2) = \ell_{\mu} \tilde{B}_1(\ell, m_1, m_2),$$
 (C.16)

$$\tilde{B}_1(\ell, m_1, m_2) = -A_0(m_2) + m_1^2 B_1(\ell, m_1, m_2), \tag{C.17}$$

$$\tilde{B}_0(\ell, m_1 m_2) = A_0(m_2) + m_1^2 B_0(\ell, m_1, m_2). \tag{C.18}$$

For the three-point functions we have the relations

$$C_{\mu}(\ell, s, m_1, m_2, m_3) = \ell_{\mu}C_{11} + s_{\mu}C_{12},$$
 (C.19)

$$C_{\mu\nu}(\ell, s, m_1, m_2, m_3) = \ell_{\mu}\ell_{\nu}C_{21} + s_{\mu}s_{\nu}C_{22} + (\ell_{\mu}s_{\nu} + \ell_{\nu}s_{\mu})C_{23} + g_{\mu\nu}C_{24},$$
(C.20)

where

$$C_{11} = \frac{1}{\kappa} \left[ s^2 R_1 - \ell \cdot s R_2 \right], \tag{C.21}$$

$$C_{12} = \frac{1}{\kappa} \left[ -\ell \cdot sR_1 + \ell^2 R_2 \right], \tag{C.22}$$

$$C_{24} = \frac{1}{4} \left[ B_0(s, m_2, m_3) + r_1 C_{11} + r_2 C_{12} + 2m_1^2 C_0 + 1 \right], \tag{C.23}$$

$$C_{21} = \frac{1}{\kappa} \left[ s^2 R_3 - \ell \cdot s R_5 \right], \tag{C.24}$$

$$C_{22} = \frac{1}{\kappa} \left[ -\ell \cdot sR_4 + \ell^2 R_6 \right], \tag{C.25}$$

$$C_{23} = \frac{1}{\kappa} \left[ -\ell \cdot sR_3 + \ell^2 R_5 \right] = \frac{1}{\kappa} \left[ s^2 R_4 - \ell \cdot sR_6 \right]. \tag{C.26}$$

with

$$\kappa = \ell^2 s^2 - (\ell \cdot s)^2. \tag{C.27}$$

$$r_1 = \ell^2 + m_1^2 - m_2^2. (C.28)$$

$$r_2 = (\ell + s)^2 - \ell^2 + m_2^2 - m_3^2.$$
 (C.29)

$$R_1 = \frac{1}{2} \left[ B_0(\ell + s, m_1, m_3) - B_0(s, m_2, m_3) - (\ell^2 + m_1^2 - m_2^2) C_0 \right].$$
 (C.30)

$$R_2 = \frac{1}{2} \left[ B_0(\ell, m_1, m_2) - B_0(\ell + s, m_1, m_3) + (\ell^2 - (\ell + s)^2 - m_2^2 + m_3^2) C_0 \right],$$

(C.31)

$$R_3 = -C_{24} - \frac{1}{2} \left[ r_1 C_{11} - B_1(\ell + s, m_1, m_3) - B_0(s, m_2, m_3) \right], \tag{C.32}$$

$$R_4 = -\frac{1}{2} \left[ r_1 C_{12} - B_1(\ell + s, m_1, m_3) + B_1(s, m_2, m_3) \right], \tag{C.33}$$

$$R_5 = -\frac{1}{2} \left[ r_2 C_{11} - B_1(\ell, m_1, m_2) + B_1(\ell + s, m_1, m_3) \right], \tag{C.34}$$

$$R_6 = -C_{24} - \frac{1}{2} \left[ r_2 C_{12} + B_1(\ell + s, m_1, m_3) \right]. \tag{C.35}$$

### C.3 UV-divergent parts of tensor integrals

For practical calculations it is useful to know the UV-divergent parts of the tensor integrals explicitly. We give directly the pole structures of the divergent one-loop

tensor coefficient integrals up to terms of the order  $\mathcal{O}(\epsilon)$ 

$$A_0(m) = \frac{m^2}{\epsilon}, \tag{C.36}$$

$$B_0(\ell, m_1, m_2) = \frac{1}{\epsilon}, \tag{C.37}$$

$$B_1(\ell, m_1, m_2) = -\frac{1}{2\epsilon},$$
 (C.38)

$$B_{21}(\ell, m_1, m_2) = \frac{1}{3\epsilon}, \tag{C.39}$$

$$B_{22}(\ell, m_1, m_2) = -\frac{1}{12} \left( \ell^2 - 3m_1^2 - 3m_2^2 \right),$$
 (C.40)

$$C_{24}(\ell, s, m_1, m_2, m_3) = \frac{1}{4\epsilon}.$$
 (C.41)

### C.4 Scalar two-point function

For the two-point function  $B_0$ , we notice that the Feynman parameter integration itself cannot result in a pole, cf. Eq. C.7, therefore we can use a series expansion in  $\epsilon$  to simplify the integration. The relevant  $B_0$  functions used in this calculation are listed below.

$$B_{0}(0,0,0) = 0,$$

$$B_{0}(\hat{s},0,m_{t}^{2}) = \frac{iC_{\epsilon}}{16\pi^{2}} \left\{ \frac{1}{\epsilon} + 2 - \frac{\hat{s}_{1}}{\hat{s}} \ln \frac{\hat{s}_{1}}{m_{t}^{2}} \right\},$$

$$B_{0}(m_{t}^{2},0,0) = \frac{iC_{\epsilon}}{16\pi^{2}} \left\{ \frac{1}{\epsilon} + 2 - i\pi \right\},$$

$$B_{0}(\hat{s},0,0) = \frac{iC_{\epsilon}}{16\pi^{2}} \left\{ \frac{1}{\epsilon} + 2 - \ln \frac{\hat{s}}{m_{t}^{2}} + i\pi \right\},$$

$$B_{0}(0,m_{t}^{2},0) = \frac{iC_{\epsilon}}{16\pi^{2}} \left\{ \frac{1}{\epsilon} + 1 \right\},$$

$$B_{0}(m_{t}^{2},m_{t}^{2},0) = \frac{iC_{\epsilon}}{16\pi^{2}} \left\{ \frac{1}{\epsilon} + 2 \right\},$$

$$B_0(\hat{s}, m_t^2, m_t^2) = \frac{iC_{\epsilon}}{16\pi^2} \left\{ \frac{1}{\epsilon} + 2 + \beta \ln \xi \right\}, \tag{C.42}$$

$$B_0(0, m_t^2, m_t^2) = \frac{iC_{\epsilon}}{16\pi^2} \frac{1}{\epsilon}, \tag{C.43}$$

where

$$C_{\epsilon} = \left(\frac{4\pi\mu^2}{m_t^2}\right)^{\epsilon} \Gamma(1+\epsilon),$$

$$\hat{s}_1 = \hat{s} - m_t^2,$$

$$\beta = \sqrt{1 - \frac{4m^2}{\hat{s}}},$$

$$\xi = \frac{1-\beta}{1+\beta}.$$

The  $B_1$  function can be easily derived from  $B_0$  function through the following relation,

$$B_1(x, m_1, m_2) = \frac{(m_2 - m_1) (B_0(x, m_1, m_2) - B_0(0, m_1, m_2))}{2x} - \frac{1}{2} B_0(x, m_1, m_2).$$
(C.44)

Then, we obtain

$$B_1(0,0,0) = 0, (C.45)$$

$$B_1(m_t^2, m_t^2, 0) = \frac{iC_{\epsilon}}{16\pi^2} \left\{ -\frac{1}{2\epsilon} - \frac{3}{2} \right\}, \tag{C.46}$$

$$B_1(\hat{s}, 0, 0) = \frac{iC_{\epsilon}}{16\pi^2} \left\{ -\frac{1}{2\epsilon} - 1 + \frac{1}{2} \ln \frac{\hat{s}}{m_t^2} \right\}, \tag{C.47}$$

$$B_1(\hat{s}, 0, m_t^2) = \frac{iC_{\epsilon}}{16\pi^2} \left\{ -\frac{1}{2\epsilon} - \frac{\hat{s}_1}{\hat{s}} - \frac{m_t^2}{2\hat{s}} + \frac{\hat{s}_1^2}{2\hat{s}^2} \ln \frac{\hat{s}_1}{m_t^2} \right\}.$$
 (C.48)

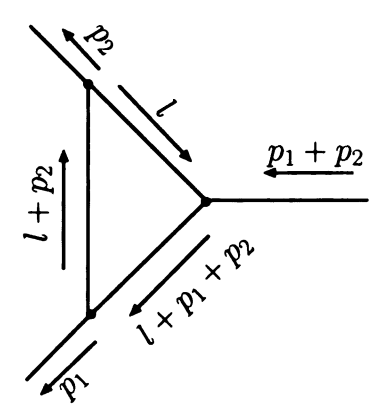


Figure C.1: The three-point green function with massless internal particles.

### C.5 Scalar three-point function

## **C.5.1** Analytical result of $C_0(p_1^2, p_2^2, 0, 0, 0)$

When the loop momentum in the scalar function goes to infinity, the ultra-violet divergence will appear and can be factorized from the rest finite components. Beside of the UV divergence, the infrared divergence may also arise in the case of the massless internal particles when the loop momentum goes to zero.

The exchange of gluon between the initial state massless quarks leads to the following divergent three-point integral:

$$C_0(p_1^2, p_2^2, 0, 0, 0) \equiv C_0^{\mathcal{A}} = \mu^{2\epsilon} \int \frac{d^n \ell}{(2\pi)^n} \frac{1}{\ell^2 (\ell + p_1)^2 (\ell + p_1 + p_2)^2}.$$
 (C.49)

The integral looks impossible, and in fact it will not be easy. The evaluation of such integrals requires another piece of computational technology, known as the method

of Feynman parameters \*After the Feynman parameterization, we get

$$C_0^{\mathcal{A}} = \mu^{2\epsilon} \int_0^1 dx \int_0^1 dy \int \frac{d^n \ell}{(2\pi)^n} \frac{1}{\left\{ [\ell + (p_1 + xp_2)y]^2 + \hat{s}xy(1 - y) \right\}^3}, \quad (C.50)$$

where  $\hat{s} = (p_1 + p_2)^2$ . Making the substitution,

$$\ell \to k - (p_1 + xp_4)y$$

the scalar function becomes

$$C_0^{\mathcal{A}} = \mu^{2\epsilon} \int_0^1 dx \int_0^1 dy \, (2y) \int \frac{d^n k}{(2\pi)^n} \frac{1}{\{k^2 + \hat{s}xy(1-y)\}^3}$$

$$= \mu^{2\epsilon} \int_0^1 dx \int_0^1 dy \, (2y) \frac{-i}{(4\pi)^{\frac{n}{2}}} \frac{\Gamma(3 - \frac{n}{2})}{\Gamma(3)} \left[ -\hat{s}xy(1-y) \right]^{\frac{n}{2} - 3}$$

$$= \frac{i}{16\pi^2} \left( \frac{4\pi\mu^2}{\hat{s}} \right)^{\epsilon} \frac{\Gamma(1+\epsilon)}{\Gamma(3)} \frac{2}{\hat{s}} (-1)^{\epsilon} \int_0^1 \frac{dx}{x^{1+\epsilon}} \int_0^1 dy \frac{y}{[y(1-y)]^{1+\epsilon}}$$

$$= \frac{i}{16\pi^2} \left( \frac{4\pi\mu^2}{\hat{s}} \right)^{\epsilon} \frac{\Gamma(1+\epsilon)}{\Gamma(3)} \frac{2}{\hat{s}} (-1)^{\epsilon} \frac{\Gamma^2(-\epsilon)}{\Gamma(1-2\epsilon)}, \tag{C.51}$$

where we have chosen  $n = 4 - 2\epsilon$ .

$$\frac{1}{A_1^{m_1}A_2^{m_2}\cdots A_n^{m_n}} = \int_0^1 dx_1\cdots dx_n \delta\left(\sum x_i - 1\right) \frac{\prod x_i^{m_i-1}}{[\sum x_i A_i]^{\sum m_i}} \frac{\Gamma(m_1 + \cdots + m_n)}{\Gamma(m_1)\cdots\Gamma(m_n)}.$$

The function FeynmanParameterization is defined as following:

$$Feynman Parameterization[p: \{\{\_,\_\}..\}, x\_List]/; \ Length[x] === Length[p] := Module[$$

$${d,a}, {d,a} = Transpose[p];$$

$$\frac{Gamma[Plus @@ a]}{Times @@ Gamma[a]} (DiracDelta[1-Plus @@ x] Times @@  $x^{a-1})/(Plus @@ (d x))^{Plus @@ a}]$$$

Usage:

FeynmanParameterization[
$$\{\{A_1, m_1\}, \cdots, \{A_n, m_n\}\}, \{x_1, \cdots, x_n\}$$
].

<sup>\*</sup>Here is the MATHEMATICA code for Feynman parameterization:

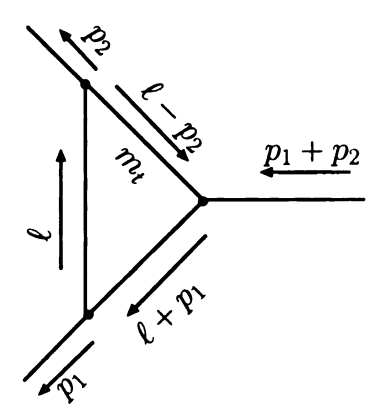


Figure C.2: The three-point green function with one massive internal particle.

Using the properties of  $\Gamma$ -functions in F and the following relations

$$\Re(-1)^{\epsilon} = 1 - \frac{\pi^2}{2} \epsilon^2, \tag{C.52}$$

$$\left(\frac{\hat{s}}{m_t^2}\right)^{-\epsilon} = 1 - \epsilon \ln \frac{\hat{s}}{m_t^2} + \frac{\epsilon^2}{2} \ln^2 \left(\frac{\hat{s}}{m_t^2}\right), \tag{C.53}$$

we get the three-point scalar function with massless internal particles as

$$C_0^{\mathcal{A}} = \frac{i}{16\pi^2} \left( \frac{4\pi\mu^2}{m_t^2} \right)^{\epsilon} \frac{\Gamma(1+\epsilon)}{\hat{s}} \left\{ \frac{1}{\epsilon^2} - \frac{1}{\epsilon} \ln \frac{\hat{s}}{m_t^2} + \frac{1}{2} \ln^2 \left( \frac{\hat{s}}{m_t^2} \right) - \frac{2\pi^2}{3} \right\}.$$
 (C.54)

Here the double poles shows up as one expects due to the soft and collinear singularities.

### C.5.2 Analytical result of $C_0((p_1 + p_2)^2, (-p_2)^2, 0, m_t^2, 0)$

The exchange of gluon between the final state top quark and bottom quarks leads to the following divergent three-point integral (cf. Fig. C.2):

$$C_0\left((-p_2)^2, (p_1+p_2)^2, 0, m_t^2, 0\right) \equiv C_0^{\mathcal{B}} = \mu^{2\epsilon} \int \frac{d^n \ell}{(2\pi)^n} \frac{1}{\ell^2 (\ell + p_1)^2 \left((\ell - p_2)^2 - m_t^2\right)}.$$
(C.55)

After the Feynman parameterization we obtain

$$C_0^{\mathcal{B}} = \mu^{2\epsilon} \int_0^1 dx \int_0^1 dy \, (2y) \int \frac{d^n \ell}{(2\pi)^2} \frac{1}{\{\ell^2 + 2\ell \cdot p\}^3},\tag{C.56}$$

where  $p = [xp_1 - (1-x)p_2]y$ . After substitution  $\ell \to k-p$ , we have

$$C_0^{\mathcal{B}} = \mu^{2\epsilon} \int_0^1 dx \int_0^1 dy \, (2y) \int \frac{d^n k}{(2\pi)^n} \frac{1}{\{k^2 - p^2\}^3}$$

$$= -\frac{i}{16\pi^2} (4\pi\mu^2)^{\epsilon} \Gamma(1+\epsilon) \int_0^1 dx \, (1-x)^{-1-\epsilon} (m_t^2 - \hat{s}x)^{-1-\epsilon} \int_0^1 dy \, y^{-1-2\epsilon}$$

$$= \frac{i}{16\pi^2} \left(\frac{4\pi\mu^2}{m_t^2}\right)^{\epsilon} \frac{\Gamma(1+\epsilon)}{m_t^2} \frac{1}{2\epsilon} \frac{\Gamma(-\epsilon)}{\Gamma(1-\epsilon)} {}_2F_1\left(1+\epsilon, 1, 1-\epsilon, \frac{\hat{s}}{m_t^2}\right). \quad (C.57)$$

In the limit  $\epsilon \to 0$ ,

$$2F_{1}\left(1+\epsilon,1,1-\epsilon,\frac{\hat{s}}{m_{t}^{2}}\right)$$

$$=\left(1-\frac{\hat{s}}{m_{t}^{2}}\right)^{-1-2\epsilon} {}_{2}F_{1}\left(-2\epsilon,-\epsilon,1-\epsilon,\frac{\hat{s}}{m_{t}^{2}}\right)$$

$$=\left(-\frac{\hat{s}_{1}}{m_{t}^{2}}\right)^{-1-2\epsilon} \times \left[1+2\epsilon^{2}\operatorname{Li}\left(\frac{\hat{s}}{m_{t}^{2}}\right)\right],$$
(C.58)

therefore,

$$C_0^{\mathcal{B}} = \frac{i}{16\pi^2} \left( \frac{4\pi\mu^2}{m_t^2} \right)^{\epsilon} \frac{\Gamma(1+\epsilon)}{\hat{s}_1} \left\{ \frac{1}{2\epsilon^2} - \frac{1}{\epsilon} \ln\left(-\frac{\hat{s}_1}{m_t^2}\right) - \text{Li}_2\left(\frac{\hat{s}}{\hat{s}_1}\right) + \frac{1}{2} \ln^2\left(-\frac{\hat{s}_1}{m_t^2}\right) \right\}. \tag{C.59}$$

The logarithm is commonly defined with a branch cut along the negative real axis, therefore

$$\ln\left(-\frac{\hat{s}}{m^2}\right) \to \ln\left(-\frac{\hat{s} + i\epsilon m^2}{m^2}\right) = \ln\left(\frac{\hat{s}}{m^2}\right) - i\pi. \tag{C.60}$$

Applying Eq. C.60 into  $C_0^{\mathcal{B}}$ , we obtain

$$C_0^{\mathcal{B}} = \frac{i}{16\pi^2} C_{\epsilon} \frac{1}{\hat{s}_1} \left\{ \frac{1}{2\epsilon^2} - \frac{1}{\epsilon} \ln\left(\frac{\hat{s}_1}{m_t^2}\right) - \text{Li}_2\left(\frac{\hat{s}}{\hat{s}_1}\right) + \frac{1}{2} \ln^2\left(\frac{\hat{s}_1}{m_t^2}\right) - \frac{\pi^2}{2} \right\}, \text{ (C.61)}$$

where

$$C_{\epsilon} = \left(\frac{4\pi\mu^2}{m_t^2}\right)^{\epsilon} \Gamma(1+\epsilon).$$

Note that we only keep the real parts in the calculation and discard the imaginary parts since it will contribute at the next-leading order.

# Appendix D

## Virtual Corrections

### D.1 Virtual correction to $W^{+*} \rightarrow \bar{q}q'$

The virtual correction to the process  $W^* \to \bar q q'$  comes from the diagram in Fig. D.1. The amplitude reads

$$i\mathcal{M} = \epsilon^{\mu}(q)(-ig_{s})^{2}i\frac{g}{\sqrt{2}}C_{F}$$

$$\times \mu^{2\epsilon} \int \frac{d^{n}k}{(2\pi)^{n}}\bar{u}(p_{1})\gamma_{\rho}\frac{i(\not k+\not p_{1}+\not p_{2})}{(k+p_{1}+p_{2})^{2}}\gamma_{\mu}P_{L}\frac{i\not k}{k^{2}}\gamma_{\sigma}v(p_{2})\frac{-ig_{\rho\sigma}}{(k+p_{2})^{2}}$$

$$= \epsilon^{\mu}(q)\frac{gg_{s}^{2}}{\sqrt{2}}C_{F}$$

$$\times \mu^{2\epsilon} \int \frac{d^{n}k}{(2\pi)^{n}}\bar{u}(p_{1})\left[\frac{\gamma_{\rho}(\not k+\not p_{1}+\not p_{2})\gamma_{\mu}\not k\gamma^{\rho}}{k^{2}(k+p_{2})^{2}(k+p_{1}+p_{2})^{2}}\right]P_{L}v(p_{2}), \tag{D.1}$$

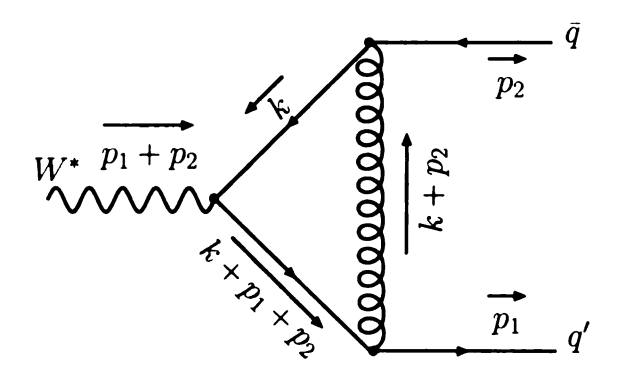


Figure D.1: Feynman diagram for process  $W^* \to q' \bar{q}$ .

where  $q = p_1 + p_2$ .

In the DRED, the tensor in the loop integral can be further simplified

$$n_{\mu} = \gamma_{\rho} (\not k + \not p_{1} + \not p_{2}) \gamma_{\mu} \not k \gamma^{\rho}$$

$$= -4k^{\mu} \not k - 4k^{\mu} \not q + 2\gamma^{\mu} \not k \not k + 2\gamma^{\mu} \not k \not q.$$

Using the scalar function and tensor reduction, we obtain

$$\begin{split} &\mu^{2\epsilon} \int \frac{d^n k}{(2\pi)^n} \frac{n_\mu}{k^2 (k+p_2)^2 (k+p_1+p_2)^2} \\ = & -4 \left[ q_\mu \not q C_{21} + p_{1\mu} \not p_2 C_{22} - (q_\mu \not p_1 + p_{1\mu} \not q) C_{23} + \gamma_\mu C_{24} \right] \\ & + 2\gamma_\mu \left[ \not q \not q C_{21} + \not p_1 \not p_1 C_{22} - (\not q \not p_1 + \not p_1 \not q) C_{23} + 4C_{24} \right] \\ & + 2\gamma_\mu \left[ \not q \not q C_{11} - \not p_1 \not q C_{12} \right], \end{split}$$

where the scalar coefficients  $(C_{ij})$  stand for  $C_{ij}(p_1 + p_2, -p_1, 0, 0, 0)$ . Using the onshell conditions of the massless quarks  $(\bar{q} \text{ and } q')$ 

$$\bar{u}(p_1) \not p_1 = 0,$$
 $\not p_2 v(p_2) = 0,$ 

and

$$\label{eq:q_def} \not q \not q \ = \ \frac{1}{2} \left\{ \gamma^\alpha \gamma^\beta + \gamma^\beta \gamma^\alpha \right\} q_\alpha q_\beta = q^2,$$

we obtain

$$\mu^{2\epsilon} \int \frac{d^n k}{(2\pi)^n} \frac{n_{\mu}}{k^2 (k+p_2)^2 (k+p_1+p_2)^2}$$

$$= \gamma_{\mu} \left\{ 4C_{24} + 2\hat{s} \left( C_{21} - C_{23} + C_{11} \right) \right\}, \tag{D.2}$$

where  $\hat{s} = q^2$ . In order to restore gauge invariance in the DRED scheme, we need add a counterterm whose contribution is just a constant "-1" always associated with the

UV-divergent term  $1/\epsilon$ . Thus we replace

$$4C_{24} \rightarrow 4C_{24} - 1,$$

which leaves the amplitude as

$$i\mathcal{M} = \frac{gg_s^2}{\sqrt{2}} C_F \bar{u}(p_1) \gamma_{\mu} \left\{ 4C_{24} + 2\hat{s} \left( C_{21} - C_{23} + C_{11} \right) \right\} P_L v(p_2) \epsilon^{\mu}(q)$$
$$= i\mathcal{M}_{Born} \times g_s^2 C_F \left\{ 4C_{24} - 1 + 2\hat{s} \left( C_{21} - C_{23} + C_{11} \right) \right\},$$

where  $\mathcal{M}_{Born}$  stands for the Born level amplitude.

In the DREG, both momentum and  $\gamma$ -matrices are handled in  $n=4-2\epsilon$  dimensions. The tensor in the loop integral is

$$n_{\mu} = \gamma_{\rho}(\not k + \not q)\gamma_{\mu} \not k \gamma^{\rho}$$

$$= -2 \not k \gamma_{\mu}(\not k + \not q) + 2\epsilon(\not k + \not q)\gamma_{\mu} \not k$$

After integrating over k and using the scalar function and tensor reduction, we obtain

$$\mu^{2\epsilon} \int \frac{d^n k}{(2\pi)^n} \frac{n_\mu}{k^2 (k+p_2)^2 (k+p_1+p_2)^2} = \gamma_\mu \left\{ 4C_{24} - 2 + 2\hat{s} \left( C_{21} - C_{23} + C_{11} \right) \right\},\tag{D.3}$$

therefore, the amplitude becomes

$$i\mathcal{M} = i\mathcal{M}_{Born} \times g_s^2 C_F \left\{ 4C_{24} - 2 + 2\hat{s} \left( C_{21} - C_{23} + C_{11} \right) \right\}.$$

In order to get the analytical expression of the form factor, we can further decom-

pose the scalar coefficients,  $C_{ij}$ , to  $B_0$  and  $C_0$  functions:

$$C_{11} = -C_0 - \frac{1}{\hat{s}} B_0(q, 0, 0) = -C_0 - \frac{1}{\hat{s}\hat{\epsilon}} - \frac{2}{\hat{s}} + \frac{1}{\hat{s}} \ln\left(\frac{\hat{s}}{\mu^2}\right), \tag{D.4}$$

$$C_{12} = -C_0 - \frac{2}{\hat{s}} B_0(q, 0, 0) = -C_0 - \frac{2}{\hat{s}\epsilon} - \frac{4}{\hat{s}} + \frac{2}{\hat{s}} \ln\left(\frac{\hat{s}}{\mu^2}\right), \tag{D.5}$$

$$C_{21} = -C_{11} - \frac{1}{\hat{s}} B_1(q, 0, 0) = C_0 + \frac{3}{2\hat{s}\epsilon} + \frac{3}{\hat{s}} - \frac{3}{2\hat{s}} \ln\left(\frac{\hat{s}}{\mu^2}\right), \tag{D.6}$$

$$C_{24} = \frac{1}{4} + \frac{1}{4}B_0(q, 0, 0) = \frac{3}{4} + \frac{1}{4\epsilon} - \frac{1}{4}\ln\left(\frac{\hat{s}}{\mu^2}\right),$$
 (D.7)

$$C_{22} = C_{12} + \frac{4}{\hat{s}}C_{24} - 2C_{12} = C_0 + \frac{3}{\hat{s}\epsilon} + \frac{7}{\hat{s}} - \frac{2}{\hat{s}}\ln\left(\frac{\hat{s}}{\mu^2}\right), \tag{D.8}$$

$$C_{23} = C_0 + \frac{5}{2\hat{s}\epsilon} + \frac{11}{2\hat{s}} - \frac{5}{2\hat{s}} \ln\left(\frac{\hat{s}}{\mu^2}\right). \tag{D.9}$$

Using the analytical expression of  $C_0$  (cf. Eq. C.54), we obtain

$$i\mathcal{M} = -\frac{ig}{\sqrt{2}}\bar{u}(p_1)\gamma_{\mu}P_Lv(p_2)\epsilon^{\mu}(q) f_1^{W^* \to \bar{q}q'(\mathrm{virt})},$$

where

$$f_1^{W^* \to \bar{q}q'(\text{virt})} = \frac{\alpha_s}{4\pi} C_F C_\epsilon \left\{ -\frac{2}{\epsilon^2} + \frac{2}{\epsilon} \ln \frac{\hat{s}}{m_t^2} - \frac{3}{\epsilon} + \frac{4\pi^2}{3} + 3 \ln \frac{\hat{s}}{m_t^2} - \ln^2 \frac{\hat{s}}{m_t^2} + I_{\text{scheme}}^{W^* \to \bar{q}q'(\text{virt})} \right\}.$$
 (D.10)

The scheme dependent term  $I_{\text{scheme}}^{W^* \to \bar{q}q'(\text{virt})}$  is

$$I_{\text{Scheme}}^{W^* \to \bar{q}q'(\text{virt})} = \begin{cases} -8 & \text{in DREG scheme,} \\ -7 & \text{in DRED scheme.} \end{cases}$$

Now we can cross the final state particles into the initial state to get the form factors discussed in section 3.4.1 and 3.4.3, respectively.

• For the  $q - \bar{q'} - W^*$  vertex (s-channel initial state):

$$\begin{array}{ccc} p_{\bar{q}} & \to & -p_q, \\ \\ p_{q'} & \to & -p_{\bar{q'}}, \end{array}$$

which gives

$$f_1^{q\bar{q'}\to W^*(\text{virt})} = \frac{\alpha_s}{4\pi} C_F C_\epsilon \left\{ -\frac{2}{\epsilon^2} + \frac{2}{\epsilon} \ln \frac{\hat{s}}{m_t^2} - \frac{3}{\epsilon} + \frac{4\pi^2}{3} + 3\ln \frac{\hat{s}}{m_t^2} - \ln^2 \frac{\hat{s}}{m_t^2} + I_{\text{scheme}}^{q\bar{q'}\to W^*(\text{virt})} \right\}.$$

• For the  $q - W^* - q'$  vertex (t-channel light quark line):

$$p_{\bar{q}} \rightarrow -p_q,$$

which gives

$$f_1^{q \to Wq'(\text{virt})} = \frac{\alpha_s}{4\pi} C_F C_\epsilon \left\{ -\frac{2}{\epsilon^2} + \frac{2}{\epsilon} \ln(\frac{-\hat{t}}{m_t^2}) - \frac{3}{\epsilon} + \frac{\pi^2}{3} + 3\ln(\frac{-\hat{t}}{m_t^2}) - \ln^2(\frac{-\hat{t}}{m_t^2}) + I_{\text{scheme}}^{q \to Wq'(\text{virt})} \right\}.$$

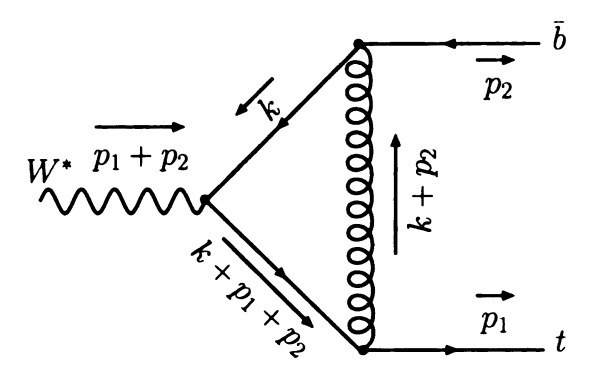


Figure D.2: Feynman diagram for process  $W^* \to t\bar{b}$ .

### **D.2** Virtual correction to $W^{+*} \rightarrow t\bar{b}$

The virtual correction to the process  $W^* \to t\bar{b}$  comes from the diagram in Fig. D.2. The amplitude reads

$$i\mathcal{M} = \epsilon^{\mu}(q)(-ig_{s})^{2}i\frac{g}{\sqrt{2}}C_{F}$$

$$\times \mu^{2\epsilon} \int \frac{d^{n}k}{(2\pi)^{n}}\bar{u}(p_{1})\gamma_{\rho}\frac{i(\not k+\not p_{1}+\not p_{2}+m_{t})}{(k+p_{1}+p_{2})^{2}-m_{t}^{2}}\gamma_{\mu}P_{L}\frac{i\not k}{k^{2}}\gamma_{\sigma}v(p_{2})\frac{-ig_{\rho\sigma}}{(k+p_{2})^{2}}$$

$$= \epsilon^{\mu}(q)\frac{gg_{s}^{2}}{\sqrt{2}}C_{F}$$

$$\times \mu^{2\epsilon} \int \frac{d^{n}k}{(2\pi)^{n}}\bar{u}(p_{1})\left[\frac{\gamma_{\rho}(\not k+\not q)\gamma_{\mu}\not k\gamma^{\rho}+m_{t}\gamma_{\rho}\gamma_{\mu}\not k\gamma^{\rho}}{k^{2}(k+p_{2})^{2}\left((k+q)^{2}-m_{t}^{2}\right)}\right]P_{L}v(p_{2}), (D.11)$$

where  $q = p_1 + p_2$ . The tensor in the loop integral can be further simplified

$$\begin{array}{lll} n_{\mu} & = & \gamma_{\rho}(\not\! k + \not\! q) \gamma_{\mu} \not\! k \gamma^{\rho} + m_{t} \gamma_{\rho} \gamma_{\mu} \not\! k \gamma^{\rho} \\ \\ & = & -4k_{\mu} \not\! k - 4k_{\mu} \not\! q + 2\gamma_{\mu} \not\! k \not\! k + 2\gamma_{\mu} \not\! k \not\! q + 4m_{t} k_{\mu}. \end{array}$$

Using the scalar function and tensor reduction, we obtain

$$\mu^{2\epsilon} \int \frac{d^n k}{(2\pi)^n} \frac{n_{\mu}}{k^2 (k+p_2)^2 (k+p_1+p_2)^2}$$

$$= \gamma_{\mu} \left[ 4C_{24} + 2m_t^2 \left( C_{21} - 2C_{23} + C_{22} + C_{11} - C_{12} \right) + 2\hat{s}_1 \left( C_{21} - C_{23} + C_{11} \right) \right]$$

$$+ \frac{(p_2 - p_1)_{\mu}}{m_t} \left[ 2m_t^2 \left( C_{23} - C_{22} \right) \right].$$

where the scalar coefficients  $(C_{ij})$  stand for  $C_{ij}(p_1+p_2,-p_2,0,m_t,0)$  and  $\hat{s}_1=\hat{s}-m_t^2$ . Here, we take advantage of the fact that the W-boson couples to the massless quarks  $(\bar{q} \text{ and } q')$  in the initial state

$$\bar{u}(p_1) dv(p_2) = 0,$$

and

$$\label{eq:problem} \not q \not q = \frac{1}{2} \left\{ \gamma^\alpha \gamma^\beta + \gamma^\beta \gamma^\alpha \right\} q_\alpha q_\beta = q^2,$$

Again, we also need replace  $4C_{24}$  by  $4C_{24} - 1$  in the DRED scheme, while replacing  $4C_{24}$  by  $4C_{24} - 2$  in the DREG scheme. As explained in section C.2, we can further decompose the scalar coefficients,  $C_{ij}$ , to  $B_0$  and  $C_0$  functions:

$$C_{11} = -C_0 - \frac{1}{\hat{s}_1 \epsilon} - \frac{2}{\hat{s}_1} + \frac{1}{\hat{s}} \ln \left( \frac{\hat{s}_1}{\mu^2} \right) + \frac{2m_t^2}{\hat{s}\hat{s}_1} \ln \left( \frac{\hat{s}_1}{m_t^2} \right), \tag{D.12}$$

$$C_{12} = -C_0 - \frac{1}{\hat{s}_1 \epsilon} - \frac{2}{\hat{s}_1} + \frac{2}{\hat{s}_1} \ln \left( \frac{\hat{s}_1}{\mu^2} \right), \tag{D.13}$$

$$C_{11} - C_{12} = -\frac{1}{\hat{s}} \ln \left( \frac{\hat{s}_1}{m_t^2} \right),$$
 (D.14)

$$C_{21} - C_{23} = \frac{1}{2\hat{s}} \left( -1 + \frac{m_t^2}{\hat{s}} \ln \left( \frac{\hat{s}_1}{m_t^2} \right) + \frac{2\hat{s}_1}{\hat{s}} \ln \left( \frac{\hat{s}_1}{m_t^2} \right) \right), \tag{D.15}$$

$$C_{22} - C_{23} = -\frac{1}{2\hat{s}} \ln \left( \frac{\hat{s}_1}{m_t^2} \right).$$
 (D.16)

The on-shell renormalization scheme is adapted in our calculation to get rid of the UV-divergence. A counterterms of the wave function of top quark  $(\delta Z_t)$  is introduced

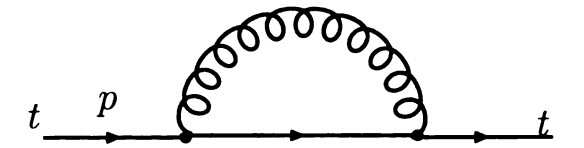


Figure D.3: Feynman diagram of the self-energy correction to top quark.

such that

$$\delta \mathcal{M} = \frac{\delta Z_t}{2} \times \mathcal{M}_{Born},$$

where

$$\delta Z_t = \frac{\partial \Sigma(\mathbf{p})}{\partial \mathbf{p}} |_{p^2 = m_t^2}.$$

The self energy correction to top quark is shown in Fig. D.3 and can be written in terms of two-point scalar functions:

$$i\Sigma(p) = -g_s^2 C_F \mu^{2\epsilon} \int \frac{d^n q}{(2\pi)^n} \frac{\gamma_\mu i(q + m_t) \gamma^\mu}{(q^2 - m_t^2)(q + p)^2}$$

$$= i(-g_s^2) \frac{1}{16\pi^2} C_F C_\epsilon \left[ (2 - 2\epsilon) B_1(p^2, m_t, 0) \not p + (4 - 2\epsilon) m_t B_0(p^2, m_t, 0) \right].$$

Furthermore, the UV-divergent parts of  $B_0$  and  $B_1$  function are

$$B_0 = \frac{1}{\epsilon} + \mathcal{O}(\epsilon),$$

$$B_1 = -\frac{1}{2\epsilon} + \mathcal{O}(\epsilon),$$

which lead to

$$(2-2\epsilon)B_1 \rightarrow 2B_1 - 2\epsilon \times (-\frac{1}{2\epsilon}) = 2B_1 + 1,$$
  
 $(4-2\epsilon)B_0 \rightarrow 4B_0 - 2\epsilon \times \frac{1}{\epsilon} = 4B_0 - 2.$ 

The final result of the top quark self-energy becomes

$$\Sigma(\not p) = -g_s^2 \frac{1}{16\pi^2} C_F C_\epsilon \left\{ \left[ 2B_1(p^2, m_t, 0) + 1 \right] \not p + m_t \left[ 4B_0(p^2, m_t, 0) - 2 \right] \right\}.$$

The fermionic self-energy on the top mass shell is ultraviolet divergent but finite in the infrared regime, whilst its derivative,  $\partial \Sigma(p)/\partial p^2|_{p^2=m_t^2}$ , develops a singularity due to the zero mass of the photon, which is of infrared origin. It is easy to derive

$$\frac{\partial}{\partial p^2} B_0 \left( p^2, m_t, 0 \right) = \frac{1}{2m_t^2} \left( \frac{1}{\epsilon} + 2 \right),$$

$$\frac{\partial}{\partial p^2} B_1(p^2, m_t, 0) = -\frac{1}{2m_t^2} \left( \frac{1}{\epsilon} + 3 \right),$$

from which we derive

$$\begin{split} \delta Z_t &= \left. \frac{\partial \Sigma(\not p)}{\partial \not p} \right|_{p^2 = m_t 2} \\ &= \left. - \frac{\alpha_s}{4\pi} C_F C_\epsilon \left[ 2B_1(p^2, m_t, 0) + 1 - 4m_t^2 \frac{\partial}{\partial p^2} B_1(p^2, m_t, 0) \right|_{p^2 = m_t^2} \\ &- 8m_t^2 \frac{\partial}{\partial p^2} B_0(p^2, m_t, 0) \right|_{p^2 = m_t^2} \right] \\ &= \left. - \frac{\alpha_s}{4\pi} C_F C_\epsilon \left( \frac{3}{\epsilon} + 4 \right). \end{split}$$

Including the contribution from the wave function counterterm and using the analytical expression of  $C_0^{\mathcal{B}}$  (cf. Eq. C.5.2), we obtain

$$i\mathcal{M} = \frac{-ig}{\sqrt{2}}\bar{u}(p_1)\left[f_1^{W^*\to t\bar{b}(\mathrm{virt})}\gamma_\mu + f_2^{W^*\to t\bar{b}(\mathrm{virt})}\frac{(p_1-p_2)_\mu}{m_t}\right]P_Lv(p_2)\epsilon^\mu(q),$$
 where  $f_1^{W\to t\bar{b}}$ ,  $f_2^{W\to t\bar{b}}$  are

$$f_{1}^{W \to t\bar{b}(\text{virt})} = \frac{\alpha_{s}}{4\pi} C_{F} C_{\epsilon} \left\{ -\frac{1}{\epsilon^{2}} - \frac{5}{2\epsilon} + \frac{2}{\epsilon} \ln \frac{\hat{s}_{1}}{m_{t}^{2}} + \pi^{2} + 2 \text{Li}_{2}(\frac{\hat{s}}{\hat{s}_{1}}) + 3 \ln \frac{\hat{s}_{1}}{m_{t}^{2}} - \frac{m_{t}^{2}}{\hat{s}} \ln \frac{\hat{s}_{1}}{m_{t}^{2}} - \ln^{2} \frac{\hat{s}_{1}}{m_{t}^{2}} + I_{\text{Scheme}}^{W \to t\bar{b}(\text{virt})} \right\}, \quad (D.17)$$

$$f_2^{W \to t\bar{b}(\text{virt})} = \frac{\alpha_s}{4\pi} C_F C_\epsilon \left\{ \frac{m_t^2}{\hat{s}} \ln \frac{\hat{s}_1}{m_t^2} \right\}, \tag{D.18}$$

where  $\hat{s}=(p_1+p_2)^2,\ \hat{s}_1=2p_1\cdot p_2=\hat{s}-m_t^2$  and the scheme dependent term  $I_{\text{Scheme}}^{W\to t\bar{b}(\text{virt})}$  is

$$I_{\text{Scheme}}^{W \to t\bar{b}(\text{virt})} = \begin{cases} -6 & \text{in DREG scheme,} \\ -5 & \text{in DRED scheme.} \end{cases}$$

Now we can cross the final state particles into the initial state to get the form factors of the  $b-W^*-t$  vertex (t-channel heavy quark line) discussed in section 3.4.4:

$$p_{\bar{b}} \rightarrow -p_b,$$

which gives  $f_1^{bW \to t}$ ,  $f_2^{bW \to t}$  as

$$\begin{split} f_1^{bW \to t (\text{virt})} &= \frac{\alpha_s}{4\pi} C_F C_\epsilon \left\{ -\frac{1}{\epsilon^2} - \frac{5}{2\epsilon} + \frac{2}{\epsilon} \ln(\frac{-\hat{t}_1}{m_t^2}) + 2 \text{Li}_2(\frac{\hat{t}}{\hat{t}_1}) \right. \\ &+ 3 \ln(\frac{-\hat{t}_1}{m_t^2}) - \frac{m_t^2}{\hat{t}} \ln(\frac{-\hat{t}_1}{m_t^2}) - \ln^2(\frac{-\hat{t}_1}{m_t^2}) + I_{\text{Scheme}}^{bW \to t (\text{virt})} \right\}, \\ f_2^{bW \to t (\text{virt})} &= \frac{\alpha_s}{4\pi} C_F C_\epsilon \left\{ \frac{m_t^2}{\hat{t}} \ln(\frac{-\hat{t}_1}{m_t^2}) \right\}, \end{split}$$

where  $\hat{t}_1 = \hat{t} - m_t^2 = -2p_b \cdot p_t$ , and the scheme dependent term  $I_{\text{Scheme}}^{bW \to t(\text{virt})}$  is

$$I_{\text{Scheme}}^{bW \to t(\text{virt})} = \begin{cases} -6 & \text{in DREG scheme,} \\ -5 & \text{in DRED scheme.} \end{cases}$$

# Appendix E

### Real corrections: Soft and Collinear

E.1 
$$W^* \rightarrow \bar{q}q'$$

#### E.1.1 Soft contribution

Under the soft approximation in the soft region, the squared matrix element can be written as a factor multiplying the squared Born matrix element:

$$\Theta(2s_{min} - \left|s_{\bar{q}g}\right| - \left|s_{q'g}\right|) \left|\mathcal{M}(W^* \to \bar{q}q'g)\right|^2 \xrightarrow{p_g \to 0} \hat{f}_{soft}^{W^* \to \bar{q}q'g} \left|\mathcal{M}(W^* \to \bar{q}q')\right|,$$

where we have defined the eikonal factor  $\hat{f}_{soft}^{W^* \to \bar{q}q'g}$  as

$$\hat{f}_{soft}^{W^* \to \bar{q}q'g} = g_s C_F \mu^{2\epsilon} \frac{4(2p_{\bar{q}} \cdot p_{q'})}{(2p_{\bar{q}} \cdot p_g)(2p_{q'} \cdot p_g)}.$$

In the c.m. frame of  $W^*$ , we can choose the explicit momentum of final state

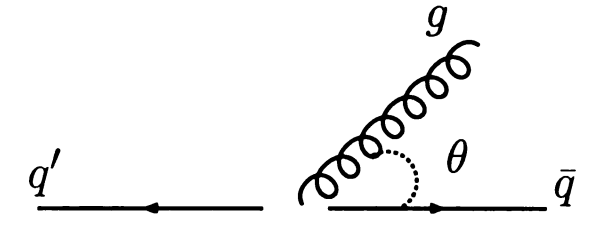


Figure E.1: Kinematics of  $\bar{q}$ , q' and g in the rest frame of  $W^*$ .

particles as shown in Fig. E.1,

$$p_{\bar{q}} = \left(\frac{\sqrt{\hat{s}}}{2}, 0, 0, \frac{\sqrt{\hat{s}}}{2}\right)$$

$$p_{q'} = \left(\frac{\sqrt{\hat{s}}}{2}, 0, 0, -\frac{\sqrt{\hat{s}}}{2}\right)$$

$$p_{g} = \left(E_{g}, 0, E_{g} \sin \theta_{1}, E_{g} \cos \theta_{1}\right),$$

which lead to

$$\hat{f}_{soft}^{W^* \to \bar{q}q'} = g_s C_F \mu^{2\epsilon} \frac{1}{E_q^2 (1 + \cos \theta_1)(1 - \cos \theta_1)}.$$
 (E.1)

The soft phase space boundary condition  $\mathcal{F}_2$  can be written as

$$\Theta(2s_{min} - s_{\bar{q}g} - s_{q'g}) = \Theta\left(2s_{min} - 2(p_{\bar{q}} + p_{q'}) \cdot p_g\right) 
= \Theta\left(2s_{min} - 2p_{W^*} \cdot p_g\right) 
= \Theta\left(2s_{min} - 2\sqrt{\hat{s}}E_g\right),$$
(E.2)

which gives

$$E_g \le \frac{s_{min}}{\sqrt{\hat{s}}}. ag{E.3}$$

In the last two steps of Eq. E.2 we have used the facts that  $p_{W^*} = p_{\bar{q}} + p_{q'} + p_g$  and  $p_{W^*} = (\sqrt{\hat{s}}, 0, 0, \sqrt{\hat{s}})$  in the c.m. frame of the W-boson. In the soft region, the 3-body phase space can be separated into a 2 body phase space factor times a soft phase space factor:

$$d^{n}\Phi_{3} = \int \frac{d^{n-1}p_{\bar{q}}}{2E_{p_{\bar{q}}}(2\pi)^{n-1}} \int \frac{d^{n-1}p_{q'}}{2E_{p_{q'}}(2\pi)^{n-1}} \cdot (2\pi)^{n} \delta^{n}(p_{W^{*}} - p_{\bar{q}} - p_{q'} - p_{g})$$
$$\cdot \int \frac{d^{n-1}p_{g}}{2E_{q}(2\pi)^{n-1}}.$$
 (E.4)

For the soft limit, we set the gluon momenta  $p_g = 0$  in the delta function and the phase space then factorizes:

$$d^{n}\Phi_{3} \xrightarrow{p_{g} \to 0} d^{n}\Phi_{2} \int \frac{d^{n-1}p_{g}}{2E_{g}(2\pi)^{n-1}}$$
 (E.5)

The phase space is most easily evaluated by choosing an explicit representation for the gluon momentum,

$$p_q = E_q(1, \dots, \sin \theta_1 \sin \theta_2, \sin \theta_1 \cos \theta_1, \cos \theta_1), \tag{E.6}$$

yielding,

$$d^{n-1}p_{g} = d |\vec{p}_{g}| |\vec{p}_{g}|^{n-2} d\Omega_{n-2}$$

$$= dE_{g}E_{g}^{n-2} \sin^{n-3}\theta_{1} d\theta_{1} \sin^{n-4}\theta_{2} d\theta_{2} d\Omega_{n-4}$$
(E.7)

where,

$$\Omega_{n-4} = \frac{2\pi^{(n-3)/2}}{\Gamma(\frac{n-3}{2})}. (E.8)$$

Now the phase space in the soft region becomes

$$d^{n}\Phi_{3} \xrightarrow{p_{g}\to 0} d^{n}\Phi_{2} \frac{1}{8\pi^{2}} \frac{(4\pi)^{\epsilon}}{\Gamma(1-\epsilon)} E_{g}^{1-2\epsilon} \sin^{-2\epsilon}\theta \, dE_{g} d\cos\theta. \tag{E.9}$$

It is very simple to analytically integrate the eikonal factors  $\hat{f}_s^{W^* \to \bar{q}q'g}$  (cf. Eq. E.1) in d dimensions over the soft gluon momentum and get the soft factor

$$I_{\text{soft}}^{W^* \to \bar{q}q'g} = \int \hat{f}_{\text{soft}}^{W^* \to \bar{q}q'g} \frac{d^{n-1}p_g}{2E_g(2\pi)^{n-1}} \Theta(2s_{min} - s_{\bar{q}g} - s_{q'g}). \tag{E.10}$$

Substituting Eqs. E.3, E.1 and E.9 into Eq. E.10, we obtain

$$I_{\text{soft}}^{W^* \to \bar{q}q'g} = \frac{1}{8\pi} \frac{(4\pi)^{\epsilon}}{\Gamma(1-\epsilon)} 4g_s^2 \mu^{2\epsilon} C_F$$

$$\times \int_0^{\frac{s_{min}}{\sqrt{\hat{s}}}} \frac{E_g^{1-2\epsilon}}{E_g^2} dE_g \int_{-1}^1 \frac{(\sin^2 \theta_1)^{-\epsilon}}{(1+\cos \theta_1)(1-\cos \theta_1)} d\cos \theta_1. \quad (E.11)$$

It is straightforward to integrate over the soft gluon energy,

$$\int_{0}^{\frac{s_{min}}{\sqrt{\hat{s}}}} E_g^{-1-2\epsilon} dE_g = -\frac{1}{2\epsilon} \left( \frac{s_{min}}{\sqrt{\hat{s}}} \right)^{-2\epsilon} + \mathcal{O}(s_{min}), \tag{E.12}$$

but the integration over the polar angle,  $I_{\theta}$ , is more complicated as shown below. At first we simplify the integration over  $\theta_1$  angle by changing variables  $\cos \theta_1 \to t-1$ ,

$$I_{\theta} = \int_{-1}^{1} \frac{d\cos\theta_{1}}{(1+\cos\theta_{1})^{1+\epsilon} (1-\cos\theta_{1})^{1+\epsilon}}$$

$$= 2 \int_{-1}^{0} \frac{d\cos\theta_{1}}{(1+\cos\theta_{1})^{1+\epsilon} (1-\cos\theta_{1})^{1+\epsilon}}$$

$$= 2^{-\epsilon} \int_{0}^{1} t^{-1-\epsilon} (2-t)^{-1-\epsilon} dt.$$
(E.13)

This is just a hyper-geometry function which is defined as

$$_{2}F_{1}(a,b,c,z) \equiv rac{\Gamma(c)}{\Gamma(b)\Gamma(c-b)} \int_{0}^{1} (1-x)^{c-b-1} x^{b-1} (1-xz)^{-a} dx,$$

therefore,  $I_{\theta}$  becomes

$$I_{\theta} = 2^{-\epsilon} \frac{\Gamma(-\epsilon)\Gamma(1)}{\Gamma(1-\epsilon)} {}_{2}F_{1}(1+\epsilon, -\epsilon, 1-\epsilon, \frac{1}{2})$$

$$= 2^{-\epsilon} \left(-\frac{1}{\epsilon}\right) \left(1 - \frac{1}{2}\right)_{2}^{\epsilon} F_{1}(-\epsilon, -2\epsilon, 1-\epsilon, -1)$$

$$= -\left[\frac{1}{\epsilon} - 2\ln 2 + 2\epsilon \ln^{2} 2 - \frac{\pi^{2}}{6}\epsilon\right] + \mathcal{O}(\epsilon^{2}), \tag{E.14}$$

where we have used the properties of the hyper-geometry functions:

$$_{2}F_{1}(a,b,c,z) = (1-z)^{-b}{_{2}F_{1}(b,c-a,c,\frac{z}{z-1})},$$

and

$$_{2}F_{1}(\alpha\epsilon, \beta\epsilon, 1 + \gamma\epsilon, z) = 1 + \epsilon^{2}\alpha\beta \text{Li}_{2}(z).$$

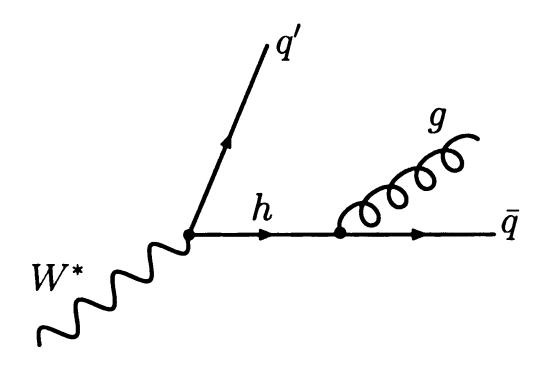


Figure E.2: Kinematics of  $\bar{q}, q'$  and g in the collinear region  $g \parallel \bar{q}$  in  $W^* \to \bar{q}q'g$ .

Substituting Eqs. E.12 and E.14 into Eq. E.11, we obtain the soft factor as

$$I_{\text{soft}}^{W^* \to \bar{q}q'g} = \frac{g_s^2}{16\pi^2} \frac{C_F}{\Gamma(1-\epsilon)} \left(\frac{4\pi\mu_d^2}{s_{min}}\right)^2 \left\{\frac{2}{\epsilon^2} - \frac{4\ln 2}{\epsilon} - \frac{2}{\epsilon}\ln\left(\frac{s_{min}}{\hat{s}}\right) + 4\ln^2 2 - \frac{\pi^2}{3} + \ln^2\left(\frac{s_{min}}{\hat{s}}\right) + 4\ln 2\ln\left(\frac{s_{min}}{\hat{s}}\right)\right\}.$$
 (E.15)

#### E.1.2 Collinear contribution

In addition to being singular in the soft gluon region, the matrix elements are also singular in the collinear region  $(\mathcal{F}_3)$  where the matrix elements exhibit an overall factorization. In the limit  $g \parallel \bar{q}$ , we define

$$p_g \xrightarrow{g \parallel \bar{q}} (1 - \xi) p_h, \qquad p_{\bar{q}} \xrightarrow{g \parallel \bar{q}} \xi p_h,$$

with  $p_h = p_g + p_{\bar{q}}$ , as shown in Fig. E.2.

In the collinear limit,

$$\Theta(\left|s_{q'g}\right| - 2s_{min})\Theta(s_{min} - \left|s_{\bar{q}g}\right|) \left|\mathcal{M}(W^* \to \bar{q}q'g)\right|^2 \xrightarrow{g \parallel \bar{q}} \hat{c}^{\bar{q}g \to \bar{q}} \left|\mathcal{M}(W^* \to \bar{q}q')\right|^2,$$

where the collinear factor  $\hat{c}^{\bar{q}g \to \bar{q}}$  is defined as

$$\hat{c}^{\bar{q}g \to \bar{q}} = g_s^2 \mu^{2\epsilon} C_F \frac{P^{\bar{q}g \to \bar{q}}(\xi)}{2p_g \cdot p_{\bar{q}}}.$$

The function  $P^{\bar{q}g \to \bar{q}}$  is related to the Altarelli-Parisi splitting function:

$$P^{\bar{q}g \to \bar{q}}(\xi) = \begin{cases} 2\frac{1+\xi^2 - \epsilon(1-\xi)^2}{1-\xi}, & \text{in DREG scheme,} \\ 2\frac{1+\xi^2}{1-\xi}, & \text{in DRED scheme.} \end{cases}$$
(E.16)

In the collinear region, we get

$$\left| s_{q'g} \right| = \left| p_g + p_{q'} \right| = (1 - \xi) s_{q'h} = (1 - \xi) \hat{s},$$

therefore, the collinear phase space boundary condition can be written as

$$\Theta(\left|s_{q'g}\right| - 2s_{min})\Theta(s_{min} - \left|s_{\bar{q}g}\right|) = \Theta(s_{min} - \left|s_{\bar{q}g}\right|)\Theta((1 - \xi)\hat{s} - 2s_{min}).$$

The phase space in the collinear region  $(p_{\bar{q}} \parallel p_g)$  can also be factorized as

$$\frac{d^{n-1}p_{\bar{q}}}{(2\pi)^{n-1}2E_{\bar{q}}}\frac{d^{n-1}p_g}{(2\pi)^{n-1}2E_q} = \frac{1}{16\pi^2}\frac{(4\pi)^{\epsilon}}{\Gamma(1-\epsilon)}\left[s_{\bar{q}g}\xi(1-\xi)\right]^{-\epsilon}ds_{\bar{q}g}d\xi \times \left(\frac{d^{n-1}p_h}{(2\pi)^{n-1}2E_h}\right).$$

After integrating over the collinear phase space for the case  $g \parallel \bar{q}$ , we obtain the collinear factor

$$\begin{split} I_{g||\bar{q}}^{W*\to\bar{q}q'g} &= \int_{0}^{s_{min}} ds_{\bar{q}g} \int_{0}^{1-\frac{2s_{min}}{\hat{s}}} d\xi \left[ 2g_{s}^{2}\mu^{2\epsilon}C_{F} \frac{p^{\bar{q}g\to\bar{q}}}{s_{\bar{q}g}} \right] \frac{1}{16\pi^{2}} \frac{(4\pi)^{\epsilon}}{\Gamma(1-\epsilon)} \left[ s_{\bar{q}g}\xi(1-\xi) \right]^{-\epsilon} \\ &= \frac{g_{s}^{2}}{8\pi^{2}} \frac{(4\pi\mu^{2})^{\epsilon}}{\Gamma(1-\epsilon)} C_{F} \int_{0}^{s_{min}} s_{\bar{q}g}^{-1-\epsilon} ds_{\bar{q}g} \int_{0}^{1-\frac{2s_{min}}{\hat{s}}} d\xi \, P^{\bar{q}g\to\bar{q}}(\xi) \left[ \xi(1-\xi) \right]^{-\epsilon} (\text{E}.17) \end{split}$$

It is straightforward to integrate over the invariant mass of  $\bar{q}$  and g  $(s_{\bar{q}g})$ ,

$$\int_0^{s_{min}} s_{\bar{q}g}^{-1-\epsilon} ds_{\bar{q}g} = -\frac{1}{\epsilon} s_{min}^{-\epsilon} + \mathcal{O}(s_{min}), \tag{E.18}$$

but the integration over the momentum fraction  $\xi$  ( $I_{\xi}$ ) is regularization scheme dependent due to the splitting kernel (cf. Eq. E.16), therefore needs to be calculated

separately in different scheme. In the DRED scheme,

$$I_{\xi}^{DRED} = \int_{0}^{1 - \frac{2s_{min}}{\hat{s}}} d\xi \frac{1 + \xi^{2}}{1 - \xi} [\xi(1 - \xi)]^{-\epsilon}$$

$$= \int_{0}^{1 - \frac{2s_{min}}{\hat{s}}} d\xi \left\{ \frac{1 + \xi^{2}}{1 - \xi} - (1 + \xi)^{2} \left( \frac{\ln \xi}{1 - \xi} + \frac{\ln(1 - \xi)}{1 - \xi} \right) \epsilon \right\}$$

$$= -2 \left( \ln \frac{2s_{min}}{\hat{s}} + \frac{3}{4} \right) - 3 + \frac{\pi^{2}}{3} + \ln^{2} \frac{2s_{min}}{\hat{s}} + \mathcal{O}(s_{min}), \quad (E.19)$$

while in the DREG scheme,

$$I_{\xi}^{DREG} = -2\left(\ln\frac{2s_{min}}{\hat{s}} + \frac{3}{4}\right) - \frac{7}{2} + \frac{\pi^2}{3} + \ln^2\frac{2s_{min}}{\hat{s}} + \mathcal{O}(s_{min}).$$
 (E.20)

Substituting Eqs. E.18, E.19 and E.20 into Eq. E.17, and also considering the contribution from the region  $p_g \parallel p_{q'}$ , we obtain the collinear factor

$$I_{\text{col}}^{W^* \to \bar{q}q'g} = \frac{g_s^2}{16\pi^2} \frac{C_F}{\Gamma(1-\epsilon)} \left(\frac{4\pi\mu_d^2}{s_{min}}\right)^{\epsilon}$$

$$\times \left\{ \frac{4}{\epsilon} \ln\left(\frac{2s_{min}}{\hat{s}}\right) + \frac{3}{\epsilon} - \frac{2\pi^2}{3} - 2\ln^2\left(\frac{2s_{min}}{\hat{s}}\right) + I_{\text{Scheme}}^{W^* \to \bar{q}q'}(\tilde{E}) \right\}$$

where the scheme dependent factor  $I_{\text{Scheme}}^{W^* \to \bar{q}q'(\text{col})}$  is

$$I_{\text{Scheme}}^{W^* \to \bar{q}q'(\text{col})} = \begin{cases} 7 & \text{in DREG scheme,} \\ 6 & \text{in DRED scheme.} \end{cases}$$

### E.2 $W^* \rightarrow t\bar{b}$

#### E.2.1 Soft contribution

Under the soft approximation, in the soft region  $(\mathcal{F}_2)$ , the squared matrix element can be written as a factor multiplying the squared Born matrix element:

$$\Theta(2s_{min} - s_{tg} - s_{\bar{b}g}) \left| \mathcal{M}(W^* \to t\bar{b}g) \right|^2 \xrightarrow{p_g \to 0} \hat{f}_s^{W^* \to tbg} \left| \mathcal{M}(W^* \to t\bar{b}) \right|,$$

where we have defined the  $\emph{eikonal}$  factor  $\hat{f}_s^{W^* \rightarrow t\bar{b}g}$  as:

$$\hat{f}_s^{W^* \to t\bar{b}g} = g_s C_F \mu^{2\epsilon} \frac{4(2p_t \cdot p_{\bar{b}})}{(2p_t \cdot p_g)(2p_{\bar{b}} \cdot p_g)} - \frac{4m_t^2}{(2p_t \cdot p_g)^2}.$$

In the c.m. frame of t and  $\bar{b}$  system, we can choose the explicit momentum of final state particles as follows:

$$p_t = (E_t, 0, 0, p_t),$$

$$p_{\bar{b}} = (E_t, 0, 0, -E_t),$$

$$p_a = (E_a, 0, E_a \sin \theta, E_a \cos \theta),$$

where  $E_t$ ,  $E_b$  and  $E_g$  is the energy of top quark, anti-bottom quark and gluon energy, respectively, and  $\theta$  is the angle between the gluon and the top quark. It is easy to show the eikonal factor can be written as

$$\hat{f}_s^{W^* \to t\bar{b}g} = \frac{1}{E_q^2 E_t} \left( \frac{2\sqrt{t_{tb} + m^2}}{(1 + \cos\theta)(1 - \beta_{tb}\cos\theta)} - \frac{m_t^2}{E_t(1 - \beta_{tb}\cos\theta)^2} \right), \quad (E.22)$$

where

$$t_{tb} = 2\beta E_t^2 (1+\beta),$$

$$\beta_{tb} = \frac{t_{tb}}{t_{tb} + 2m^2},$$

$$E_t = \frac{t_{tb} + 2m_t^2}{2\sqrt{t_{tb} + m_t^2}}.$$

Now let us calculate the phase space boundary condition with the choice of momentum above. We have

$$t_{bg} = 2\beta E_t E_g (1 + \cos \theta),$$
  
 $t_{tg} = 2E_t E_g (1 - \beta \cos \theta),$ 

therefore,

$$t_{tg} + t_{bg} = 2E_t E_g (1+\beta)$$
  
=  $2E_g \sqrt{t_{tb} + m_t^2}$ . (E.23)

Substituting Eq. E.23 into the soft phase space boundary condition  $\mathcal{F}_2$ , we obtain

$$E_g \le \frac{s_{min}}{\sqrt{t_{tb} + m_t^2}} \equiv E_g^{max}.$$

We then integrate the eikonal factors  $\hat{f}_s^{W^* \to t \bar{b} g}$  in d dimensions over the soft gluon momentum,

$$I_{\text{soft}}^{W^* \to t\bar{b}g} = \frac{g_s^2}{16\pi^2} \frac{(4\pi\mu^2)^{\epsilon}}{\Gamma(1-\epsilon)} C_F \int_0^{E_g^{max}} dE_g E_g^{-1-2\epsilon}$$

$$\int_{-1}^1 d\cos\theta \sin^{-2\epsilon}\theta \frac{1}{E_t} \left( \frac{2\sqrt{t_{tb} + m_t^2}}{(1+\cos\theta)(1-\beta\cos\theta)} - \frac{m_t^2}{E_t(1-\beta\cos\theta)^2} \right),$$

and obtain the soft factor

$$I_{\text{soft}}^{W^* \to t\bar{b}g} = \frac{g_s^2}{16\pi^2} \frac{C_F}{\Gamma(1-\epsilon)} \left(\frac{4\pi\mu_d^2}{s_{min}}\right)^2 \left(\frac{s_{min}}{\hat{s}_1 + m_t^2}\right)^{-\epsilon}$$

$$\times \left\{\frac{1}{\epsilon^2} - \frac{1}{\epsilon} \left[\ln\left(1 + \frac{\hat{s}_1}{m_t^2}\right) + 2\ln 2 - 1\right]\right\}$$

$$-\frac{\pi^2}{6} + 2\ln^2 2 - 2\ln 2 + \left[2\ln 2 + \frac{\hat{s}_1 + 2m_t^2}{\hat{s}_1}\right] \ln \left(1 + \frac{\hat{s}_1}{m_t^2}\right)$$
$$-\frac{1}{2}\ln^2 \left(1 + \frac{\hat{s}_1}{m_t^2}\right) - 2\text{Li}_2\left(\frac{\hat{s}_1}{\hat{s}_1 + m_t^2}\right)\right\},$$

where  $\hat{s}_1 \equiv t_{tb}$ .

#### E.2.2 Collinear contribution

In the collinear region  $(\mathcal{F}_3)$ , where  $g\parallel \bar{b}$ , the matrix elements exhibit an overall factorization as

$$\Theta(s_{tg} - 2s_{min})\Theta(s_{min} - s_{\bar{b}g}) \left| \mathcal{M}(W^* \to t\bar{b}g) \right|^2 \xrightarrow{g \parallel \bar{b}} \hat{c}^{\bar{b}g \to \bar{b}}(\xi) \left| \mathcal{M}(W^* \to t\bar{b}) \right|^2,$$

where the collinear factor  $\hat{c}^{ar{b}g 
ightarrow ar{b}}$  is defined as:

$$\hat{c}^{\bar{b}g \to \bar{b}} = g_s^2 \mu^{2\epsilon} C_F \left[ \underbrace{\frac{P^{\bar{b}g \to \bar{b}}(\xi)}{2p_{\bar{b}} \cdot p_g}}_{I} - \underbrace{\frac{4m_t^2}{(2p_t \cdot p_g)^2}}_{II} \right]. \tag{E.24}$$

where  $P^{\bar{b}g \to \bar{b}}(\xi)$  is same as Eq. (E.16).

Integrating the first term in Eq. E.24 over the collinear phase space is same as the one we have shown in the calculation of  $W^* \to \bar{q}q'$ , so we only present the final result:

$$I_{\text{col}}^{W^* \to t\bar{b}g}(I) = \frac{g_s^2}{16\pi^2} \frac{C_F}{\Gamma(1-\epsilon)} \left(\frac{4\pi\mu_d^2}{s_{min}}\right)^{\epsilon}$$

$$\times \left\{ \frac{2}{\epsilon} \left[ \ln^2 \left(\frac{2s_{min}}{\hat{s}}\right) + \frac{3}{4} \right] - \ln^2 \left(\frac{2s_{min}}{\hat{s}}\right) - \frac{\pi^2}{3} + I_{\text{Scheme}}^{W^* \to t\bar{b}g(\text{col})} \right\}$$
(E.25)

where the scheme dependent factor  $I^{W^* \to t\bar{b}g(\text{col})}_{\text{Scheme}}$  is

$$I_{\text{Scheme}}^{W^* \to t\bar{b}g(\text{col})} = \begin{cases} \frac{7}{2} & \text{in DREG scheme,} \\ 3 & \text{in DRED scheme.} \end{cases}$$

The second term in Eq. E.24 contributes

$$\begin{split} I_{\text{col}}^{W^* \to t \bar{b} g}(II) &= -\frac{4g_s^2}{16\pi^2} \frac{(4\pi\mu^2)^{\epsilon}}{\Gamma(1-\epsilon)} C_F \frac{m_t^2}{t_{tb}^2} \\ &\times \int_0^{s_{min}} dt_{bg} \, t_{bg}^{-\epsilon} \int_0^{1-\frac{2s_{min}}{t_{tb}}} dz \, \left[ z(1-z) \right]^{2-\epsilon} \\ &= -\frac{g_s^2}{16\pi^2} \left( \frac{4\pi\mu^2}{s_{min}} \right)^{\epsilon} \frac{C_F}{\Gamma(1-\epsilon)} \frac{m_t^2}{t_{tb}^2} + \mathcal{O}(s_{min}). \end{split}$$

Summing up the contributions from the first term and the second term, we get the collinear factor

$$I_{\text{col}}^{W^* \to t\bar{b}g} = \frac{g_s^2}{16\pi^2} \frac{C_F}{\Gamma(1-\epsilon)} \left(\frac{4\pi\mu_d^2}{s_{min}}\right)^{\epsilon}$$

$$\times \left\{ \frac{2}{\epsilon} \left[ \ln^2 \left(\frac{2s_{min}}{\hat{s}}\right) + \frac{3}{4} \right] - \ln^2 \left(\frac{2s_{min}}{\hat{s}}\right) - \frac{\pi^2}{3} - \frac{m_t^2}{\hat{s}_1} + I_{\text{Scheme}}^{W^* \to t\bar{b}g(\text{col})} \right\}$$

# Appendix F

## $\Gamma$ function

In computations, it will be necessary to understand the behavior of the  $\Gamma$  function in the vicinity of its poles. The following Laurent expansions, in the limit  $\delta \to 0$ , should be sufficient:

$$\Gamma(\delta) = \frac{1}{\delta} - \gamma_E + \mathcal{O}(\delta). \tag{F.1}$$

From this expansion, it is easy to prove

$$\Gamma(\delta - n) = \frac{1}{(\delta - 1)(\cdots)(\delta - n)} \Gamma(\delta)$$

$$= \frac{(-1)^n}{n!} \left( \frac{1}{\delta} + 1 + \frac{1}{2} + \cdots + \frac{1}{n} - \gamma_E \right) + \mathcal{O}(\delta), \tag{F.2}$$

where  $\gamma_E$ , Euler's constant, and  $\gamma_n$  are give by

$$\gamma_E \simeq .5772,$$
 (F.3)

$$\gamma_n \equiv 1 + \frac{1}{2} + \dots + \frac{1}{n} - \gamma_E. \tag{F.4}$$

Using the relation  $\Gamma(z)\Gamma(1-z)=\pi/\sin(\pi z)$  with  $z=\delta$ , we can compute the coefficients of positive powers of  $\delta$  in the Laurent expansion of  $\Gamma(\delta)$ . For example,

$$\Gamma(\delta) = \frac{1}{\delta} - \gamma_E + \left(\frac{\pi^2}{12} + \frac{\gamma_E^2}{2}\right) \delta + \mathcal{O}(\delta^2).$$
 (F.5)

Since the  $\Gamma$ 's have simple poles, it is necessary to expand every other  $\delta$ -dependent factor up to order  $\delta$  if we are to get the correct finite part as  $\delta \to 0$ . The following Laurent expansion will be sufficient:

$$z^{\delta} = 1 + \delta \ln z + \mathcal{O}(\delta^2). \tag{F.6}$$

Commonly, we shall use these expansion in the combination, for example,

$$\Gamma(\delta - n)z^{\delta} = \frac{(-1)^n}{n!} \left(\frac{1}{\delta} + \gamma_n + \mathcal{O}(\delta)\right) (1 + \delta \ln z + \mathcal{O}(\delta))$$

$$= \frac{(-1)^n}{n!} \left(\frac{1}{\delta} + \gamma_n + \ln z\right) + \mathcal{O}(\delta). \tag{F.7}$$

Some useful  $\Gamma$  functions are listed below, where we have change the argument of  $\Gamma$  function to be the small dimension  $\epsilon$  in the dimensional regularization,

$$\Gamma(1 - \epsilon) = -\epsilon \Gamma(\epsilon) + \mathcal{O}(\epsilon), \tag{F.8}$$

$$\Gamma(1+\epsilon) = 1 - \gamma_E \epsilon + \frac{\epsilon^2}{2} (\gamma_E^2 + \frac{\pi^2}{6}) + \mathcal{O}(\epsilon^3), \tag{F.9}$$

$$\Gamma(-\epsilon) = -\frac{1}{\epsilon} - \gamma_E + \mathcal{O}(\epsilon),$$
 (F.10)

$$\Gamma(1-2\epsilon) = 1 + 2\gamma_E \epsilon + \mathcal{O}(\epsilon^2),$$
 (F.11)

$$\frac{\Gamma^2(1-\epsilon)}{\Gamma(1-2\epsilon)} = 1 - \frac{\pi^2}{6}\epsilon^2 + \mathcal{O}(\epsilon^3). \tag{F.12}$$

### **Bibliography**

- [1] P. Azzi, i in. Combination of cdf and d0 results on the top-quark mass. 2004.
- [2] A. Sirlin. Ten years of precision electroweak physics. Int. J. Mod. Phys., A15S1:398-415, 2000.
- [3] Ikaros I. Y. Bigi, Yuri L. Dokshitzer, Valery A. Khoze, Johann H. Kuhn, Peter M. Zerwas. Production and decay properties of ultraheavy quarks. *Phys. Lett.*, B181:157, 1986.
- [4] C.-P. Yuan. Strategies for probing cp properties in the top quark system at e-e+ and hadron colliders. *Mod. Phys. Lett.*, A10:627-638, 1995.
- [5] David Atwood, Shaouly Bar-Shalom, Gad Eilam, Amarjit Soni. Cp nonconservation in  $p\bar{p} \to t\bar{b}x$  at the tevatron. Phys. Rev., D54:5412-5416, 1996.
- [6] S. Bar-Shalom, D. Atwood, A. Soni. Cp violation in single top quark production and decay via p anti-p -> t anti-b + x -> w+ b anti-b + x within the mssm: A possible application for measuring arg(a(t)) at hadron colliders. *Phys. Rev.*, D57:1495-1517, 1998.
- [7] Gordon L. Kane, G. A. Ladinsky, C.-P. Yuan. Using the top quark for testing standard model polarization and cp predictions. *Phys. Rev.*, D45:124-141, 1992.
- [8] Douglas O. Carlson, Ehab Malkawi, C.-P. Yuan. Probing the couplings of the top quark to gauge bosons. *Phys. Lett.*, B337:145–151, 1994.
- [9] Thomas G. Rizzo. Single top quark production as a probe for anomalous moments at hadron colliders. *Phys. Rev.*, D53:6218-6225, 1996.
- [10] Ehab Malkawi, Tim Tait, C. P. Yuan. A model of strong flavor dynamics for the top quark. *Phys. Lett.*, B385:304-310, 1996.
- [11] Tim Tait, C.-P. Yuan. Anomalous t-c-g coupling: The connection between single top production and top decay. *Phys. Rev.*, D55:7300-7301, 1997.
- [12] A. Datta, X. Zhang. Non-universal correction to z -> b anti-b and single top quark production at tevatron. *Phys. Rev.*, D55:2530-2532, 1997.
- [13] Chong Sheng Li, Robert J. Oakes, Jin Min Yang. Supersymmetric electroweak corrections to single top quark production at the fermilab tevatron. *Phys. Rev.*, D55:5780–5785, 1997.

- [14] Elizabeth H. Simmons. New gauge interactions and single top quark production. *Phys. Rev.*, D55:5494-5500, 1997.
- [15] K. Whisnant, Jin-Min Yang, Bing-Lin Young, X. Zhang. Dimension-six cp-conserving operators of the third-family quarks and their effects on collider observables. *Phys. Rev.*, D56:467-478, 1997.
- [16] Philip Baringer, Pankaj Jain, Douglas W. McKay, Lesley L. Smith. Single top from technipion production. *Phys. Rev.*, D56:2914-2919, 1997.
- [17] Chong-Sheng Li, Robert J. Oakes, Jin-Min Yang, Hong-Yi Zhou. Supersymmetric qcd corrections to single top quark production at the fermilab tevatron. *Phys. Rev.*, D57:2009-2012, 1998.
- [18] Tim Tait, C.-P. Yuan. The phenomenology of single top quark production at the fermilab tevatron. hep-ph/9710372, 1997.
- [19] Ken-ichi Hikasa, K. Whisnant, Jin Min Yang, Bing-Lin Young. Probing anomalous top quark interactions at the fermilab tevatron collider. *Phys. Rev.*, D58:114003, 1998.
- [20] Tao Han, M. Hosch, K. Whisnant, Bing-Lin Young, X. Zhang. Single top quark production via fcnc couplings at hadron colliders. *Phys. Rev.*, D58:073008, 1998.
- [21] Hong-Jian He, C. P. Yuan. New method for detecting charged (pseudo-)scalars at colliders. *Phys. Rev. Lett.*, 83:28-31, 1999.
- [22] Edward Boos, Lev Dudko, Thorsten Ohl. Complete calculations of w b anti-b and w b anti-b + jet production at tevatron and lhc: Probing anomalous w t b couplings in single top production. *Eur. Phys. J.*, C11:473-484, 1999.
- [23] D. Espriu, J. Manzano. Measuring effective electroweak couplings in single top production at the lhc. *Phys. Rev.*, D65:073005, 2002.
- [24] Sally Dawson. The effective w approximation. Nucl. Phys., B249:42-60, 1985.
- [25] Scott S. D. Willenbrock, Duane A. Dicus. Production of heavy quarks from w gluon fusion. *Phys. Rev.*, D34:155, 1986.
- [26] C.-P. Yuan. A new method to detect a heavy top quark at the tevatron. *Phys. Rev.*, D41:42, 1990.
- [27] G. A. Ladinsky, C.-P. Yuan. The w top background to heavy higgs production. *Phys. Rev.*, D43:789–793, 1991.
- [28] S. Cortese, R. Petronzio. The single top production channel at tevatron energies. *Phys. Lett.*, B253:494–498, 1991.
- [29] R. K. Ellis, Stephen J. Parke. Top quark production by w gluon fusion. *Phys. Rev.*, D46:3785–3788, 1992.
- [30] Douglas O. Carlson, C.-P. Yuan. Studying the top quark via the w gluon fusion process. *Phys. Lett.*, B306:386–390, 1993.

- [31] G. Bordes, B. van Eijk. Calculating qcd corrections to single top production in hadronic interactions. *Nucl. Phys.*, B435:23-58, 1995.
- [32] T. Stelzer, S. Willenbrock. Single top quark production via q anti-q → t anti-b. *Phys. Lett.*, B357:125–130, 1995.
- [33] A. P. Heinson, A. S. Belyaev, E. E. Boos. Single top quarks at the fermilab tevatron. *Phys. Rev.*, D56:3114-3128, 1997.
- [34] Martin C. Smith, S. Willenbrock. Qcd and yukawa corrections to single-top-quark production via q qbar -> t bbar. Phys. Rev., D54:6696-6702, 1996.
- [35] S. Mrenna, C.-P. Yuan. Effects of qcd resummation on w+ h and t anti-b production at the tevatron. *Phys. Lett.*, B416:200-207, 1998.
- [36] T. Stelzer, Z. Sullivan, S. Willenbrock. Single-top-quark production via w-gluon fusion at next-to-leading order. *Phys. Rev.*, D56:5919-5927, 1997.
- [37] Stefano Moretti. Single-top production in the t w+- channel and higgs signals via h -> w+ w- at the large hadron collider. *Phys. Rev.*, D56:7427-7433, 1997.
- [38] T. Stelzer, Z. Sullivan, S. Willenbrock. Single top quark production at hadron colliders. *Phys. Rev.*, D58:094021, 1998.
- [39] A. S. Belyaev, E. E. Boos, L. V. Dudko. Single top quark at future hadron colliders: Complete signal and background study. *Phys. Rev.*, D59:075001, 1999.
- [40] Tim M. P. Tait. The tw- mode of single top production. *Phys. Rev.*, D61:034001, 2000.
- [41] A. Belyaev, E. Boos. Single top quark t w + x production at the lhc: A closer look. *Phys. Rev.*, D63:034012, 2001.
- [42] Tim Tait, C.-P. Yuan. Single top quark production as a window to physics beyond the standard model. *Phys. Rev.*, D63:014018, 2001.
- [43] B. Abbott, i in. Search for electroweak production of single top quarks in p anti-p collisions. *Phys. Rev.*, D63:031101, 2001.
- [44] D. Acosta, i in. Optimized search for single top quark production at the fermilab tevatron. *Phys. Rev.*, D69:052003, 2004.
- [45] D. Acosta, i in. Search for electroweak single top quark production in p anti-p collisions at  $s^{**}(1/2) = 1.96$ -tev. Phys. Rev., D71:012005, 2005.
- [46] A. Stange, William J. Marciano, S. Willenbrock. Higgs bosons at the fermilab tevatron. *Phys. Rev.*, D49:1354–1362, 1994.
- [47] A. Stange, William J. Marciano, S. Willenbrock. Associated production of higgs and weak bosons, with h → b anti-b, at hadron colliders. Phys. Rev., D50:4491-4498, 1994.

- [48] A. Belyaev, E. Boos, L. Dudko. Light and intermediate higgs boson bearch at tevatron energies. *Mod. Phys. Lett.*, A10:25–38, 1995.
- [49] Qing-Hong Cao, Shinya Kanemura, C.-P. Yuan. Associated production of cpodd and charged higgs bosons at hadron colliders. *Phys. Rev.*, D69:075008, 2004.
- [50] Kosuke Odagiri. Searching for heavy charged higgs bosons in the neutrino tau decay mode at lhc. hep-ph/9901432, 1999.
- [51] B. W. Harris, E. Laenen, L. Phaf, Z. Sullivan, S. Weinzierl. The fully differential single top quark cross section in next-to-leading order qcd. *Phys. Rev.*, D66:054024, 2002.
- [52] Zack Sullivan. Understanding single-top-quark production and jets at hadron colliders. *Phys. Rev.*, D70:114012, 2004.
- [53] Shouhua Zhu. Next-to-leading order qcd corrections to b g -> t w- at cern large hadron collider. hep-ph/0109269, 2001.
- [54] John Campbell, R. K. Ellis, Francesco Tramontano. Single top production and decay at next-to-leading order. *Phys. Rev.*, D70:094012, 2004.
- [55] Qing-Hong Cao, C. P. Yuan. Single top quark production and decay at next-to-leading order in hadron collision. *Phys. Rev.*, D71:054022, 2005.
- [56] Qing-Hong Cao, Reinhard Schwienhorst, C. P. Yuan. Next-to-leading order corrections to single top quark production and decay at tevatron. i: s-channel process. *Phys. Rev.*, D71:054023, 2005.
- [57] Qing-Hong Cao, Reinhard Schwienhorst, Jorge A. Benitez, Raymond Brock, C. P. Yuan. Next-to-leading order corrections to single top quark production and decay at the tevatron. ii: t-channel process. hep-ph/0504230, 2005.
- [58] Gerard 't Hooft, M. J. G. Veltman. Regularization and renormalization of gauge fields. *Nucl. Phys.*, B44:189-213, 1972.
- [59] Z. Bern, A. De Freitas, Lance J. Dixon, H. L. Wong. Supersymmetric regularization, two-loop qcd amplitudes and coupling shifts. *Phys. Rev.*, D66:085002, 2002.
- [60] K. Melnikov, Oleg I. Yakovlev. Final state interaction in the production of heavy unstable particles. *Nucl. Phys.*, B471:90-120, 1996.
- [61] W. Beenakker, A. P. Chapovsky, Frits A. Berends. Non-factorizable corrections to w pair production. *Phys. Lett.*, B411:203-210, 1997.
- [62] W. Beenakker, A. P. Chapovsky, Frits A. Berends. Non-factorizable corrections to w-pair production: Methods and analytic results. *Nucl. Phys.*, B508:17-63, 1997.
- [63] Warren Siegel. Supersymmetric dimensional regularization via dimensional reduction. *Phys. Lett.*, B84:193, 1979.

•e-	

- [64] D. M. Capper, D. R. T. Jones, P. van Nieuwenhuizen. Regularization by dimensional reduction of supersymmetric and nonsupersymmetric gauge theories. *Nucl. Phys.*, B167:479, 1980.
- [65] I. Jack, D. R. T. Jones, K. L. Roberts. Equivalence of dimensional reduction and dimensional regularization. Z. Phys., C63:151-160, 1994.
- [66] Michael S. Chanowitz, M. Furman, I. Hinchliffe. The axial current in dimensional regularization. *Nucl. Phys.*, B159:225, 1979.
- [67] Jurgen G. Korner, Michael M. Tung. Dimensional reduction methods in qcd. Z. Phys., C64:255-265, 1994.
- [68] B. Kamal. Qcd corrections to spin dependent drell-yan and a global subtraction scheme. *Phys. Rev.*, D53:1142–1152, 1996.
- [69] G. Passarino, M. J. G. Veltman. One loop corrections for e+ e- annihilation into mu+ mu- in the weinberg model. *Nucl. Phys.*, B160:151, 1979.
- [70] Guido Altarelli, G. Parisi. Asymptotic freedom in parton language. Nucl. Phys., B126:298, 1977.
- [71] T. Kinoshita. Mass singularities of feynman amplitudes. J. Math. Phys., 3:650–677, 1962.
- [72] T. D. Lee, M. Nauenberg. Degenerate systems and mass singularities. *Phys. Rev.*, 133:B1549–B1562, 1964.
- [73] F. Gutbrod, G. Kramer, G. Schierholz. Higher order qcd corrections to the three jet cross- sections: Bare versus dressed jets. Z. Phys., C21:235, 1984.
- [74] H. Baer, J. Ohnemus, J. F. Owens. A next-to-leading logarithm calculation of jet photoproduction. *Phys. Rev.*, D40:2844, 1989.
- [75] F. Aversa, M. Greco, P. Chiappetta, J. P. Guillet. Jet inclusive production to o (alpha-s\*\*3): Comparison with data. *Phys. Rev. Lett.*, 65:401-403, 1990.
- [76] W. T. Giele, E. W. N. Glover. Higher order corrections to jet cross-sections in e+ e- annihilation. *Phys. Rev.*, D46:1980-2010, 1992.
- [77] W. T. Giele, E. W. N. Glover, David A. Kosower. Higher order corrections to jet cross-sections in hadron colliders. *Nucl. Phys.*, B403:633-670, 1993.
- [78] Stephane Keller, Eric Laenen. Next-to-leading order cross sections for tagged reactions. *Phys. Rev.*, D59:114004, 1999.
- [79] R. K. Ellis, D. A. Ross, A. E. Terrano. The perturbative calculation of jet structure in e+ e- annihilation. *Nucl. Phys.*, B178:421, 1981.
- [80] Stephen D. Ellis, Zoltan Kunszt, Davison E. Soper. The one jet inclusive cross-section at order alpha-s\*\*3. 1. gluons only. *Phys. Rev.*, D40:2188, 1989.
- [81] S. Bethke, Z. Kunszt, D. E. Soper, W. James Stirling. New jet cluster algorithms: Next-to-leading order qcd and hadronization corrections. *Nucl. Phys.*, B370:310-334, 1992.

- [82] Michelangelo L. Mangano, Paolo Nason, Giovanni Ridolfi. Heavy quark correlations in hadron collisions at next-to-leading order. Nucl. Phys., B373:295-345, 1992.
- [83] S. Frixione, Z. Kunszt, A. Signer. Three-jet cross sections to next-to-leading order. *Nucl. Phys.*, B467:399-442, 1996.
- [84] S. Catani, M. H. Seymour. The dipole formalism for the calculation of qcd jet cross sections at next-to-leading order. *Phys. Lett.*, B378:287-301, 1996.
- [85] S. Catani, M. H. Seymour. A general algorithm for calculating jet cross sections in nlo qcd. *Nucl. Phys.*, B485:291-419, 1997.
- [86] Arnd Brandenburg, Peter Uwer. Next-to-leading order qcd corrections and massive quarks in e+ e- -> 3jets. Nucl. Phys., B515:279-320, 1998.
- [87] Chong Sheng Li, Robert J. Oakes, Tzu Chiang Yuan. Qcd corrections to t → w+ b. Phys. Rev., D43:3759-3762, 1991.
- [88] D. Amidei, R. Brock. Report of the tev2000 study group. 1996.
- [89] J. Pumplin, i in. New generation of parton distributions with uncertainties from global qcd analysis. *JHEP*, 07:012, 2002.
- [90] V. M. Abazov, i in. A precision measurement of the mass of the top quark. *Nature*, 429:638-642, 2004.
- [91] Qing-Hong Cao, C.-P. Yuan. Combined effect of qcd resummation and qed radiative correction to w boson observables at the tevatron. *Phys. Rev. Lett.*, 93:042001, 2004.
- [92] J. Alitti, i in. Inclusive jet cross-section and a search for quark compositeness at the cern anti-p p collider. *Phys. Lett.*, B257:232-240, 1991.
- [93] F. Abe, i in. The topology of three jet events in anti-p p collisions at  $s^{**}(1/2)$  = 1.8-tev. *Phys. Rev.*, D45:1448-1458, 1992.
- [94] S. Abachi, i in. Studies of topological distributions of the three- and four-jet events in p anti-p collisions at  $\sqrt{s} = 1800$  gev with the do detector. *Phys. Rev.*, D53:6000-6016, 1996.
- [95] S. Catani, Yuri L. Dokshitzer, B. R. Webber. The k-perpendicular clustering algorithm for jets in deep inelastic scattering and hadron collisions. *Phys. Lett.*, B285:291-299, 1992.
- [96] Stephen D. Ellis, Davison E. Soper. Successive combination jet algorithm for hadron collisions. *Phys. Rev.*, D48:3160–3166, 1993.
- [97] Stephen D. Ellis, Zoltan Kunszt, Davison E. Soper. The one jet inclusive cross-section at order alpha-s\*\*3: Gluons only. *Phys. Rev. Lett.*, 62:726, 1989.
- [98] William B. Kilgore, W. T. Giele. Next-to-leading order gluonic three jet production at hadron colliders. *Phys. Rev.*, D55:7183-7190, 1997.

- [99] Gordon L. Kane, C.-P. Yuan. How to study longitudinal ws in the tev region. *Phys. Rev.*, D40:2231, 1989.
- [100] Chuan-Ren Chen, F. Larios, C. P. Yuan. General analysis of single top production and w helicity in top decay. 2005.
- [101] Gregory Mahlon, Stephen J. Parke. Angular correlations in top quark pair production and decay at hadron colliders. *Phys. Rev.*, D53:4886-4896, 1996.
- [102] Stephen J. Parke, Yael Shadmi. Spin correlations in top quark pair production at e+ e- colliders. *Phys. Lett.*, B387:199-206, 1996.
- [103] Gregory Mahlon. Spin polarization in single top events. 1998.
- [104] Gregory Mahlon, Stephen J. Parke. Improved spin basis for angular correlation studies in single top quark production at the tevatron. *Phys. Rev.*, D55:7249–7254, 1997.
- [105] Gerard 't Hooft, M. J. G. Veltman. Scalar one loop integrals. Nucl. Phys., B153:365-401, 1979.
- [106] A. Denner. Techniques for calculation of electroweak radiative corrections at the one loop level and results for w physics at lep-200. Fortschr. Phys., 41:307-420, 1993.

